Distribution Agreement

In presenting this thesis or dissertation as a partial fulfillment of the requirements for an advanced degree from Emory University, I hereby grant to Emory University and its agents the non-exclusive license to archive, make accessible, and display my thesis or dissertation in whole or in part in all forms of media, now or hereafter known, including display on the world wide web. I understand that I may select some access restrictions as part of the online submission of this thesis or dissertation. I retain all ownership rights to the copyright of the thesis or dissertation. I also retain the right to use in future works (such as articles or books) all or part of this thesis or dissertation.

Signature:

_____	_____
Analia J. Vazquez Cegla	Date

Determining the effects of hyperglycemia on WT and CF bronchial epithelial barrier function

By

Analia J. Vazquez Cegla
Doctor of Philosophy
Graduate Division of Biological and Biomedical Science
Molecular and Systems Pharmacology
2024

Nael A. McCarty, Ph.D.
Advisor

Joshua D. Chandler, Ph.D.
Committee Member

Michael Koval, Ph.D.
Committee Member

Samantha M. Yeligar, M.S., Ph.D.
Committee Member

Accepted:

Kimberly Jacob Arriola, Ph.D, MPH
Dean of the James T. Laney School of Graduate Studies

Date

Determining the effects of hyperglycemia on WT and CF bronchial epithelial barrier function

By

Analia J. Vazquez Cegla
B.S., Smith College, May 2018

Advisor: Nael A. McCarty, Ph.D.

An abstract of
A dissertation submitted to the Faculty of
the James T. Laney School of Graduate Studies of Emory University
in partial fulfillment of the requirements for the degree of
Doctor of Philosophy
in Molecular and Systems Pharmacology
2024

Abstract

Determining the effects of hyperglycemia on WT and CF bronchial epithelial barrier function

By Analia J. Vazquez Cegla

Cystic fibrosis (CF) is an autosomal recessive disease caused by mutations in the cystic fibrosis transmembrane conductance regulator (CFTR) gene. Dysfunction of the CFTR protein, which primarily functions as anion channel, leads to multiorgan disease. However, the leading cause of CF mortality is respiratory failure. CFTR dysfunction in the lungs leads to inflammation, bacterial infections, as well as neutrophil recruitment and activation of neutrophils in the airways. All these factors lead to progressive lung tissue damage in CF. Highly effective modulator therapies (HEMTs) have drastically improved the life quality and increased the life expectancy of people with CF (pwCF) who are able to take them. As a result, CF co-morbidities might soon become the life-limiting factor for pwCF. The most common CF co-morbidity is cystic fibrosis related-diabetes (CFRD), affecting around half of pwCF by adulthood. CFRD is a devastating co-morbidity since it leads to more frequent pulmonary exacerbations and accelerates the rate of lung function decline. Despite the negative impact on patient health, the mechanisms driving CFRD pathophysiology are unknown. It is also unclear whether current HEMTs will have an impact on CFRD onset and disease progression. We hypothesize that hyperglycemia in the context of CF induces severe alterations in airway epithelial monolayers that prevent the formation of proper tight junctions (TJs) between cells. To investigate this hypothesis, we took several distinct yet complementary approaches. We studied the physiological changes experienced by 16HBE cells expressing either wildtype (WT) or ΔF508 CFTR (CF) in response to hyperglycemia. Further, we developed a programmable automated cell culture system (PACCS) capable of mimicking blood glucose fluctuations experienced by CFRD patients to better study CFRD *in vitro*. We also tested the effects of chronic hyperglycemia in a Scnn1b-Tg murine model, an *in vivo* model that develops similar lung pathology as seen in CF. Finally, we created a novel *in vitro* model to study the mechanisms driving neutrophil transmigration across airway epithelial monolayers. Using 16HBE cells, gene expression analyses identified claudin-4 (CLDN4) as a key tight junction protein dysregulated in CF cells in response to hyperglycemia. Further investigation into CLDN4 protein localization using a novel confocal microscopy technique revealed increased CLDN4 abundance at TJs in CF cells, which was further increased under hyperglycemic conditions. Treatment with HEMT reversed this trend, normalizing CLDN4 expression levels at TJs in CF cells toward WT levels. Bulk RNA sequencing showed differing transcriptional responses to hyperglycemia between WT and CF cells, thereby highlighting a few promising targets for further investigation. Culturing immortalized and primary airway epithelial cell monolayers using PACCS showed that our system could be successfully used to culture airway epithelial cells with meal-like glucose fluctuations, better mimicking CFRD-like conditions. Our studies using Scnn1b-Tg mice showed that chronic hyperglycemia aggravated the lung pathology of this mouse model, mimicking lung pathology seen in pwCF. Our novel *in vitro* assay to study neutrophil transmigration across epithelial monolayers showed that transmigrated PMNs differ from naïve PMNs, and that they are differentially impacted by the cell monolayer they transmigrate through. Further, pretreatment of the epithelial monolayers with high glucose media impacted PMN transmigration, with lower PMN transmigration efficiency in CF 16HBE cells. Overall, our research aims to identify mechanisms driving CFRD pathophysiology with the goal of informing the development of future therapeutics to prevent its deleterious effects.

Determining the effects of hyperglycemia on WT and CF bronchial epithelial barrier function

By

Analia J. Vazquez Cegla
B.S., Smith College, May 2018

Advisor: Nael A. McCarty, Ph.D.

A dissertation submitted to the Faculty of
the James T. Laney School of Graduate Studies of Emory University
in partial fulfillment of the requirements for the degree of
Doctor of Philosophy
in Molecular and Systems Pharmacology
2024

Acknowledgments

First, I would like to thank my parents who live in Paraguay for their love and support. I am forever thankful for the sacrifices they have made so that their children can have access to better education. Thank you for teaching me the value of education and to encourage me to dream big. It has been difficult to be so far away from them, but I hope that they are proud of the accomplishments I was able to achieve in this foreign country. I would have liked to spend Paraguayan holidays and family celebrations together. Thank you for understanding my decision to pursue higher education in the Unites States and being supportive throughout the process. I am also thankful for my siblings, aunts, uncles and cousins which have kept my parents accompanied while I am away. I am thankful for your encouragement and support.

Second, I want to thank my husband Alex who is living with cystic fibrosis (CF) and has cystic fibrosis related diabetes (CFRD). You are the main motivation that keeps me going when times are difficult. I am beyond amazed by your courage and determination. Despite the challenges you face every day, you still have such a calm and positive outlook on life. I am thankful for your calming presence and support during graduate school. We faced the challenges of graduate school together, while figuring out how to build a family in the process. We are a great team, and I cannot wait to see what the future holds for us in the years to come. Thank you for being an amazing husband, father, and friend. I hope we can teach our children the importance of education, and that they grow up to be joyful, resilient and kind individuals. I also want to thank our son, Hazael, for bringing so much joy and happiness into our lives. I hope you never lose your curious, goofy and loving personality. I am looking forward to seeing you become a big brother early next year!!

I would also like to thank my mentor, Dr. Nael McCarty, for making my time Emory a positive and rewarding experience. Thank you for your mentorship all these years, and for caring

about my development both at the professional and personal level. You are truly a kind and wonderful person, and I am forever thankful to have you as a mentor. I am also thankful to other McCarty Lab members for their unwavering support. Thank you to Guiying, Kymry, Jonica, and Jon for creating a positive environment for learning and growing as a scientist. I am thankful for their kindness and encouragement which kept me going through difficult times. Thank you for your positive energy and for always being available to help me think through tough problems. You made it fun to go to the lab every day, and I am thankful for all the small talk and inside jokes we have shared these last few years. I hope we stay in touch, and I cannot wait to see the amazing things you accomplish in the future!

Finally, I want to thank all my other mentors at Emory, especially the members of my dissertation committee Sam, Mike and Joshua. Thank you for taking the time to be part of my committee and provide feedback during the process. I had some very difficult times during my time at Emory. Your encouragement and support meant a lot to me, and they kept me going through those difficult times. I hope we stay in touch, and I wish you all the best in the years to come!

Table of Contents

List of Figures

List of Tables

List of Abbreviations

16HBE	Human bronchial epithelial cell line
16HBE-WT	16HBE cells expressing WT-CFTR
16HBE-ΔF508	16HBE cells expressing ΔF508-CFTR
ABC transporter	ATP-binding cassette transporter
ABS	ATP binding Site
ALI	Air-liquid interface
Amil	Amiloride
ASL	Airway surface liquid
ATP	Adenosine triphosphate
BALF	Bronchoalveolar lavage fluid
BP	Biological process
BSA	Bovine serum albumin
CC	Cellular compartment
cDNA	complementary DNA
CF	Cystic Fibrosis
CFBE	Human CF bronchial epithelial cell line
CFhBE	Primary CF human bronchial epithelial cells, with ΔF508-CFTR
CFKO	CFTR knockout
CFTR	Cystic Fibrosis transmembrane conductance regulator
CFRD	Cystic Fibrosis-related diabetes
CGM	Continuous glucose monitor
CLDN	Claudin
C_T	Cycle threshold
DAPI	4′,6-diamidino-2-phenylindole
DESeq	Differential expression sequence analysis tool
DMEM	Dulbecco's modified eagle medium
ENaC	Epithelial sodium channel
FBS	Fetal bovine serum
FDA	Food and Drug Administration
FEV1	Forced expiratory volume in the first second
fMLF	N-formylmethionyl-leucyl-phenylalanine
FSK	Forskolin
GO	Gene ontology
GSEA	Gene set enrichment analysis
HBE	Human bronchial epithelial cells from explant tissue
HEMT	Highly effective modulator therapy
HG	High glucose
IF	Immunofluorescence
IL	Interleukin
INH172	CFTR inhibitor
I_{sc}	Transepithelial short-circuit current
KRH	Krebbs Ringers HEPES buffer
LTB4	Leukotriene B4
MEM	Minimum essential medium

MF	Molecular function
NBD	Nucleotide binding domain
NG	Normal glucose
NGT	Normal glucose tolerance
NhBE	Primary normal human bronchial epithelial cells, with WT-CFTR
NPPB	5-Nitro-2-(3-phenylpropylamino) benzoic acid
PACCS	Programmable Automated Cell Culture System
PBS	Phosphate-buffered saline
PCR	Polymerase chain reaction
PFA	Paraformaldehyde
PMN	Polymorphonuclear leukocytes (neutrophils)
Pen/strep	Penicillin/streptomycin
pajd	P-value adjusted for multiple comparisons
pwCF	People with Cystic Fibrosis
qRT-PCR	Real-time quantitative reverse transcription polymerase chain reaction
RNA	Ribonucleic acid
SCNN1B	Sodium channel epithelial 1 subunit beta
STZ	Streptozotocin
TEER	Transepithelial electrical resistance
TJ	Tight Junction
Tg	Transgenic
TMD	Transmembrane domain
ZO	Zonula Occludens
WT	Wild-type

Chapter 1 – Introduction

1.1. Cystic Fibrosis: an overview

Cystic Fibrosis (CF) is an autosomal recessive disease caused by mutations in the Cystic Fibrosis Transmembrane Conductance Regulator (CFTR) gene located in chromosome 7 of the human genome[1]. It affects close to 40,000 people in the United States and around 105,000 people worldwide[2]. CF is the most common genetic disease affecting people of European descent, but it can affect people of any racial or ethnic group[3]. CF is a multiorgan disease. However, its leading cause of mortality is respiratory failure[4].

The CFTR gene encodes a transmembrane protein that is responsible for the movement of chloride ions (Cl^-) ions and bicarbonate, typically from inside to outside of cells[5]. Proper CFTR function maintains water homeostasis at the surface of tissues throughout the body, which is particularly important for the health of the lungs (**Figure 1.1a)**. Airway epithelial cells are covered by a thin mucus layer, which catches inhaled pathogens and potentially harmful debris for clearance out of the lungs. In healthy airways, the mucus layer is well hydrated and thin. Hair-like structures called cilia also line the airways, and their rhythmic beating helps move thin mucus out of the lungs[6]. However, mucus clearance from the lungs is impaired in CF due to dysfunctional CFTR (**Figure 1.1b**). Since Cl^- ion movement is impaired in CF, the mucus becomes dehydrated and viscous, making it difficult for cilia to clear it out of the lungs[7]. As a result, mucus accumulates and causes obstructions in the CF airways. This creates a beneficial environment for bacteria to colonize the lungs[8]. Periods of bacterial overgrowth and worsened pulmonary symptoms are called pulmonary exacerbations. Recurrent bacterial infections lead to inflammation and lung tissue damage[9]. This vicious cycle of infection, inflammation, and tissue damage progressively leads to lung function decline and eventually respiratory failure.

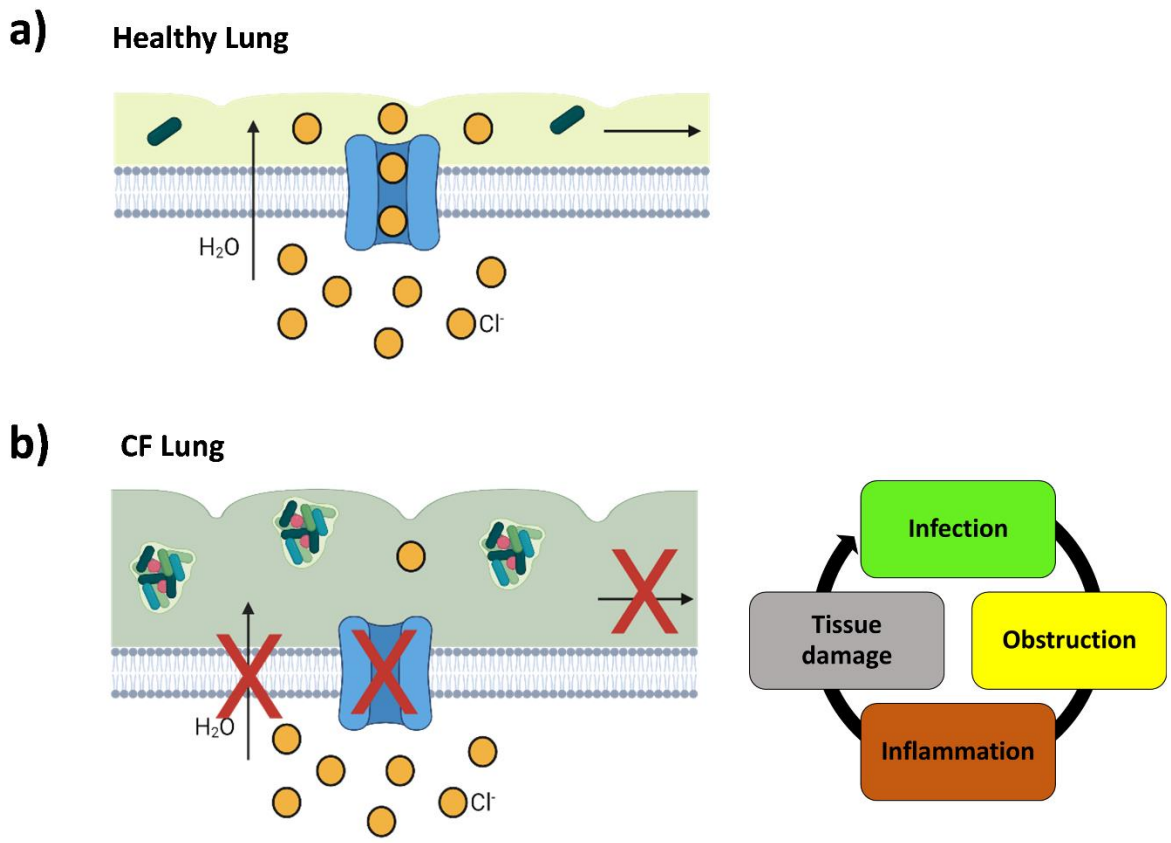

Figure 1.1. Proper CFTR function is essential to maintain a healthy lung.

a) Lungs are covered by a thin mucus layer, which traps pathogens and other harmful substances for clearance out of the lung. CFTR allows for the movement of chloride ions to the airway epithelial surfaces, which maintains the airways hydrated, keeping the mucus thin and easy to clear. b) In the CF airways, the mucus lining the airways is thick and difficult to clear due to CFTR dysfunction. Mucus plugs create an optimal environment for bacterial infections to take place. The CF airway is characterized by the vicious cycle between infection, obstruction, inflammation, and tissue damage (Created with BioRender).

1.1.1. Discovery of the disease and the CFTR gene

CF was first described by Dr. Dorothy Anderson in 1938, a brilliant pathologist who was investigating the mysterious cause of death of children who had failure to thrive. Dr. Anderson found large cysts and fibrosis in the pancreas of the autopsied patients[10]. Thus, she concluded that the pancreas was the primary organ affected and named the condition "cystic fibrosis of the pancreas." She also proposed that the disease was caused by a recessive mutation[11]. Dr. Anderson's work was groundbreaking as it identified CF as a separate disease, and it laid the foundation for future investigations. Over the following decades, significant advances were made to elucidate the genetic basis of the condition.

The CFTR gene was discovered in 1989 as a result of a collaboration between multiple research teams. The gene responsible for CF was mapped to the long arm of chromosome 7 with the use of positional cloning[12,13]. Through further research, scientists were able to isolate the CFTR gene, consisting of 189,000 base pairs and containing 27 exons[13]. Researchers were also able characterize the primary mutation responsible for CF disease, mutation ΔF508, found in around 88% of U.S. CF patients nowadays. This mutation leads to a phenylalanine deletion at position 508 of the CFTR protein sequence, causing the protein to misfold and be targeted for degradation before being trafficked to the plasma membrane. Currently, there are more than 2,500 CFTR mutations identified worldwide[14].

While the exact origin of CFTR mutations are unknown, there are hypotheses that state that bearing CFTR mutations could have been evolutionarily beneficial in ancient times to survive periods of crisis, such as the bubonic plaque [15,16]. More research is needed to identify the origins and potential evolutionary advantages of carrying CFTR mutations[14].

1.1.2. CFTR protein structure and function

The CFTR protein is a member of ATP-Binding Cassette (ABC) transporter superfamily and is also known as ABCC7[17]. Most ABC transporters use ATP binding and hydrolysis to actively transport substrates across the cell membrane, even against the concentration gradient in some cases. However, CFTR does not function as a regular ABC transporter[18]. Instead, CFTR is the only ABC transporter that works as an ion channel. CFTR allows the movement of chloride and bicarbonate across the membrane following their respective concentration gradients.

The CFTR gene is transcribed in the nucleus, translated in the Endoplasmic Reticulum (ER), and the protein is fully glycosylated in the Golgi before being trafficked to the outer cell membrane. The mature fully processed CFTR protein is 170-180 KDa, known as band C[19,20]. In terms of protein structure, the CFTR protein has two transmembrane domains (TMDs), each comprised of six transmembrane helices, two nucleotide binding domains (NDBs) and a regulatory domain (R-domain)[21]. A graphical representation is shown in **Figure 1.2**. For the channel to open, there are a series of steps that need to happen concurrently. The R-domain needs to be phosphorylated, primarily by cAMP-dependent protein kinase (PKA), and the NBDs need to bind ATP to dimerize. The channel closes when ATP is hydrolyzed, and the NBDs dissociate.

1.1.3. CFTR variants

CFTR mutations or variants are common worldwide. It is estimated that there are almost 10 million CF carriers in the United States alone[22]. As previously mentioned, the most common CFTR variant is ΔF508 found in ~80% of CF patients. However, there are more than 2,500 variants identified in the CFTR gene[14]. Generally, mutations producing lower amounts of functional CFTR protein are associated with increased disease severity[23]. Variants can be broadly classified into five classes, briefly described in **Table 1.1**.

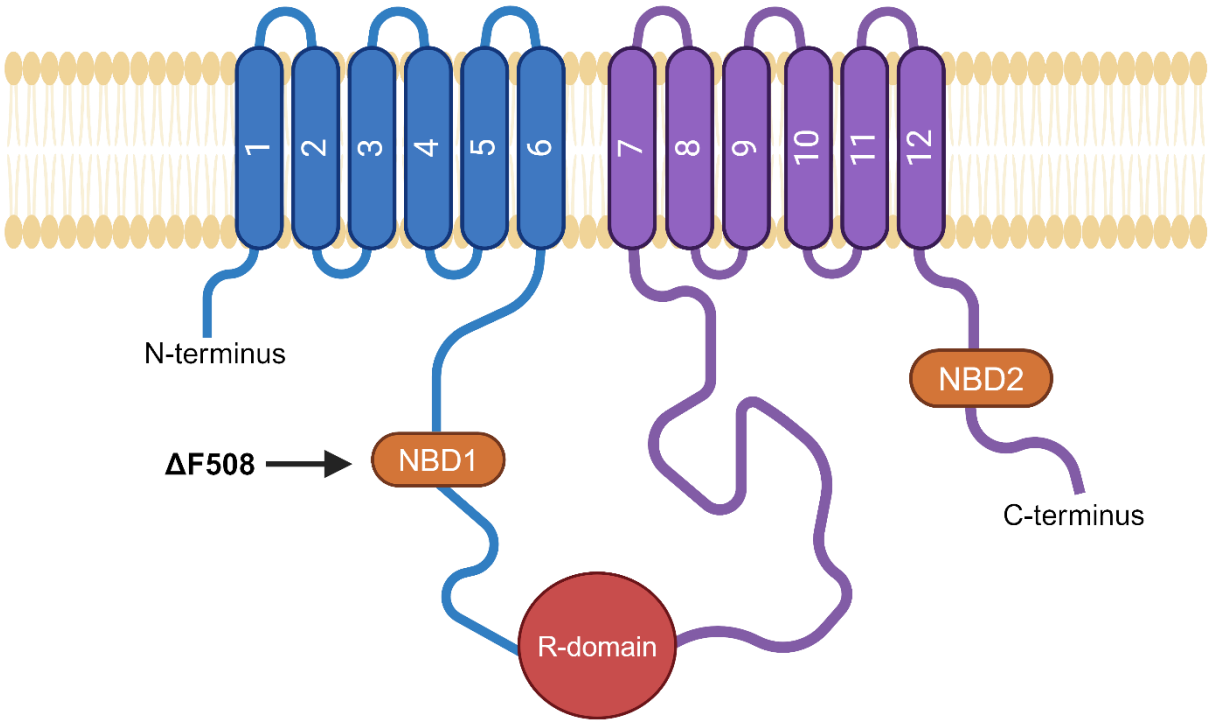

Figure 1.2. Graphical representation of the CFTR protein structure at the cell membrane.

The cartoon shows two transmembrane domains, each comprised of six transmembrane helices, two nucleotide-binding domains (NDBs) and a regulatory domain (R-domain). The location of the most common CFTR mutation, ΔF508, is highlighted at NBD1 (Created with BioRender).

Table 1.1. CFTR variant class description with examples, incidence, and disease severity information[24,25].

Class	Description	Examples	Incidence	Disease Severity
Class I	Impaired protein production	G552X W1282X R553X	22%	More severe
Class II	Impaired protein processing	ΔF508 N1303K I507del	88%	
Class III	Faulty protein gating	G551D S549N	6%	
Class IV	Faulty protein conductance	D1152H R347P R117H	6%	Less severe
Class V	Insufficient protein production	3849+10kbC→T 2789+5G→A A455E	5%	

CFTR variants are classified based on their effects on CFTR protein abundance or function, with variants leading to more severe disease receiving a lower class number[24,25]. Class I variants lead to no CFTR protein production. The most common variants in this class are nonsense mutations[26]. These mutations introduce a premature stop codon in the gene's sequence, leading to dysfunctional or truncated protein that is quickly targeted for degradation. Class II variants lead to some protein production, but the protein cannot be properly folded. The most common variant in this class is ΔF508, and it affects the large majority of CF patients[27]. Misfolded protein is degraded before reaching the cell surface. Class III variants lead to defects in CFTR protein gating. CFTR protein is trafficked to the cell surface, but it does not open to allow for movement of ions. The most common mutation found in this class is G551D[28]. Class IV variants lead to CFTR protein with faulty conductance at the cell surface. CFTR protein is produced and trafficked to the membrane, but it does not open and close properly. This interferes with appropriate ion movement. An example of a mutation in this class is R117H[29]. Class V variants lead to decreased amounts of CFTR protein at the cell surface. CFTR protein is produced and trafficked to the cell surface at insufficient amounts. However, CFTR protein that does reach the membrane is functional. An example of a mutation in this class is 3849+10kbC→T.

1.2. CF pathology

1.2.1. Organs affected by CF

Even though the effects of CF are usually associated with the lungs, CF affects multiple organ systems throughout the body. Some examples include the liver, pancreas, intestines, sweat glands, and the reproductive tract[30]. A graphical representation of organs affected by CF is shown in **Figure 1.3**.

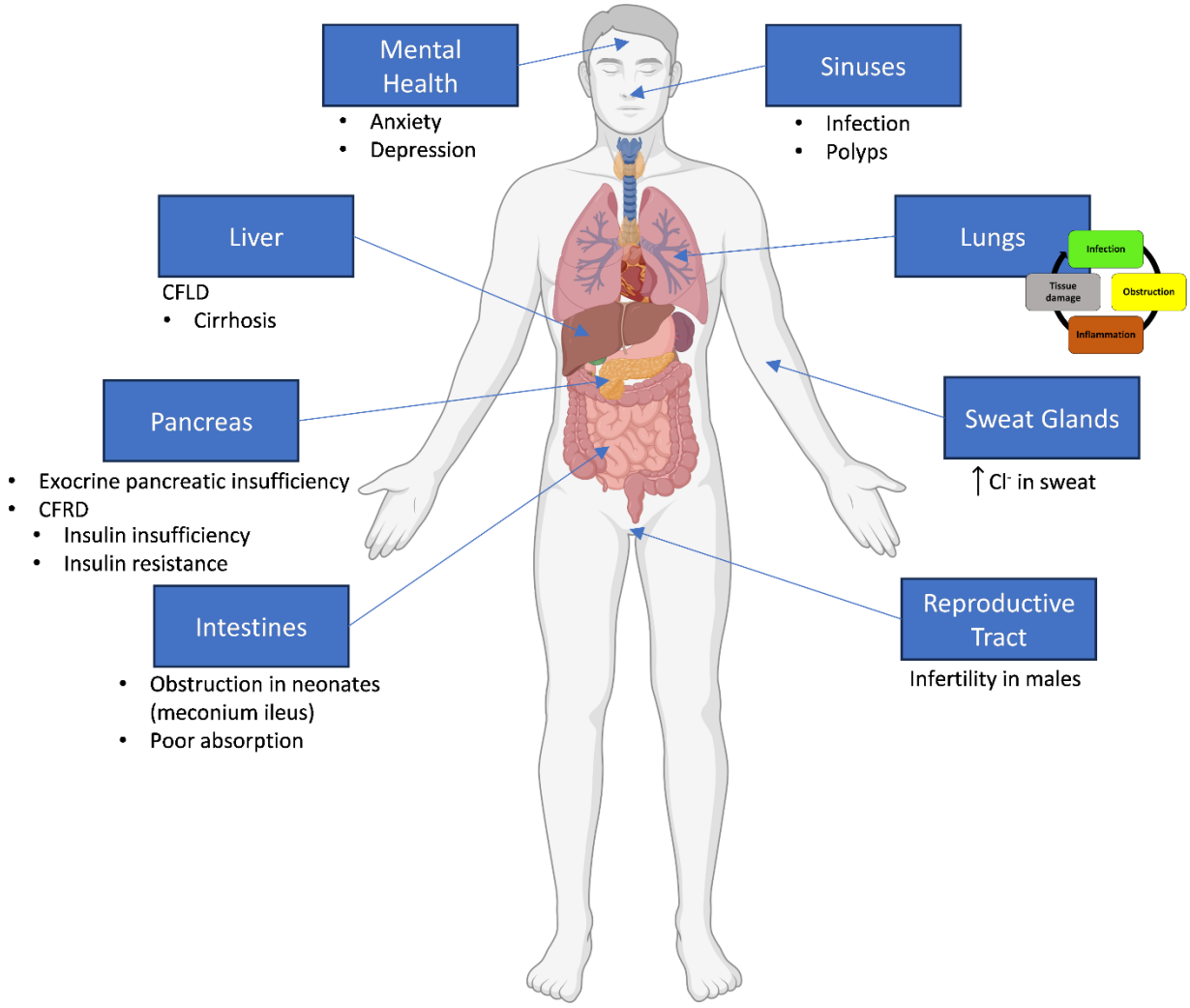

Figure 1.3. CF is a multi-organ disease.

Organs affected include the liver, pancreas, intestines, reproductive tracts, lungs, sinuses, and sweat glands. The mental health of patients with CF is also affected. The effects of CF throughout the body are highlighted in this figure (Created with BioRender).

The effects of CF on the human body are extensive, most of which are caused by blockage of proper organ function by thick secretions. Blocked bile ducts in the liver can cause liver disease (CFLD), which can result in cirrhosis and portal hypertension[31]. Blocked ducts in the pancreas can prevent digestive enzymes from reaching the intestines. This interferes with proper absorption of nutrients and can lead to malnutrition. Further, blocked pancreatic ducts can lead to tissue damage in the pancreas. When the exocrine function of the pancreas is compromised by CF, patients are considered pancreatic insufficient and need to take exogenous enzymes with every meal in order to digest food. Impaired exocrine pancreatic function can also interfere with its endocrine function. Thus, the majority of patients that are pancreatic insufficient also become insulin insufficient and develop Cystic Fibrosis-Related Diabetes (CFRD) later in life[32]. Insulin resistance is another hallmark of CF, but the potential causes are unknown. Blockages in the intestines are also common in CF. CFTR dysfunction leads to decreased bicarbonate secretion, which increases acidity and dehydration causing epithelial damage and intestinal obstruction[33]. Intestinal obstructions can also happen before birth, a condition called meconium ileus, which is usually one of the first indicators that a child might have CF. High chloride in sweat is another indication that a child might have CF. When a child fails newborn screening, sweat chloride tests are conducted as part of the diagnosis[34]. Blocked sinus passages can lead to infections and polyp formation[30]. Blocked airways can lead to lung infections, inflammation and tissue damage[4]. In males, the reproductive tract can also be affected by CF. Most males (~98%) are born with congenital bilateral absence of the vas deferens (CBAVD), which leads to infertility[35,36]. It is also important to mention that mental health is additionally affected by CF. The burden of the disease can lead to anxiety and depression[37], a topic that is gaining more attention in the field.

1.2.2. CF and respiratory bacterial pathogens

The airway of CF patients is colonized by bacterial pathogens from an early age. *Staphylococcus aureus* (SA) is the most common bacterial pathogen isolated from pediatric patients, a Gram-positive microbe ubiquitously found in our environment[38]. The skin and sinuses of healthy individuals are also colonized by SA; however, this pathogen bears little to no burden on healthy individuals. Due to impaired pathogen clearance, SA can cause pulmonary exacerbations and lung tissue damage in CF patients. As patients age, the population of SA is outcompeted by another opportunistic pathogen, *Pseudomonas aeruginosa* (PAO1)[39] (**Figure 1.4**).

PAO1 is a Gram-negative bacteria also ubiquitously found in our environments, posing little to no threat to healthy individuals. However, this pathogen can form biofilms and establish a pattern of chronic infections in the CF lung, which makes this pathogen almost impossible to eradicate[38]. As a result, PAO1 is the most common bacteria found in adult sputum cultures. Pulmonary exacerbations caused by PAO1 cause more severe reductions in pulmonary function, and PAO1 is the dominant pathogen found in end-stage CF lung disease[40].

Exacerbations caused by either SA or PAO1 can be treated with systemic antibiotic administration. However, repeated antibiotic treatment can lead to antibiotic resistance, a rising challenge in CF care[41]. Other pathogens such as *Burkholderia cepacia* and nontuberculous mycobacteria (NTM) also play a role in CF pulmonary exacerbations. These non-traditional pathogens are often associated with a faster rate of lung function decline[38]. However, they are found with less frequency in both pediatric and adult populations.

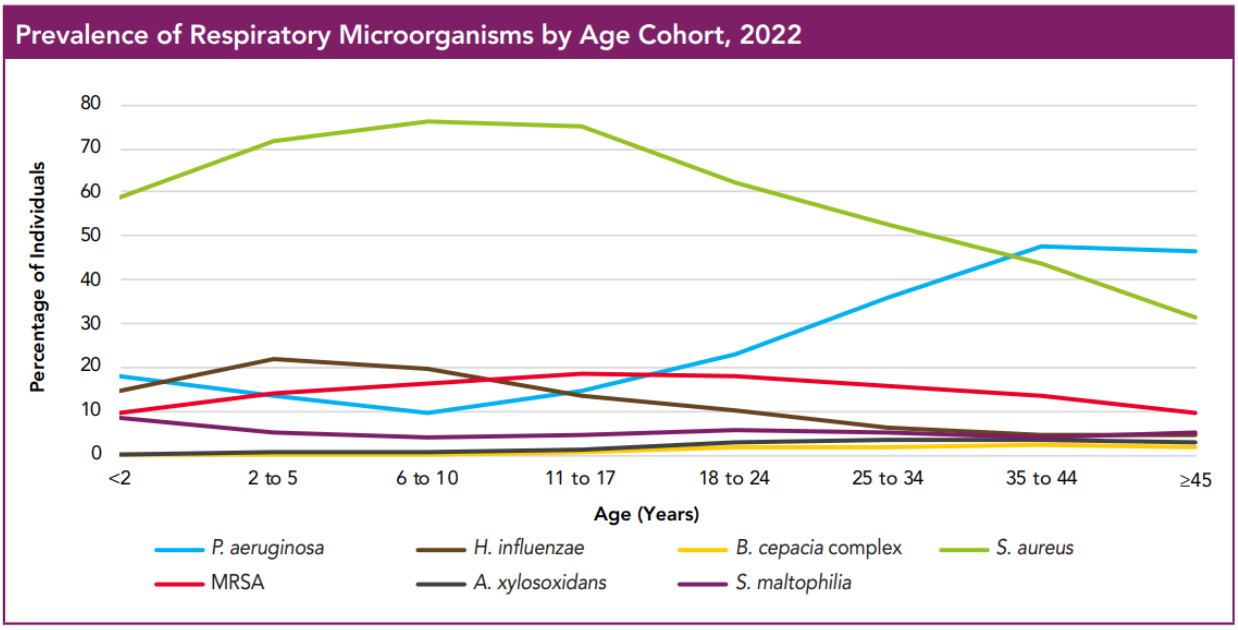

Figure 1.4. Prevalence of respiratory microorganisms in the CF airways by patients' age.

Data from the CF foundation's patient registry annual report, 2022[42]. The graph highlights SA as the prevalent CF pathogen in pediatric patients, which is outcompeted by PAO1 in the adult population.

1.2.3. CF and the immune system

Even though CF is not a disease of the immune system, evidence shows that immune responses are dysregulated in CF-affected tissues[43]. Persistent bacterial infections lead to an overactive and constant state of immune cell activation in the lungs, which leads to inflammation and worsened pulmonary disease. When a pathogen enters the airways, it is first encountered by resident macrophages which are ineffective at killing the pathogen. Instead, they release pro-inflammatory cytokines, such as IL-1β and IL-8, signaling the recruitment of monocyte-derived macrophages and neutrophils from peripheral blood to the airways to clear the pathogen[44]. Monocyte-derived macrophages can polarize into a pro-inflammatory (M1) or anti-inflammatory (M2) phenotype. The ratio of M1/M2 macrophages is altered in patients with CF, with macrophages favoring the M1 phenotype[45]. However, M1 macrophages are still able to phagocytose and kill pathogens. Aberrant macrophage function in CF may go beyond the canonical M1/M2 phenotypic designations. Even though macrophages play an important role in CF airway disease, neutrophils are the most prominent immune cell type in the CF airways.

The lungs of CF patients are overloaded with neutrophilic infiltration. However, similarly to macrophages, neutrophils are ineffective at killing airway pathogens[46]. Instead, neutrophils get overactivated and release harmful substances into the airways, such as neutrophil elastase and reactive oxygen species. This harmful phenotype is called “GRIM”, which stands for granule releasing, immunomodulatory, and metabolically active[47]. GRIM neutrophils increase oxidative stress in the airways, enhancing inflammation and tissue damage. GRIM neutrophils can also suppress other immune cells in the airways[48]. The underlying causes of macrophage and neutrophil dysfunction are unknown. Immunoregulatory agents, such as inhibitors of neutrophil elastase or neutrophil exocytosis, might be beneficial for the treatment of CF patients[49].

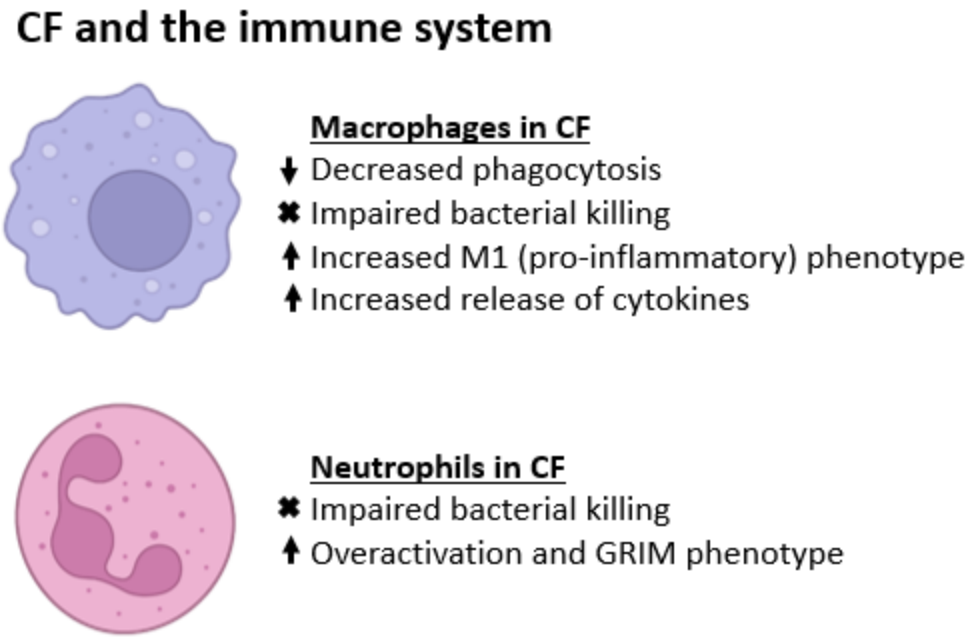

Figure 1.5. Graphical representation of how myeloid immune cells are affected in CF.

Resident macrophages in the lung have decreased phagocytosis ability, impaired bacterial killing and increased release of cytokines. Recruited neutrophils to the airway have impaired bacterial killing ability, are overactivated and display a GRIM phenotype (Created with BioRender).

1.2.4. CF and metabolism

The overall energy expenditure of CF patients is much higher than that of healthy individuals due to a series of factors. Persistent lung infections, chronic inflammation, an overactive immune system and a state of constant tissue repair increase the basal metabolic rate (BMR) of CF patients[50]. Digestion and absorption of nutrients is also compromised in CF, making dietary interventions necessary for CF patients to thrive. High-caloric diets, pancreatic enzyme replacement therapy, and supplementation with vitamins and minerals are commonly used to treat patients with CF[51].

The metabolism of fatty acids, cholesterol, and sphingolipids is also impaired in CF. However, the mechanism is not well understood. It is believed to be related to ceramide imbalance, increased inflammation and, oxidative stress[52]. Interestingly, the metabolism of phospholipids and fatty acids is closely related to glutathione (GSH), a ubiquitous thiol that acts as a scavenger for free radicals to prevent redox imbalance. GSH gets oxidized to glutathione disulfide (GSSG) in a NADPH-dependent manner to neutralize free radicals. CF patients have low levels of GSH in the airways and in blood[53,54]. Phospholipid metabolism is related to thiol metabolism through the methionine-homocysteine cycle, in which choline plays an essential role by providing methyl groups for the production of methionine and amino acid precursors for the synthesis of GSH and phosphatidylcholine (PC) enriched in docosahexaenoic acid (DHA)[55]. Choline, PC and DHA are also decreased in CF, and they are recommended to be taken as supplements to support patient's health[56]. Overall, metabolism in CF is compromised by a series of factors, such as inflammation and redox imbalance, affecting the quality of life of CF patients.

1.3. CF therapies

Managing CF exerts a heavy burden on patients and their families[57]. Treatment options are both expensive and time consuming. Most patients require hours of chest physical therapy and multiple daily medications to manage their disease[25]. A large majority of CF therapies focus on mucus clearance from the lungs, as well as prevention and treatment of airway infections. When pulmonary exacerbations take place, patients are usually hospitalized for multiple days or weeks to receive IV antibiotics. Repeated rounds of antibiotic treatment can cause bacteria to develop antibiotic resistance[59,60]. Other medications used to manage CF focus on decreasing inflammation and aiding with nutrient absorption. Patients with pancreatic insufficiency need to take enzymes with every meal in order to digest food. Patients are also recommended to follow a high-caloric diet, including vitamin and mineral supplementation to aid with weight gain. A summary of therapies used to treat clinical manifestations of CF is shown on **Table 1.2**. Recently, the use of highly effective CFTR modulator therapies (HEMT) has revolutionized CF care. These pills are usually taken twice a day, and they can partially restore CFTR protein function[61]. However, not every CF patient is legible to take HEMTs based on their genotype or adverse effects.

1.3.1. Airway clearance

Airway clearance is an integral part of the CF care regimen. It relies on a combination of chest physical therapy and inhaled medications to clear mucus from the lungs. During physical chest therapy, patients usually wear an oscillation vest that creates mechanical stimuli to loosen up the mucus[62]. Common inhaled therapies include hypertonic saline and dornase alfa, the first hydrates the airways and the second enzymatically digests DNA to decrease the viscosity of mucus[63,64].

Table 1.2. Common treatment approaches for CF clinical manifestations

CF Clinical Manifestations	Common Treatment Approaches
Pulmonary	Airway clearance
	Chronic inhaled pulmonary medications 3.1. Examples: Hypertonic saline and dornase alpha
	Bronchodilators to open the airways
	Inhaled corticosteroids
	Inhaled antibiotics
	Close monitoring with a pulmonologist with expertise in the field
	Lung transplant for patients with advanced lung disease
Infections	Oral, inhaled or IV antibiotics
Exocrine pancreatic insufficiency	Pancreatic enzyme replacement
	High-calorie diet
	Vitamin and mineral supplementation
	Close monitoring with a nutritionist with expertise in the field
Intestinal complications	Surgical interventions to release obstructions
Liver disease	Ursodiol can be used if liver function test results are elevated
	Close monitoring with a hepatologist with expertise in the field
	May need a liver transplant
Diabetes (CFRD)	Insulin replacement therapy
	Continuous glucose monitoring (CGM)
	Close monitoring with an endocrinologist with expertise in the field
Infertility	Family planning counseling
	In-vitro fertilization with intracytoplasmic sperm injection, required for males with absence of the vas deferens
	Intrauterine insemination for females with CF
Mental Health	Counseling

1.3.2. Highly effective modulator therapies

Until recently, most available CF therapies only addressed the symptoms of the disease but not its underlying cause. That changed when HEMTs were first approved by the Food and Drug Administration (FDA) in 2012. The fist HEMT approved was VX770, also referred to as Ivacaftor (commercial name in the U.S. Kalydeco®), and it functions as a CFTR potentiator by stabilizing its open state[65,66]. However, this compound by itself was not effective at treating the most common CFTR mutation, ΔF508. In 2015, VX809 was approved to be used in combination with VX770 for the treatment of patients with two copies of the ΔF508 mutation (commercial name in the U.S. Orkambi®). The VX809 compound is also referred to as Lumacaftor, and it works as a CFTR corrector by stabilizing misfolded protein so it can be properly trafficked to the cell membrane[67]. However, further research showed that chronic treatment with VX770/VX809 was not effective as VX770 decreased VX809's corrector effects[68]. In 2018, VX809 was replaced by VX661 due to negative interactions between VX809 and VX770. VX661, Tezacaftor, also works as a CFTR corrector[69]. The new VX770/VX661 combination therapy received the commercial name Symdeko® in the U.S. However, this combination therapy had similar negative adverse effects. In 2019, a triple combination therapy containing VX445/VX661/VX770 was approved. The new compound VX445, Elexacaftor, also works as a corrector. However, it works synergistically with VX661 and its corrector effects are not negatively influence by chronic treatment with VX770[70,71]. This therapy containing Elexacaftor/Tezacaftor/Ivacaftor (ETI) has the commercial name Trikafta® in the U.S., and it is currently used for the treatment of patients with at least one copy of ΔF508. Elexacaftor and Tezacaftor both bind to the bind to the transmembrane domain (TMD) of CFTR, and they work synergistically to stabilize misfolded CFTR protein, aiding with protein folding and trafficking to the cell membrane[72]. Ivacaftor binds to the nucleotide binding domain 2 (NBD2) of

CFTR, and it stabilizes the open conformation of the CFTR channel, helping it stay open for longer and increase chloride flux outside the cell[66]. Overall, ETI has drastically improved the quality of life and life expectancy of patients who are able to take it. Research is being conducted to develop a new generation of correctors and potentiators that reduces the negative side effects associated with ETI therapy and are able to also target rare CFTR mutations.

1.3.3. New CF therapies under development

Potential avenues for new therapies are broad and have the potential to benefit all patients with CF regardless of their CFTR mutation[73]. Gene therapy aims to deliver functional copies of CFTR mRNA to target tissue, such as to lung cells through encapsulation in nanoparticle formulations and nebulization, so that functional CFTR protein is produced in the target tissue[74,75]. However, penetration of nebulized particles and delivery to the right cell types remain two of the main challenges for gene therapy[76,77]. Gene editing approaches focus on correcting point mutations in the CFTR gene or delivering functional copies of CFTR DNA alongside gene editing tools, such as CRISPR/Cas9, to edit out defective CFTR DNA replacing it with functional copies of this gene[78]. Encapsulation and delivery of all these necessary components are challenges that remain to be addressed. Additionally, off-target insertions and deletions are additional concerns when considering gene editing therapies.

Personalized therapies for specific mutations are also being investigated. For example, read-through agents for non-sense mutations could benefit patients with premature stop codon mutations, allowing for full-CFTR protein to be produced. Other therapies being developed are improved mucolytic and anti-inflammatory agents. Even though these therapies do not aim to correct the underlying defects in CFTR, they could still be therapeutically beneficial for CF patients.

1.4. Cystic Fibrosis Related Diabetes: the main CF co-morbidity

Even though modulator therapies are expected to increase the life expectancy of CF patients, evidence thus far suggests that they may not prevent the development of CF co-morbidities such as cystic fibrosis related diabetes (CFRD)[79]. Studies investigating the effects of modulator therapies on development of CFRD show limited benefit, particularly in adults with established disease. Some studies claim that patients depend less upon insulin administration, although CFRD patients can rarely stop their insulin therapy[80–82]. Continuous glucose monitoring data showed that adults with CFRD had higher than 250 mg/dL blood glucose 4.6% of time before ETI, compared to 4.9% after ETI[83]. This evidence shows that modulators alone may not provide effective glucose control in CFRD.

1.4.1. What is CFRD?

CFRD is the main comorbidity linked to CF, since about half the patients develop this condition by adulthood (**Figure 1.6**). Patients diagnosed with CFRD are usually insulin-dependent and develop severe CF lung disease more quickly than CF patients with normal glycemic control[84]. The link between CFRD and accelerated pulmonary function decline is still unknown. Diabetic patients without CF do not experience recurrent lung infections, which suggests that their airways can adapt to hyperglycemia[85–87]. In healthy individuals, the level of glucose in the airway surface liquid (ASL) is proportional to the glucose levels in the serum[88]. In contrast, early evidence shows that ASL glucose concentration is elevated in CF patients, and it is even further elevated in patients with CFRD[89]. We confirmed elevated ASL glucose using a diabetic S*cnn1b*-Tg mouse model, described in Chapter 4. CFRD patients experience approximately a six-fold higher rate of lung function decline compared to their non-diabetic CF counterparts[90]. The mechanisms that lead to elevated levels of glucose in the CF airways are unknown.

1.4.2. How is CFRD different from type 1 and type 2 diabetes?

CFRD shares some similarities with type 1 and type 2 diabetes (**Table 1.3**). Patients with CFRD experience insulin resistance, similar to type 1 diabetes patients. Further, patients with CFRD experience insulin insufficiency, similar to type 2 diabetes patients. However, the leading cause of mortality for CFRD patients is respiratory failure, not heart attack or stroke[91].

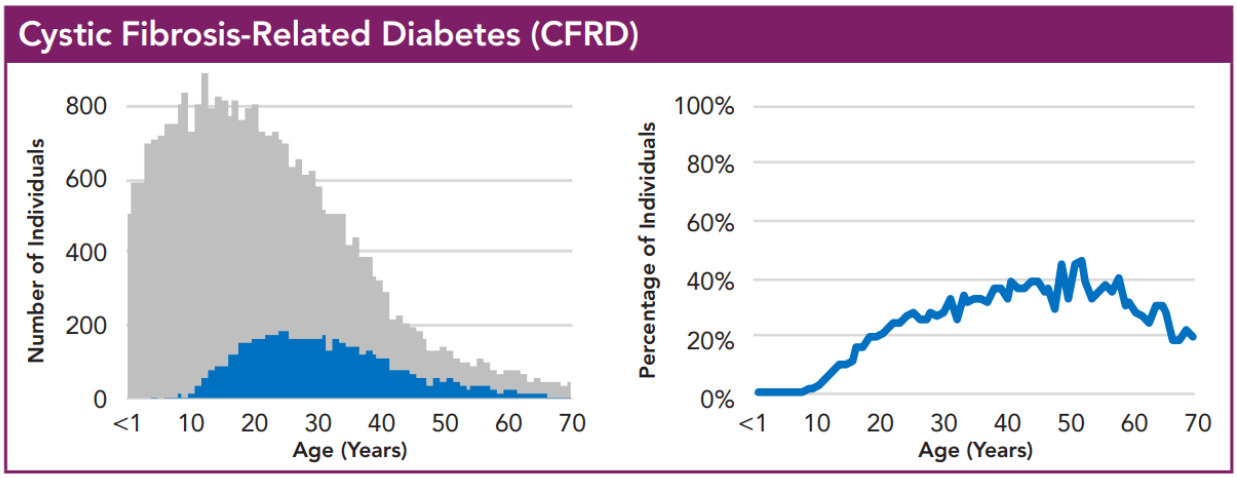

Figure 1.6. CFRD incidence.

Data from the CF foundation's patient registry annual report, 2022[42]. On the left, the plot shows the number of individuals with CFRD (blue) compared to the entire CF population (gray). On the right, the plot shows percentage of individuals with CFRD based on age.

Table 1.3. Commonalities and differences between type 1 diabetes, type 2 diabetes, and CFRD.

	Type 1 diabetes	Type 2 diabetes	CFRD
Onset	Acute	Insidious	Insidious
Common age of onset	Childhood and adolescence	Adulthood	Adolescence and early adulthood
Autoimmunity	Yes	No	No
Insulin secretion	Low to none	Low	Low
Insulin resistance	Moderate	Severe	Moderate
Treatment	Insulin	Insulin, dietary changes, drugs available	Insulin
Ketoacidosis	Yes	Rare	Rare
Diet	Normal	Calorie restricted	High calorie
Macrovascular complications	Yes	Yes	No
Microvascular complications	Yes	Yes	Yes
Cause of death	Nephropathy and cardiovascular disease	Cardiovascular disease	Pulmonary disease

1.4.3. Potential causes of CFRD

The causes of CFRD are unknown. However, there are two main hypothesis that could explain the root of the disease. The first is the "bystander effect" hypothesis, which states that CFRD is caused by destruction of pancreatic endocrine function as a result of exocrine pancreatic dysfunction[90,92]. CFTR dysfunction in pancreatic ductal cells causes an increase in mucin production and acidification of pancreatic juices, leading to obstruction of pancreatic ducts. Obstructed ducts can lead to pancreatic fibrosis due to auto-digestion of pancreatic tissue. Islet cells, responsible for producing insulin, might be damaged as a result. The second hypothesis states that CF patients already have dysfunctional islet cells, even before pancreatic damage occurs. Improper CFTR folding and trafficking in islet cells might interfere with its endocrine function[32,93].

1.4.4. CFRD diagnosis

The Cystic Fibrosis Foundation (CFF) recommends that CF patients are screened for CFRD once a year, starting at 10 years of age. CFRD is tested by conducting an oral glucose tolerance test (OGTT). The test requires patients to fast for at least 8 hours before ingesting a drink with high glucose. Their blood glucose levels are then monitored at different time points. A fasting glucose level ≥ 126 mg/dL (7.0 mmol/L) and/or a 2 h OGTT glucose level ≥ 200 mg/dL (11.1 mmol/L) are used to diagnose CFRD. A blood glucose reading ≥ 140 mg/dL (7.8 mmol/L) and < 200 mg/dL (<11.1 mmol/L) is considered impaired glucose tolerance, and those patients are at a higher risk of developing CFRD in the near future (**Table 1.4**)[94,95]. Another test commonly used to diagnose diabetes is to measure hemoglobin A1c (HbA1c) in blood. This test is less burdensome than an OGTT, since it does not require fasting nor multiple blood draws. However, this test has proven to not be sensitive enough to diagnose CFRD[96].

Table 1.4. Blood glucose guidelines used when conducting an oral glucose tolerance test (OGTT) to diagnose CFRD.

Category	Fasting glucose mmol/dL (mg/dL)	2-hour time point mmol/dL (mg/dL)
Normal glucose tolerance (NGT)	< 5.6 (100)	< 7.8 (140)
Impaired fasting glucose (IFG)	> 5.6 (100)	< 7.8 (140)
Impaired glucose tolerance (IGT)	> 5.6 (100) < 7.0 (126)	> 7.8 (140) < 11.1 (200)
Cystic Fibrosis-Related Diabetes (CFRD)	≥ 7.0 (126)	> 11.1 (200)

1.4.5. CFRD treatments

The pathophysiology driving CFRD is still unknown. Thus, there are no therapies available to treat the underlying cause of CFRD. Instead, CFRD treatments mainly focus on keeping blood sugar levels within a normal range. The only available therapy for CFRD is insulin replacement[94]. Patients are encouraged to monitor their blood sugar levels by finger pricking or by using a continuous glucose monitor (CGM). Carbohydrate counting is recommended with each meal or snack to administer the right amount of insulin. Insulin pumps are also commonly used, and newer models can be synchronized with CGMs for automatic insulin delivery[97]. Changes in lifestyle, such as consistent moderate exercise and a healthy diet, also help keep blood glucose levels in range.

1.4.6. CFRD challenges and unmet needs

Early CFRD detection and intervention are crucial to minimize negative effects on pulmonary function as much as possible. However, CFRD onset is insidious making it challenging to diagnose. CFRD is commonly diagnosed through OGTT screening. However, there is significant variability in OGTT results upon repeated testing. OGTT screens are also viewed as tedious and burdensome by patients and doctors, affecting adherence to testing once a year[98]. Further, the guidelines used to diagnose diabetes through OGTT testing are based on type 2 diabetes data. These guidelines are based on increased risk of retinopathy in type 2 diabetes patients. However, modified guidelines that test for glycemic concentrations that begin to affect pulmonary function or body mass index (BMI) might be better suited to diagnose patients with CFRD[99]. The use of CGM data is also being investigated as a potential alternative for CFRD diagnosis. Among the unmet needs, CFRD patients need a less labor-intensive way to manage their blood sugar levels.

1.5. *In vitro* models to study CFRD

There are several *in vitro* models available to study CFRD. In order to study the negative effects of CFRD on pulmonary function, the two most common *in vitro* models available are immortalized airway epithelial cells and primary airway epithelial cells. Each has their pros and cons, which will be discussed further below.

1.5.1. Immortalized airway epithelial cells

Immortalized cell lines have been genetically modified to survive for longer periods and are widely used in CF research. Their advantages include ease of use, reproducibility, and availability in a wide range of genotypes. The use of immortalized cells is particularly beneficial during early stages of testing, while troubleshooting and protocol optimization is taking place. These cells usually have a fast turnover rate, and do not require expensive specialized media components. Further, they have been widely used in the field, and there is plenty of data available for reference. A disadvantage of using these cell lines is that they do not always accurately recapitulate *in vivo* airway physiology. They might express different levels of CFTR protein abundance than physiologically relevant or might not fully differentiate into all the cell types present in the airways. Despite their disadvantages, their use can still be very informative in CF research. Common immortalized cell lines used in the lab are Fischer Rat Thyroid (FRT), CF bronchial epithelial cells (CFBE), and gene-edited human bronchial epithelial cells (16HBE).

FRT cells have been available for more than 20 years and are widely used for drug discovery. These cells use Flp-In™ technology, meaning that they bear an insertion site that can be used to generate multiple CFTR variant cell lines and lead to consistent rates of transcription. However, these cells are not of human origin, and are not from airway. CFTR trafficking and folding might be different than in human airway epithelia[100].

CFBE cells were created in 2015 from the bronchial epithelium of a homozygous ΔF508 CF patient. They can polarize into apical and basolateral sides and can form good tight junctions. These cells have been stably transduced to express a variety of CFTR genotypes also using the Flp-In™ system. However, this cell line only contains a single recombination target site, which achieves a single integration of CFTR cDNA[101].

16HBE (16HBE14o-) is another type of human bronchial epithelial cell line. Parental cells were isolated from a 1-year-old male in 1994 and immortalized using Simian Virus 40 (SV40). The SV40 sequence was inserted into one of the CFTR alleles during the immortalization process. Only the other allele generates functional CFTR, rendering the cell line monoallelic for functional CFTR expression. The cell line also underwent gene editing using CRISPR/Cas9 to create an isogenic cell line (16HBEge) expressing a wide range of CFTR variants. These cells polarize into an apical and basolateral side, and form good tight junctions[102,103]. These are the immortalized cells I have used the most for research. Chapter 2 of this dissertation focuses on understanding the effects of hyperglycemia on airway epithelial barrier function using 16HBE cells expressing either WT or ΔF508 CFTR. In this chapter, I go into detail about the effects of hyperglycemia on tight junction integrity. A representative graph highlighting important cell-cell junctions, highlighting important tight junction proteins, is shown on **Figure 1.7**.

Overall, immortalized cells are valuable tools to study the pathophysiology of complex diseases such as CFRD. However, research findings obtained using immortalized cells should be also investigated primary cells. A combination of the use of immortalized and primary cells in research provides researchers with the flexibility and accuracy needed to move research forward.

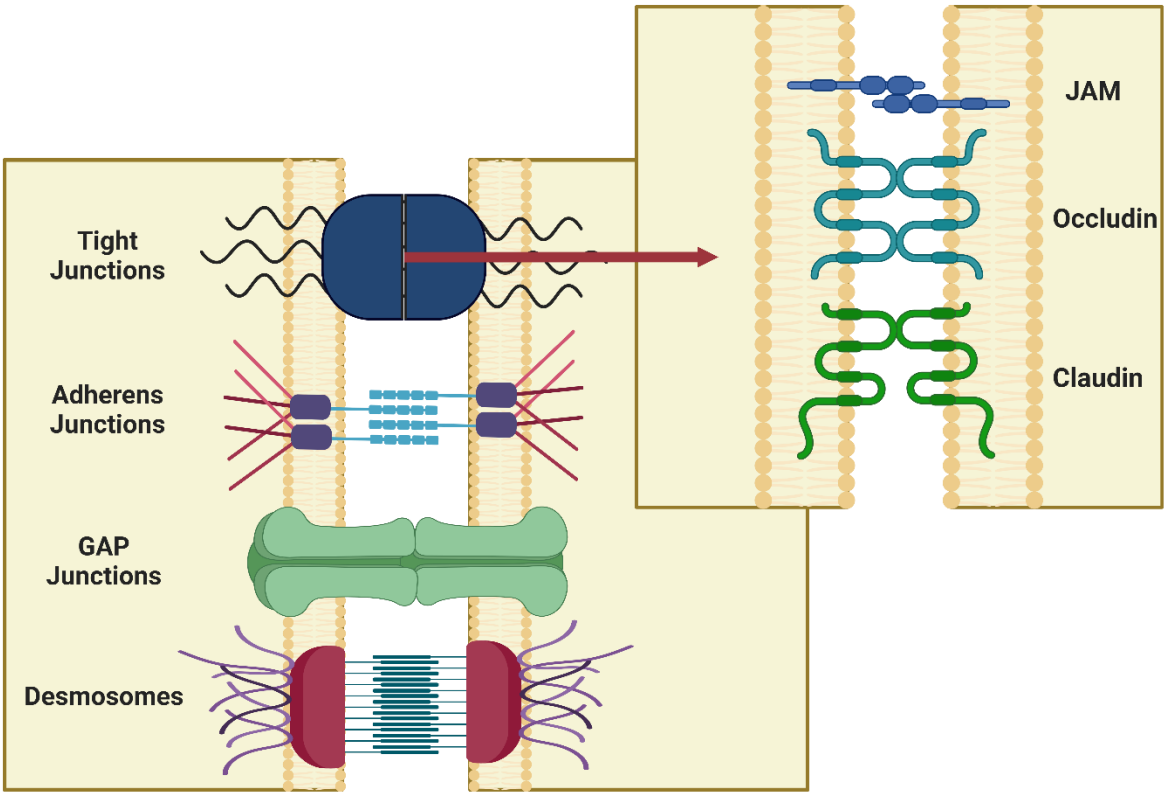

Figure 1.7. Representative graph of cell-cell junctions, highlighting important tight junction proteins.

Tight junctions, adherens junctions, gaps junctions and desmosomes are represented (created with BioRender).

1.5.2. Primary airway epithelial cells

Primary airway epithelial cells are the gold standard in CF research. With the right culture conditions, these cells differentiate into a complex monolayer containing all the major cell types found in the native airways (**Figure 1.8)**[104]. Basal cells are the most abundant and they act as airway progenitor cells that sit at the base of the epithelium and can differentiate into any cell type. Goblet cells are mucus producing, while ciliated cells contain hair-like structures (cilia) to move mucus out of the airway. Club cells are also known as secretory cells, as they produce pulmonary surfactant to prevent the collapse of the small airways. Club cells also have the ability to differentiate into ciliated cells. There are also rare cell types such as tuft cells, neuroendocrine cells and ionocytes. These cells are less abundant, but they are essential for the proper function of the airway. Tuft and neuroendocrine cells are chemosensory, as they respond in changes to their environment such as chemicals or mechanical stimuli. Ionocytes are the most rare, yet they express high levels of CFTR[105,106].

Primary epithelial cells can be isolated using non-invasive approaches such as nasal brushing. Nasal epithelial cells share many similarities with conducting and terminal airway cells[105]. However, airway epithelial cells taken from bronchoscopies or lung explants are preferred. However, these cells have short differentiation capacity. Traditional methods for culturing primary cells rely on freezing primary cells at early passages for future use. These cells can only be used for a few passages[107]. Another method, called conditional reprograming conditioning (CRC), relies on propagating basal cells using rho kinase inhibitors and irradiated fibroblasts to generate cells that can be later differentiated to a pseudostratified epithelium[108]. This method increases the expansion capacity of cells, allowing for better reproducibility. CRC is our preferred culture method when working with primary cells.

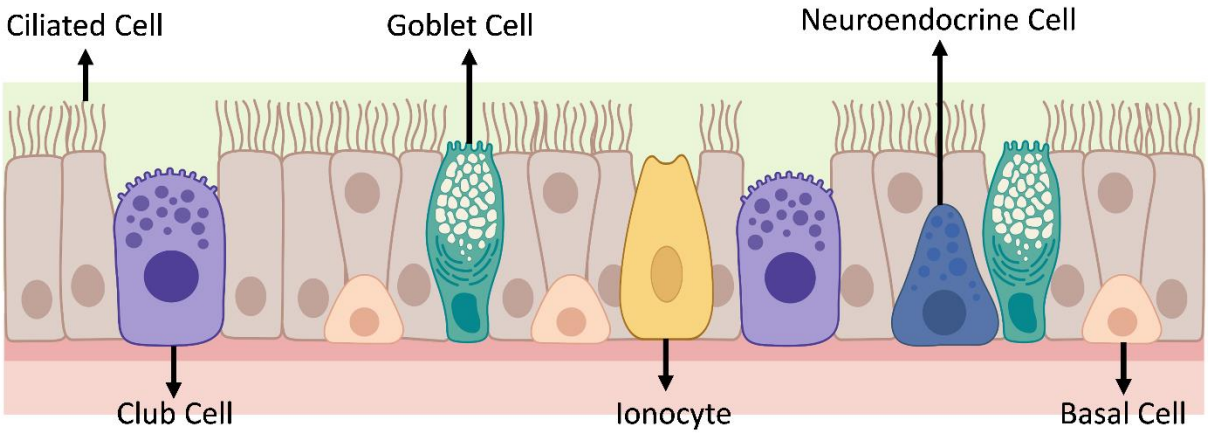

Figure 1.8. The differentiated airway epithelium is comprised of several cell types.

The diagram highlights ciliated cells, club cells, goblet cells, ionocytes, neuroendocrine cells and basal cells (Created with BioRender).

1.6.In vivo models to study CFRD

Several animal models are available to study CF. The most commonly used animal models include mouse, pig, and ferret. Each model has its advantages and challenges, and it is up to each research group to choose the model best suited for their research[109]. I will describe each model in detail below.

Mouse models are the preferred animal model used among numerous research labs across the country and the world. These animals have short lifespans, but they can be obtained cheaply and are easy to breed[110]. Further, there are several CF models already available. These models include total CFTR knockout, total CFTR knockout with gut correction, ΔF508 mutant CFTR, and others. The total CFTR knockout mouse has proven to be difficult to maintain, as they require a liquid diet and have shorter than usual lifespans. The lethal intestinal dysfunction on these mice was addressed by re-inserting CFTR only into gut tissue[111]. Even though this mouse model was an improvement from the complete CFTR knockout model, mouse models bearing CFTR variants, such as ΔF508, might better recapitulate CF disease as they present problems with folding and trafficking[112]. Interestingly, even mouse models with CFTR variants do not always recapitulate CF disease, especially in the airways. As a result, a mouse model overexpressing the β-subunit of ENaC (*Snn1b* mice) in the lungs is commonly used as a CF model. The airways of these mice are dehydrated and mucus producing, similar to the airways of CF patients[113]. The *Snn1b* mouse model was used in Chapter 4 of this dissertation. These mice were made diabetic to test the effects of systemic hyperglycemia in CF-like lung pathology.

Besides mice, pigs can also be used in CF research. They are more expensive and more difficult to maintain alive than mice. However, their airway physiology better resembles that of a human[114]. There are two main models available, a CFTR knockout model that is gut-corrected and

a model carrying the ΔF508 mutation[115]. Interestingly, the ΔF508 pig model develops long-term CF lung pathology, as shown by thickening of the airways by CT scans. Further, their lungs also show signs of mucus plugging with infiltration of immune cells (neutrophils and macrophages). Further, infection with SA showed that these pigs had impaired bacterial clearance compared to their WT controls[116]. Overall, pigs can be used as successful CF models. However, they might not be accessible by many research labs due to cost and demanding care.

Ferrets are also commonly used in CF research. Their lung physiology better resembles that of humans compared to mouse models[117]. Their lifespan is also longer than that of mice, which makes them useful for longer-term studies. Further, they are smaller in size, cheaper to obtain and easier to maintain compared to pig models. There are two main available ferret models, a total CFTR knockout model and a gut corrected CFTR knockout model. The gut corrected CFTR knockout model has better survival rates[118]. However, their weight is still reduced when compared to WT controls. Interestingly, CFTR knockout ferrets develop spontaneous airway disease with progressive lung function decline similarly to human CF patients. Further, neutrophilic inflammation occurs even before an infection takes place[119]. The disadvantage of ferret models is their lack of genotype variety. There is ferret model homozygous for the G551D mutation. This mutation affects CFTR gating, and the ferret model has been shown to develop spontaneous lung disease similar to humans[120,121].

Choosing an animal model will depend on the overall goals and resources of each research lab. The available mouse, pig and ferret models all present their own advantages and challenges which researchers should be aware of before choosing a model. Despite the complexity of animal models, they are valuable tools that need to be further developed to enhance CF research.

Chapter 2 - Effects of hyperglycemia on airway epithelial barrier function in WT and CF 16HBE cells

Preface

This chapter is an adaptation of a paper submitted to Scientific Reports, which highlights the differences in barrier function between WT and CF 16HBE cells in response to hyperglycemia. I collected and analyzed the data. I also wrote the manuscript. This is groundbreaking work in the field, since little is known about the effects of hyperglycemia on airway epithelial barrier function. This work contributes novel information about changes in transepithelial resistance, paracellular flux, gene expression, and protein localization of essential tight junction proteins claudin-4 and zona occludens-1. Bulk RNA sequencing highlights differences in transcriptomic responses in WT and CF cells in response to hyperglycemia, identifying PTPRG as an interesting target for future investigation. Overall, this work aims to expand our knowledge about the mechanisms driving accelerated lung function decline in patients with CFRD.

Full citation

Vazquez Cegla, A. J.; Jones, K. T.; Cui, G.; Cottrill, K. A.; Koval, Michael; McCarty, N. A. Effects of hyperglycemia on airway epithelial barrier function in WT and CF 16HBE cells. *Scientific Reports* **2024.** Manuscript under peer-review**.**

2.1. Introduction

Cystic fibrosis (CF) is an autosomal recessive disease caused by mutations in the gene encoding the Cystic Fibrosis Transmembrane Conductance Regulator (CFTR)[1]. Even though CF is a multiorgan disease, the leading cause of CF mortality is respiratory failure[4]. CF patients have impaired mucus clearance from the lungs, which leads to partial obstruction of the airways by thick mucus secretions. This creates an ideal environment for bacteria to proliferate; recurring bacterial infections exacerbate inflammation and progressive lung tissue damage, leading to a gradual decline in lung function. Recent pharmacological advances can restore partial CFTR function for select mutations[8,9]. The triple combination therapy, Elexacaftor/Ivacaftor/Texacaftor (ETI), is a capable of correcting the folding and potentiating the ion channel activity of CFTR. This has had a positive impact on the quality and length of life of people with CF (pwCF) that are eligible for this therapy. However, not all CF patients are eligible for this new medication due to their CFTR genotype or due to adverse effects[122,123]. Further, it is still unknown whether this new therapy can prevent the development of CF related co-morbidities. Thus, these co-morbidities might soon become the life-limiting factor for pwCF.

The main CF co-morbidity is CF related diabetes (CFRD), which begins to develop during early childhood and affects around 50% of adult CF patients[90,91]. CFRD is different from Type I and Type II diabetes. Non-CF diabetic patients do not experience recurrent bacterial infections that lead to lung disease, which suggests that their airways can adapt to hyperglycemia[85,87]. In contrast, diabetes in the context of CF leads to rapid lung disease progression and overall health deterioration. CFRD is associated with more frequent episodes of acute pulmonary exacerbations requiring intravenous antibiotics[40]. As a result, patients with CFRD experience an approximate six-fold higher rate of lung function decline compared to their non-diabetic CF counterparts[90]. In

healthy individuals, the level of glucose in the airway surface liquid (ASL) is proportional to the level of glucose in the serum. In contrast, early evidence shows that ASL glucose concentration is elevated in CF patients, and it is further elevated in patients with CFRD[124]. Previous data from our lab show that there is a direct link between expression of mutant CFTR and dysregulation of glucose homeostasis in human airway epithelial cells and mouse lungs[89,125]. We showed that insulin receptors are expressed apically in human airway epithelial cells. However, insulin-dependent glucose uptake is defective in CF cells[126]. This is a concerning problem since airway glucose serves as a nutrient for bacteria, which then proliferate, and also may worsen oxidative stress in the airways.

Polarized cells, such as airway epithelia, have distinct apical and basolateral domains. Tight junctions (TJs) are located at cell-cell junctions and play important roles in separating solutes in the apical and basolateral fluid compartments[127]. Thus, TJs limit paracellular permeability by acting as a seal at cell-cell junctions through the action of dynamic plasma membrane proteins from several families, including claudins[128]. Claudins can be classified as pore-forming (claudin-2, -10, -15) or sealing (claudin-1, -3,-4, -5, -7 and -18). Lung epithelia tend to favor the expression of sealing claudins[129]. Claudins can anchor to the actin cytoskeleton through interaction with scaffolding proteins such as zonula occludens 1 (ZO-1) and can be actively recruited into and out of the TJs as needed[128,130]. We hypothesize that in non-disease conditions, proper function of TJ proteins prevents leak of glucose from interstitial fluid into the airways. However, the integrity of TJ proteins may be compromised in patients with CF and further exacerbated in patients with CFRD. Overall, the pathways that drive CFRD disease pathophysiology are still not understood. Identification of these pathways will inform the development of new therapeutics to improve the quality and length of life for CF patients.

2.1. Methods

Unless otherwise specified, chemical reagents were purchased from MilliporeSigma.

2.1.1. Airway epithelial cell culture

Immortalized 16HBE14o- Human Bronchial Epithelial cells (16HBEs) were studied. 16HBE cells expressing WT CFTR (16HBE-WT) were kindly provided by Dr. Jason Hansen (Brigham Young University). 16HBE cells expressing ΔF508/V470 CFTR (16HBE-CF) were obtained from the CF Foundation Therapeutics lab (CFFT). Both cell lines were cultured following recommendations made by the CFFT [131] with some exceptions. Flasks were not coated with collagen. 16HBE-WT cells were cultured in MEM media for 1 week before being plated for experiments. 16HBE-CF cells were cultured in DMEM media for 2 weeks, then switched to MEM media for 1 week before being plated for experiments. MEM complete media contained 90% MEM (Gibco, 11095-072), 10% fetal bovine serum (FBS) (R&D, S11150H), and 1% Penicillin/Streptomycin (Pen/Strep, Gibco 15070-063). DMEM complete media contained 90% DMEM (Gibco 11885-084) with the same amounts of FBS and Pen/Strep. Both cell lines were used for a maximum of 12 weeks from the day of thawing from frozen aliquots. Cells were plated on the apical side of Costar 3470 Transwell plates (0.4 μm pore size, polyester, Corning) at a density of 150,000 cells per well or on Costar 3460 Transwell plates (0.4 μm pore size, polyester, Corning) at a density of 250,000 cells per well using complete MEM media containing 5.5 mM glucose. Glucose conditioning started 2 days after seeding. Cells underwent daily media changes receiving complete MEM media containing either 5.5 mM or 17.5 mM glucose. Glucose conditioning lasted 5 to 7 days. Cells were cultured at liquid-liquid interface.

2.1.1. Short-circuit current measurements

Short-circuit current experiments were performed using an Ussing chamber system from Physiologic Instruments with Acquire & Analyze software. Normal chloride buffer was used on the basolateral side and it contained 115 mM NaCl, 5 mM KCl, 1 mM $MgCl_2$, 2 mM $CaCl_2$, 10 mM glucose, 10 mM HEPES, 25 mM $NaHCO_3$, pH 7.4. Low chloride buffer was used on the apical side and it contained 115 mM Na gluconate, 5 mM KCl, 1 mM $MgCl_2$, 4 mM $CaCl_2$, 10 mM glucose, 10 mM HEPES, 25 mM $NaHCO_3$, pH 7.4. Chambers were bubbled with 95:5% O2:CO2 and maintained at 37°C during experiments. Cells in the Ussing chambers were stabilized for 30 min prior to treatment to inhibit or activate channel pathways. Cells were treated with 20 μM amiloride added to the apical side to inhibit ENaC-mediated sodium currents, 10 μM forskolin added to the apical and basolateral sides to activate CFTR currents, and 10 μM INH172 subsequently added to the apical side to inhibit CFTR.

2.1.2. Paracellular dye flux experiment

Paracellular dye flux experiments were conducted as previously reported [126] . Briefly, cells plated on Transwells (Corning, 3460) were conditioned with normal or high glucose media for 5-7 days. Membranes were washed and placed in bilateral Krebs-Ringer HEPES (KRH) buffer (1 g/L D-glucose, 50 mM HEPES, 137 mM NaCl, 4.7 mM KCl, 1.85 mM $CaCl_2$, and 1.3 mM $MgSO_4$, pH 7.4) for 90 minutes to remove all growth factors. The solutions were replaced with fresh KRH, where the apical solution contained 4 μg/mL Calcein (0.62 KDa) and 0.1 mg/mL Texas Red Dextran (10 kDa). Samples (100 μL) were collected from the basolateral side every 30-60 minutes for 3 hours. A plate reader was used to measure abundance (excitation/emission 485/515 nm for Calcein and 585/615 nm for Dextran). Flux rates were calculated by taking the linear slope of the flux vs time plots.

2.1.3. Quantitative reverse transcription PCR (qRT-PCR)

Cells from two large Transwells were pooled (6 wells, 3 collection tubes, for each treatment) and centrifuged at 500g for 10 min at 4°C. RNA was extracted using Trizol® according to the manufacturer's directions. A reverse transcription kit (Qiagen, Cat No. 205311) was used to make cDNA with a starting RNA concentration of 100 ng per reaction. SYBR Green was added to diluted cDNA (1:1) and 20 µl was used per PCR reaction. The PCR reactions were run using a StepONEPlus Real-Time PCR System (AB Applied Biosystems). Cycle threshold values were normalized using the housekeeping gene, hypoxanthine phosphoribosyltransferase 1 (HPRT1).

2.1.4. ETI and insulin conditioning

Cells were plated on Transwells and cultured as previously described. Hyperglycemic conditioning started three days after seeding with daily media changes from day 3 to day 9. Elexacaftor/Tezacaftor treatment with or without insulin was applied on day 7. Elexacaftor/Tezacaftor/Ivacaftor treatment with or without insulin was applied on day 8. The final concentrations in culture were 5 µM Elexacaftor, 18 µM Tezacaftor, 1 µM Ivacaftor, and 400 nM insulin.

2.1.5. Immunostaining

Cells plated on Transwells (Corning 3470) were fixed using 2% paraformaldehyde in 1X PBS for 10 minutes, followed by a 2-minute incubation with 1:1 methanol acetone. Samples were blocked using 2% BSA in PBS (PBS/BSA) and incubated overnight at 4ºC with primary antibodies targeting CLDN4 (#36-4800, ThermoFisher) and ZO-1 (#33-9100, ThermoFisher). Samples were washed and incubated with secondary antibodies Alexa Fluor-488 anti-rabbit (1:500) and Alexa Fluor-594 anti-mouse (1:500) for 1 hour. Transwells were cut and mounted with the apical side pointing toward the coverslip. Vectashield antifade with DAPI (Vector Laboratories, #H-1200-10)

was used during mounting. All steps were performed at room temperature unless otherwise noted. Images were collected using a Nikon SoRa confocal microscope using a 40X water immersion objective.

2.1.6. Image Analysis

To test whether CLDN4 was present at the plasma membrane of airway epithelial cells in a position associated with the TJs, we employed a novel image analysis technique. The analysis was blinded by deidentifying file names, which contained genotype and glucose condition information, while keeping a record linking code names to file names hidden from the researcher conducting the analysis. Deidentified confocal image stacks were opened using ImageJ and fluorescence channels were split. Working only with the ZO-1 fluorescence channel, the maximum Z projection (Max-Z) was taken. This provided spatial information of where the boundary of each cell was located. A point tool was used to numerically label each visible cell. A random number generator was used to randomly select 8 non-adjacent cells per image for analysis. The line tool was used to manually draw the cell outlines of the randomly selected cells. All labels and outlines were saved in the ROI manager. The fluorescence intensity of ZO-1 staining coming from the selected cell outlines was measured and saved. The cell outlines then were overlayed onto the CLDN4 channel. The fluorescence intensity of CLDN4 staining coming from the outlines of the selected cells was measured and saved. Labels and outlines were overlayed using the "flatten" function on ImageJ. Max-Z projection images and ROI manager windows were saved.

2.1.7. RNA Sequencing

Cells plated on Transwells (Corning, 3460) were washed once with 1XPBS. Cells were scraped and pooled into 1 mL conical tubes (2 Transwells per sample) and centrifuged at 500g for 10 min at 4°C. RNA was isolated using a Quick-RNA Miniprep Kit (#R1054, Zymo Research).

RNA was sequenced and analyzed in bulk by Novogene. Volcano plots and heatmaps were generated in RStudio (v4.2.3) using the ggplot2 package (v3.4.2). Gene ontology analysis was conducted using the Bioconductor clusterProfiler package (v4.6.2).

2.1.8. Gene Set Enrichment Analysis

Gene Set Enrichment Analysis (GSEA)[132] was conducted to identify gene sets enriched in CF versus WT cells in response to glucose concentration in culture. The GSEA analysis tool (v4.2.1) and the "Hallmark" gene set from Molecular Signatures Database (MSigDB) were used for this purpose.

2.1.9. Statistical analysis

Data were analyzed and plotted using GraphPad Prism software unless otherwise specified. One-way and two-way ANOVA for multiple comparisons were used. Tukey corrections were used as recommended by Prism.

2.1.10. Data Accessibility

Bulk RNA sequencing data generated for this study can be found in Gene Expression Omnibus (GEO) with the accession code GSE268909.

2.2. Results

2.2.1. Hyperglycemia increases CFTR current and decreases trans-epithelial electrical resistance in WT cells but leads to no change in CF cells.

16HBE-WT and 16HBE-CF cells were conditioned with normal or high glucose media for a period of 7 days. Media was changed daily to ensure the glucose concentrations in culture stayed close to their initial levels. Normal glucose media contained 5.5 mM glucose (100 mg/dL), while the high glucose media contained 17.5 mM glucose (315 mg/dL). We also included a higher glucose group which contained 30 mM glucose (540 mg/dL), and a mannitol control with the same molarity. After one week of culture in these conditions, we conducted Ussing Chamber analysis of short-circuit currents. The change in current after addition of INH172 was recorded as total CFTR current. Representative current tracings for WT cells can be found in **Figure 2.1A, B**. The quantification of CFTR current and membrane trans-epithelial electrical resistance (TEER) in WT cells can be found in **Figure 2.1C, D**. Representative current tracings for CF cells can be found in **Figure 2.1E, F**. The quantification of CFTR current and TEER measured in CF cells can be found in **Figure 2.1G, H**. Results show a moderate increase in CFTR current and a prominent decrease in TEER in WT cells in response to hyperglycemia. These observations can be seen in both the 17.5 mM and 30 mM glucose conditioned groups when compared to their normal glycemic control. These effects were not due to changes in osmolality, since the 30 mM mannitol control was not significantly different from the control group. In contrast, CF cells only exhibited a modest increase in CFTR current in the 30 mM glucose group. No changes in TEER were seen in CF cells, suggesting that these cells are limited in their ability to respond to hyperglycemia.

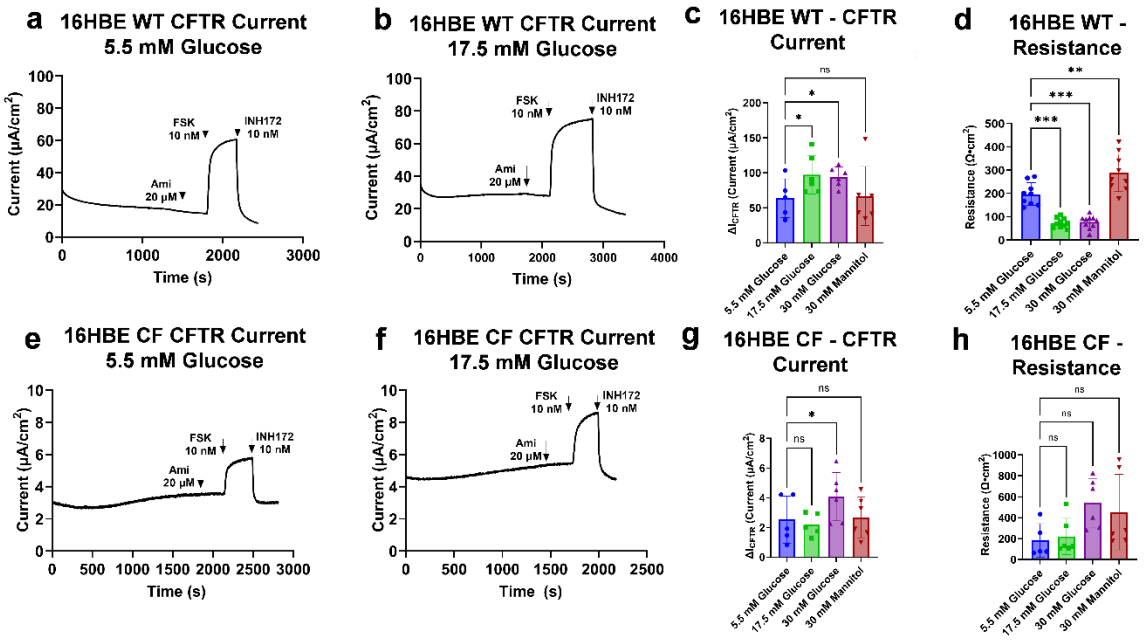

Figure 2.1. Ussing chamber results show decreased resistance and increased CFTR current in 16HBE WT cells but not in CF cells in response to hyperglycemia for 7 days.

(A) Representative current tracing for WT cells treated with normal or (B) high glucose. (C) CFTR current and (D) initial resistance measured in WT cells. (E) Representative current tracing for CF cells treated with normal or (F) high glucose. (G) CFTR current and (H) initial resistance measured in CF cells. Statistics: One-way ANOVA for multiple comparisons, Tukey correction, *** $p<0.001$, **$p<0.01$, *$p<0.05$ (N=3, 6-9 Transwells per group).

Repeated bacterial infections are one of the hallmarks of CF airway disease, but not much is known about the effects of bacterial infections on barrier function in the context of CFRD. Lipopolysaccharide (LPS) is a major component of Gram-negative bacteria cell walls, and it is known to trigger an immune response which leads to the release of proinflammatory factors in vivo[8]. When testing the effects of LPS treatment (2 μg/ml for 7 days), WT cells showed decreased TEER under normal but not under high glucose conditions. This trend was not seen in CF cells at either glucose concentration, suggesting a lack of adaptive response in CF cells (**Figure 2.2**).

2.2.2. Increased paracellular flux in CF cells under hyperglycemia upon insulin treatment

Changes in TEER do not necessarily correlate with changes in paracellular flux 17,20. To further assess barrier integrity, we conducted paracellular dye flux experiments. After conditioning cells with either normal or high glucose media, calcein (0.62 kDa) and Texas Red dextran (10 kDa) were used to test paracellular flux in WT and CF cells. No changes in calcein or dextran flux were seen in WT or CF cells in response to hyperglycemia (**Figure 2.3A, D**). Previous results indicated that WT and CF cells exhibit different responses to insulin, in terms of barrier function15. Dye flux experiments showed no change in paracellular flux of either calcein or dextran in WT cells after 400 nM insulin treatment (**Figure 2.3B, E**). However, CF cells showed increased paracellular flux of both calcein and dextran in response to 400 nM insulin treatment (**Figure 2.3C, F**). Overall, these results highlight that airway epithelial cell barrier integrity is compromised in CF cells in response to hyperglycemia and insulin treatment. WT cells appear to be better able to adapt to hyperglycemia under insulin conditioning.

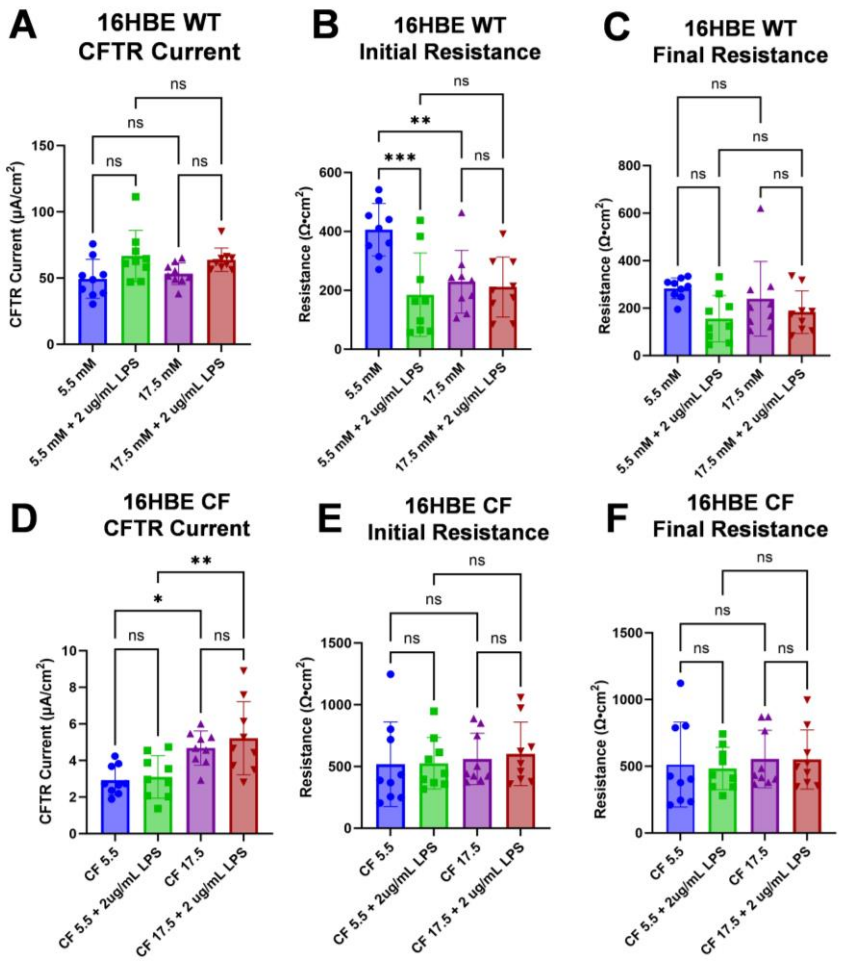

Figure 2.2. Treatment with LPS does not change CFTR current under normal or high glucose for 7 days.

(A) Summary of CFTR currents and (B) TEER in response to hyperglycemia and LPS treatment (2 μg/mL) in WT cells. (C) Final transepithelial resistance after inhibition of ENaC and CFTR in WT cells. (D) Summary CFTR currents and (E) transepithelial resistance in response to hyperglycemia and LPS treatment (2 μg/mL) in CF cells. (F) Final transepithelial resistance after inhibition of ENaC and CFTR in CF cells. Statistics: Two-way ANOVA for multiple comparisons, Tukey correction, *** $p<0.001$, ** $p<0.01$, * $p<0.05$ (N=3, 8-9 Transwells total).

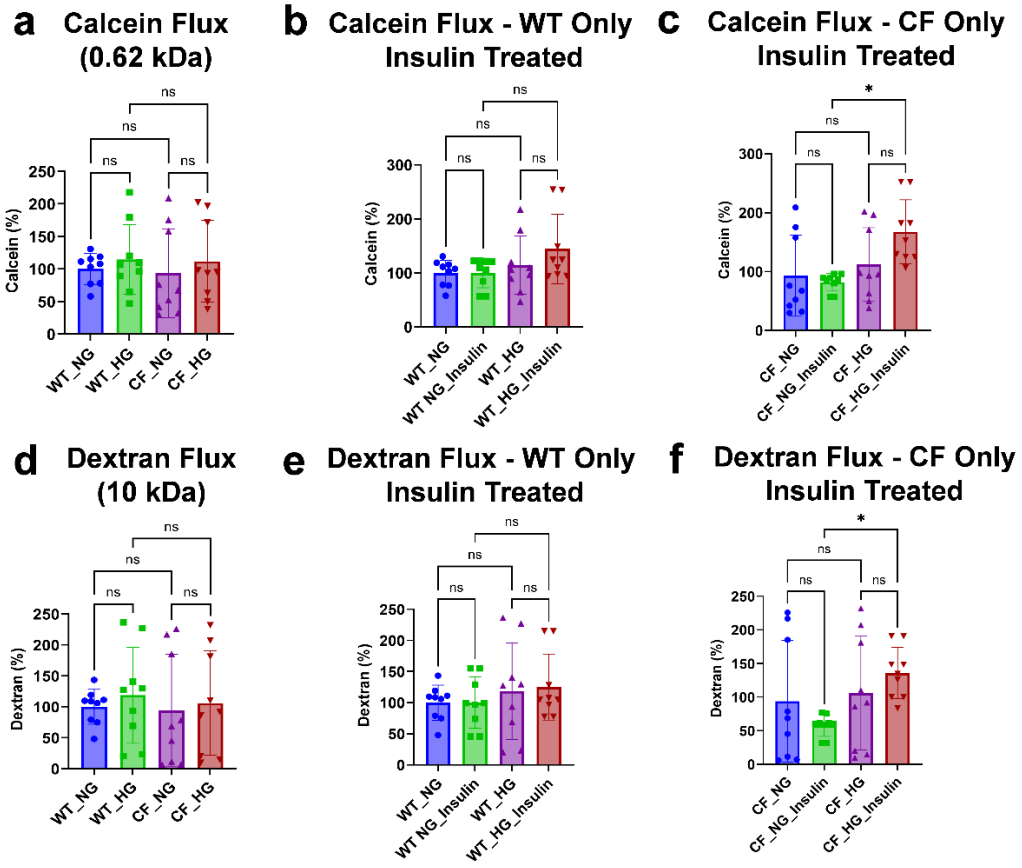

Figure 2.3. Hyperglycemia for 7 days increases flux of both calcein (0.62 kDa) and dextran (10 kDa) in CF cells but not WT cells upon insulin treatment (400 nM).

(A) Calcein flux of WT and CF cells under normal or hyperglycemic conditions. (B) Calcein flux after insulin treatment under normal glucose or hyperglycemia in WT cells only. (C) Calcein flux after insulin treatment under normal glucose or hyperglycemia in CF cells only. (D) Dextran flux of WT and CF cells under normal or hyperglycemic conditions. (E) Dextran flux after insulin treatment under normal glucose or hyperglycemia in WT cells only. (F) Dextran flux after insulin treatment under normal glucose or hyperglycemia in CF cells only. (NG= normal glucose, HG= high glucose). Dye flux experiment conducted after 90-minute serum starvation in Krebs-Ringers HEPES-buffered solution (KRH) to remove effects of insulin. Each replicate was normalized to its WT normal glucose control group (N=3).

2.2.3. Rescue of CFTR by ETI in CF cells is not compromised by hyperglycemia or insulin treatment.

ETI is a novel treatment in the CF field. Patients who are eligible to take it show great clinical improvement regarding their airway disease. It is unknown whether hyperglycemia or insulin treatment might impact the effectiveness of ETI. Ussing chamber experiments were conducted to address this question. Initial resistance was defined as the TEER measured by Ussing Chamber after a 30-minute equilibration, but before the addition of any small molecules to activate or inhibit specific ion transport proteins. Final resistance was defined as the TEER measured after inhibition of ENaC and CFTR. Results show that neither CFTR current nor initial resistance were affected by ETI or ETI with insulin under normal or high glucose culture conditions in 16HBE-WT cells (**Figure 2.4A, B)**. This was expected since WT cells already have functional CFTR. However, WT cells treated with ETI and insulin under hyperglycemic conditions exhibited elevated final resistance (**Figure 2.4C**). This suggests that, under hyperglycemia, insulin induced changes in the epithelial barrier that led to higher TEER independent of CFTR and ENaC function. In contrast, 16HBE-CF cells exhibited an increase in CFTR current in response to ETI, as expected. CFTR current rescue was comparable under normal and high glucose. Adding insulin treatment did not interfere with CFTR rescue by ETI (**Figure 2.4D**). In contrast to WT cells, both initial and final TEER decreased in CF cells treated with ETI under both normal and high glucose (trending toward significance in high glucose), and this was not impacted by insulin (**Figure 2.4E, F**). Total CFTR protein expression was also analyzed by Western Blot. Results show no detrimental effects caused by insulin treatment under normal or hyperglycemic conditions in the presence or absence of ETI (**Figure 2.5**).

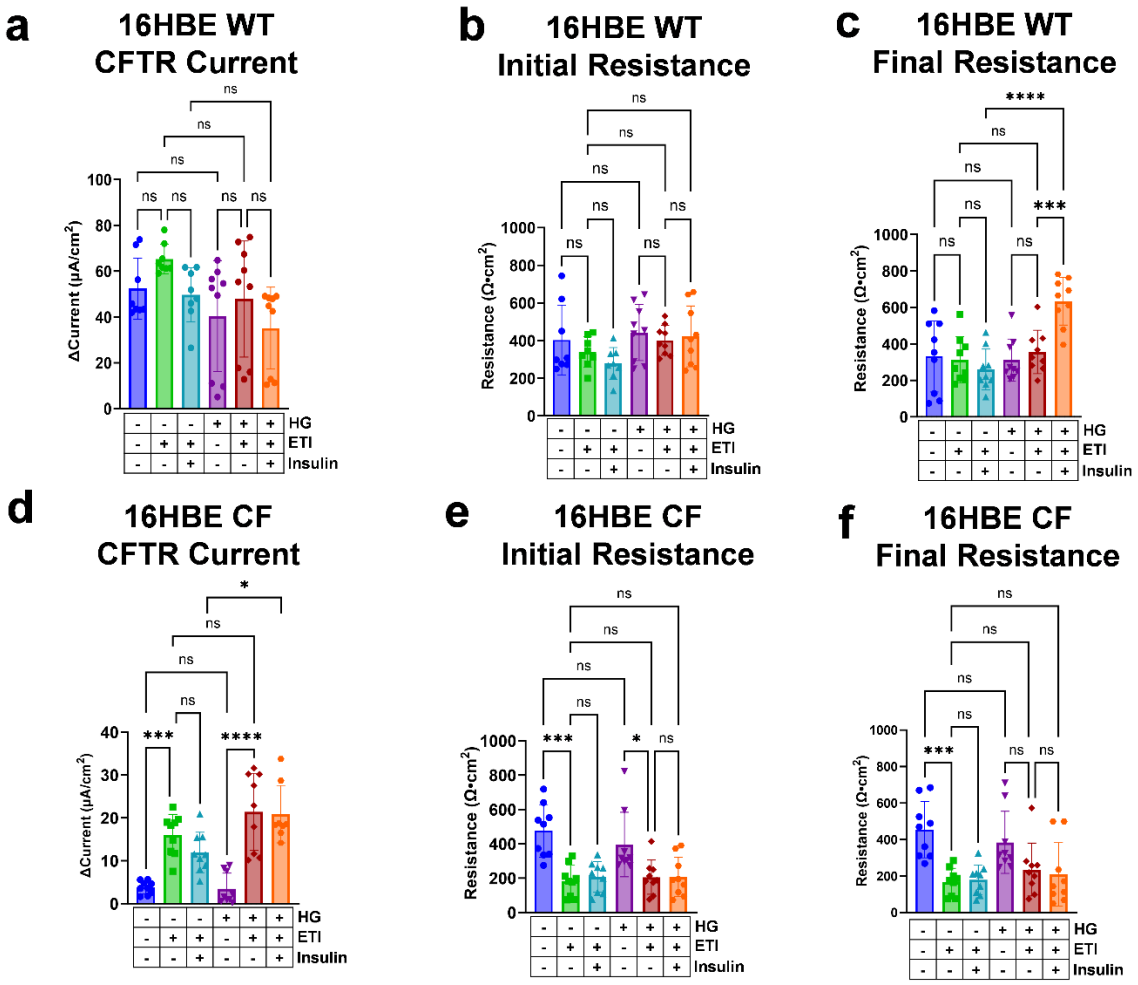

Figure 2.4. Treatment with ETI leads to decreased transepithelial resistance in 16HBE-CF cells cultured under normal or hyperglycemic conditions.

(A) Summary CFTR currents and (B) initial transepithelial resistance in response to hyperglycemia, ETI, and ETI with insulin in WT cells. (C) Final transepithelial resistance after inhibition of ENaC and CFTR in WT cells. (D) Summary CFTR currents and (E) initial transepithelial resistance in response to hyperglycemia, ETI, and ETI with insulin in CF cells. (F) Final transepithelial resistance after inhibition of ENaC and CFTR in CF cells. Statistics: Two-way ANOVA for multiple comparisons, Tukey correction, **** $p<0.0001$, ***$p<0.001$, **$p<0.01$, *$p<0.05$ (N=3, 8-9 Transwells total).

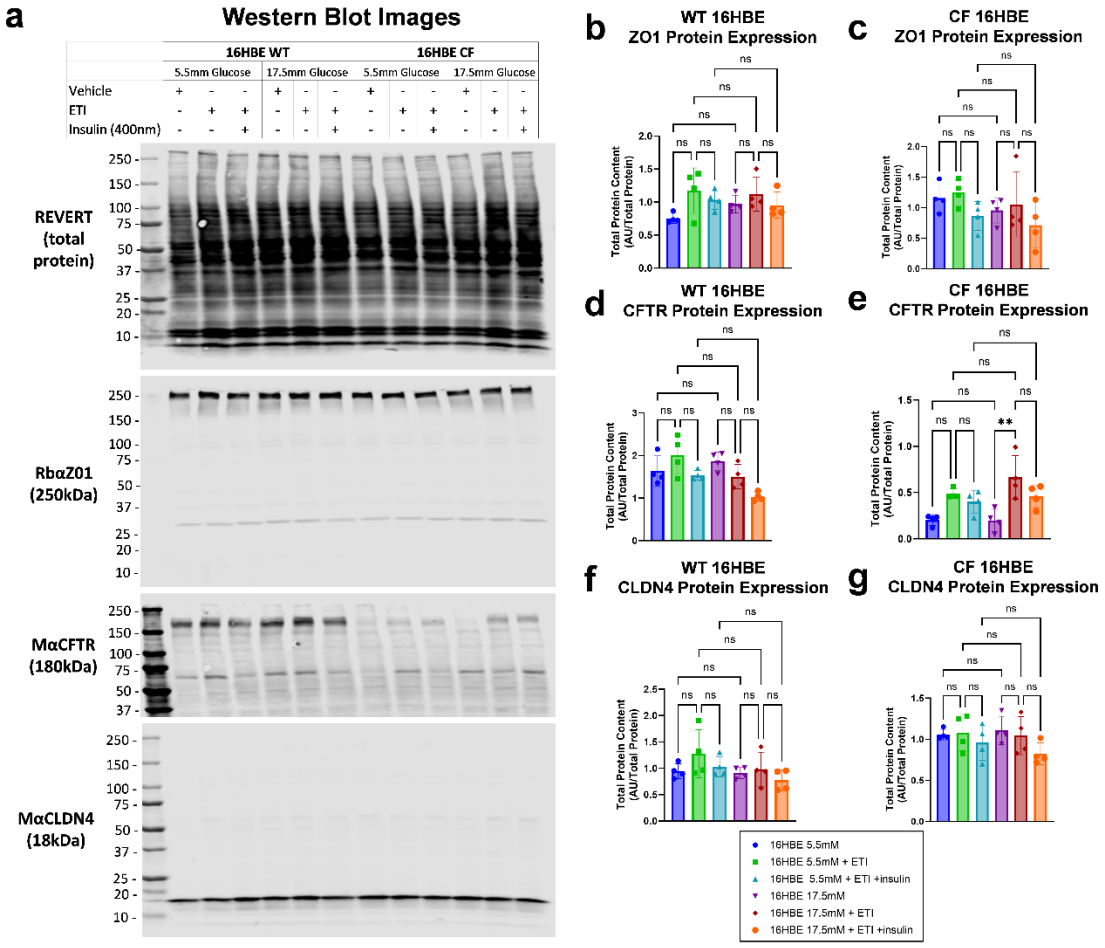

Figure 2.5. Total protein quantification of ZO-1, CFTR, and CLDN4 shows no detrimental effects on protein expression in response to insulin treatment.

Cells were cultured with normal or high glucose for 7 days. ETI with or without 400 nM insulin added during the last 48 hours. Results show (A) representative Western blot images for the proteins of interest. Quantification of total ZO-1 expression in (B) WT and (C) CF cells. Quantification of total CFTR expression in (D) WT and (E) CF cells. Quantification of total CLDN4 expression in (F) WT and (G) CF cells. Statistics: Two-way ANOVA for multiple comparisons, Tukey correction, *p<0.05 (N=3).

2.2.4. Key proteins of the airway glucose barrier are dysregulated in CF cells.

The expression of genes for key proteins that play roles in TJ integrity and glucose homeostasis was quantified using qRT-PCR. Cells were conditioned as stated before, using media with 5.5 mM or 17 mM glucose for 7 days. Results show that the transcript levels of key TJ proteins claudin -1, -3, -4, and -7 were downregulated in WT cells in response to hyperglycemia (**Figure 2.6A**). Interestingly, the expression of none of these transcripts of interest were changed in CF cells in response to hyperglycemia (**Figure 2.6B**). However, when transcript expression of CF cells was compared to WT cells at normal glycemic conditions, key TJ proteins claudin -1, -3, -4, and -7 were already downregulated in CF cells (**Figure 2.6C**). No transcripts were found to be differentially expressed when comparing CF cells vs WT cells at hyperglycemic conditions. (**Figure 2.6D**).

CLDN4 is a sealing claudin of particular interest since it is expressed throughout the airways and reports suggest that it has a protective role against lung injury [129,133–135]. Confocal microscopy was used to study protein expression and localization of this protein to the TJ of 16HBE-WT and 16HBE-CF polarized monolayers conditioned with normal or high glucose. Representative images are shown in **Figure 2.6E**. These images show an overlay of the maximum intensity projections in the Z-plane for two fluorescence intensity channels, the CLDN4 channel shown in green and the Zonula Occludens (ZO-1) channel shown in magenta. ZO-1 is almost all plasma membrane-localized and was used to identify cell boundaries and mark TJs. Little to no ZO-1 fluorescence signal comes from the cell interior. For quantification purposes, CLDN4 and ZO-1 were considered to be at the TJ when localized to the cell periphery/plasma membrane. In our novel quantification method, images were deidentified and opened with ImageJ. The ZO-1 channel was used to number all visible cells and eight non-adjacent cells per field were randomly

selected for analysis. Cell outlines were manually drawn following ZO-1 fluorescence intensity as template, using the multi-point line tool on ImageJ (**Figure 2.6F**). ZO-1 fluorescence intensity coming from the periphery of each cell was then measured, which gives an indication of total TJ-associated ZO-1. CLDN4 colocalized with ZO-1 was used to determine the relative amount of TJ-associated CLDN4 normalized to WT, normal glucose (**Figure 2.6G**). Results show that TJ-localized CLDN4 abundance remained unchanged in WT cells in response to hyperglycemia. However, under both normal glucose and hyperglycemic treatment, CF cells had elevated CLDN4 TJ abundance when compared to their WT controls (**Figure 2.6H**); more importantly, the distribution of values across cells was broad, compared to WT cells, suggesting that localization was dysregulated in CF cells. Further, CLDN4 localization to TJs increased in CF cells and the distribution was even more broad. ZO-1 TJ expression followed a similar trend (**Figure 2.6I**).

The effects of ETI treatment on CLDN4 and ZO-1 TJ localization also were studied. There was no change in CLDN4 TJ localization in WT cells treated with hyperglycemia and ETI. However, CF cells showed a decrease in CLDN4 abundance at the cell periphery in response to hyperglycemia when treated with ETI. CF cells treated with normal glucose and ETI had elevated CLDN4 TJ abundance when compared to their WT control. However, in CF cells treated with ETI, the response to hyperglycemia indicated a reduced abundance of CLDN4 at the cell periphery (**Figure 2.6J**). In this case, ZO-1 TJ abundance did not follow the same trends as CLDN4 with ETI. Both WT and CF cells showed increased ZO-1 TJ abundance in response to hyperglycemia when ETI also was present. Further, there was no difference between ZO-1 TJ abundance in WT and CF cells at normal or high glucose in the presence of ETI (**Figure 2.6K**).

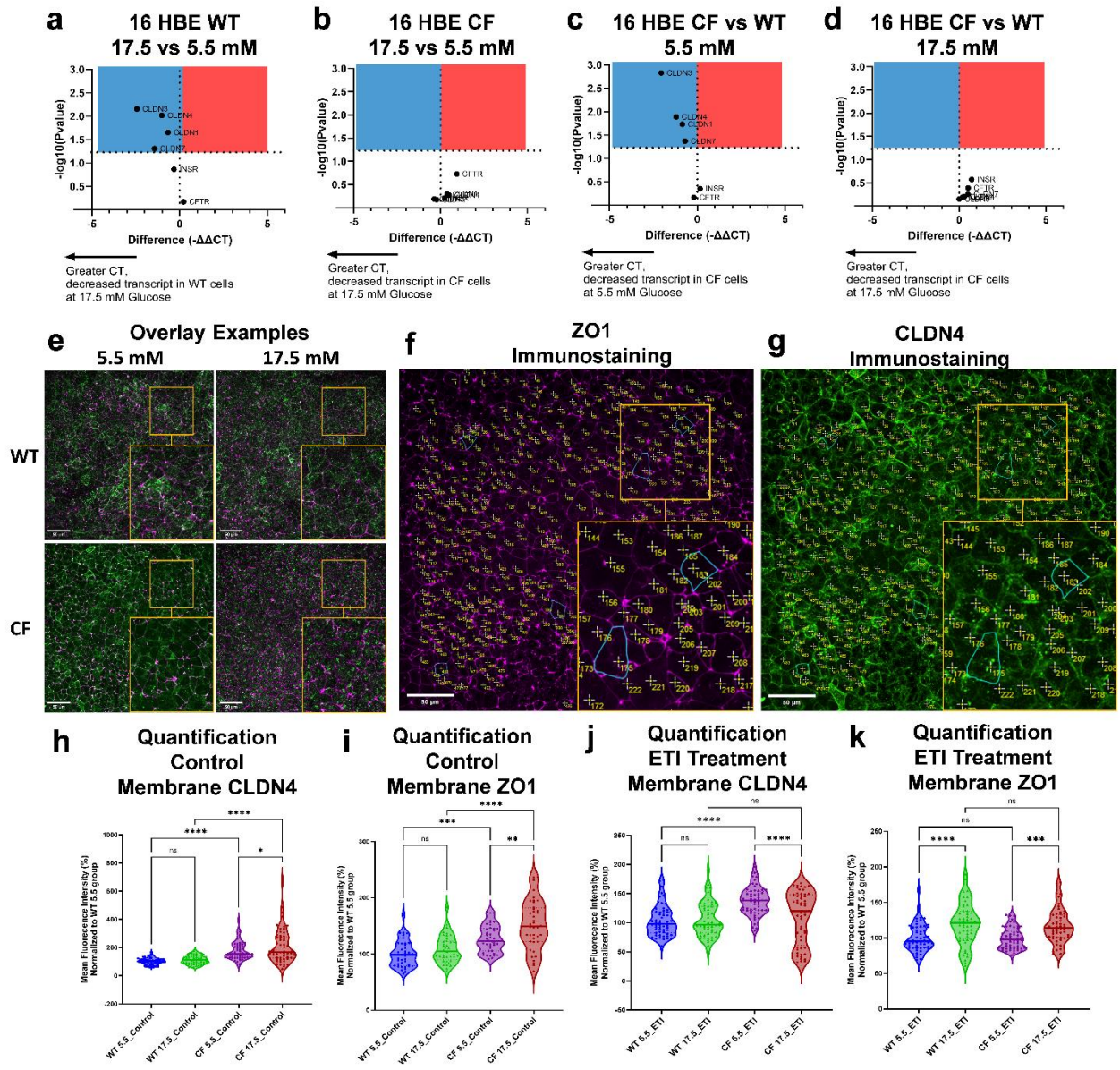

Figure 2.6. Hyperglycemia leads to dysregulation of essential glucose barrier components in 16HBE cells.

Cells were conditioned with normal or high glucose for 7 days. Elexacaftor (5 μM)/Texacaftor (18 μM) added in the last 48 hours. Elexacaftor (5 μM)/Texacaftor (18 μM)/Ivacaftor (1 μM) added in the last 24 hours. Results show (A) volcano plot of key tight junction genes upregulated (red) or downregulated (blue) in WT cells, or (B) in CF cells in response to hyperglycemia. (C) Volcano

plot of key tight junction genes upregulated (red) or downregulated (blue) in WT vs CF cells at 5.5 mM glucose and (D) in WT vs CF cells at 17.5 mM glucose. (E) Representative confocal microscopy images of overlayed CLDN4 (green) and ZO-1 (magenta) immunostaining. (F) Representative ZO-1 immunostaining image showing quantification technique. Example cells outlines used for quantification analysis shown in cyan. (G) Representative CLDN4 immunostaining image showing quantification technique. Example cells outlines used for quantification analysis shown in cyan. (H) Quantification of control membrane CLDN4 expression. (I) Quantification of control membrane ZO-1 expression. (J) Quantification of membrane CLDN4 expression after ETI treatment. (K) Quantification of membrane ZO-1 expression after ETI treatment. Statistics: Two-way ANOVA for multiple comparisons, Tukey correction, **** $p<0.0001$*** $p<0.001$, ** $p<0.01$, * $p<0.05$. Each replicate was normalized to its WT normal glucose control group (N=3, 2-3 Transwells per experiment, 16-24 cells analyzed per condition per experiment).

2.2.5. Transcriptional responses are different in CF versus WT cells under normal or high glucose.

Data thus far suggest that WT and CF cells exhibit differences in the barrier function response to hyperglycemic conditions. To determine if this was due to differences in gene expression in an untargeted manner, bulk RNA sequencing of cells grown on permeable supports under normal glucose or hyperglycemic conditions was performed; results show different transcriptional responses in CF cells compared to WT cells when cultured under either normal or high glucose (5.5 mM or 17.5 mM, respectively). Differentially expressed genes were defined as genes with a $|\log2FoldChange| \geq 1$ and a $padj < 0.05$. CF cells showed 572 downregulated genes and 370 upregulated genes compared to WT cells when cultured under normal glucose; CF cells showed 474 downregulated and 317 upregulated genes compared to WT cells when cultured under high glucose (**Figure 2.7A)**. Normal glucose results are shown in **Figure 2.7B-D**. High glucose results are shown in **Figure 2.7F-H**. A Venn diagram taking all differentially expressed genes from CF versus WT cells at normal and high glucose shows that 573 genes are found in common between both sets, with 369 genes uniquely differentially expressed under normal glucose and 218 genes uniquely differentially expressed under high glucose (**Figure 2.7E**). Differential expression of WT high glucose versus WT normal glucose, as well as CF high glucose versus CF normal glucose is shown in **Figure 2.8**.

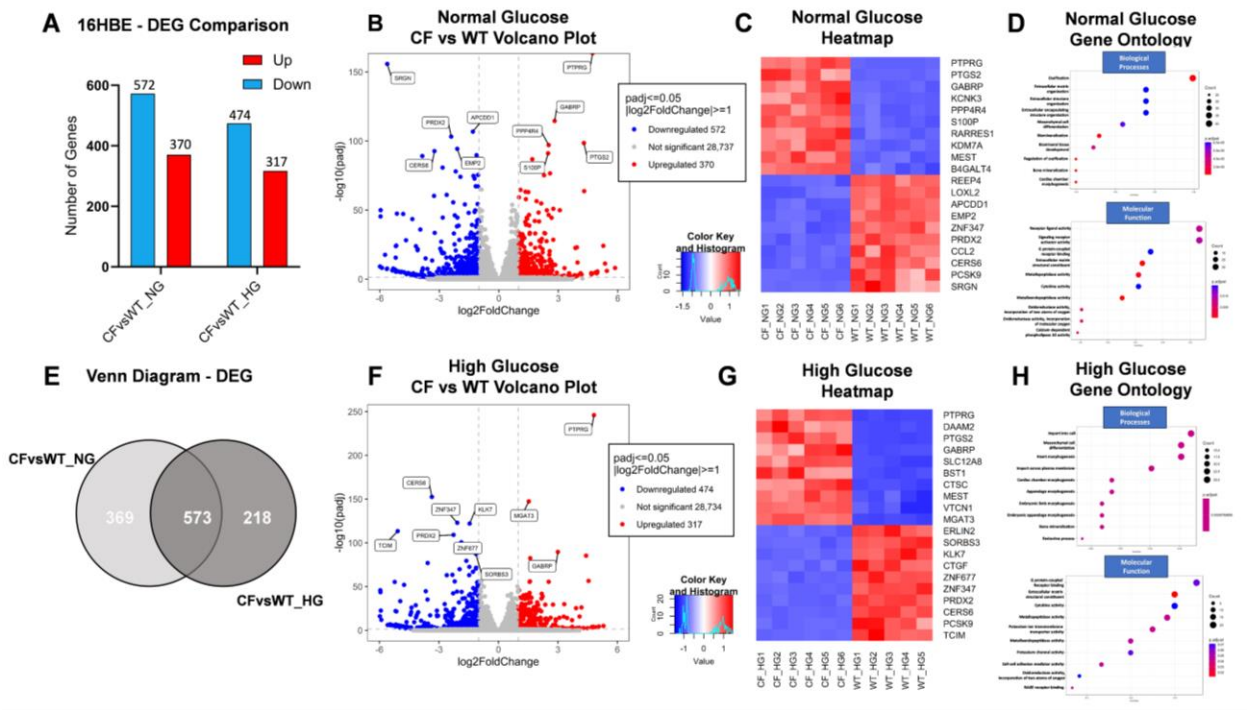

Figure 2.7. CF cells differ in transcriptional responses compared to WT cells when cultured with normal and high glucose media for 7 days.

(A) Summary of the number of genes upregulated and downregulated. (B) Volcano plot highlighting the differentially expressed genes in CF vs WT cells in response to normal glucose culture (red = upregulated, blue = downregulated). (C) Heatmap of the top differentially expressed genes under normal glucose in CF vs WT cells. (D) Gene ontology analysis of differentially expressed genes under normal glucose in CF vs WT cells (top = biological processes, bottom = molecular function). (E) Venn diagram highlighting the number of genes differentially expressed in each group, as well as the overlap. (F) Volcano plot highlighting the differentially expressed genes under hyperglycemia in CF vs WT cells (red = upregulated, blue = downregulated). (G) Heatmap of the top differentially expressed genes under hyperglycemia in CF vs WT cells. (H) Gene ontology hyperglycemia in CF vs WT cells (top = biological processes, bottom = molecular function) (N=5-6).

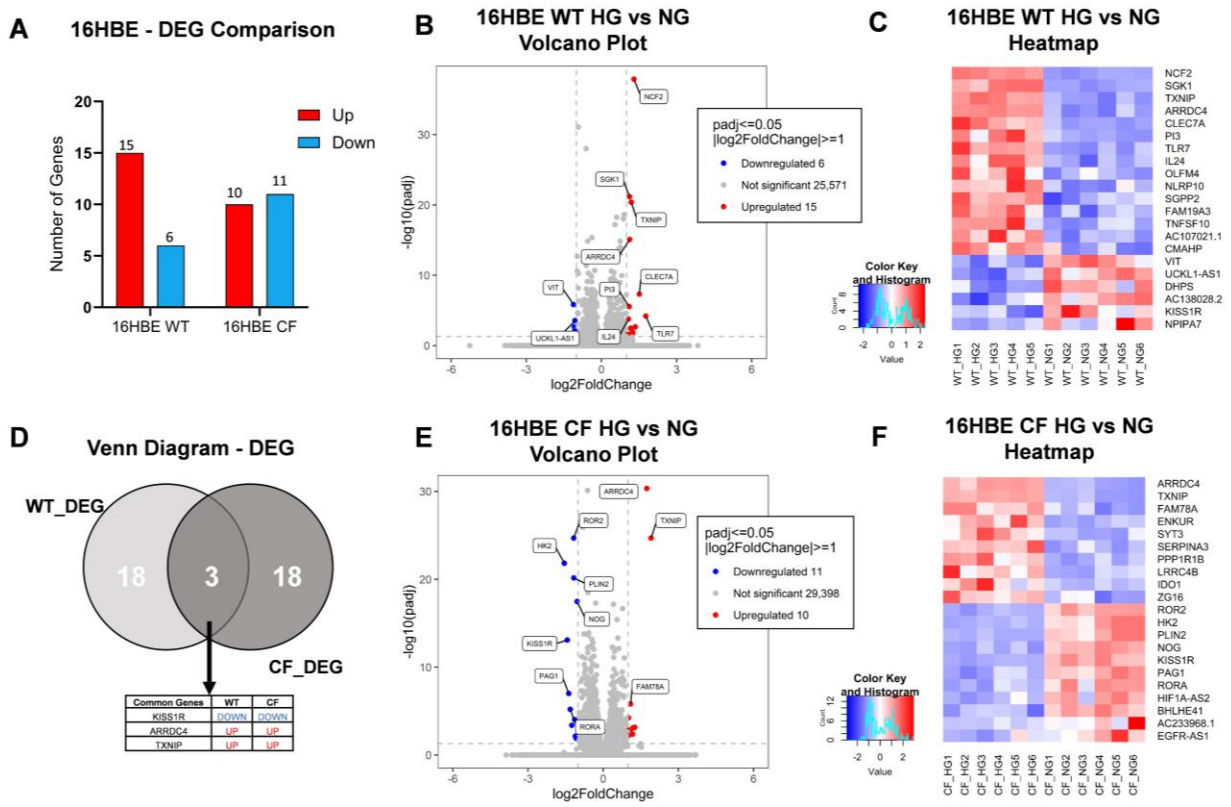

Figure 2.8. WT and CF cells conditioned with hyperglycemia have different transcriptional responses after 7 days of treatment.

(A) Summary of the number of genes upregulated or downregulated in WT and CF cells in response to hyperglycemia. (B) Volcano plot highlighting the differentially expressed genes in WT cells (red = upregulated, blue = downregulated in response to hyperglycemia). (C) Heatmap of the differentially expressed genes in WT cells. (D) Venn diagram highlighting the number of genes differentially expressed in each group, with the common genes shown in a table. (E) Volcano plot highlighting the differentially expressed genes in CF cells (red = upregulated, blue = downregulated in response to hyperglycemia). (F) Heatmap of the differentially expressed genes in CF cells (N=5-6).

2.2.6. Gene set enrichment analysis shows that hallmark gene sets are dysregulated in CF versus WT cells under normal and high glucose culture conditions.

Taking the DESeq2 normalized count data from bulk RNA sequencing, gene set enrichment analysis (GSEA) was run to identify Hallmark gene sets dysregulated in CF compared to WT cells under normal conditions and hyperglycemia. Gene sets with a false discovery rate (FDR) q-value less than 0.2 were considered significantly enriched. Under normal glucose, 14 Hallmark gene sets were dysregulated in CF cells (**Figure 2.9A**). The top 6 enrichment plots are shown in **Figure 2.9B**. Under high glucose, 8 Hallmark gene sets were dysregulated in CF cells (**Figure 2.9C**). The top 6 enrichment plots are shown in **Figure 2.9D**.

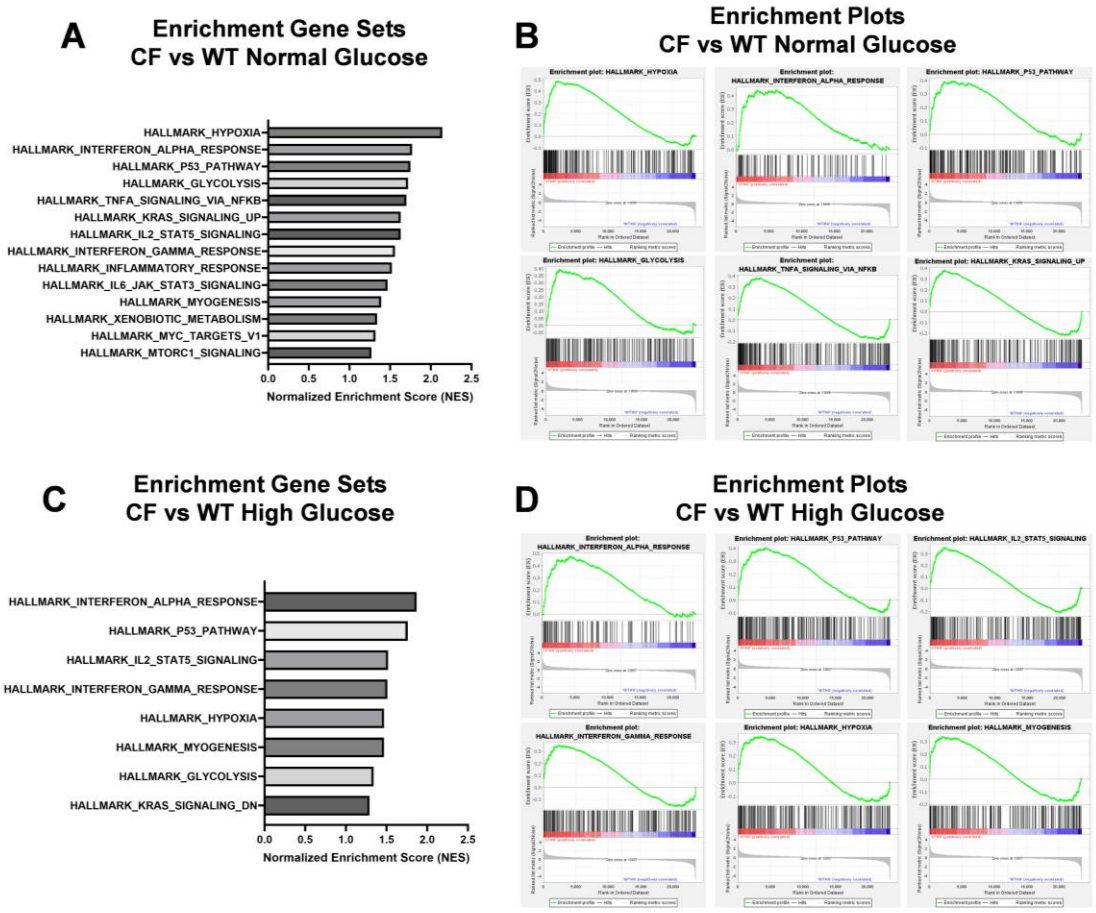

Figure 2.9. Gene set enrichment analysis (GSEA) results highlight hallmark gene sets dysregulated in CF versus WT under normal glucose or high glucose after 7 days.

(A) Plot highlighting all the hallmark gene sets enriched in CF versus WT cells at normal glucose (5.5 mM). (B) Enrichment plots for the top six gene sets enriched in CF versus WT cells under normal glucose. (C) Plot highlighting all the hallmark gene sets enriched in CF versus WT cells at high glucose (17.5 mM). Gene sets with a false discovery rate (FDR) q-value <0.2 were defined as enriched. The normalized enrichment scores (NES) for each gene set are shown on the x-axis. (D) Enrichment plots for the top six gene sets enriched in CF versus WT cells under high glucose. Normalized gene counts from DESeq2 were used as the input for GSEA (N=5-6).

2.3. Discussion

In this study, we utilized 16HBE cells as a model cell line to test the effects of hyperglycemia on airway epithelial barrier function in the context of CF. Data presented here indicate that WT cells can adapt to hyperglycemia, while CF cells lack the same adaptive response. After exposure to hyperglycemic media for 5-7 days, WT cells showed decreased TEER with a slight increase in CFTR current. TEER is a direct measure of barrier integrity. Our findings in WT cells agree with previous publications, which highlight a decrease in TEER in response to hyperglycemia in intestinal, retinal, and renal epithelia[136–138]. Interestingly, CF cells showed no change in TEER in response to hyperglycemia and only a slight increase in CFTR current at extremely high glucose levels (30 mM). However, CF cells showed increased paracellular flux of 10 kDa Dextran in response to hyperglycemia, which indicates impaired barrier function. Paracellular leak increased when insulin (400 nM) treatment was introduced, with increased flux of both Calcein (0.62 kDa) and Dextran (10 kDa) in CF cells under hyperglycemia, consistent with our prior results with normal glucose conditioning[126]. The mechanisms driving defective insulin signaling and its negative effects on barrier integrity are not yet understood.

Many CFRD patients are now taking ETI. Yet, it is still unclear whether the pulmonary effects of ETI might be diminished in the context of CFRD. We tested whether hyperglycemia and insulin conditioning might impair rescue of CFTR by ETI. Our results show that hyperglycemia with or without insulin was not detrimental to rescue of CFTR by ETI. On the contrary, we saw slightly higher CFTR currents in the ETI and high glucose CF group when insulin was present. However, the airway epithelial barrier integrity might still be compromised.

The findings in this study suggest that key TJ proteins are dysregulated in response to hyperglycemia. Out of the several TJ proteins found to be dysregulated at the mRNA level in CF

cells, we further investigated localization of CLDN4 protein to the TJ. CLDN4 is an interesting TJ protein because it has been reported to be expressed throughout the airway and to have a protective effect against lung injury[129,133–135]. The lungs of CLDN4 knock-out mice showed increased inflammatory markers such as IL-1B and modestly increased paracellular permeability [139]. Inflammation is a hallmark of CF airway disease, so it is possible that dysregulated expression of TJ proteins such as CLDN4 could play a role in the upregulation of pro-inflammatory cytokines in the CF airways. Further, other studies have shown that overexpression of CLDN4 increased TEER in primary rat alveolar epithelial cells[135], while knockdown of CLDN4 using siRNA decreased TEER in human distal lung epithelial cells[133]. Upregulation of CLDN4 expression also has been associated with better lung fluid clearance and adequate injury response to mechanical stressors and hyperoxia [133,139]. All these observations make CLDN4 an interesting target for further investigation in CF.

Employing a novel confocal microscopy technique for protein quantification, we were able to measure CLDN4 localization specifically at the membrane periphery of 16HBE cells. Overall, our data show increased CLDN4 abundance at the periphery in CF cells at both normal and high glucose, compared to WT cells, with ZO-1 abundance following the same trend. However, while the average abundance for these two TJ proteins is higher in CF cell membranes, the data are widely distributed between cells, suggesting lack of focal, organized localization compared to in WT cell membranes. Increased protein expression at the TJs does not necessarily correlate with stronger barrier integrity. In contrast, an excessive amount of CLDN4 in CF TJs might lead to aberrant barrier integrity, if this impacts other TJ proteins. Interestingly, treatment with ETI reversed the increase in CLDN4 abundance seen in CF cells at high glucose and led to tighter distribution of localization more closely resembling that seen in WT cells. These observations

suggest that modulator therapies that correct CFTR folding and function may have downstream consequences on proteins impacted by mutant CFTR and might impact tight junction barrier integrity. Future work is needed to assess changes of other essential TJ proteins in response to hyperglycemia and ETI treatment.

To identify differentially expressed genes in CF versus WT cells, we conducted bulk RNA sequencing of polarized 16HBE cells conditioned with normal or high glucose. Our results show that CF and WT transcriptomes differ under both normal and high glucose culture. The top ten differentially expressed genes in CF versus WT cells at normal glucose (based on padj) were PTPRG, SRGN, GABRP, APCDD1, PRDX2, PTGS2, PPP4R4, EMP2, CERS6, S100P, LOXL2, and PCSK9. The top ten differentially expressed genes in CF versus WT cells at high glucose were PTPRG, CERS6, MGAT3, ZNF347, KLK7, TCIM, PRDX2, ZNF677, SORBS3, and GABRP. In both cases, PTPRG was the top differentially expressed gene. It was found to be upregulated in CF versus WT cells, with a slightly higher log2FoldChange under high glucose versus normal glucose (4.82 vs 4.71, respectively). The PTPRG gene encodes a receptor-type protein tyrosine phosphatase. This gene plays a role in cell signaling, adhesion, differentiation, growth, and oncogenesis[140]. Further, PTPRG was found to play a role in hepatic inflammation and insulin resistance in mouse models[141]. PTPRG also was found to inhibit Akt signaling to suppress carcinoma tumor growth[142]; inhibition of Akt by increased PTPRG expression could also explain defects in insulin signaling that we previously observed in CF cells[126]. Gene ontology analysis identified mesenchymal cell differentiation as a biological pathway dysregulated in CF versus WT cells under both normal and high glucose. A possible driver of mesenchymal cell differentiation in CF cells could be nuclear factor-kappa B (NF-κB), since it was previously found to drive epithelial-mesenchymal transition in lung fibrosis[143]. Further, GSEA Hallmark gene set analysis identified

aberrant tumor necrosis factor alpha (TNFα) signaling via NF-κB in CF cells compared to WT cells under normal glucose. Interestingly, a previous publication found that NF-κB binds to the promoter region of the PTPRG gene and increases PTPRG expression in hepatic mouse tissue[141]. These observations highlight that CF cells might undergo aberrant tissue remodeling even under normal glucose culture and that the genes involved in this pathway might also be linked to aberrant insulin signaling in CF. Further, decreasing PTPRG expression might be a potential therapeutic target to improve insulin sensitivity and reduce airway glucose burden in CFRD.

Limitations of this study include a relatively short exposure time of airway epithelial cells to chronic hyperglycemia, and the use of immortalized cells which may not fully recapitulate *in vivo* airway physiology. WT and CF 16HBE cells were conditioned with normal or high glucose media for 5-7 days, which might not be sufficient time to elicit similar changes seen in the airways of CFRD patients that have spent years living with this disease. The amount of time we were able to condition monolayers with hyperglycemic media was constrained by the system. 16HBE cells can only be grown on Transwells for up to 9 days before their TEER decreases. However, our RNA sequencing data does show differential responses to glucose conditioning in WT vs CF cells even with our short glucose conditioning exposure protocol. Further, we also see changes at the protein level by quantifying CLDDN4 expression at TJs. Another limitation worth addressing in the future is the lack of proinflammatory factors in our media. These are found in high levels in CF airways and have been shown to play a role in regulation of tight junction assembly[144,145]. Addition of immune cells, such as neutrophils, would also better mimic the CF airway environment and influence barrier integrity[146]. Overall, our current study shows that the use of immortalized model cell lines such as 16HBE cells in research is extremely valuable; however, further studies are needed to confirm our findings in primary cells. This is challenging to accomplish because

common base media formulations required to culture primary cells already contain high glucose concentration. PneumaCult^{TM}-ALI media, for example, contains 17.5 mM glucose[147]. We are actively working on improving culture conditions to study the effects of hyperglycemia on primary airway epithelial cells.

2.4. Conclusion and Future Directions

Our current study shows that the use of immortalized model cell lines such as 16HBE cells in research is extremely valuable; however, further studies are needed to confirm our findings in primary cells. Other essential tight junction proteins could also be investigated in future studies. Overall, our data provide meaningful insights into the pathophysiology of CFRD and identify a few interesting targets, such as CLDN4 and PTPRG, for further investigation. Gaining a better understanding of the pathways that play a role in CFRD will inform future therapeutic agents to treat this devastating co-morbidity and improve the quality and length of life of patients with CFRD.

Chapter 3 – Development of a Programmable Automated Cell Culture System to Study the Lung Pathophysiology of Cystic Fibrosis Related Diabetes

Preface

The way we culture cells *in vitro* is not physiologically relevant. This hinders scientific research findings. This chapter covers information about the creation and development of an automated cell culture system, which can be programmed to change media on the basolateral side of Transwells multiple times a day. This novel system addresses the need for automation in cell culture, especially to better mimic glucose fluctuations in culture to better mimic human physiology. This work contributes a novel invention to the field that could be used for multiple applications with minimal modifications. Overall, this system was tested in the context of CFRD. Both WT and CF cells could be successfully cultured using this system.

Full citation

Vazquez Cegla, A. J.; Hedden, C.; Imhoff, B. R.; Cui, G.; McCarty, N. A. Development of a Programmable Automated Cell Culture System to Study the Lung Pathophysiology of Cystic Fibrosis Related Diabetes. *Heliyon* **2024. https://doi.org/10.1016/j.heliyon.2024.e37977.**

3.1. Introduction

Cystic Fibrosis-Related Diabetes (CFRD) is the most common Cystic Fibrosis (CF) co-morbidity, and its pathophysiological consequences are severe[148]. CF is an autosomal recessive disease caused by mutations in the gene encoding the Cystic Fibrosis Transmembrane Conductance Regulator (CFTR) [17,149]. CFTR is expressed at the surface of epithelial cells throughout the body, and is essential to the function of key systems, such as the respiratory and digestive tracts[150]. Recently, pharmacological advances in the CF field have greatly increased the life expectancy of people with CF (pwCF)[151]. As a result, CFRD has become more prominent. CFRD starts to develop during early childhood, and about half of pwCF develop CFRD by adulthood[9,91]. This is concerning since CFRD patients experience more rapid lung function decline, approximately six-fold greater than pwCF without diabetes, due to more frequent pulmonary exacerbations[85,90,152]. The link between CFRD and accelerated lung function decline is unknown, and there are no good *in vitro* models to study this devastating disease.

Immortalized and primary airway epithelial cells expressing either WT or mutant CFTR, the most common mutation being ΔF508, are available. However, common protocols used in the field involve culturing airway epithelial cells using media containing extremely high levels of glucose. DMEM for example, a common base media component, contains 450 mg/dL of glucose[153]. This is >3.5 times higher than what is considered the upper limit for normal blood glucose at fasting (125 mg/dL)[154]. Further, cells *in vivo* experience glucose fluctuations after meals and snacks, as shown by continuous glucose monitoring (CGM) data[83]. In contrast, cells cultured *in vitro* are initially exposed to media with high glucose concentration, which gets progressively depleted until the next media change, typically days later[155]. It is also possible that cells experience hypoglycemic periods, especially when cultured in small volumes, which might introduce harmful

changes in cell behavior (**Figure 3.1**). Overall, current patterns of glucose exposure used to study CF *in vitro* do not resemble human physiology. Automation of cell culture, a rapidly growing field, could be used to address this issue.

Automation has been successfully used to culture adherent cells to tightly control their chemical and biological environment[156]. Custom chambers created using 3D printing and pumps are commonly used to control media flow in and out microfluidic chambers[157]. However, the field of cell culture automation has mostly focused on the development of lab-on-a-chip devices for high-throughput screening[158]. Limitations in the field include cost and ease of use of such devices. Further, there are currently no effective ways to automate cell culture of airway epithelial cells plated on permeable Transwell supports, necessary to better study the effects of CFRD on airway physiology.

To allow for better glycemic control while doing *in vitro* cell culture, we developed a programmable Automated Cell Culture System (PACCS) capable of simulating meal-like glucose fluctuations (**Figure 3.2**). The system uses a combination of peristaltic pumps, pinch valves, and a programmable controller to change the media in custom-designed 3D-printed cell culture plates multiple times a day. The system requires minimal user intervention and can run meal-like glucose fluctuation programs for several days on multiple plates. This novel tool was used to evaluate the effects of episodes of acute hyperglycemia in WT and CF immortalized and primary airway epithelial cells, but it could be used for a wide range of applications. In this paper, we tested changes in the transepithelial electrical resistance (TEER) of airway epithelial monolayers in response to PACCS culture, as a measure of health of the epithelium. Overall, PACCS is a cost-effective and compact novel cell culture tool that addresses major limitations in the cell culture field and allows for better simulation of CFRD conditions *in vitro*.

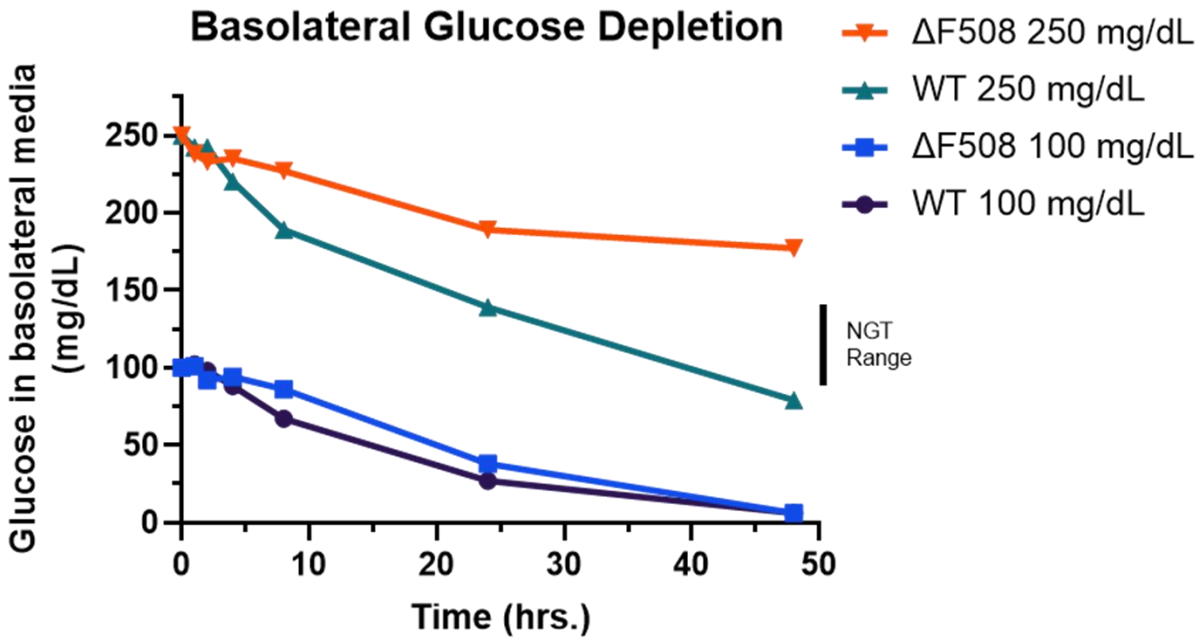

Figure 3.1. Utilization of basolateral glucose by 16HBE immortalized human bronchial epithelial cells in Transwells.

Cells expressing wildtype or ΔF508 CFTR were grown to confluency in Transwells with media containing either 100 mg/dL glucose or 250 mg/dL glucose. At time zero, media bathing the basolateral surface was exchanged. At multiple times over the following 48 hours, 100 uL of media was removed from the basolateral chamber of the Transwell and assayed for glucose concentration using a colorimetric kit (Cayman Chemical; #10009582). Glucose was rapidly depleted from the basolateral bathing media, with kinetics slightly different between WT and ΔF508 cells with 250 mg/dL initial glucose. Importantly, only Transwells with 250 mg/dL glucose media and WT cells exhibited basolateral glucose concentrations that are within the normal glucose tolerance (NGT) range, as indicated by the black vertical bar at the right of the figure, and even that, only for part of the two-day experiment. These results are representative of N=3 with similar outcomes.

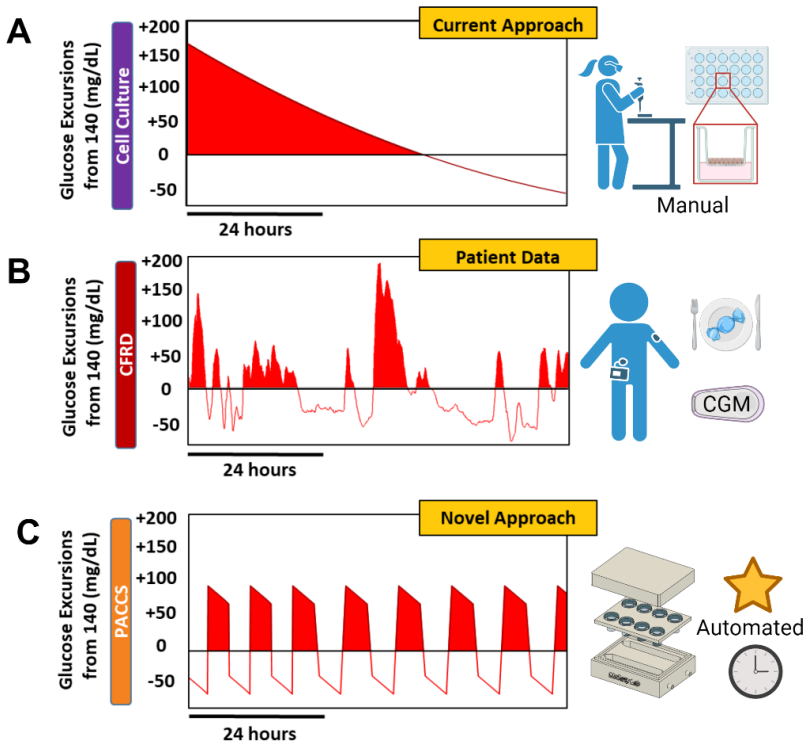

Figure 3.2. Current cell culture protocols do not resemble CFRD physiology.

A) Representative plot highlighting glucose depletion on the basolateral side of Transwells during traditional *in vitro* cell culture after receiving hyperglycemic media. Note that cells are exposed to hyperglycemic media for an extended period, with progressive depletion of glucose for 72 hours. Manual media changes are required. B) Representative blood glucose excursions experienced by a CFRD patient over 72 hours. Patterns of fluctuation in and out of the hyperglycemic region, in response to meals, are evident in the graph. Data were taken by continuous glucose monitoring (CGM). C) Representative glucose patterns that can be achieved using PACCS, better resembling patterns experienced by CFRD patients. This novel approach is automated and requires minimal user interaction. Note that in all plots zero represents 140 mg/dL glucose. Any measurements above are considered to fall in the hyperglycemia region. The area under the curve on hyperglycemia regions was highlighted (created with BioRender).

3.2. Materials and Methods

3.2.1. Cell culture of CFBE immortalized cell line

Immortalized CFBE41o- Human Bronchial Epithelial cells (CFBE) expressing WT-CFTR (CFBE-WT) were kindly provided by Dr. K. Oliver (Emory). Cells were cultured in MEM complete media containing 90% MEM (Gibco, 11095-072), 10% FBS (ThermoFisher, 26140), and 1% Penicillin/Streptomycin (Gibco 15070-063). Cells were expanded in collagen-coated plates PureCol (Advanced Biomatrix #5005-B) and 2 μg/mL puromycin (Sigma, P8833) was used as the selection agent. For PACCS experiments, cells were plated in collagen-coated Transwells (Corning, #3470) at a density of 100,000 cells per well at liquid-liquid interface. The next day after seeding, cells were put at air-liquid interface (ALI). Experimental Transwells were transferred to PACCS, while control Transwells received manual media changes. Cells were exposed to either daily media changes or meal-like glucose fluctuations for 7 days. Selection agent was not added to cells undergoing experimentation.

3.2.2. Culture of primary cells

Primary human bronchial epithelial cells expressing either WT- (NhBE) or ΔF508-CFTR (CFhBE) were kindly provided by Dr. M. Koval (Emory). Cells were expanded and plated in Transwells (Corning, #3470) as previously described[108]. Briefly, previously expanded epithelial cells were plated onto Type IV collagen-coated Transwells at a density of 100,000 cells per well at liquid-liquid interface using E-ALI media. E-ALI is based on a 50:50 mixture of low-glucose DMEM containing 100 mg/dL glucose, without L-glutamine and with sodium pyruvate (Sigma, D5546), and LHC Basal Medium (ThermoFisher, 12677–019) containing additives. After 48 hours of plating, the basolateral medium was replaced with fresh E-ALI and the apical medium was removed to bring the cells to ALI. Media was changed every 2 to 3 days. After 14 days,

experimental Transwells were transferred to PACCS while control Transwells received manual media changes. Cells were exposed to either daily media changes or meal-like media changes for 7 days.

3.2.3. Programmable and automated control of PACCS

The ValveBank 8 Controller (Automate Scientific, #01-08) was used to make the PACCS system programmable and automated. This controller allows the user to make loop programs without the need of a computer. The controller was used to control peristaltic pumps (Adafruit, #1150) connected to media reservoirs containing normal or high glucose media (5.5 vs 17.5 mM glucose, respectively). We used autoclavable Nalgene bottles (Thermo, #2105-0016), but replaced the lids with filling/venting closures (Thermo, #2162-0531). Media bottles were connected to the pumps and the pumps were connected to the PACCS plate using autoclavable tubing (Cole-Parmer, #EW-96440-16).

3.2.4. Design iterations of PACCS cell culture plate components

There are no commercially available plates that could be used with our system. Thus, we designed and 3D-printed a cell culture plate that contained three main components: a main body to hold media, a tray to hold Transwells in place, and a lid to maintain sterility. Design iterations were made using Fusion 360 (AutoDESK). Variations between designs were made with the goal of reducing media consumption and ensuring good media exchange.

3.2.5. 3D-Printing

All design iterations were printed at Emory's "Tech Lab". STL files were printed using a Form2 printer (FormLabs) and clear standard resin (FormLabs, Product #RS-F2-GPCL-04).

3.2.6. PACCS quality control

Chicago Sky Blue 6B (Sigma, C-8679) and Phenol Red (Sigma, P-5530) dyes were dissolved in 500 mL of water to a final concentration of 0.5 mg/mL in separate containers to simulate normal and high glucose media, respectively. These blue and red solutions were used to test solution exchange in PACCS plate iterations. The ratio of red versus blue absorbance (400 nm versus 620 nm) was compared at each Transwell location. Empty Transwells were used at the time of testing. A small amount of sample (100 µL) was collected from the basolateral side and transferred to a transparent 96-well plate for absorbance measurements. Absorbance measurements were performed using a SpectroMax M2 plate reader (Molecular Devices).

3.2.7. Running PACCS

Media bottles were cleaned and autoclaved. To sterilize the PACCS tubing, 70% ethanol was run through the lines for 2 minutes, later closing the lines and allowing ethanol to sit inside for 15 minutes. The lines were then drained, and their openings covered with sterile foil. Media was added to media bottles and transferred to the incubator. Using the final design iteration, running PACCS for 7 days required 170 mL of normal glucose media (5.5 mM) and 170 mL of high glucose media (17.5 mM) for one full meal-like plate. An additional bottle with 340 mL of normal glucose media (5.5 mM) was required for the control plate. To sterilize the PACCS plate, all components were thoroughly sprayed down with 70% ethanol and allowed to airdry inside a cell culture hood. Transwells were put at ALI and transferred to the PACCS plate inside the cell culture hood. The PACCS plate holding the Transwells was transferred to the cell culture incubator, and inputs and outputs were connected. Fasting media (5.5 mM glucose) was introduced into the lines using the manual run function on the controller. This ensures that all lines have media before starting the PACCS program. The lines were visually inspected for air bubbles, and then the PACCS meal-like program was started. This program was designed to change media three times a

day for 7 days. The flowrate was ~285 µL/second. The inputs were opened for 28 seconds, dispensing ~8 mL of media divided between 2 reservoirs in each plate (~4 mL of media per reservoir). The vacuum was run for 20 seconds by itself, and then it overlapped with the inputs for 12 seconds to wash away any waste media left on the plate.

3.2.8. Ussing chamber analysis of cells cultured with PACCS and controls

The electrophysiological properties of airway epithelial cells were assessed by performing Ussing chamber analysis using standard protocols[159,160]. We report only the resistance values here.

3.2.9. Data Analysis

Data were analyzed using both Microsoft Excel and GraphPad Prism.

3.3. Results

3.3.1. The PACCS design incorporates several unique components to create a reliable automated cell culture platform for mammalian cells plated on permeable Transwell supports

We developed a novel programmable and automated cell culture system by combining several essential components. The main components of PACCS are shown in **Figure 3.3**. Hyperglycemic exposure patterns can be programmed using a commercially available and user-friendly controller, the ValveBank perfusion controller, which allows the user to create and store several programs to change media as often as desired. The controller powers peristaltic pumps that connect media storage bottles with the PACCS plate. The controller also powers a pinch valve that connects a waste container (fluid flow driven by vacuum) to the PACCS plate (**Figure 3.3A**). The PACCS plate has a main body, a tray, and a lid. The main body of the plate serves as the media reservoir, and it has inputs and outputs to allow for fluid exchange (**Figure 3.3B**). The tray holds up to eight Transwells in place (**Figure 3.3C**), while the lid prevents contamination. The PACCS

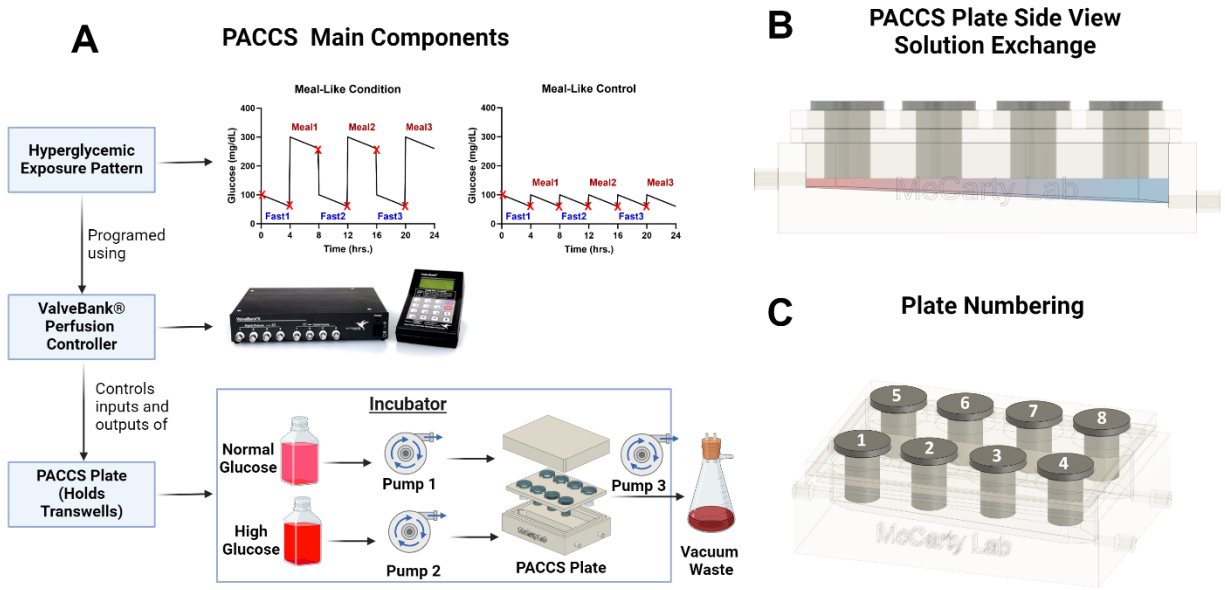

Figure 3.3. Graphical representation of the PACCS design.

A) Hyperglycemic exposure patterns (top) are programed using a commercially available perfusion controller (middle), which controls fluid flow from media bottles connected to a custom 3D printed cell culture plate (bottom). The red "Xs" shown on the top graphs represent automatic media changes performed by PACCS. B) Images of the PACCS cell culture plate highlighting fluid being exchange from fasting to a meal. C) Transwell location (created with BioRender).

plate, pumps, valves, and media bottles are small and can be stored inside an incubator, with the perfusion controller outside.

3.3.2. PACCS plate design iterations to reduce media consumption and improve fluid exchange

An essential element of PACCS is its cell culture plate. There are no commercially available plates compatible with our needs. Thus, we designed and 3D-printed our own cell culture plate. The evolution of the main body of the plate design is shown in **Figure 3.4**. The first design had a large media reservoir with a slanted surface to drive media flow from the inputs to the output. The plate had 2 inputs; one could be connected to a normal glucose media bottle and the other to a high glucose media bottle (**Figure 3.4A**). Transwells cultured at ALI need the bottom of the permeable supports to be submerged in media, while the apical side of the Transwell can be left exposed to air. The first plate design required ~15 mL of media for Transwells to be submerged in media. This was not feasible for future experiments since we needed to perform multiple media changes each day for multiple days. Thus, the second plate design incorporated octagon-shaped columns to reduce unoccupied space and decrease media consumption. Channels between columns were added to allow for fluid to flow (**Figure 3.4B**). However, when this design was tested with mock solutions, media exchange was troublesome. The third plate design replaced the octagon-shaped columns with cylindrical pillars, increasing the fluid channel width to aid with fluid exchange. This design also incorporated overflow safety valves (**Figure 3.4C**). The first three designs could hold twelve Transwells. However, all Transwells were exposed to the same media reservoir. Hence, WT and CF cells could not be cultured in the same plate. Thus, design 4 modified the main plate body to be able to hold only four Transwells, and it incorporated large side columns to reduce media consumption (**Figure 3.4D**). The design required separate plates for WT and CF cells. To reduce the number of plates needed to run an experiment, design 5 had two separate media

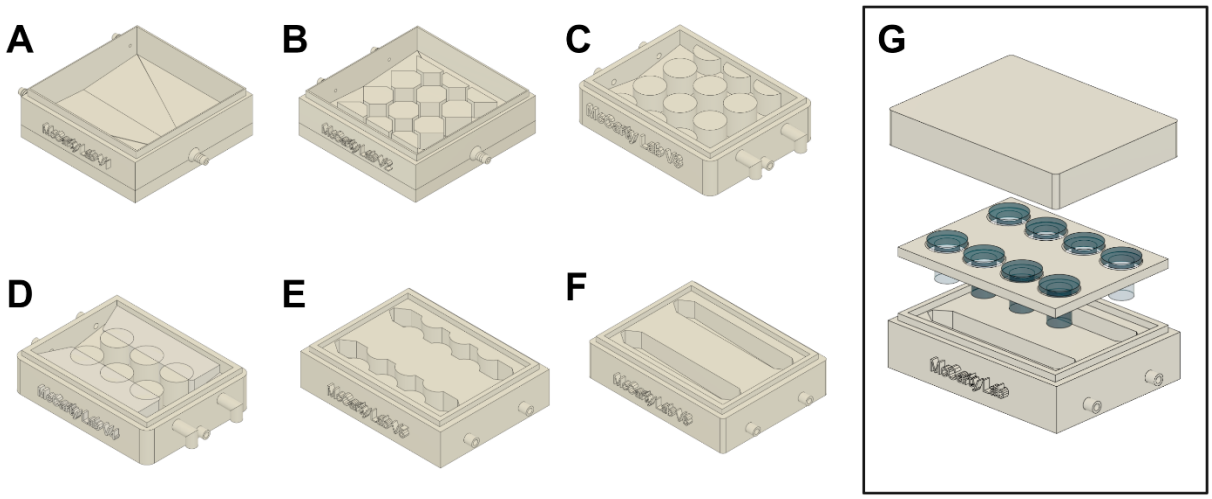

Figure 3.4. Progression of the PACCS plate design.

A) The initial design consisted of a large media reservoir with a slanted surface to drive fluid flow. This plate was able to accommodate 12 small Transwells, and it had two inputs and one output for media exchange. B) The second design incorporated octagon-shaped columns to reduce media consumption. C) The third design incorporated cylinder-shaped columns to aid with fluid exchange. This version also included a safety mechanism to prevent media overflow. D) The fourth design was able to accommodate 4 Transwells and incorporated large columns to the sides to minimize media consumption. E) The fifth design had two separated media reservoirs capable of accommodating 4 small Transwells each with their own inputs and outputs. F) The sixth design still consisted of two separated reservoirs, but columns were removed to aid with fluid exchange. G) Representation of the final design highlighting the main components of the PACCS plate: a lid (top), a tray capable of holding 8 small Transwells (middle), and the main body of the plate (created with BioRender).

reservoirs in a single plate, each able to hold four Transwells (**Figure 3.4E**). Since the media reservoirs are separate, WT and CF cells could now be cultured in the same plate. The safety valves were removed from the design, as they proved to be unnecessary in later models. However, this plate did not exhibit good fluid exchange. The final plate design removed cylindrical columns to optimize fluid flow (**Figure 3.4F**). Each reservoir had its own input and output for fluid exchange. Upon testing with mock solutions, the final plate design showed good fluid exchange, and it was able to reduce media consumption requiring around 4 mL of media per reservoir. The graphical representation of the final PACCS plate design also shows the tray and lid components (**Figure 3.4G, Figure 3.5**). This plate was used for further experiments.

3.3.3. Quality control of the final PACCS plate design showed good media exchange from fasting to meal-like conditions

PACCS was initially tested with mock solutions to check that its components were working correctly. Testing the system with mock solutions was also beneficial to assess fluid exchange on plate iterations. Mock solutions consisted of separate bottles containing either Phenol Red, to simulate a meal-like solution, or Chicago Sky Blue, to simulate a fast-like solution. The controller was used to create a program to mimic four fasting states and three meals, taking overall 24 minutes to run, simulating a whole day of meal-like media changes. The PACCS protocol used to run this experiment is shown in **Table 3.1.** The program could be paused in-between media changes to collect samples from each Transwell location. Absorbance readings at 400 nm and 620 nm were collected to test red and blue dye abundance, respectively (**Figure 3.6**). Standard curves showed that the absorbance of both dyes followed a linear trend, and that the data collected were within the linear range for absorbance (**Figure 3.6A**). Phenol Red absorbance readings remained low during fasting and increased during meals (**Figure 3.6B**). Chicago Sky Blue absorbances showed

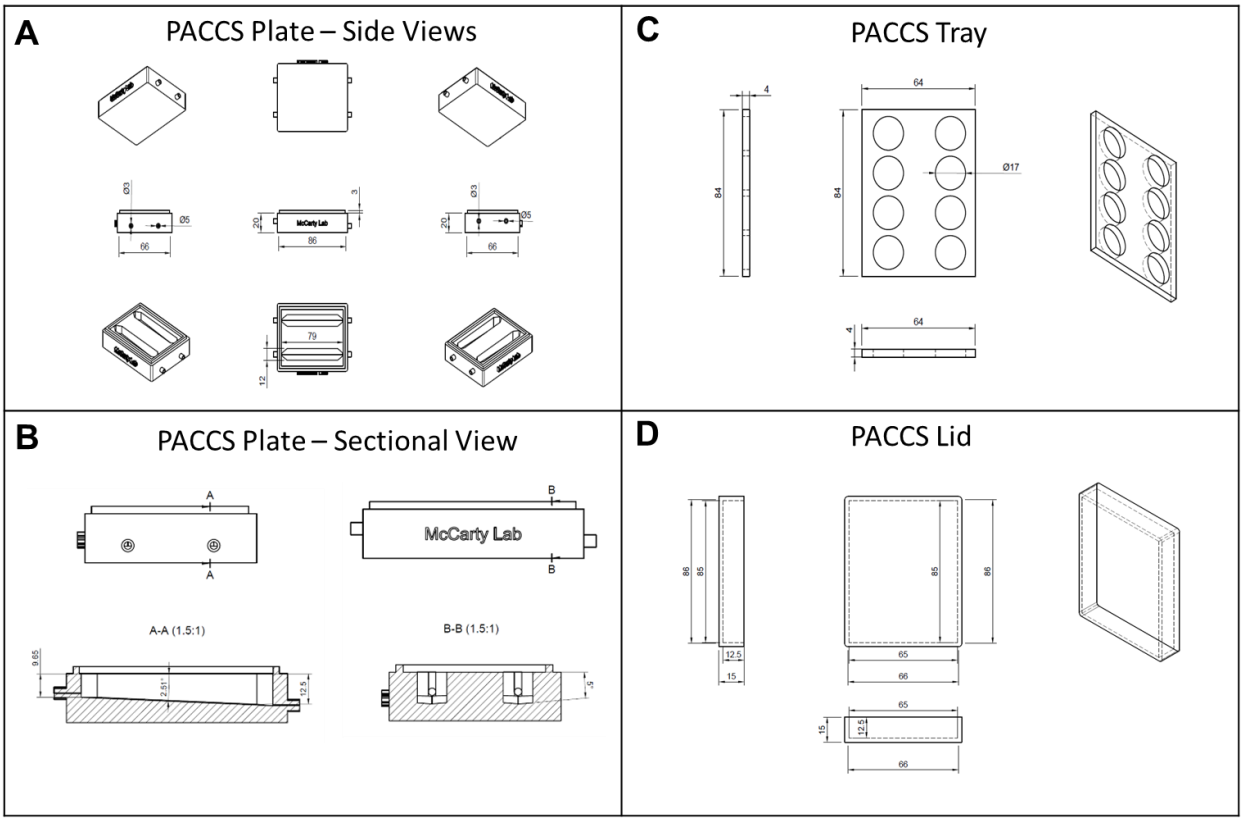

Figure 3.5. Technical drawings of the 3D designed PACCS plate.

A) Main body of the PACCS plate showing multiple side views. B) Main body sectional views highlighting surface incline which drives fluid flow. C) PACCS tray. D) PACCS lid. Note: All measurements are shown in millimeters.

Table 3.1. PACCS settings used to test media exchange in cell culture plate iterations, following meal-like fluctuations using blue and red solutions to simulate fasting versus meal-like solutions, respectively.

The settings were programed and stored using the ValveBank controller. Total run time was 24 minutes, simulating 24 hours of media changes. This program looped seven times, simulating 7 days of media conditioning. Channel 1 exclusively changed the media on the control plate, receiving only blue solution. Channels 2 and 3 were used to change media on the meal-like plate. Channel 8 ran the vacuum.

Channel 1 (First Input) Blue Solution for Control Plate	Channel 2 (Second Input) Blue Solution for Meal Plate	Channel 3 (Third Input) Red Solution for Meal Plate	Channel 8 (Vacuum)
00:00:00.00 Loop Start (07)	00:00:00.00 Loop Start (07)	00:00:00.00 Loop Start (07)	00:00:00.00 Loop Start (07)
00:00:00.00 Open Valve	00:00:00.00 Open Valve		00:00:00.00 Open Valve
00:00:28.00 Close Valve	00:00:28.00 Close Valve		00:00:12.00 Close Valve
00:04:00.00 Open Valve		00:04:00.00 Open Valve	00:03:40.00 Open Valve
00:04:28.00 Close Valve		00:04:28.00 Close Valve	00:04:12.00 Close Valve
00:08:00.00 Open Valve	00:08:00.00 Open Valve		00:07:40.00 Open Valve
00:08:28.00 Close Valve	00:08:28.00 Close Valve		00:08:12.00 Close Valve
00:12:00.00 Open Valve		00:12:00.00 Open Valve	00:11:40.00 Open Valve
00:12:28.00 Close Valve		00:12:28.00 Close Valve	00:12:12.00 Close Valve
00:16:00.00 Open Valve	00:16:00.00 Open Valve		00:15:40.00 Open Valve
00:16:28.00 Close Valve	00:16:28.00 Close Valve		00:16:12.00 Close Valve
00:20:00.00 Open Valve		00:20:00.00 Open Valve	00:19:40.00 Open Valve
00:20:28.00 Close Valve		00:20:28.00 Close Valve	00:20:12.00 Close Valve
00:24:00.00 Loop End	00:24:00.00 Loop End	00:24:00.00 Loop End	00:23:40.00 Open Valve
02:48:00.00 End of List	02:48:00.00 End of List	02:48:00.00 End of List	00:24:00.00 Close Valve
			24:00:00.00 Loop End
			68:00:00.00 End of List

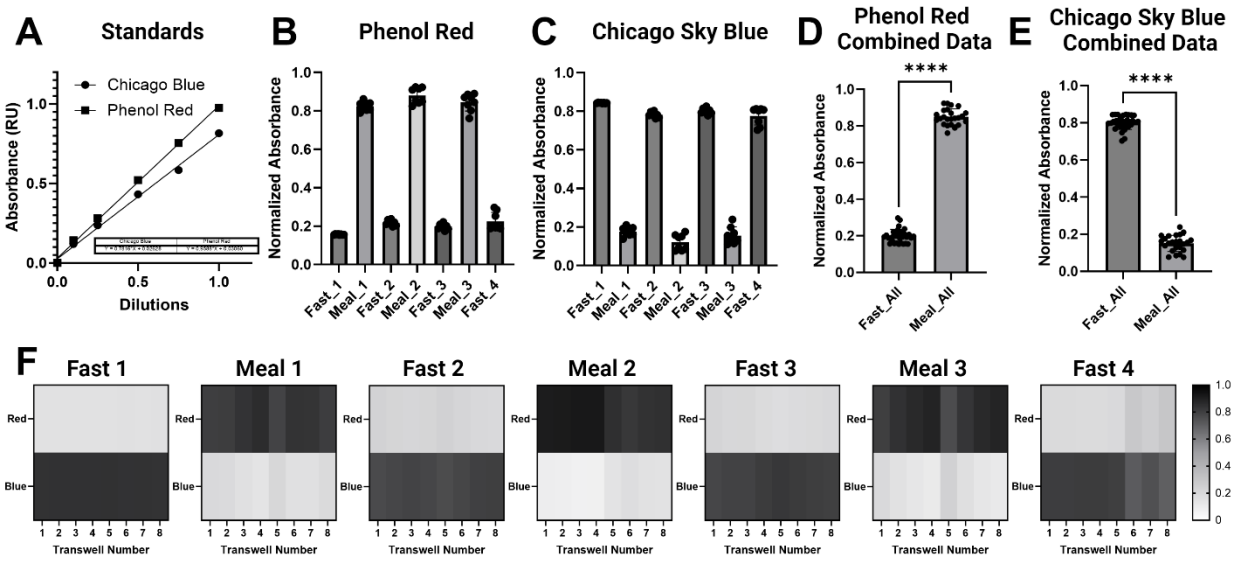

Figure 3.6. Final design of the PACCS plate showed good solution exchange between fasting and meals.

A) Standard curve for dyes used for fluid exchange tests: Phenol Red and Chicago Sky Blue. B) Phenol Red signal readings after each media change. C) Chicago Sky Blue signal readings after each media change. D) Summary of all Phenol Red data combined. E) Summary of all Chicago Sky Blue data combined. F) Heatmap showing the intensity readings at each time point for blue versus red signals. Data were normalized to the maximum absorbance intensity for the dye alone controls (n=8, T-test, **** $p<0.0001$) (created with BioRender).

an opposite trend, remaining high during fasting and decreasing during meals (**Figure 3.6C**). It is worth noting that the absorbance of either dye was never zero due to some spectral overlap between the two dyes. However, combining the data for all fasting and meal periods showed very significant differences in normalized absorbance, indicating good solution exchange between fasting and meals (**Figure 3.6D, E**). Heatmaps graphing the normalized absorbance readings at each Transwell location show that fluid exchange is slightly different at each Transwell location (**Figure 3.6F**). However, fluid exchange was sufficient to move forward and test PACCS with airway epithelial cells.

3.3.4. Immortalized cells and primary airway epithelial cells can be successfully cultured with PACCS

After initial testing of PACCS with mock solutions was completed, PACCS was used to culture airway epithelial cells. PACCS media bottles were stored inside the incubator, keeping the media at a constant temperature of 37ºC. Media bottles were connected to peristaltic pumps, which controlled media input into the 3D-printed plate. The PACCS plate was also connected to a vacuum waste container, with media suction out of the plate controlled by a pinch valve. These components fit inside a cell culture incubator as shown in **Figure 3.7A**. Only the perfusion controller used to create and store the PACCS programs was stored outside of the incubator. Immortalized airway epithelial cells expressing WT-CFTR (CFBE-WT) were first used to test whether PACCS could be successfully used to culture airway epithelial cells. These cells were chosen because they can be grown at air-liquid interface, since only basolateral media can be changed using PACCS. Daily media changes were performed by PACCS or by hand (control) for 7 days, with all Transwells receiving only 5.5 mM glucose media during initial experiments. Results show that TEER was not significantly different between PACCS and control cultures (**Figure 3.7B**). This result

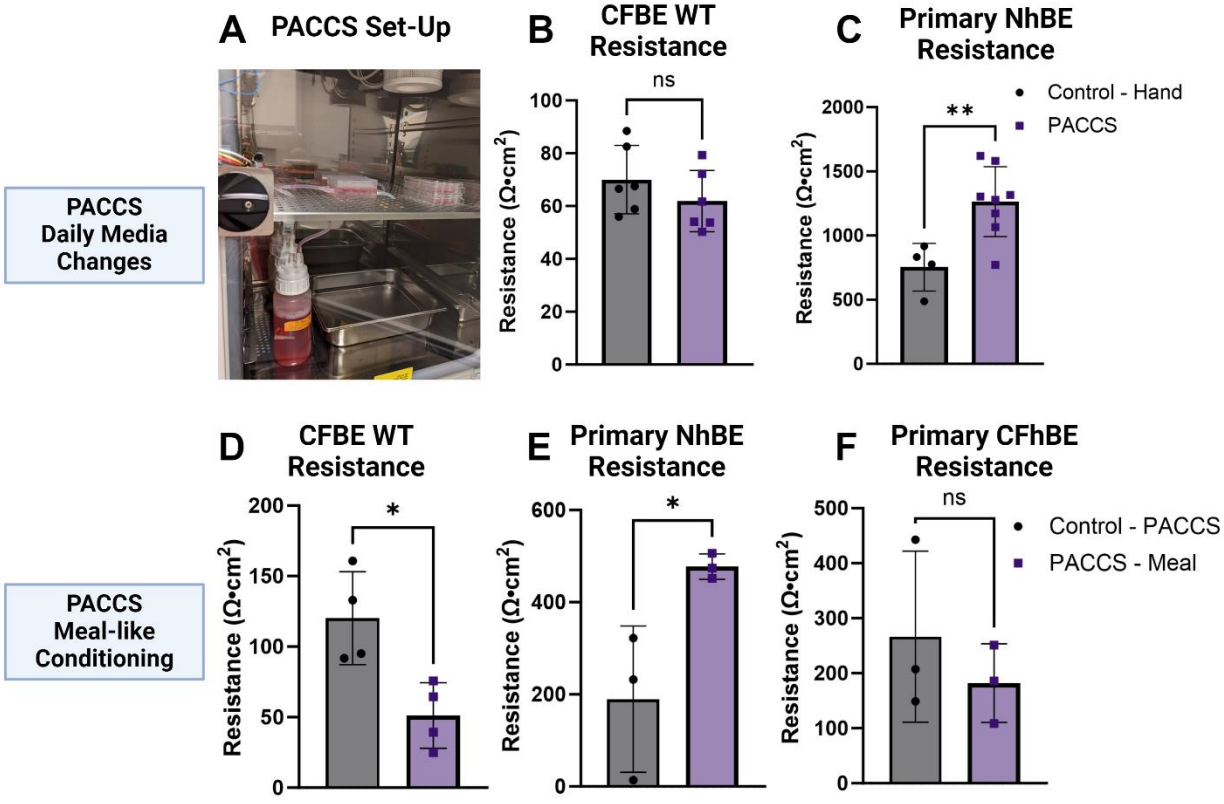

Figure 3.7. Airway epithelial cells can be successfully cultured with PACCS using daily media changes or meal-like media changes.

A) Representative image of PACCS components inside a cell culture incubator. Two media bottles can be seen connected to the 3D printed plate. Control plates (media changed by hand) shown on the incubator shelf at the right. B) Transepithelial electrical resistance (TEER) of CFBE WT and C) primary NhBE cells cultured with daily media changes via PACCS compared to control (daily manual media changes), using only media with 5.5 mM glucose. D) TEER of CFBE-WT, E) primary NhBE, and F) primary CFhBE cells cultured with meal-like media changes via PACCS (alternating between 5.5 mM and 17.5 mM glucose media) compared to PACCS control (media changes performed by PACCS at the same time points, but only receiving fresh 5.5 mM glucose media) (N=3, T-test, * $p<0.05$, ** $p<0.01$) (created with BioRender).

demonstrated that PACCS can be successfully used to culture airway epithelial cells, suggesting that using PACCS is not detrimental to cell health. We then moved forward to test whether primary airway epithelial cells expressing WT-CFTR (NhBEs) could be cultured with PACCS. Following a similar experimental approach, results show that NhBEs cultured with PACCS had greater TEER than NhBEs cultured by hand (**Figure 3.7C**). The discrepancy seen between immortalized and primary cells might be due to primary cells being more sensitive to changes in temperature and carbon dioxide fluctuations that the cells experience when removed from the incubator for culture by traditional methods. We then tested both immortalized and primary cells with meal-like glucose fluctuation patterns using PACCS. The protocol used to run these experiment is shown in **Table 3.2**. The control for this experiment was media changes performed by PACCS at the same time, but control plates only received fresh 5.5 mM glucose media at each solution change. TEER for CFBE-WT cells decreased (**Figure 3.7D**), while TEER for NhBE cells was initially much higher and increased in response to meal-like glucose fluctuations compared to controls receiving fresh 5.5 mM glucose media (**Figure 3.7E**). The difference in responses to PACCS meal-like glucose fluctuations between immortalized and primary cells might be due to differential expression of tight junction proteins in each model, and it highlights the importance of using primary cells when studying airway physiology. Primary cells expressing ΔF508-CFTR (CFhBEs) were also tested with meal-like glucose patterns. Results showed no significant differences in TEER in CFhBEs in response to meal-like glucose fluctuations compared to control (**Figure 3.7F**). This result suggests that CFhBE lack the same adaptive response to glucose fluctuations as seen in NhBE cells, possibly due to CFTR dysfunction and dysregulation of tight junction proteins. Overall, preliminary data shows that PACCS can be successfully used to culture airway epithelia, both immortalized and primary cells, and exposure to glucose fluctuations leads to different responses in WT and CF cells.

Table 3.2. PACCS settings used to culture airway epithelial cells using meal-like glucose fluctuations.

The settings were programed and stored using the ValveBank controller. The program included information for 24 hours of media changes. The program looped seven times automatically, simulating 7 days of meal-like media conditioning. Channel 1 exclusively changed the media on the control plate, receiving only normal glucose media (5.5 mM glucose). Channel 2 controlled the input of normal glucose media (5.5 mM) into the meal-like plate. Channel 3 controlled the input of high glucose media (17.5 mM) into the meal-like plate. Channel 8 ran the vacuum.

Channel 1 (First Input) Low Glucose Control Plate	**Channel 2 (Second Input) Low Glucose Meal Plate**	**Channel 3 (Third Input) High Glucose Meal Plate**	**Channel 8 (Vacuum)**
00:00:00.00 Loop Start (07)	00:00:00.00 Loop Start (07)	00:00:00.00 Loop Start (07)	00:00:00.00 Loop Start (07)
00:00:00.00 Open Valve	00:00:00.00 Open Valve		00:00:00.00 Open Valve
00:00:28.00 Close Valve	00:00:28.00 Close Valve		00:00:12.00 Close Valve
04:00:00.00 Open Valve		04:00:00.00 Open Valve	03:59:40.00 Open Valve
04:00:28.00 Close Valve		04:00:28.00 Close Valve	04:00:12.00 Close Valve
08:00:00.00 Open Valve	08:00:00.00 Open Valve		07:59:40.00 Open Valve
08:00:28.00 Close Valve	08:00:28.00 Close Valve		08:00:12.00 Close Valve
12:00:00.00 Open Valve		12:00:00.00 Open Valve	11:59:40.00 Open Valve
12:00:28.00 Close Valve		12:00:28.00 Close Valve	12:00:12.00 Close Valve
16:00:00.00 Open Valve	16:00:00.00 Open Valve		15:59:40.00 Open Valve
16:00:28.00 Close Valve	16:00:28.00 Close Valve		16:00:12.00 Close Valve
20:00:00.00 Open Valve		20:00:00.00 Open Valve	19:59:40.00 Open Valve
20:00:28.00 Close Valve		20:00:28.00 Close Valve	20:00:12.00 Close Valve
24:00:00.00 Loop End	24:00:00.00 Loop End	24:00:00.00 Loop End	23:59:40.00 Open Valve
68:00:00.00 End of List	68:00:00.00 End of List	68:00:00.00 End of List	24:00:00.00 Close Valve
			24:00:00.00 Loop End
			68:00:00.00 End of List

3.4. Discussion

We developed a novel cell culture system, PACCS, that enables programed and automated media changes to culture airway epithelial cells plated on permeable Transwells. This is a valuable tool to study the pathophysiology of many diseases, such as CFRD. Patients with CFRD experience blood glucose fluctuations after meals. However, current cell culture protocols do not resemble CFRD physiology with respect to exposure to extracellular glucose levels. Thus, CFRD research is limited by the *in vitro* cell culture tools available to researchers. The system we have developed addresses this limitation by better mimicking blood glucose fluctuations. The system could also be used for other clinical applications, such as timed exposure to small molecules or other potential therapeutic agents.

To our knowledge, this is the first user-friendly, compact, and low-cost cell culture system of its kind. This system is an improvement from other existing devices in terms of being easily adaptable. Other groups have created automated cell culture systems to culture stem cells[161] and organoids[162]; however their set-ups cannot be easily modified to culture airway epithelial cells on Transwells and simulate meal-like blood glucose fluctuations. One group was able to develop a miniaturized automated cell culture system for 96-well Transwells to culture airway epithelial cells[163]. However, their system is bulky and requires specialized equipment, such as robotic arms and a multi-plate media dispensing machine, both of which are not easily accessible by most research labs due to their high cost and complex operational requirements. In contrast, PACCS components are user-friendly, compact, and easily accessible. The PACCS plate has two separate media reservoirs, a tray that holds up to eight Transwells (with 0.33 cm^2 surface area), and a lid to protect from contamination. The inner surface of the plate reservoirs has a slight incline to drive

fluid flow from the input to the outputs. This was a useful addition to our system that greatly improved fluid exchange, an improvement from commercially available plates with flat surfaces.

Even though PACCS offers many advantages over other existing devices, PACCS also has some limitations. Currently, the material used to 3D print the cell culture plate is not autoclavable. For future studies, we recommend using medical grade resin, such as BioMed Clear (FormLabs), which can be autoclaved for easy repeated use. Further, PACCS media consumption is high especially when running the meal-like glucose fluctuation protocol. It currently requires 4 mL of media per reservoir per media change. This might be burdensome for labs that utilize cells that require expensive components in their media. To address this limitation, the plate can undergo further optimization to reduce media consumption.

To decrease media consumption while improving media exchange, the main body of the PACCS plate already underwent several design iterations. We found that having plain media reservoirs without columns/channels was best to optimize media exchange, even if it increased media consumption slightly. Further, we found that adding two separate reservoirs per plate was optimal to study two different genotypes (or treatments) in parallel without the possibility of cross-contamination between cell lines. After the plate design optimization was complete, the final PACCS plate iteration was used to culture airway epithelial cells. Both immortalized and primary cells were used to test whether PACCS could be used to culture airway epithelial cells. The last plate iteration proved to have good fluid exchange and could be successfully used to culture both immortalized and primary airway epithelial cells with either daily media changes or meal-like glucose fluctuation media changes for up to a week.

When cells were tested with daily media changes, all at 5.5 mM glucose, there was no significant difference in CFBE TEER between the PACCS and control groups. However, NhBE

cells cultured with PACCS had higher TEER compared to their control group. This observation was unexpected, but it provides further evidence of the utility of PACCS. We hypothesize that primary cells might be more sensitive to changes in temperature and carbon dioxide levels; thus, they might fare better when cultured with PACCS compared to manual media changes that include removal from the incubator. Further, discrepancies in results obtained when using immortalized cells versus primary cells highlight the need to always confirm findings in primary cells. Interestingly, NhBE cells increased their TEER in response to glucose fluctuations while CFhBE cells did not experience changes in TEER, indicating a lack of an adaptive response in CF primary cells challenged with meal-like glucose fluctuations.

Future studies will focus on using PACCS to condition immortalized and airway epithelial cells using CFRD-like glucose fluctuations. We will later test other endpoint measurements, besides TEER, that could help identify the mechanisms driving CFRD pathophysiology. Tight junction proteins, for example, play a role in barrier integrity and are believed to play a role in CFRD pathophysiology[128,129]. We will condition airway epithelial cells using PACCS and will then test gene expression changes of essential tight junction proteins, such as claudins and occludins, with the goal of identifying potential targets for therapeutic intervention. Overall, PACCS offers a novel and accessible platform to better mimic *in vivo* physiologically relevant conditions to study a range of diseases, such as CFRD.

3.5. Conclusions and Future Directions

We developed a programmable and automated cell culture system, PACCS, to better mimic physiologically relevant blood glucose fluctuations to study CFRD *in vitro*. This novel system has proven to be successful for cell culture, and it could be used for a wide range of applications. Future studies will focus on employing other quantitative techniques to measure differences in WT and CF airway epithelial monolayers in response to PACCS meal-like conditioning. Overall, understanding the pathophysiology of CFRD would allow us to develop therapies to combat this comorbidity, further improving quality of life and life expectancy for pwCF.

Chapter 4 – Chronic hyperglycemia aggravates lung function in a Scnn1b-Tg murine model

Preface

This chapter is an adaptation of a paper accepted for publication[159]. The manuscript was written by Dr. Guiying Cui. I was involved in collecting data, creating figures, and proofreading the manuscript. My most significant contribution to this paper was bulk RNA sequencing analysis of mouse lung tissue samples (Figure 4). This work is novel and significant because it addresses the increasing need for animal models that recapitulate CF-like lung disease to study CFRD. Through this work, we were able to establish a chronic CFRD-like mouse model using the *Scnn1b*-Tg transgenic mice overexpressing the epithelial sodium channel β subunit made diabetic by injection of streptozotocin (STZ). Interestingly, S*cnn1b*-Tg diabetic mice had more severe lung disease compared to their WT diabetic controls. Further, mice were challenged with intranasal PAO1 to simulate a CF-like lung infection. This infection led to severe lung leukocytic infiltration, as commonly seen in humans. The model can be utilized for future studies toward understanding the mechanisms underlying the lung pathophysiology associated with CFRD and developing novel therapeutics for CFRD lung disease.

Full citation

Cui, G.; Moustafa, D. A.; Zhao, S.; **Vazquez Cegla, A**.; Lyles, J. T.; Goldberg, J. B.; Chandler, J. D.; McCarty, N. A. Chronic Hyperglycemia Aggravates Lung Function in a Scnn1b-Tg Murine Model. *Am J Physiol Lung Cell Mol Physiol* **2024**. https://doi.org/10.1152/ajplung.00279.2023.

4.1. Introduction

Cystic fibrosis-related diabetes (CFRD) is the most common comorbidity in cystic fibrosis (CF) and occurs in up to 20% of adolescents and 50% of adults with CF[99]. As individuals with CF live longer due to the successes of highly effective modulator therapies (HEMTs), age-dependent complications, such as CFRD, are becoming more prevalent. CFRD patients have significantly increased frequency of acute pulmonary exacerbations and mortality due to increased rate of pulmonary decline[164–166]. Even early glucose abnormalities in young patients are associated with more severe lung disease[167].

While airway surface liquid (ASL) glucose is tightly controlled, we found that CF airway epithelia expressing ΔF508-CFTR failed to efficiently modulate glucose uptake in response to insulin[126]. In fact, CFTR mutation in the CF lung is a unique player that combined with hyperglycemia leads to damaging lung function since diabetic patients without CFTR mutation typically do not develop lung complications until late stage of the disease[168]. Many studies proposed recently that high glucose in ASL promotes lung infections, such as by PAO1 and SA[125,169], worsened chronic lung inflammation, elevated lung oxidative stress, and more[170]. Nonetheless, the mechanisms by which chronic hyperglycemia in CF leads to enhanced lung function decline and worse outcomes remain unclear.

The recent development of CFTR-knockout (CFKO) models in pig and ferret provides new avenues for investigating the pathogenesis of CFRD. However, both CF pigs and CF ferrets developed significant bacterial lung infections after birth which require labor-intensive care and costly husbandry to keep the animals alive[117,119,171,172]. Although CFKO mouse models failed to present lung phenotype as seen in CF patients, the transgenic mice that over expressed the epithelial sodium channel, β subunit in the airway (S*cnn1b*-Tg) exhibited a CF-like lung

phenotype[111,173,174]. Adult mice exhibit chronic neutrophilic airway inflammation, mucus hypersecretion, goblet cell metaplasia and other CF-like lung phenotypes[175–178]. In addition, the advantages of the mouse model are enormous, such as short time to sexual maturity with high production of genetically identical offspring.

This study aimed to investigate the effects of chronic hyperglycemia on lung damage using the CF-like murine model, S*cnn1b*-Tg mice. We adopted previously used protocols for induction of diabetes by injection of streptozotocin (STZ) and successfully developed the first chronic diabetes model in S*cnn1b*-Tg mice up to 8 weeks of age. We then tested the murine lung phenotype at multiple levels and our findings suggest that chronic hyperglycemia exaggerates murine lung dysfunction.

4.2. Materials and Methods

4.2.1. Experimental Animals

Animals were maintained and studies performed under protocols approved by the Emory University Institutional Animal Care and Use Committee (IACUC). All experiments were performed according to the principles outlined by the National Institutes of Health guidelines for the care and use of animals in biomedical research. S*cnn1b*-Tg mice (C57BL/6NJ genetic background) were originally purchased from the Jackson Laboratory, JAX:005304, and were maintained and bred by the Division of Animal Resources at Emory University. C57BL/6 wildtype (WT) age- and sex-matched littermates were used as controls for this study. All animals were housed in specific pathogen-free housing with 12-hour light / dark cycles. Animals were fed a regular chow diet and given water *ad libitum* except for predetermined fasting states prior to STZ injections[89,179].

4.2.2. Electrogenic Ion Transport Measurements

Transepithelial ion transport studies were performed in freshly excised mouse tracheal tissues by Ussing chamber recording as previously described[180–182]. In brief, tissues were mounted on tissue holding sliders (model #P2307) in Ussing chambers (EasyMount P2300, Physiologic Instruments, Reno, NV) and bathed on both sides by 4 mL of 140 NaCl solution containing (in mM): NaCl 140, KCl 5, K_2HPO_4 0.36, KH_2PO_4 0.44, $CaCl_2$ 1.3, $MgCl_2$ 0.5, $NaHCO_3$ 4.2, NaHEPES 10, Glucose 10. The pH was adjusted to 7.4 with NaOH. The solution was continuously gassed with blood gas (5% CO_2 and 95% O_2, Airgas USA, Radnor, PA). Tissues were short-circuited using a multichannel voltage/current clamp (Physiologic Instruments Inc., model VCC MC6) and connected to a computerized data acquisition system (Acquire & Analyze software version 2.3.8). Tissues were allowed to stabilize for at least 30 minutes before adding compounds to isolate specific currents: apical amiloride (Amil) 20 μM, forskolin (FSK) 10 μM on both sides, apical $CFTR_{inh}172$ (INH172) 10 μM, apical Adenosine triphosphate (ATP) 100 μM, and 5-Nitro-2-(3-phenylpropylamino) benzoic acid (NPPB) 200 μM on both sides were used as indicated. ΔI in this study was background subtracted current change, including ΔI_{Amil}, ΔI_{FSK}, $\Delta I_{ATP\text{-}initial}$, and $\Delta I_{ATP\text{-}steady}$.

4.2.3. CFRD animal model

Adult WT and S*cnn1b*-Tg mice (≥14 weeks age), including males and females at roughly equal proportions, underwent serial intraperitoneal injections of STZ (50 mg/kg body weight) for 5 days following a 4-hour fast[89]. Weight measurements were recorded continually one day before (day 0) and on different days after STZ injection for a total of 8 weeks. Tail blood glucose levels were measured using a commercially available glucometer (Freestyle Lite; Abbott, Alameda, CA) on days 0 and ≥ 8 weeks post-STZ administration. Mice that did not demonstrate blood glucose values above 200 mg/dl on day 14 were removed from further analysis. The glucometer had a

maximum range of ≥450 mg/dl; these values were recorded as 450 mg/dl. Mice were monitored for a total of 8 weeks after STZ injection (WT-D and S*cnn1b*-Tg-D).

4.2.4. BALF collection and BALF cell counting

The procedure for collection of Bronchoalveolar Lavage Fluid (BALF) in mice followed our prior publication[183], with some modification. After euthanasia with isoflurane (NDC 46066-755-04, Aspen Veterinary Resources, LTD, Liberty, MO 64068), the chest cavity was opened carefully without damaging the lungs and a catheter (made with HTX 20G needle in the lab, Component Supply company, Sparta, TN) was inserted into the trachea. BALF was collected with sterile 1x PBS solution, 1 mL per infusion and two infusion per mouse. The total volume of BALF collected was recorded. The total BALF was centrifuged at 400 x g for 10 minutes at 4 °C, the supernatant transferred to a new tube, aliquoted, and stored at -80 ºC until subsequent analysis. The cytokines in BALF were measured with commercially available Enzyme-linked immunosorbent assay (ELISA) kits following the manufacturer's instructions, including tumor necrosis factor alpha (TNF-α, Invitrogen, 88-7324-22), interleukin 8 (IL-8, AFG Bioscience, EK732214), and interleukin 1 beta (IL-1β, Sigma, RAB0274). The cell pellet was resuspended in 200 µl of cold ACK lysing buffer (150 mM NH_4Cl, 10 mM $KHCO_3$, 0.1 mM Na_2EDTA) on ice for ≤10 minutes[89,183]. The ACK buffer was diluted by addition of 1 mL cold 1x PBS, followed by centrifugation. The supernatant was discarded, and the cells were resuspended in 400 µl of 1x PBS. The cell suspension (200 µl) was centrifuged at 500 x g for 5 minutes using a Shandon Cytospin 4 (Thermo Electron Corporation). The slides were briefly air-dried and stained with a modified Giemsa stain (Diff Quick; Thermo Scientific, Kalamazoo, MI) and allowed to dry for 24 hours. Slides were then read with a Zeiss upright microscope, counting leukocytes on 10 sequential high-powered (40x) fields.

4.2.5. Glucose Determination using Mass Spectrometry

BALF glucose concentration was determined by isotope-dilution mass spectrometry. Metabolites were extracted from a 50 μL aliquot of murine BAL fluid with 100 μL of 1:1 acetonitrile:methanol containing U-$^{13}C_6$-glucose (Cambridge Isotope Laboratories) at 0.05 mM as an internal standard. The extraction mixture was vortexed for 5 seconds, extracted on ice for 30 minutes, followed by centrifugation at 20,000 g and 4 °C for 10 minutes. A 100 μL portion of supernatant was transferred into a new tube and stored at −80 °C. A small, equal volume of each sample was pooled with others to make a global quality control sample (QC). Prior to analysis, samples were thawed on ice and centrifuged. Then, a 20 μL aliquot of each sample and QC was transferred into HPLC vials.

Data acquisition was conducted using a Vanquish™ Horizon Binary ultrahigh performance liquid chromatography system coupled to a Q Exactive High Field Hybrid Orbitrap mass spectrometer (ThermoFisher). A 2.5 μL injection was made onto a 5 micrometer, 2.1 × 150-millimeter iHILIC-(P) classic column (HILICON) at 40 °C. The sample was eluted at a flow rate of 0.2 mL/min using a 15-minute gradient of (A) 15 mM ammonium acetate in water, pH 9.4 and (B) acetonitrile. Initial conditions were 10% A and progressed to 76.7% A at 12.5 minutes, then to 90% A at 13 minutes, followed by a 1.5-minute hold and a 5.5-minute re-equilibration of the column at 10% A. The column eluate was introduced to a heated electrospray ionization source held at 320 °C and −2.75 kV and an ion capillary temperature of 275 °C. The Sheath and AUX gas flow rates were 40 and 8 arbitrary units, respectively. The automatic gain control (AGC) was set to 1×10^6 ions with a maximum injection time of 200 millisecond. Scan range was 67–1000 *m/z* and Orbitrap resolution was 120,000 full widths at half maximum. Data was collected in Xcalibur 4.6.67 (Thermo Fisher Scientific).

After data acquisition, the MS chromatograms for the (M+H) ions of glucose and U-$^{13}C_6$-glucose were extracted and the peaks integrated using FreeStyle 1.8 SP2 QF1 and Quan Browser 4.7.69.37 (Thermo Fisher Scientific). The concentration of glucose in murine BAL fluid was calculated by the ratio of the peak areas using Excel for Microsoft 365 (Version 2402).

4.2.6. Lung tissue RNA sequencing and analysis

Fresh right caudal and middle lung lobes were collected from both WT-D and S*cnn1b*-Tg-D mice after BALF collection and immediately frozen in liquid nitrogen. The tissues then were stored at -80 °C and later delivered to the Emory National Primate Research Center (NPRC) Genomics Core on dry ice for RNA purification and RNA sequencing (RNA-seq). Tissues were homogenized in 350 µL of Buffer RLT and then extracted using the RNeasy Mini kit (Qiagen) with on-column DNase digestion. RNA quality was assessed using a TapeStation 4200 (Agilent) and then 10 ng of total RNA was used as input for cDNA synthesis using the Clontech SMART-Seq v4 Ultra Low Input RNA kit (Takara Bio) according to the manufacturer's instructions. Amplified cDNA was fragmented and appended with dual-indexed barcodes using the Nextera XT DNA Library Preparation kit (Illumina). Libraries were validated by capillary electrophoresis on a TapeStation 4200, pooled at equimolar concentrations, and sequenced with PE100 reads on an Illumina NovaSeq6000, yielding ~25 million reads per sample on average. Quality control (QC) was performed on all sequencing reads using the FastQC package developed by the Babraham Institute bioinformatics group. Reads with poor quality were trimmed and adapter sequences were removed by cutadapt. Reads were then aligned to the mouse genome (mm10, GRC38) using STAR and quantified by featureCounts[184,185]. Alignment qualities were checked by QC3[186]. Significantly differentially expressed genes with FDR-adjusted p-value < 0.05 and absolute fold change > 1.5 were detected by DESeq2[187]. Heatmap3 was used for cluster analysis and visualization[188]. Gene

Ontology and KEGG pathway over-representation analysis was performed on differentially expressed genes using the WebgestaltR package[189].

4.2.7. PAO1 *inoculum preparation and* PAO1 *infection*

For mouse infection, a non-mucoid lab strain of *Pseudomonas aeruginosa* (PAO1) was grown from glycerol stocks on Brain Heart Infusion agar and then cultured overnight in synthetic CF sputum (SCFM) at 37 °C shaking at 200 rpm. Subsequently, the overnight cultured PAO1 was diluted in synthetic CF sputum (SCFM-2) and incubated without shaking for additional 6 hours to reach log phase[190]. Mice were anesthetized by intraperitoneal injection of 0.2 mL of a mixture of ketamine (6.7 mg/mL) and xylazine (1.3 mg/mL). Mice were intranasally instilled with 50 µl PAO1 (~3 x10^6 CFU/mouse), 25 µl per nostril[179,191]. Mice were monitored for 24 hours post infection with free access to water and water-soaked soft food. Tail blood glucose was measured right before euthanasia.

4.2.8. Histopathological evaluation

Murine whole lungs were collected under different experimental conditions and were inflated with 1 mL of 4 % paraformaldehyde (PFA) in 1x PBS sterile solution through a tracheal catheter. The lungs were removed and maintained in 4 % PFA at 4 °C. Tissue sections were prepared by the Histology Core of the Emory National Primate Research Center at Emory University. In brief, the tissues were rinsed in water and dehydrated through increasing concentrations of ethanol. The tissues then were cleared in Xylene (Fisher brand, X3P1GAL) and embedded in paraffin (Type 6 Epredia Brand, 8336). The prepared paraffin blocks were cut into 5 µm thick slices, paraffin was melted, and samples transferred to the slide. The prepared slides were stained with hematoxylin and eosin (H&E) using the Tissue-Tek Prisma Plus Automated Slide

Stainer (SAKURA, 6170). Images were taken at the Integrated Cellular Imaging Core of Emory University[180].

4.2.9. Source of Reagents

Unless otherwise noted, all reagents were obtained from Sigma Chemical Co. (St. Louis, MO). $CFTR_{inh}172$ was purchased from Calbiochem (Burlington, MA). VX-770 was obtained from Selleckchem (Houston, TX). All chemicals were diluted to a final concentration in experimental solution immediately prior to use.

4.2.10. Statistical Analysis

Non-genomics data were analyzed with Sigmaplot 13.1 (SYSTAT, Palo Alto, CA) and are reported as mean ± SEM. Statistical analyses were performed using an unpaired Student's t test, one-way ANOVA, and two-way ANOVA. $P < 0.05$ was accepted to indicate statistical significance.

4.3. Results

4.3.1. Bioelectric studies on mouse tracheas

Differences in the genetic background of mice used for experiments may directly affect the results and subsequent conclusions[192]. Reported fractional survival to age 3 weeks of S*cnn1b*-Tg mice varied from ~5% to ~85% depending on the mouse strain[173,175,192,193]. We therefore used only S*cnn1b*-Tg mice on the C57BL/6NJ background and their genetic background-matched wildtype (WT) mice as controls. We used only adult surviving mice older than 12 weeks, to avoid the possible intrinsic death that is not related to the current experiment condition.

To test whether the S*cnn1b*-Tg mice exhibit other functional differences compared to WT mice, we measured the bioelectric properties of freshly excised trachea in Ussing chamber short-circuit current experiments (**Figure 4.1**)[194].

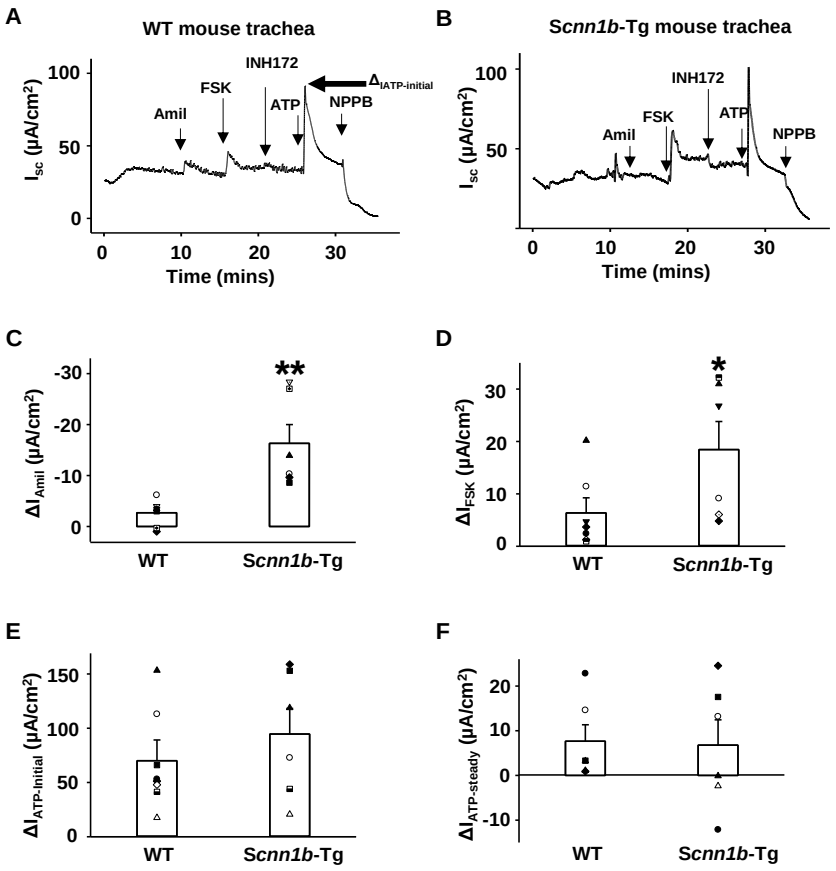

Figure 4.1. S*cnn1b*-Tg mice exhibit increased Amiloride-sensitive current (ΔI_{Amil}) and forskolin-sensitive current (ΔI_{FSK}) compared to WT mice on the same genetic background.

Ion transport properties of freshly excised tracheal tissues of adult mice were evaluated by Ussing chamber recordings, with normal Cl^- solution in both apical and basolateral chambers. Representative short-circuit current traces are shown in (A) WT and (B) S*cnn1b*-Tg. Compounds were sequentially added to the chamber: 20 μM amiloride (Amil), 10 μM forskolin (FSK), 10 μM $CFTR_{inh}172$ (INH172), 100 μM ATP, and 200 μM NPPB. Summary data are shown for ΔI_{Amil} in (C), ΔI_{FSK} in (D), ATP-sensitive initial current ($\Delta I_{ATP\text{-}initial}$, arrow in *A*) in (E), and ATP-sensitive current at steady state ($\Delta I_{ATP\text{-}steady}$) in (F). I_{sc} was calculated by subtracting baseline current for each compound representing the current right before each drug application. *, $P < 0.05$ vs WT mice, **, $P < 0.01$ vs WT mice. n = 6 for S*cnn1b*-Tg mice. n = 8 for WT mice.

Representative short-circuit current recordings of trachea from WT (**Figure 4.1A**) and S*cnn1b*-Tg mice (**Figure 4.1B**) are shown in **Figure 4.1**. Summary data for amiloride sensitive current (ΔI_{Amil}) are presented in **Figure 4.1C**. The ΔI_{Amil} in S*cnn1b*-Tg trachea was significantly increased compared to WT control but not as high as previous reports which ranged from ~-30 to ~-180 μA/cm^2 from different ages of S*cnn1b*-Tg mice[173,175,192,193]. This is consistent with previous reports that S*cnn1b*-Tg mice that survived to adulthood had a more moderate degree of mucus obstruction, compared to mice that succumbed prior to adulthood, which could result from lower ENaC expression and therefore smaller ΔI_{Amil} currents[173].

A summary of forskolin-stimulated currents (ΔI_{FSK}) is shown in **Figure 4.1D**; the currents were significantly increased in S*cnn1b*-Tg mice compared to WT. Unlike the previous reports[166,175], the ΔI_{FSK} currents in our study were insensitive to inhibition by either 10 μM INH172 or 50 μM GlyH-101 (data not shown). In addition, 2 μM VX-770 did not potentiate the forskolin-sensitive current in tracheas of WT mice; in contrast, we previously reported that murine CFTR directly expressed in *Xenopus* oocytes was sensitive to both potentiation by VX-770 and inhibition by GlyH-101[195]. These results together suggest that the ΔI_{FSK} currents may not represent CFTR currents, perhaps arising from other Cl^- currents instead since they were sensitive to block by a non-specific Cl^- channel blocker, 200 μM NPPB, applied at the end of the experiments (**Figure 4.1A, B**). NPPB further blocked the background pre-FSK current in the recordings, suggesting that this may be a non-CFTR Cl^- current as well.

We calculated ATP activated Cl^- currents in two ways, $\Delta I_{ATP\text{-}initial}$ (the peak current activated by ATP) and $\Delta I_{ATP\text{-}steady}$ (the stable current after 5 minutes of exposure to ATP) (**Figure 4.1E, F**). 200 μM NPPB blocked the ATP-activated current and no significant differences were seen between S*cnn1b*-Tg and WT mice[196]. UTP- activated current in mouse trachea was reported to be mildly

blocked by the TMEM16A blocker, $T16A_{inh}$-A01, suggesting that TMEM16A only contributes about 50% of all UTP-induced Ca^{2+} -activated Cl^- current[196]. Hence, TMEM16A and other Ca^{2+} -activated Cl^- channels appear be to the dominant Cl^- channels in mouse airway. The notion that Ca^{2+}-activated Cl^- channels dominate in the trachea, instead of CFTR, supports the observation that CFKO mice do not exhibit a CF-like lung phenotype[171–174]. In summary, the ΔI_{Amil} in the trachea of adult S*cnn1b*-Tg mice (≥ 14 weeks) is relatively small compared to previous reports for younger animals, suggesting a relatively mild imbalance between Na^+ absorption and Cl^- secretion in the mouse airway, which may result in increased survival[197].

4.3.2. STZ-mediated induction of CF-related diabetes both murine models

Diabetes was induced in adult mice ranging in age from 14-20 weeks at the start of treatment (**Figure 4.2A-C**). S*cnn1b*-Tg mice and WT mice were induced to hyperglycemia with intraperitoneal injections (IP) of STZ as previously described[198]. Following a 4-hour fast, STZ was administered (50 mg/kg body weight) serially every 24 hours for 5 days. Weight and tail blood glucose measurements were recorded on the day before the first day injection (day 0), and then subsequently for 8 weeks after completion of treatment. Summary data are shown for body weight (**Figure 4.2A**), tail blood glucose (**Figure 4.2B**), and percent survival (**Figure 4.2C**). WT-con, WT-D, and S*cnn1b*-Tg-con mice exhibited no mortality, while S*cnn1b*-Tg-D mice less than 18 weeks age exhibited hyperglycemia-driven mortality. However, when older mice (18-22 weeks) were used, no deaths were observed for 8 weeks post-STZ injection although those mice exhibited tail blood glucose levels not different from younger mice.

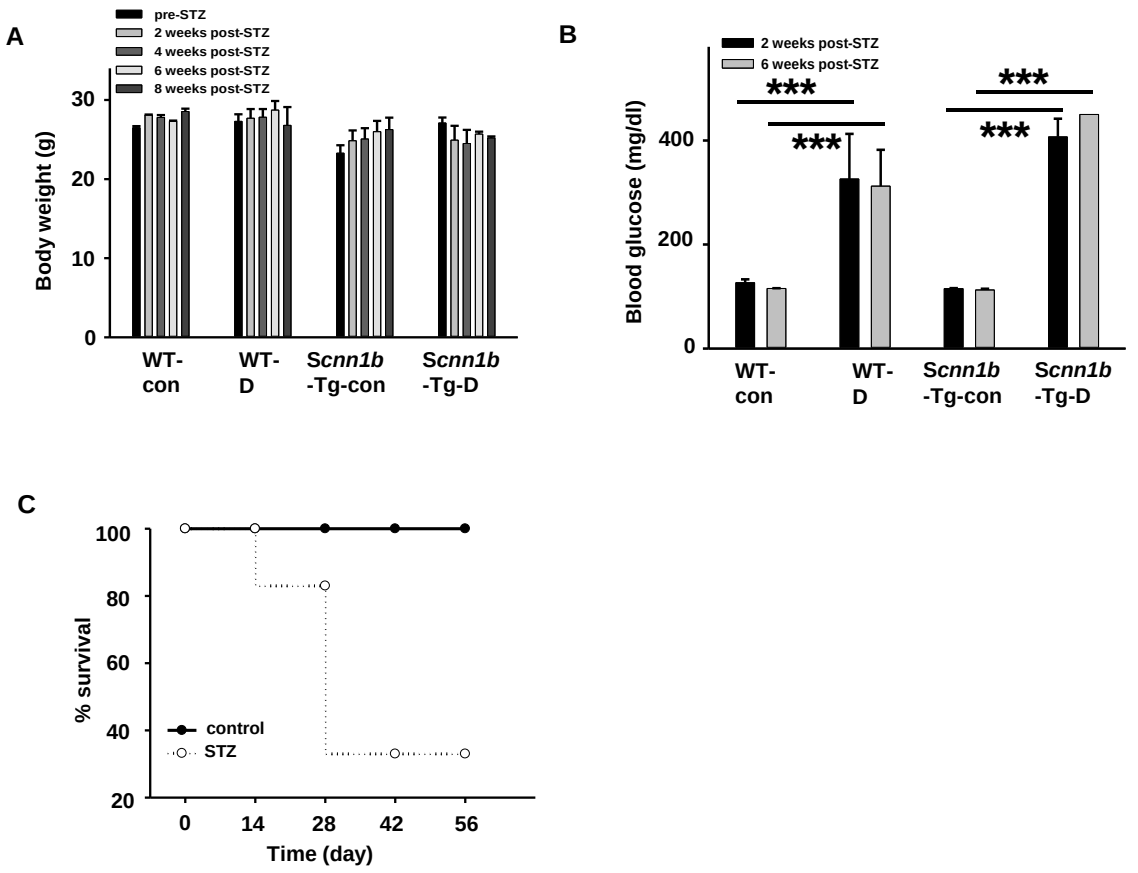

Figure 4.2. Chronic diabetic phenotypes in WT and S*cnn1b*-Tg mice.

Mice ranged in age 14-20 weeks at the first day of injection with STZ (50 mg/kg body weight). (A) Changes in mouse weight during the 8 weeks after STZ treatment. STZ-treated animals (WT-D and S*cnn1b*-Tg-D) showed a slight change of body weight with no significant difference than untreated controls regardless of genotype (WT-con and S*cnn1b*-Tg-con). (B) Increase in tail blood glucose levels in mice 6 weeks following STZ treatment. No significant difference between WT and S*cnn1b*-Tg mice in control condition (WT-con, S*cnn1b*-Tg con). At 2 weeks and 6 weeks after STZ treatments, tail blood glucose levels were significantly elevated in both WT-D and S*cnn1b*-Tg-D mice with no significant difference between genotypes. (C) Survival curves for S*cnn1b*-Tg mice indicate reduced survival in the STZ-treated group. n =5 for WT-con and WT-D. n=8 for S*cnn1b*-Tg control and S*cnn1b*-Tg-D.

4.3.3. Scnn1b-Tg-D mice exhibit increased pulmonary inflammation and infection

BALF was collected from mice 8 weeks after STZ injection, then analyzed (**Figure 4.3**). The volume of fluid collected was decreased in both *Scnn1b*-Tg diabetic and non-diabetic mice compared to their WT littermates (**Figure 4.3A**), consistent with a dehydration phenotype associated with elevated amiloride-sensitive Na^+ currents (**Figure 4.1C**). Unlike the clear BALF solutions from WT-con and WT-D mice, BALF from both groups of S*cnn1b*-Tg mice looked not only turbid but also contained mucus or other solids, supporting the previous reports indicating that S*cnn1b*-Tg mice exhibit mucus dehydration and mucus plugging[175,193].

Both cell density and total cell number in BALF were significantly increased in S*cnn1b*-Tg-con and S*cnn1b*-Tg-D groups compared to WT-con and WT-D (**Figure 4.3B, C**). No differences were seen between the WT-con and WT-D groups. In contrast, the S*cnn1b*-Tg-D group exhibited significantly increased cell density and total cell number compared to the S*cnn1b*-Tg-con group. We further quantified specific cell types in BALF using cytospin preparations as shown in **Figure 4.3D-G**. BALF total cells were significantly higher in the S*cnn1b*-Tg-D group compared to the WT-D group. BALF macrophages were significantly decreased in both the S*cnn1b*-Tg-con and the S*cnn1b*-Tg-D groups. Neutrophils and other lymphocytes were rarely seen in WT-con and WT-D group. In contrast, the number of lymphocytes were distinctly increased in S*cnn1b*-Tg-D groups (**Figure 4.3G**). We did not find evidence of spontaneous bacterial infection in the lungs of S*cnn1b*-Tg-D mice[199]. However, neutrophil-dominant inflammation and spontaneous bacterial colonization by *Staphylococcus lentus, Streptococcus mitis, Actinobacillus muris* and other species were reported previously in S*cnn1b*-Tg mice[175,177,178]. Taken together, WT-D mice did not exhibit a distinct change in lung phenotype compared to WT-con mice, while hyperglycemia significantly worsened the lung inflammation in S*cnn1b*-Tg-D mice compared to S*cnn1b*-Tg-con mice.

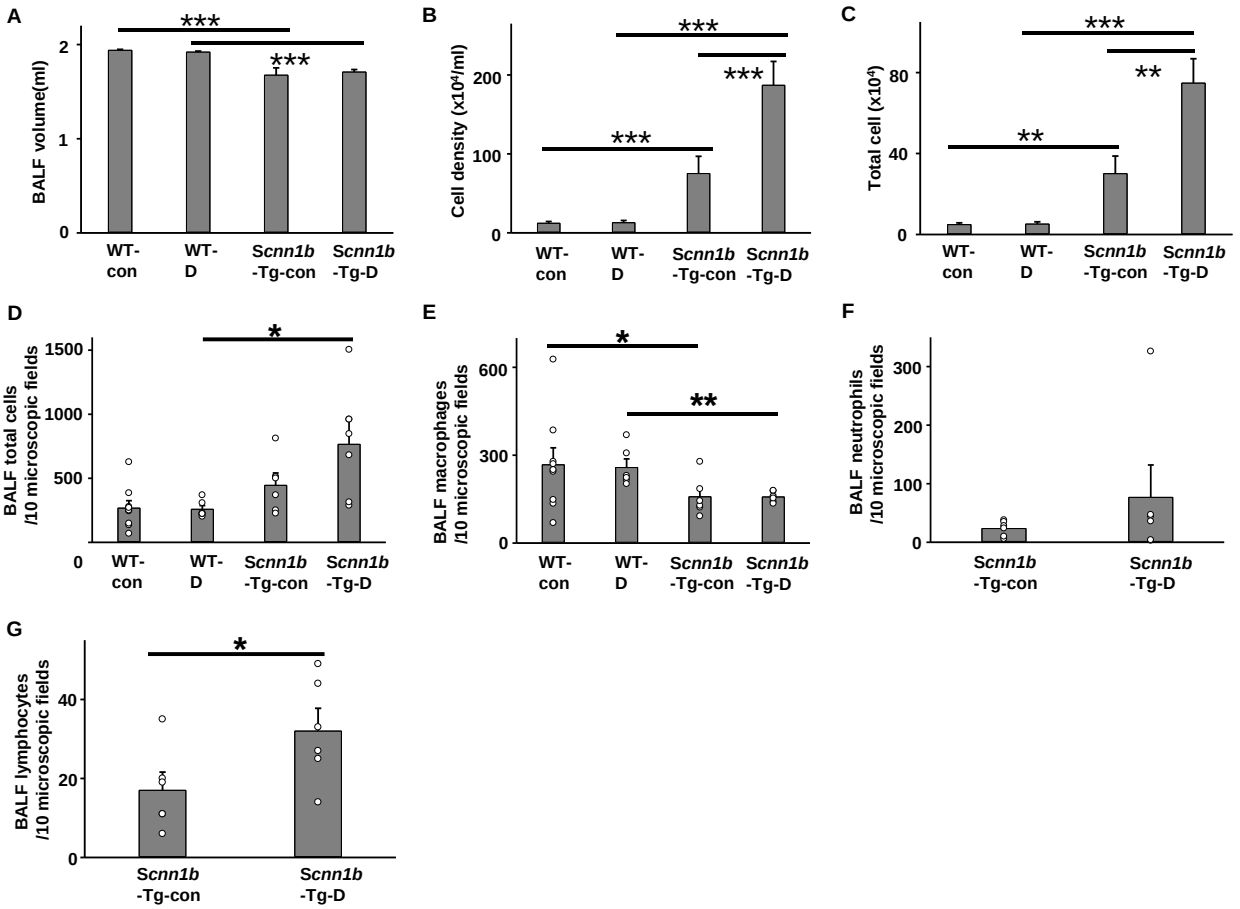

Figure 4.3. S*cnn1b*-Tg-D mice exhibit elevated lung inflammation.

Total BALF volume collected from different groups is shown in (A). Quantification of BALF cell density and total inflammatory cell numbers is shown in (B) and (C). Quantification of total cells and macrophages per 10 microscope fields is shown in (D) and (E). Neutrophil and lymphocyte count per 10 microscope fields from S*cnn1b*-Tg- con and S*cnn1b*-Tg-D is shown in (F) and (G). Neutrophils and lymphocytes were not observed in WT-con and WT-D mice. *, $P < 0.05$, **, $P< 0.01$, ***, $P<0.001$. n=9 for WT-con, n=6 for S*cnn1*b-Tg-con, n=6 for WT-D, and n=6 for S*cnn1b*-Tg-D.

4.3.4. Bulk RNA sequencing reveals distinct gene expression in WT-D and Scnn1b-Tg-D mice

To unravel the possible transcriptional changes caused by hyperglycemia in the lung in the context of a muco-obstructive phenotype, we performed bulk lung tissue RNA sequencing from both WT-D and S*cnn1b*-Tg-D mice[200]. Principal component analysis (PCA) showed WT-D and S*cnn1b*-Tg-D clustered separately with some overlap, revealing that the S*cnn1b*-Tg-D group is transcriptionally distinct from the WT-D group (**Figure 4.4A**). The top differentially expressed genes from the comparison, including both up- and down-regulated genes, are shown in the volcano plot (**Figure 4.4B**). Genes shown in blue symbols had a p-value adjusted of less than 0.1, while genes highlighted in red symbols had both a p-value adjusted of less than 0.05 and an absolute $\log_2$ fold change greater than 1.5. Gene Ontology and KEGG pathway analysis identified the top ten biological processes (**Figure 4.4C**), top 10 molecular functions (**Figure 4.4D**), and top 10 cell compartments (**Figure 4.4E**) that are implicated in the S*cnn1b*-Tg-D phenotype. The up-regulated genes in S*cnn1b*-Tg-D mice lung are associated with various intracellular pathways, including lung inflammation, remodeling, and glucose homeostasis. For example, Gm40293 is a novel transcript affiliated with the long non-coding RNA class which regulate gene expression in a variety of ways at multiple levels, including epigenetic and chromosomal remodeling[201]. The upregulated Fgf7 gene encodes fibroblast growth factor 7 which is involved in cell growth, morphogenesis, tissue repair and more[202]. The upregulated Chil4 gene encodes Chitinase-like 4 which is associated with Th2 inflammatory responses[203]. In addition, the downregulated Snx31 gene encodes a protein that may be involved in protein trafficking[204]. Compared to WT-D, the RNA-seq analysis demonstrates distinct transcriptomic mechanisms involved in the lung damage in S*cnn1b*-Tg-D mice in response to chronic hyperglycemia.

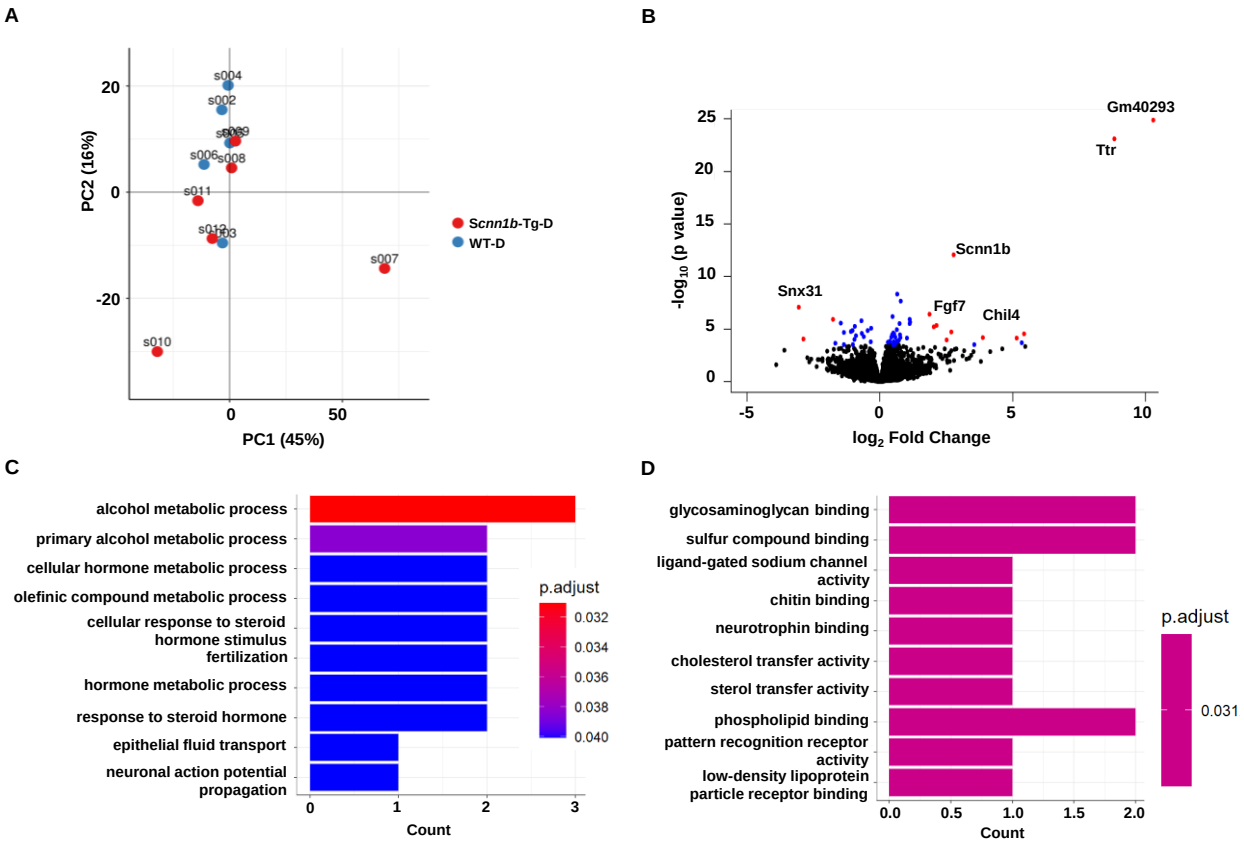

Figure 4.4. Bulk RNA-seq analysis of WT-D and S*cnn1b*-Tg-D murine lungs.

The two groups of mice were monitored for 8 weeks after STZ injection prior to removal of lungs and preparation for analysis. (A) PCA analysis of RNA-seq results of WT-D and Scnn1b-Tg-D murine lungs. (B) Volcano plots of differentially expressed genes (DEGs). (C) Biological processes enrichment analysis of DEGs. (D) Molecular function enrichment analysis of DEGs. (E) Cell compartment enrichment analysis of DEGs in WT-D and Scnn1b-Tg-D murine lung. n=6 for each group.

4.3.5. Scnn1b-Tg-con and Scnn1b-Tg-D mice exhibited histopathological lung features

In addition to the findings presented above, we further investigated lung histology features of mice in the current study. Representative lung sections stained with hematoxylin and eosin for WT-con, S*cnn1b*-Tg-con, WT-D, and S*cnn1b*-Tg-D mice are shown in **Figure 4.5**. Unlike in WT-con mice, sections from both S*cnn1b*-Tg-con and S*cnn1b*-Tg-D mice presented terminal bronchiole and parenchymal destruction with enlargement of the alveoli. In addition, sections from the terminal bronchiole showed increased thickness of the alveolar wall. The phenomena were more severe in S*cnn1b*-Tg-D mice. Sections from WT-D mice exhibited minor changes in terminal bronchiole and parenchyma compared to WT-con mice. We speculate here that longer duration of hyperglycemia might affect the WT mouse lung phenotype as occurs in late-stage human diabetes patients. Our data support prior findings that S*cnn1b*-Tg mice developed emphysema-like structural lung damage with airway inflammation and distal airspace enlargement[205,206].

4.3.6. Pulmonary infection with PAO1 in mouse models

During the 8 weeks following the STZ injection series, WT-D and S*cnn1b*-Tg-D mice exhibited symptoms of diabetes, such as frequent drinking, eating, and urinating but with a very minor decrease in body weight. At the end of 8 weeks, the mice were challenged with lung infection using PAO1 via an intranasal route for 24 hours. All 4 groups of mice, WT-con, WT-D, S*cnn1b*-Tg-con, and S*cnn1b*-Tg-D, showed severe lung infection symptoms, including hunched posture, inactivity, and no eating/drinking. At 24 hours post infection, mouse tail blood glucose was measured prior to euthanasia and the summary data are shown in **Figure 4.6A**. Both WT-con and S*cnn1b*-Tg-con mice exhibited mild hypoglycemia (60-79 mg/dl), while both WT-D and S*cnn1b*-Tg-D mice presented extremely high blood glucose levels. We collected BALF fluid and

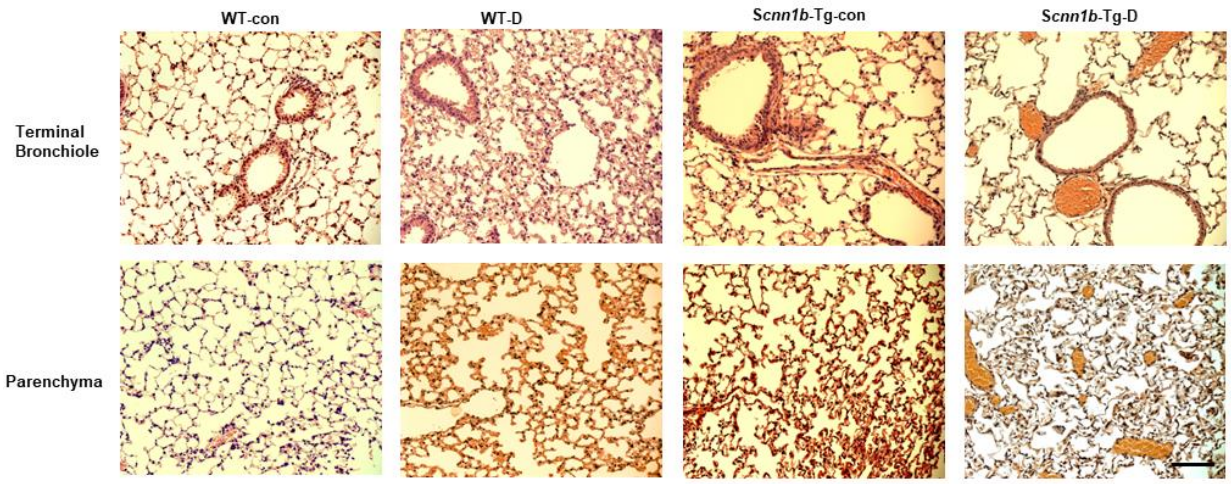

Figure 4.5. Representative lung micrographs of WT-con, S*cnn1b*-Tg –con, WT-D, and S*cnn1b*-Tg-D mice.

Lung lobes of control mice or diabetic mice 8 weeks after STZ injection were processed and stained with hematoxylin and eosin (H&E staining) for morphological analyses. Parenchymal consolidation and more severe interstitial inflammation were observed in Scnn1b-Tg-con and Scnn1b-Tg-D mice compared with WT mice. All samples were visualized at 20x. Scale bars:100 μm. n=3 for each group.

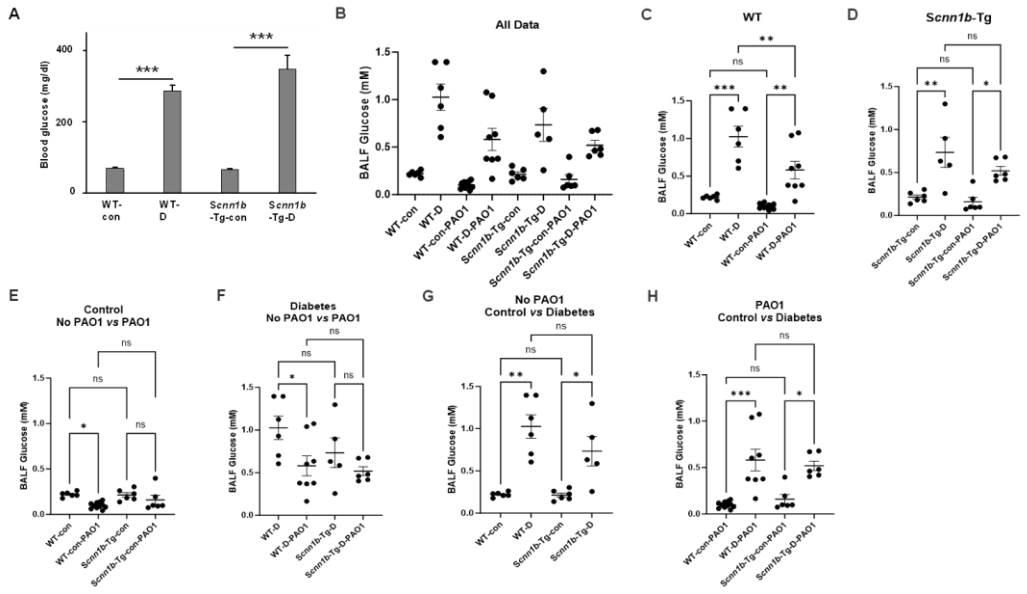

Figure 4.6. Tail blood glucose of mice after 24 hours of PAO1 pulmonary infection and BALF glucose for all groups of mice.

(A) Mice were provided soft food and water during recovery from infection. Tail blood glucose was measured right before euthanasia. Both WT-con and Scnn1b-Tg-con groups exhibited mild hypoglycemia (60-79 mg/dl glucose), while both WT-D and Scnn1b-Tg-D groups exhibited extremely high blood glucose levels. The data suggest that mice were very sick after PAO1 respiratory treatment. ***, $P < 0.001$ compared to their control group. n= 10 for WT-con. n=8 for WT-D. n=6 for Scnn1b-Tg-D. n=7 for Scnn1b-Tg-D. (B-H) BALF glucose measured with targeted Mass-Spectrometry. Data from all groups of mice are shown in (B). (C) BALF glucose in WT mice. (D) BALF glucose in Scnn1b-Tg mice. Comparisons of BALF glucose in all control groups and in all diabetes groups with and without PAO1 infection are shown (E) and (F), respectively. Comparisons of BALF glucose in both control and diabetes mice without PAO1 infection and with PAO1 infection are shown in (G) and (H), respectively. *, $P < 0.05$, **, $P < 0.01$, and ***, $P < 0.001$. The data suggest that all diabetes mice exhibited significantly high glucose concentration in their BAL.

quantified BALF glucose concentration among all groups of mice using Mass Spectrometry. To our knowledge, this is the first time that glucose in BALF from mice was detected by Mass Spectrometry. Summary data are shown in **Figure 4.6B-H**. Data show that BALF glucose concentration was significantly increased in diabetic mice, including WT-D and S*cnn1b*-Tg-D compared to their controls (**Figure 4.6C, D**). This phenomenon was maintained after 24 hours of PAO1 infection (**Figure 4.6G-H**). In addition, WT-con mice and WT-D mice exhibited significantly lower BALF glucose after PAO1 infection compared to no PAO1 infection, which was also observed in Scnn*1b*-Tg and S*cnn1b*-Tg-D mice although results did not reach significant levels (**Figure 4.6E, F**). Taken together, the data suggests that diabetic mice exhibit high systemic blood glucose as well as elevated glucose levels in their airways (**Figure 4.6C, D**). Moreover, PAO1 in mice lungs decreased overall BALF glucose abundance, possibly due to bacterial consumption of airway glucose as an energy source[207].

We next quantified BALF cell counts, and the summary data are shown in **Figure 4.7**. Compared to pre- infection conditions (**Figure 4.3**), BALF cell density (**Figure 4.7A**) and BALF total cell number (**Figure 4.7B**) were overwhelmingly increased in all groups. No significant differences were detected between the groups in reaction to the PAO1 infection. Neutrophils are the main cell type presented in every group. We further counted neutrophil numbers per 10 microscopic fields and the neutrophils number vigorously increased, compared to results without infection, without significant differences seen between groups (**Figure 4.7C**). Macrophage counts exhibited similar shifts among groups (**Figure 4.7D**). We next tested the concentrations of three pro-inflammatory cytokines in the BALF from eight groups of mice (**Figure 4.8A, E, H**). Chronic diabetes WT (WT-D) and S*cnn1b*-Tg mice (S*cnn1b*-Tg-D) did not exhibit a significant increase in the level of the tested proinflammatory cytokines in their BALF (**Figure 4.8B, F, I**).

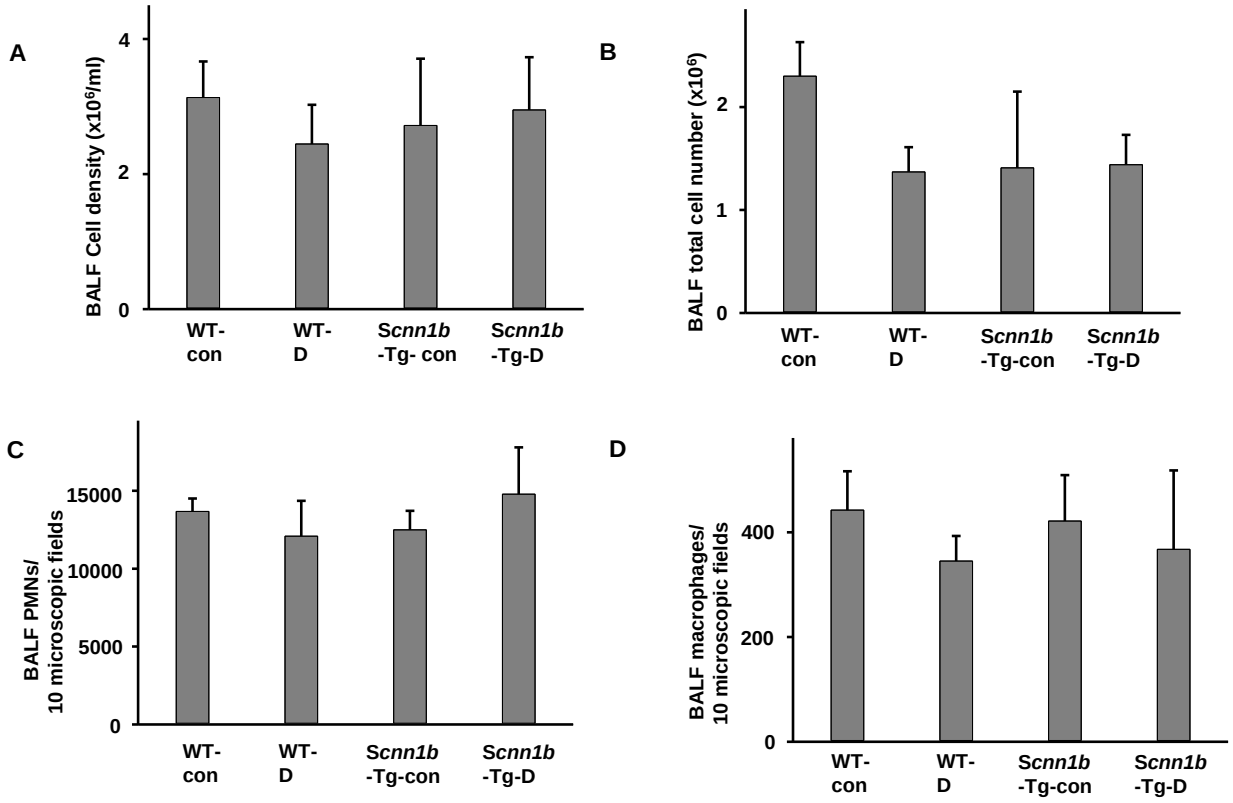

Figure 4.7. Analysis of BALF fluid harvested from the lungs of WT- and S*cnn1b*-Tg mice 24 hours after PAO1 intranasally infection.

Four groups of mice were tested, including WT-con, WT-D, S*cnn1b*-Tg-con, and S*cnn1b*-Tg-D. No differences were observed in BALF cell density (A), BALF total cell number (B), pulmonary neutrophils (PMNs) counts (C), or macrophage count (D) between the four groups. n=10 for WT-con. n=8 for WT-D. n=6 for S*cnn1b*-Tg-con. n=7 for S*cnn1b*-Tg-D.

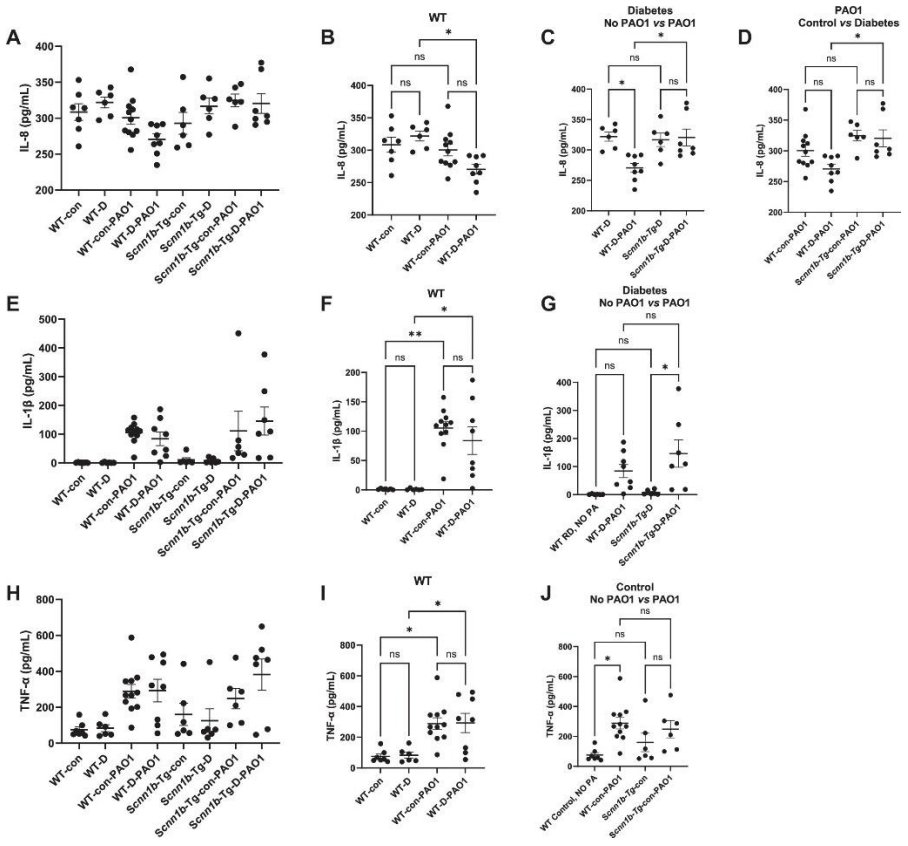

Figure 4.8. Cytokine concentrations in the BALF from different groups of mice lungs.

Each point represents an individual mouse (total of 8 groups). (A). The concentration of IL-8 was significantly decreased in WT-D-PAO1 mice compared to WT-D no PAO1 mice (B, C). IL-8 concentration significantly increased in Scnn1b-Tg-D-PAO1 mice compared to WT-D-PAO1 mice (C, D). (E-G) IL-1β. The concentrations of IL-1β were significantly increased in WT-con-PAO1 and WT-D-PAO1 mice compared to WT-con mice and WT-D mice, respectively (F). The concentration of IL-1β was significantly increased in Scnn1b-Tg-D-PAO1 mice compared to Scnn1b-Tg-D mice (G). (H-J) TNF-α. The Concentration of TNF-α in WT-con-PAO1 was significantly increased compared to WT-con (I, J). The concentration of TNF-α in WT-D-PAO1 was significantly increased compared to WT-D (I). Data are mean ± SEM *, $P < 0.05$, **, $P < 0.01$, ns, no significant difference, two-way ANOVA test.

Moreover, the levels of cytokines of both WT-con and WT-D were significantly upregulated or downregulated in their BALF after PAO1 challenge (**Figure 4.8B, F, I**), while only concentration of IL-1β was increased S*cnn1b*-Tg-D mice after PAO1 challenge (**Figure 4.8G**). In addition, the concentration of IL-8 in S*cnn1b*-Tg-D-PAO1 was significantly increased compared to WT-D-PAO1. Taken together, the data suggest that responses in S*cnn1b*-Tg mice were alleviated possibly due to the adaptation of the endogenous chronic infection and inflammation in the lung of S*cnn1b*-Tg mice[208–210] (**Figure 4.8**). Unlike pre- infection, lung histological analysis of the infected mice all exhibited massive neutrophilic infiltration and parenchymal damage (**Figure 4.9**). These data suggest that the CFU/per mouse of PAO1 loading led to severe lung infection in all groups, overwhelming the original lung damage arising from chronic hyperglycemia in the S*cnn1b*-Tg-D mice.

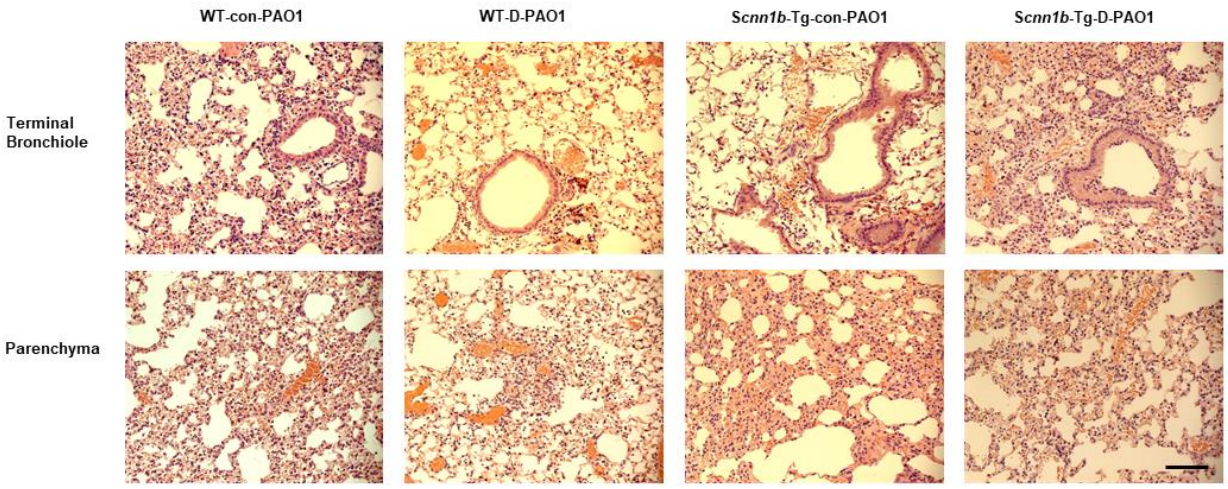

Figure 4.9. Representative micrographs of lung sections from WT and S*cnn1b*-Tg mice with PAO1 pulmonary infection.

Lung lobes of WT-con, WT-D, Scnn1b-Tg-con, and Scnn1b-Tg-D were processed and stained with H&E staining for morphological analyses. Both WT-D and Scnn1b-Tg-D mice were 8 weeks after establishment of STZ-induced diabetes. The increase in the terminal bronchiole and parenchyma leukocytic infiltrate in response to the infection by PAO1 was seen in all genotypes. All samples were visualized at 20x. Scale bars:100 µm. n=3 for each group.

4.4. Discussion

There is an increasing urgency in fully understanding and developing new treatments for CFRD-associated lung function decline in an anticipated "aging" CF population. This study demonstrates, for the first time to our knowledge, that chronic hyperglycemia in S*cnn1b*-Tg mice and elevated glucose concentration in the lung (**Figure 4.6**) aggravates lung damage with increases airway cellular inflammation, neutrophilic infiltration, and lung tissue damage and remodeling. We also found that the survival rate of chronic S*cnn1b*-Tg-D mice was related to the age at initiation of their diabetes. Older mice exhibited better resistance to diabetes-related death. In addition, 24 hours lung infection by PAO1 led to severe lung infection and inflammation in all mouse genotypes, including W-RD and S*cnn1b*-Tg-D.

Since WT-D mice exhibited a very similar lung phenotype to WT-con, we chose to explore changes in gene expression and compared the bulk RNA-seq results from lungs of WT-D and S*cnn1b*-Tg-D mice in this study (**Figure 4.4**). We expected to see up-regulated genes identified in S*cnn1b*-Tg-D mouse lungs, such as genes related to inflammation and oxidative stress due to the significant differences in their lung phenotypes (**Figures 4.2, 4.3**). Surprisingly, RNA-seq identified a very limited number of genes that were up-regulated or down-regulated in S*cnn1b*-Tg-D lung compared to WT-D lung. Given that both sets of animals exhibited high levels of hyperglycemia, these differences should reflect the impact of imposing a muco-obstructive phenotype on top of a diabetic phenotype. The identified genes in RNA-seq are related to multiple metabolic processes which support our findings that lungs of S*cnn1b*-Tg-D mice undergo enhanced rates of destruction and remodeling. A previous report showed a limited number of genes in the whole lung were significantly different in S*cnn1b*-Tg mice at postnatal day 42 compared to WT littermates, although S*cnn1b*-Tg mice exhibited dramatic lung phenotypes[211]. Our findings

presented a similar trend in that the number of differentially expressed genes seems discordant with the dramatic lung phenotypes in the S*cnn1b*-Tg-D mice. In addition, the lung tissue collected for RNA-seq in this study was first washed two times with PBS for BALF collection, then removed and immediately frozen for RNA-seq. Results may have been affected by this process.

Our lab and other groups previously reported that hyperglycemia promotes PAO1 bacterial growth counted at 6 hours after intranasal inoculum in both hyperglycemia *db/db* and *ob/ob* mice model[168] and pulmonary PAO1 clearance was reduced after 18 hours lung infection in CFKO diabetes mice[89]. We were unable to test the contribution of chronic hyperglycemia in chronic lung infection using Sc*nn1b*-Tg-D murine models because all animals exhibited a severe phenotype only 24 hours after PAO1 lung infection. Our finding of no significant differences among groups regarding leukocyte infiltration (**Figure 4.7**) could be due to multiple factors. For instance, the CFU of PAO1 loaded in the mouse lung could be too high, leading to severe infection response in all animals[212]. In addition, 8 weeks of hyperglycemia and elevated airway glucose did not induce end-stage lung damage in S*cnn1b*-Tg-D mice (**Figures 4.3, 4.4, 4.6**). Consequently, S*cnn1b*-Tg-D mice survived 24 hours with PAO1 infection as did other groups of mice. Although we did not test bacterial clearance from the lung in the current study; we speculate that pulmonary bacterial clearance could be weakened in the S*cnn1b*-Tg-D mice[179,213]. Furthermore, our data showed significant increases in the BALF cytokines between WT-D and WT-con, while mild changes in the BALF cytokines between S*cnn1b*-Tg and S*cnn1b*-Tg-D mice were detected (**Figure 4.8**). The differences could be due to the spontaneous lung infection in the S*cnn1b*-Tg mice, which consistently triggered lung proinflammatory cytokine production[175,177,178]. Consequently, S*cnn1b*-Tg mice lungs failed to increase their response when challenged with PAO1. In contrast, WT-D

mice lungs possibly remained bacterial free due to their strong reaction to PAO1 challenge and significant amount of cytokines release (**Figure 4.8**).

There is no doubt that the murine lung damage will persistently worsen because of systemic hyperglycemia and elevated glucose concentration in their lungs. It is worth mentioning that the concentrations of cytokines and glucose in the BALF reported in our study are lower than *in vivo* due to dilution of airway supernatant with 1x PBS (2 mL per mouse) during the BALF collection process. The airway surface liquid volume *in vivo* is much lower (100 ~200 μL per mouse)[214]. This suggests that the BALF glucose concentrations reported in this study are lower than actual concentration *in vivo* by 10-20-fold. Consequently, the airway glucose concentration in the diabetic mice used in this study ranged from 5 to 10 mM, which is similar to the glucose concentration found in the lungs of CFRD patients[91]. In addition, reduction of the bacterial load or use of a less virulent strain of PAO1 may enable chronic lung infection in these models[179,213].

4.5. Conclusion and Future Directions

We established a chronic CFRD-like model utilizing S*cnn1b*-Tg mice made diabetic by injection of streptozotocin. This model can be utilized for future studies toward understanding the mechanisms underlying the lung pathophysiology associated with CFRD and developing novel therapeutics. With the knowledge gained in this project, more studies are ongoing to identify hyperglycemia-specific responses longitudinally on specific region or cell types in the S*cnn1b*-Tg-D lung to fully dissect the natural disease history of CF related diabetes lung function decline.

Chapter 5 – Neutrophil transepithelial migration through monolayers of human bronchial epithelial cells is altered by chronic hyperglycemic conditioning

Preface

This chapter contains unpublished data from one of my most recent projects. Data was collected in collaboration with several members of the lab, and Dr. Guiying Cui is the primary author of this work. She performed cell seeding, neutrophil purification, and transmigration experiments. Further, she wrote the original version of this manuscript. I contributed to cell culture, experimental planning, figure development, and manuscript editing. Further, I performed all immunostaining and confocal microscopy experiments.

Full citation

Cui, G.; **Vazquez Cegla, A. J**.; Dudkin, J.; Tirouvanziam, R; McCarty, N. A. Neutrophil Transepithelial Migration Through Monolayers of Human Bronchial Epithelial Cells is Altered by Chronic Hyperglycemic Conditioning. [In preparation].

5.1. Introduction

CF is the most frequent life-shortening autosomal disease in people of European descents, caused by mutations in the gene encoding the CFTR epithelial chloride/bicarbonate ion channel[215]. Although CF is a multi-organ disease, the vast majority of morbidity and mortality in people with CF is associated with lung disease. Hallmarks of CF lung disease are persistent bacterial infections and inflammation driven by the chronic influx of blood PMNs into the airway lumen[216]. CFRD is prevalent in patients bearing the most severe genotypes such as ΔF508-CFTR. Mortality in CFRD is due to an increased rate of pulmonary decline suggesting that hyperglycemia exacerbates the already disrupted pulmonary physiology in CF[90,98,217].

It is well documented that PMNs are the predominant leukocytes in the lungs of CF patients, although the percentage of PMNs among total cells ranged from ~15% to 95% regardless of the disease condition. In contrast, limited studies testing airway glucose concentration in CFRD patients are available with two opposite findings, airway glucose concentration remained unchanged or significantly increased compared to healthy controls[40,88,218,219]. Similarly, rare reports are available studying whether airway glucose abundance correlates with neutrophil counts, with controversy in CFRD patients. For example, Prentice and colleagues reported that the percentage of neutrophil counts in BAL of children with CF strongly and positively correlated with blood hyperglycemia[220]. In contrast, Nielsen and colleagues reported that systemic hyperglycemia seemed to be associated with fewer airway PMNs and less glucose in CF sputum[221]. Overall, the variabilities using samples from CF and CFRD patients' lungs could be due to multiple factors: (1) Patient age (infant, young, adult)[222–225]. (2) Disease condition (mild, severe, exacerbating)[47,226–228]. (3) Treatment difference (with systemic antibiotics or not)[221,223]. (4) Sample collection methods (BAL fluid, spontaneous sputum, induced sputum)[229–233]. (5) Sampled lung

location (lower airway, upper airway, alveolar)[234]. (6) Sample processing, data analysis, and more[222,225]. However, there is no doubt that the excessive neutrophil migration results in progressive lung tissue damage and lung function decline, which is worsened in CFRD patients. Unfortunately, these human subject studies are unable to address the mechanisms involved in modulating the PMN transmigration from blood to the airway.

Polarized airway epithelia have distinct apical and undersurface domains with tight junctions that limit paracellular permeability. Prior work from our lab, the Koval lab, and others show that there is a direct link between expression of mutant CFTR and dysregulation of glucose homeostasis in human airway epithelial cells and defects in expression and function of tight junction proteins[40,88,126,235]. We found that airway glucose concentrations significantly increased in CF-related diabetes mouse models (including CFTR-KO mice and *Scnn1b*-Tg mice). Interestingly, our data also showed that airway glucose serves as a nutrient for nasal introduced *Pseudomonas aeruginosa* (PAO1), since airway glucose concentration significantly decreased with PAO1 infection in CFRD mice compared to control CFRD mice without PAO1 infection[159] . In addition, neutrophils were found to be the dominant leukocyte in the CFRD mouse lungs after PAO1 infection[89,159], which agrees with multiple previous publications that study acute infection with varied pathogens in mouse lungs[236–238]. Although human and animal studies clearly showed that neutrophils migrated from blood to airway and there is much known about how PMNs traffic from blood across the endothelium, very limited information is available regarding how PMNs migrate across epithelial cells[239–242]. Due to the limitation of human subject studies, researchers have established endothelial apical culture (such as HUVECs) and epithelial undersurface culture on the Transwells with variety pore sizes to study neutrophils transendothelial and transepithelial migration over the last few decades[243–246]. The studies mainly used cell lines including T84, Calu-

3, H292, 16HBE, and Caco-2 with limited studies recently start to use primary human nasal epithelial and human small airway epithelial cells[247–255].

It is clear that CF and CFRD patients have constant neutrophil recruitment to the lung and that the damage produced by PMNs leads to most of the morbidity and mortality in patients[90,98,217]. Previous studies suggest that epithelial cells are actively involved in PMNs transmigration[249,256], while little is known concerning the mechanism underlying neutrophil-epithelial interactions. We hypothesized that bronchial epithelial cells conditioned to hyperglycemia modulate neutrophil transepithelial migration and that CFTR genotype, such as CFTR-ΔF508, directly impacts neutrophil transepithelial migration. We adopted previously used techniques with modifications to established a novel undersurface culture protocol by seeding 16HBE cells (16HBE-WT and 16HBE-ΔF508) onto the undersurface of collagen-coated Transwell filters (3 μm pore size) which can be grown to confluence with normal glucose (NG) or high glucose (HG) media[249,251,257]. Primary human PMNs were induced to transmigrate across epithelia using 100 nM fMLF which has been widely studied and used as a chemoattract for neutrophil transmigration[258,259]. A graphical representation of our experimental approach is shown in **Figure 5.1**. We further established primary human bronchial epithelial cells using our novel undersurface culture (NhBE and CFhBE) to test PMN transepithelial migration across primary cells[260].

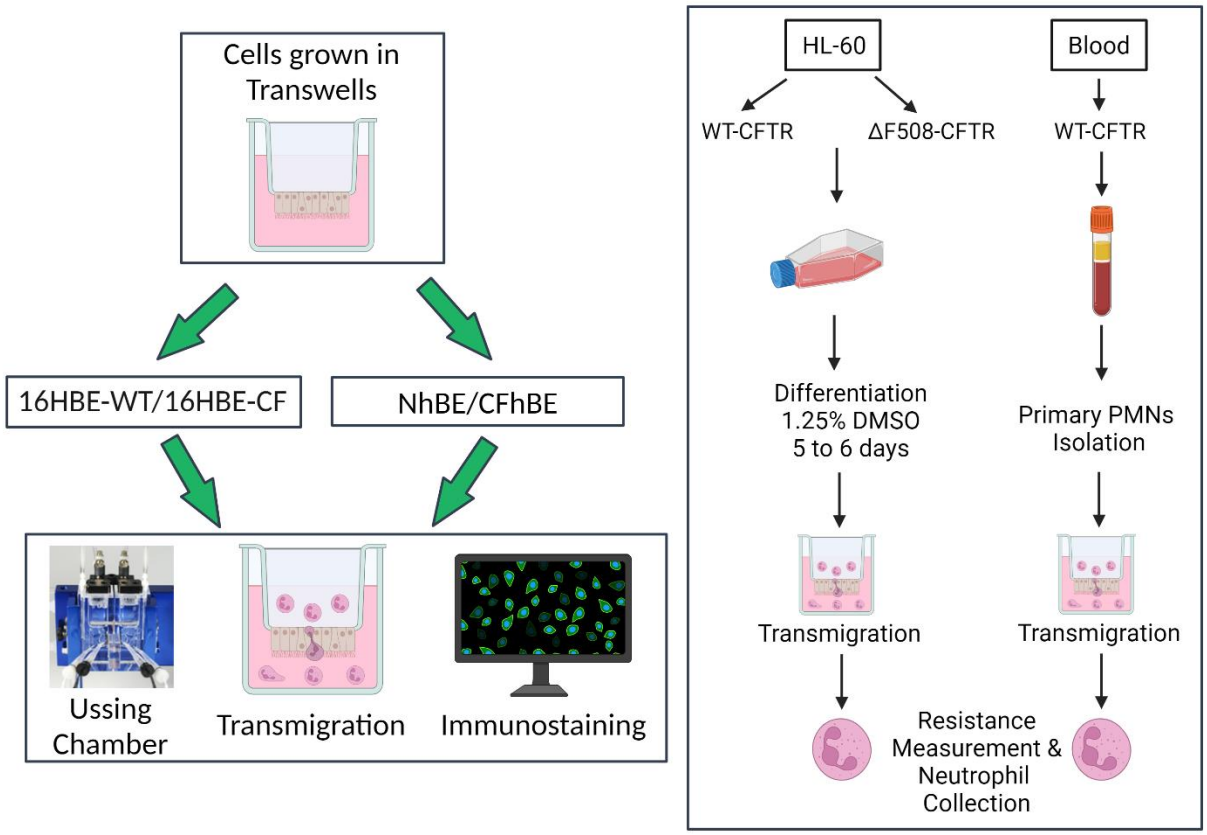

Figure 5.1. Graphical representation of our novel *in vitro* neutrophil transmigration experimental approach.

5.2. Materials and methods

5.2.1. 16HBE cell culture on the undersurface of Transwells

16HBE14o- Human Bronchial Epithelial cells expressing wildtype cystic fibrosis transmembrane conductance regulator (16HBE-WT) were kindly provided by Dr. Koval (Emory University). 16HBE-CFTR ΔF508/V470 (16HBE-ΔF508) cells were obtained from the Cystic Fibrosis Foundation (CFF). Both cell lines were cultured following the recommended protocol from CFF foundation with some modifications[131]. (1) We did not coat flasks for 16HBE cells culture used in this study. (2) Frozen vials of 16HBE-WT and 16HBE-ΔF508 cells from liquid nitrogen were thawed in a 37 ºC water bath and resuspend with 5 ml MEM medium (for 16HBE-WT) and 5 ml complete DMEM medium (for 16HBE-ΔF508) and plate the cells into flasks, respectively. (3) 16HBE-WT cells were cultured in MEM medium for 1 week before starting to passage and culture for experimental purpose. (4) 16HBE-ΔF508 cell cultured and passaged in complete DMEM media for 2 weeks, then switched to MEM media for 1 week, before starting to passage and culture for experiment purpose. MEM media contains 89% MEM (Gibco 11095-072), 10%FBS (R&D, S11150H), and 1% Penicillin/Streptomycin (Pen/Strep, Gibco 15070-063). DMEM media contains the same amount of FBS and Pen/Strep with 89% DMEM (Gibco 11885-084). Both cells were discarded 12 weeks after thawing.

For neutrophil transmigration purposes, both 16HBE-WT and 16HBE-ΔF508 cells were seeded on the undersurface of Transwells with 3 μm pore size (24 well plate, Corning 3415 and 12 well plate, Corning 3402). The seeding protocol was adopted from multiple previous publication with modifications[253,260–262]. Transwells were placed upside down onto cell culture dishes (Corning 430167) inside the hood. Undersurfaces of Transwells were coated with Collagen I at a 1:30 dilution using cell culture water (Purecol, 5005-100 ML). A final volume of 80 μL was

used for small Transwells (Corning 3415) and 300 µL was used for large Transwell (Corning 3402) added on the undersurface (Transwells upside down) in the cell culture hood and kept inside the hood for 2 hours. Transwells were washed three times with sterile water to remove nonbinding collagen I and maintained upside down in the hood for cell seeding. Both 16HBE-WT and 16HBE-ΔF508 were digested with 0.25% Trypsin/EGTA, pelleted at 350 g for 3 minutes, and resuspended with complete MEM media. Cells were counted using a hemocytometer and their viability was checked using Trypan blue. For 24 well plates with individual Transwell surface area 0.33 cm^2, we added 175,000 to 200,000 cells in 80 µl of complete MEM media. Transwells were moved to the cell culture incubator for ~ 1.5 hours before being flipped back to their original orientation in their corresponding plate. For 12 well plates with individual Transwell surface area 1.12 cm^2, we added about 300,000 to 325,000 cells in 250 µl MEM complete media. Cells were then moved to cell culture incubator for ~ 4.5 hours before being flipped back to their original orientation in the corresponding plate. Cells were cultured at liquid-liquid interface and the plates were maintained in the cell culture incubator for 2 days. We made high glucose MEM media (17.5 mM glucose) by adding extra glucose to the above MEM media (5.5 mM glucose). Hereafter, we will refer to the MEM media as 5.5 mM glucose and 17.5 mM glucose. The cells were further cultured in 5.5 mM glucose or 17.5 mM glucose for another 6 days or 7 days before neutrophil transmigration experiments were conducted. Media was changed every other day.

5.2.2. Conditionally reprogrammed Human Bronchial Epithelial cells (NhBE/CFhBE) cultured on the undersurface of Transwells

The NhBE/CFhBE cells and E-ALI/5.5 mM glucose media (E-ALI/5.5 mM) were obtained from the Koval lab at Emory University. E-ALI/5.5 mM media composition has been described previously[263]. We used the same Transwells (listed above) for the NhBE/CFhBE cell undersurface

culture coated with Collagen IV media (Collagen IV, Sigma)[126,263]. NhBE/CFhBE cells were pelleted at 350xg for 3 minutes. The supernatant was removed, and cells were resuspended with E-ALI/5.5 mM media. The cell number was counted, and viability was checked using Trypan blue and a hemocytometer. NhBE/CFhBE cells were seeded at a density >6000 cells per square millimeter[264]. When using the 24 well plate Transwells (Corning 3415), we added 250,000 to 300,000 cells in 80 µl E-ALI/5.5 mM media to each individual Transwell, which were then moved to the cell culture incubator for ~ 2.5 hours before being flipped back to their original orientation. When using 12 well plates Transwells (Corning 3402), we added about 800,000 to 900,000 cells in 300 µl E-ALI/5.5 mM media to each individual Transwell, which were then transferred to a cell culture incubator for 6.5 to 7 hours before being flipped back to their original orientation[264]. NhBE/CFhBE cells were maintained at liquid-liquid interface for three days before being switched to an air-liquid interface (ALI) using E-ALI/5.5 mM media. A volume of 0.5 mL E-ALI/5.5 mM (Coring 3402) or 0.2 mL E-ALI/5.5 mM (Corning 3415) was added on the apical side of the Transwell. Media was changed every day, and cells were allowed to differentiate over a two-week period. The cells were further cultured with E-ALI/5.5 mM or E-ALI/17.5 mM glucose (E-ALI/17.5 mM, made by adding extra glucose to E-ALI/5.5 mM media) for another 2 weeks before neutrophil transmigration.

5.2.3. HL-60 cell culture and differentiation

The HL-60 cells including HL-60-WT (expressing WT-CFTR) and HL-60-ΔF508 (expressing ΔF508-CFTR) were kind gifts from the Chandler lab (Emory University). The culture protocol used in this project is adapted from a variety source with modifications[265–267]. Three media compositions were used in the HL-60 cell culture: CM1 contained RPMI-1640 with 10%FBS, 1% GlutaMax-1, and 1% Pen/Strep. CM2 (for differentiation) contained RPMI-1640 with 10% FBS,

1% GlutaMax-1, and 1.25% DMSO. CM3 contained RPMI-1640 with 20% FBS, 1% GlutMax-1, and 1% Pen/Strep. For HL-60-WT cell culture, a frozen vial of HL-60-WT was thawed at 37 ºC. Cells were transferred to a 15 ml canonical tube with 10 mL of CM3 media and pelleted at 350 g for 5-10 minutes at RT. The supernatant was removed, the pellet was resuspended, and cells were transferred to a T75 flask with ~14 ml CM3 and cultured in a cell culture incubator. The HL-60-WT cells were maintained and cultured in CM3 media for 2 weeks, and then switched to CM1 media. When working with HL-60-ΔF508, a frozen vial was thawed 37 ºC, and cells were transferred to a 15 ml canonical tube with 10 ml of CM1 media. However, only CM1 media was used for culture. For differentiation, both HL-60-WT and HL-60-ΔF508 cells were spun down, the supernatant was removed, and cells were resuspended with 4 ml CM2. Cell numbers were counted using a hemocytometer. The process was repeated to fully remove the antibiotics. Differentiation cell density was 400,000/ml in CM2 media which contain 1.25% DMSO. The cells were differentiated for 5 days in a cell culture incubator without disturbing until used for experiments. The differentiated cells were discarded after 6 days in DMSO if not used for experiments. Differentiation was tested by immunostaining and confocal microscopy of the CD35 differentiation marker. Briefly, dHL-60-WT and dHL-60-ΔF508 were fixed with 4% PFA and stained with anti-CD 35 antibody (CD35 monoclonal antibody, ThermoFisher, MA 5-44022). Slides were mounted with Vectashield antifade containing DAPI (Vector Laboratories, # H-1200-10).

5.2.4. Isolation of human neutrophils

Healthy human blood neutrophils were purified with Polymorphprep (PMP) according to the company's manual and recommendations from the Tirouvanziam lab[268]. In brief, blood was drawn into EDTA tube, blood was added on top of the PMP, and samples were centrifuged at 400

x g for 42 minutes at room temperature. The neutrophil band was collected, mixed with equal volume of 0.45% NaCl, and centrifuged at 800 x g for 5-10 minutes. The pellet was resuspended for 30 seconds with ice-cold, sterile water to lyse red blood cells. Osmolarity was quickly restored using an equal amount of cold 1.8% NaCl, and samples were centrifuged at 800 x g for 5-10 minutes. Neutrophils were resuspended with cold RPMI-1640, cell numbers were counted, and neutrophils were maintained on ice until needed.

5.2.5. Ussing chamber analysis

Ussing chamber study was performed following the McCarty lab established technique [180]. In brief, CFTR-mediated transepithelial short-circuit Cl^- current (I_{sc}) was measured under voltage clamp conditions (clamping voltage to 0 mV) using a system that includes a VCC-MC6 amplifier and EM-RSYS-2 chambers, using P2302T sliders, with P2020-S electrodes (Physiologic Instruments, Reno, NV). Filters were inserted into the chamber and the following solutions added (in mM): undersurface solution (referred to as normal chloride solution) composed of 140 NaCl, 5 KCl, 0.36 $K_2HPO_4•3H_2O$, 0.44 KH_2PO_4, 0.5 $MgCl_2$, 1.3 $CaCl_2•2H_2O$, 4.2 $NaHCO_3$, 10 glucose, 10 HEPES, (pH 7.4); apical solution (referred to as low chloride solution) composed of 133 Na Gluconate, 5 K Gluconate, 2.5 NaCl, 0.36 $K_2HPO_4•3H_2O$, 0.44 KH_2PO_4, 0.5 $MgCl_2$, 5.7 $CaCl_2•2H_2O$, 4.2 $NaHCO_3$, 10 mannitol, 10 HEPES (pH 7.4). Both solutions were bubbled with a 95% / 5% mixture of O_2 / CO_2 and heated to 37°C. After 30 minutes stabilization, compounds were applied sequentially, including amiloride (100 μM), forskolin (FSK, 10 μM), and $CFTR_{inh}172$ (10 μM). Data were acquired using the Acquire and Analyze software and exported to Excel for analysis.

5.2.6. dHL-60 cells and PMN transmigration

Transmigration of both dHL-60 (dHL-60-WT and dHL-60-ΔF508) cells and PMNs took place at 37 °C inside a cell culture incubator with 5% CO_2. Prior to transmigration, the resistance of every Transwell (Corning 3402) was measured with an EVOM (EVOM^2, World Precision Instrument). Transwells with resistance lower than 600 Ω were not used for the experiment[126,235]. The Transwells were moved to new plates and equilibrated with RPMI-1640 for 30 minutes in a cell culture incubator. After equilibration, the solution in the basal chamber was replaced with 100 nM fMLF (or 100 nM LTB4 depending on the experiment) dissolved in RPMI-1640. Either dHL-60s or PMNs in RPMI-1640 were added to the apical side of the Transwell. Plates were moved back to a cell culture incubator for transmigration for 1-6 hours. After transmigration, Transwells were carefully removed from the plate without transferring any apical solution or cells to the bottom well. Then, the solution at the bottom of each well, containing transmigrated cells, was collected into separate tubes. Wells were washed with fresh RPMI-1640 to collect any remaining cells and that wash solution was transferred to its corresponding tube. Next, cells were pelleted at 800 x g for 5 minutes at 4 °C, the supernatant was carefully removed, and cells were resuspended with 200 µl fresh RPMI-1640. Cell numbers were then counted using a hemacytometer. After cell counting, randomly selected cell samples were centrifuged at 500 x g for 5 minutes onto microscope slides using a Shandon Cytospin 4 (Thermo Electron Corporation). Slides were then stained using Diff staining[89,159]. The slides were imaged using a Zeiss AXIO Observer A1 microscope on 40x fields. Images were taken using Axiocam 305 color camera and ZEN v3.8.99.01000 software.

5.2.7. Immunostaining and confocal microscopy

16HBE cells or primary cells (NhBE and CFhBE) were seeded on Transwells (Corning 3415) for immunostaining and confocal microscopy. Around 2.5 million PMNs were incubated

with 0.5 μM live cell stain CellTracker (CellTracker Green dye, C7025, ThermoFisher Scientific) diluted in 1 ml RPMI-1640 for 30 minutes in a well of a 24 well plate in the cell culture incubator. After staining, the CellTracker- labeled PMNs were collected and pelleted at 800 x g for 5 minutes at 4 °C. Next, the supernatant was carefully removed, and neutrophils were resuspended with 0.5 ml RPMI-1640 and pelleted at 800 x g for 5 minutes at 4 °C. The wash process was repeated 3 times to completely remove CellTracker. Neutrophils were resuspended with RPMI-1640, cell number was counted using a hemocytometer, and 75,000 to 100,000 cells were added in 100 μl RPMI-1640 to the apical chamber of Transwells with 16HBE cells or primary cells cultured at their undersurface for PMNs transmigration experiments. The transmigration duration was set to 2 to 2.5 hours. Images were taken in the integrated Cellular Image core facility of Emory University using a Nikon SoRa confocal microscope using a 40X water immersion objective.

5.2.8. Source of Reagents

Unless otherwise noted, all reagents were obtained from MilliporeSigma. IL-1β was purchased from BioLegend (Cat# 579402).

5.2.9. Statistical analysis

Data are presented as mean ± SEM and were analyzed with Sigmaplot 13.1 (SYSTAT, Palo Alto, CA). Statistical analyses were performed using an unpaired Student's t test. $P < 0.05$ was accepted for an indication of statistically significant difference.

5.3.Results

5.3.1. 16HBE cells formed monolayer cultured on the inside and undersurface of Transwells with 3 μm pore size

Our lab has well-established protocols to culture a variety of epithelial cells on 0.4 μm pore size Transwells to form monolayers, including FRT, NuLi/CuFi, and 16HBE cells[126,180,235]. However, these Transwells were not compatible for neutrophil transmigration experiments since the pore size is too small for neutrophils to migrate across it. To establish the cell culture model for neutrophil transmigration, we chose to use Transwells with 3 μm pore size and 0.33 cm^2 surface area (Corning 3415) which fit our Ussing chamber recording system and seeded 16HBE cells on either the inside or undersurface of the insert coated with Collagen I. We then measured resistance and the bioelectric properties of the two different monolayers with the Ussing chamber technique. **Figure 5.2** shows representative short circuit current recordings of 16HBE-WT (**Figure 5.2A**) and 16 HBE-ΔF508 (**Figure 5.2D**) cultured on the undersurface of the Transwell inserts. Summary data for resistances (R, Ω•cm^2) of cells cultured on apical or undersurface of the Transwell insert are presented in **Figure 5.2B** for 16HBE-WT and **Figure 5.2E** for 16HBE-ΔF508. Resistances of 16HBE-WT cultured traditionally were significantly higher than that of cultured undersurface, while no significant differences were seen in 16HBE-ΔF508 cell cultured in the two modes. CFTRinh172 sensitive current (ΔI_{INH172}) are presented in **Figure 5.2C** for 16HBE-WT and **Figure 5.2F** for 16HBE-ΔF508. In summary, the data presented here clearly indicated that monolayers formed substantial barrier properties when either 16HBE-WT or 16HBE-ΔF508 cells were cultured on the undersurface of Transwell inserts with 3 μm pore size. We successfully built a novel cell model for testing neutrophil transmigration, and all experiments described below used undersurface culture approach unless otherwise stated.

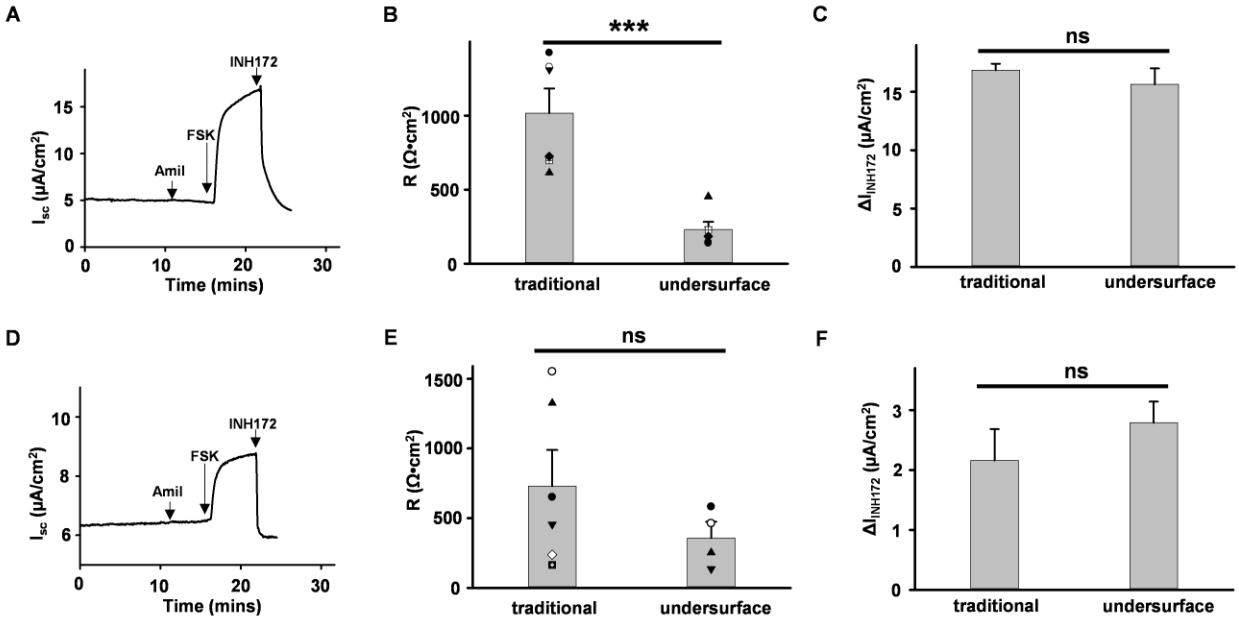

Figure 5.2. 16HBE monolayer integrity was investigated by Ussing chamber recordings.

Cells were cultured traditionally (traditional) or undersurface (undersurface) of Transwell inserts (3 μm pore size) in 5.5 mM glucose media. Representative current traces recorded on 16HBE-WT (A) and 16HBE-ΔF508 (D) monolayers cultured on the undersurfaces of Transwell inserts. Summary data for resistances (R) of 16HBE-WT (B) and 16HBE-ΔF508 (E) are shown. Summary data for $CFTR_{inh}172$ (INH172) inhibited current of 16HBE-WT (C) and 16HBE-ΔF508 (F) are shown (n = 6 for traditional culture and n = 6 for undersurface culture for 16HBE-WT. n = 6 for traditional culture and n = 4 for undersurface culture for 16HBE-ΔF508. *** $P<0.001$. ns, no significant difference).

5.3.2. Differentiated HL-60 cells transmigrated across 16HBE monolayer

Differentiated HL-60 cells expressing WT-CFTR (dHL-WT) shared neutrophil-like features and were previously used for studying transepithelial migration[265,269]. In addition, while HL-60 expressing ΔF508-CFTR (HL-60-ΔF508) were made available recently, no reports have been made so far using differentiated HL-60-ΔF508 (dHL-60-ΔF508) for transepithelial migration[267]. Both dHL60 cell lines tested positive for CD35 expression, a marker for differentiation, by immunostaining and confocal microscopy (**Figure 5.3**). We tested the transepithelial migration of dHL-WT cells across 16HBE-WT monolayer and dHL-ΔF508 cells across 16HBE-ΔF508 monolayer (**Figure 5.4**). As shown in **Figure 5.4A**, no direct correlation was seen between transepithelial resistance, and the total number of dHL-60 cells transmigrated across 16HBE cell monolayers in 6 hours. In addition, the total number of transmigrated dHL-60 cells increased according to the number of dHL-60 added to the apical chamber when the experiment was initiated, which exhibited a dose-dependent increase over a 6-h duration (**Figure 5.4B**). This phenomenon was consistent in both the 16HBE-WT/ dHL-WT group and the 16HBE-ΔF508/ dHL-ΔF508 group. However, the total number of transmigrated dHL-60 cells were extremely low even at 1 million dHL-60 added on the apical chamber for transmigration. Next, we tested effects of dHL-60 transepithelial migration on the resistance of 16HBE-WT (**Figure 5.4C**) and 16HBE-ΔF508 (**Figure 5.4D**) monolayers. The resistances of both monolayers significantly decreased after a 6-h transmigration compared to that of pre-transmigration. In summary, the efficiency of dHL-60 transmigration across epithelial monolayers was measurable but very low compared to PMNs, which is supported by previous report[270]. Hence, we turned to primary PMNs for further experiments.

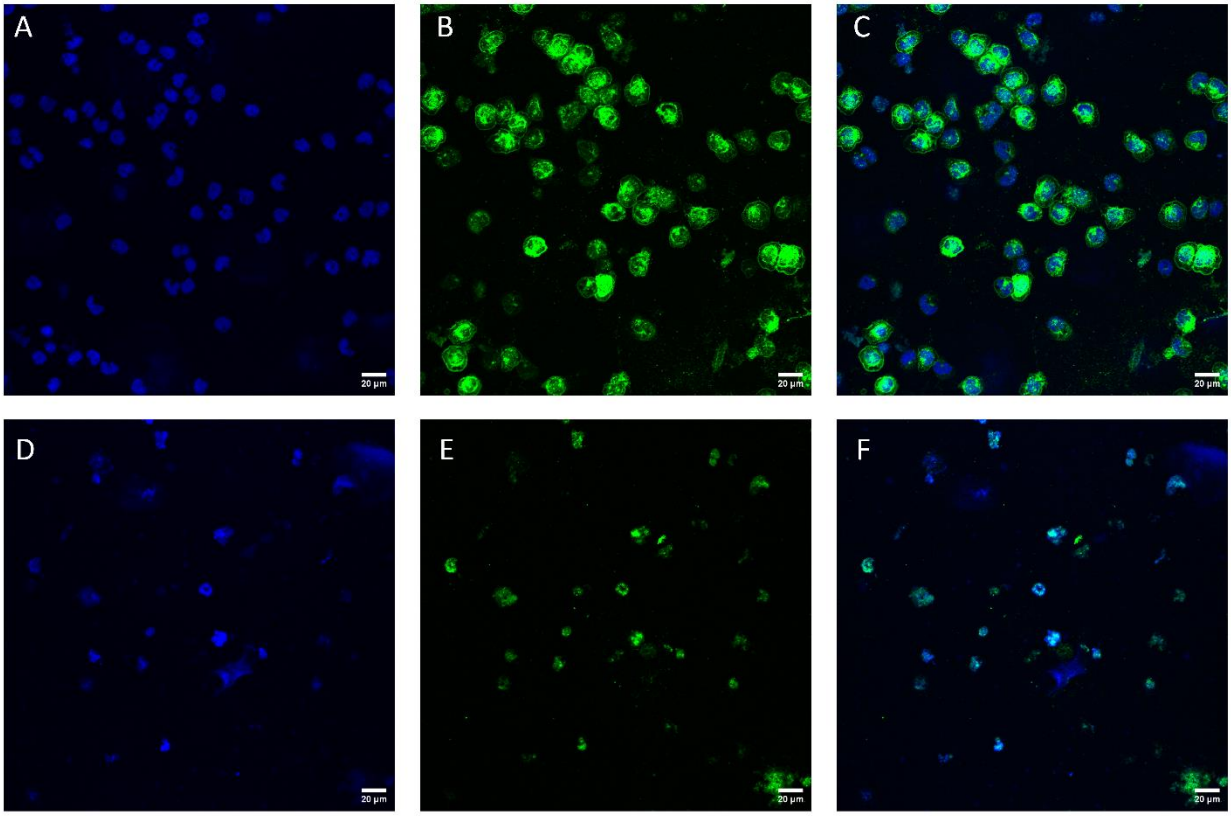

Figure 5.3. Representative images of differentiated HL60 (dHL60) cells, expressing either WT or ΔF508 CFTR, stained positive for the differentiation marker CD35.

A) DAPI staining (blue) in dHL60-WT cells. B) CD35 staining (green) in dHL60-WT cells. C) Overlay of blue and green channels for dHL60-WT cells. D) DAPI staining (blue) in dHL60-ΔF508 cells. E) CD35 staining (green) in dHL60-ΔF508. F) Overlay of blue and green channels for dHL60-ΔF508. Scale bar is 20 µm.

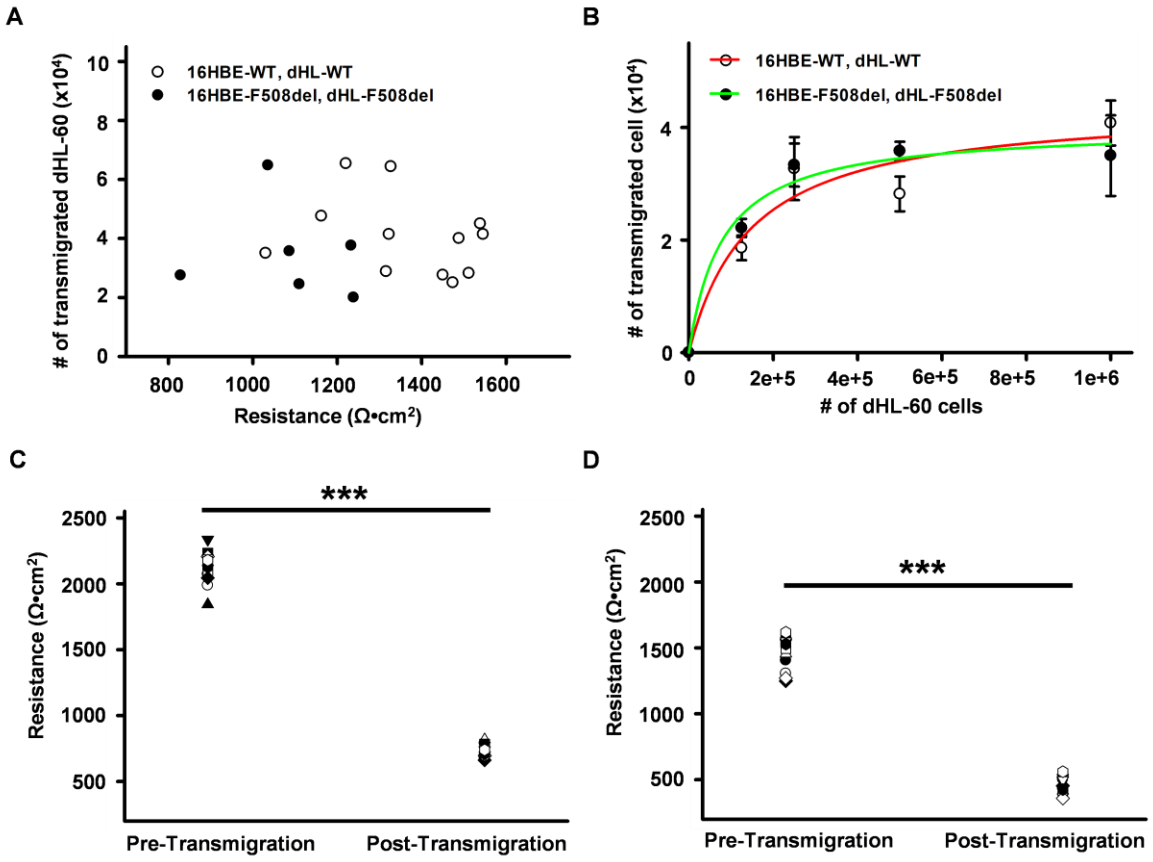

Figure 5.4. Differentiated HL-60 cells transmigrated across 16HBE monolayers cultured in 5.5 mM glucose condition.

HL-60 cells were differentiated with 1.25% DMSO for 5 to 6 days (including HL-60 cells expressing WT-CFTR, dHL-WT, and HL-60 cells expressing CFTR-ΔF508, dHL-ΔF508). (A) No direct correlation was seen between dHL-60 (dHL-WT transmigrated across 16HBE-WT; dHL-ΔF508 across 16HBE-ΔF508) transmigration in response to 100 nM fMLF and the resistance of 16HBE cell monolayers (>600 Ω•cm2) over a 6-h duration. (B) dHL-60 transmigration efficiency exhibited a dose-dependent increase over a 6-h duration. Data points represent n = 6 to 9 for each. Effects of dHL-60 transepithelial migration on the resistance of epithelia in 6-h duration (C, 16HBE-WT with dHL-WT; D, 16HBE-ΔF508 with dHL-ΔF508) (*** P<0.001). Each symbol represents one experimental measurement.

5.3.3. Transmigration of healthy human neutrophils across 16HBE cell monolayers

Healthy human blood neutrophils have been studied for decades and techniques for purifying neutrophils are well established[268]. We adopted the techniques optimized by our colleagues and used 1 million PMNs per Transwell (Corning 3402) for the current study to determine: a) the effects of PMN transepithelial migration on the resistance of the monolayers, b) the efficiency of PMN transmigration across 16HBE monolayers[268]. We measured the resistance of epithelial monolayers, collected the transmigrated neutrophils at different time points, and counted total cell number using a hemocytometer. Both 16HBE-WT and 16HBE-ΔF508 monolayers were cultured in normal (5.5 mM) as well as high glucose (17.5 mM) media. The data are shown in **Figure 5.5**. Representative data group for 16HBE-WT (**Figure 5.5A**) and 16HBE-ΔF508 monolayers (**Figure 5.5B**) are presented. Monolayer resistance dropped most dramatically within the first hour of experiment and then continued a slow decrease in both monolayer types. Summary data for the ratio of resistance changes due to PMN transepithelial migration are shown in **Figure 5.5B** (16HBE-WT) and **Figure 5.5E** (16HBE-ΔF508) cultured in 5.5 mM or 17.5 mM glucose media. Compared to high glucose cultured monolayers, the trends for resistance change were mild in both monolayer types cultured in normal glucose. Ratio of resistances (R_{post}/R_{pre}) of monolayer types cultured in normal glucose were significantly higher than those conditioned to high glucose irrespective of CFTR genotype. Moreover, the normalized resistances for 16HBE-WT monolayers were significantly higher than those for 16HBE-ΔF508 monolayers under the same culture condition and transmigration durations (**Figure 5.6**).

We collected the transmigrated neutrophils at different time points and counted cell numbers with a hemocytometer. As shown in **Figure 5.5C** and **Figure 5.5F**, the number of transmigrated neutrophils at the 1-h timepoint was very low; no significant differences were seen

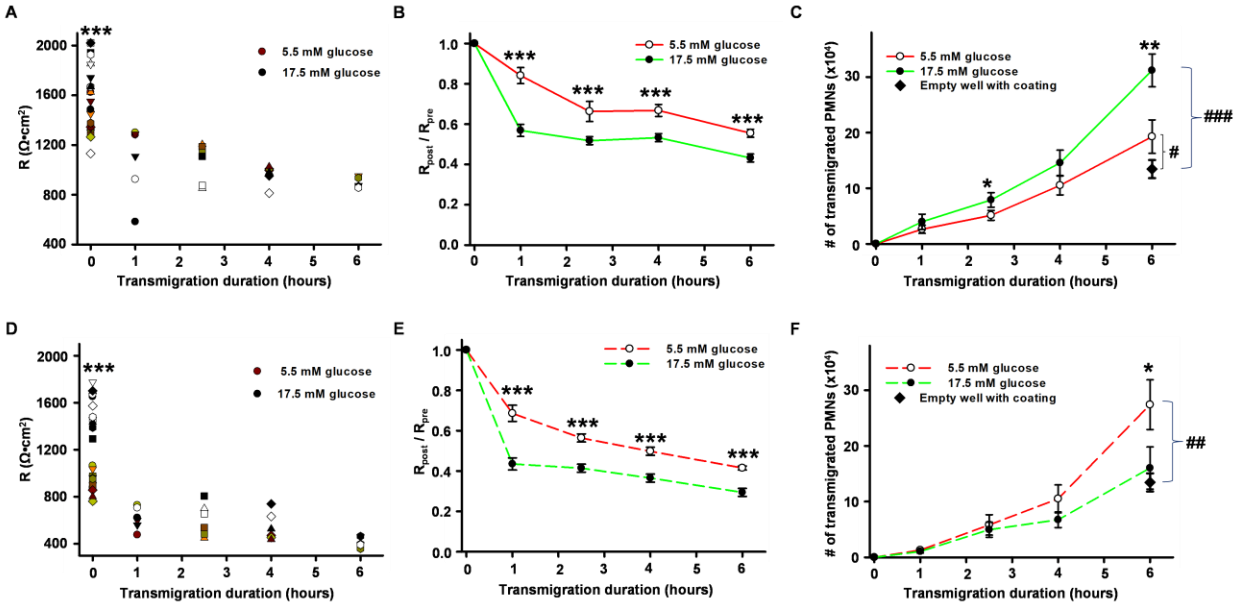

Figure 5.5. PMN transmigration across 16HBE cell monolayers cultured in 5.5 mM and 17.5 mM glucose condition. PMNs were induced by 100 nM fMLF to migrate in the basolateral-to-apical direction across cell monolayers.

Addition of 1 million PMNs in 200 µL RPMI-1640 media per well was tested (12 well plate). Representative resistance response for 16HBE-WT monolayers (A) and 16HBE-ΔF508 (D) monolayers generated by PMNs transepithelial migration over different durations. Time-dependent changes in resistance (R_{post}/R_{pre}) and the total number of transmigrated PMNs are shown for 16HBE-WT (B, C) and 16HBE-ΔF508 (E, F) conditioned in NG media (red line) or HG media (green line) (n = 8 to 12 for each; * $P < 0.05$, **$P < 0.01$, *** $P < 0.001$ comparing NG vs HG; # $P < 0.05$; ## $P < 0.01$ compared to the number of neutrophils transmigrated across empty wells (collagen coating alone).

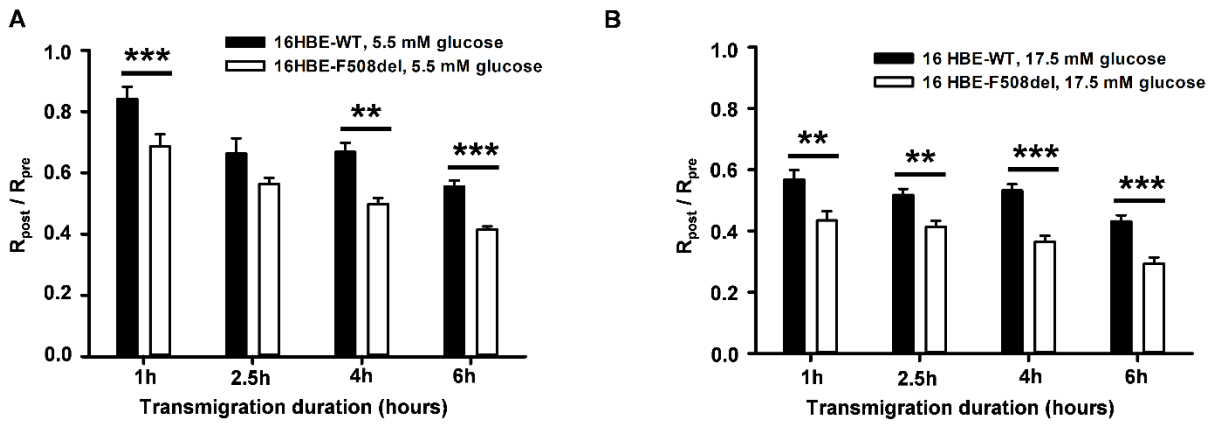

Figure 5.6. Resistance changes in airway epithelial cell monolayers conditioned with normal or hyperglycemia at different transmigration time points.

A) Normalized resistance (resistance post transmigration/resistance pre transmigration) for 16HBE-WT and 16HBE-ΔF508 monolayers conditioned with normal glucose (5.5 mM). B) Normalized resistance (resistance post transmigration/resistance pre transmigration) for 16HBE-WT and 16HBE-ΔF508 monolayers conditioned with high glucose (17.5 mM) (n = 8 to 12 for each, $^{**}P < 0.01$, $^{***}P < 0.001$).

in 16HBE-WT or 16HBE-ΔF508 monolayers regardless of cell culture condition. The total number of transmigrated PMNs at a 6-h for 16HBE-WT monolayers cultured in 17.5 mM glucose was significantly higher compared to 5.5 mM glucose. In contrast, the total number of transmigrated PMNs at 6-h duration for 16HBE-ΔF508 cultured in 5.5 mM glucose was significantly higher compared to 17.5 mM glucose cultured cells. These results suggest that the interaction between neutrophils and epithelial cells are sensitive to glucose conditioning, but the response to high glucose is dependent upon CFTR genotype. We further compared the numbers of neutrophils transmigrated across epithelial monolayers with the number of neutrophils transmigrated across empty Transwells with collagen coating only. The numbers of neutrophils that transmigrated across 16HBE-WT monolayers, cultured under either 5.5 mM or 17.5 mM glucose, were significantly higher than that of empty Transwells. This suggests the presence of productive interaction between PMNs and epithelial cells that lead to faster transmigration across two barriers compared to only one. However, in 16HBE-ΔF508 cells, this phenomenon was only seen in monolayers cultured under 5.5 mM glucose and not under 17.5 mM glucose (**Figure 5.5F**). We next tested the possible correlation of resistance and total number of transmigrated neutrophils at 4-h (**Figure 5.7A**) and 6-h time points (**Figure 5.7B**). Like dHL-60 cells, no direct correlation was seen for 16HBE-WT and 16HBE-ΔF508 monolayers cultured in either 5.5 mM or 17.5 mM glucose conditions.

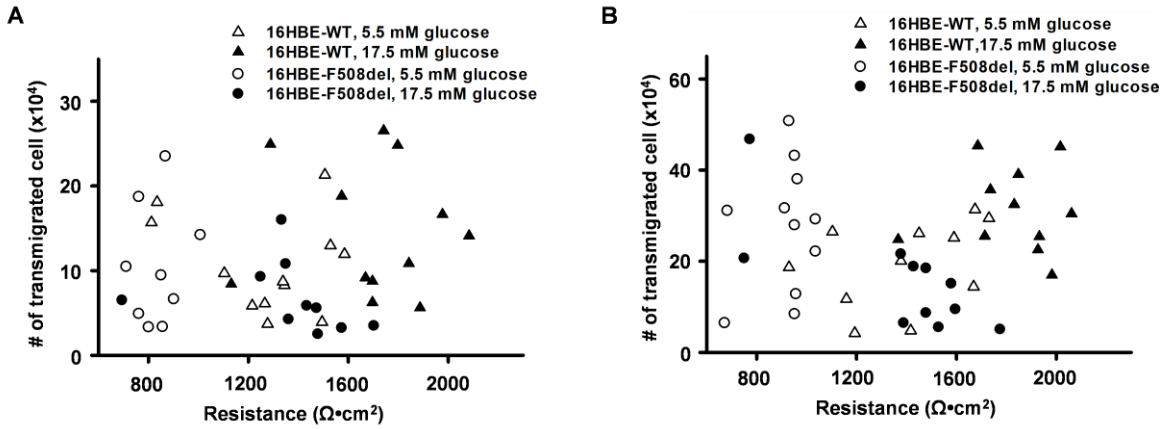

Figure 5.7. No direct correlation between PMN transepithelial migration rates and the electrical resistance of 16HBE cell monolayers.

This was true over a 4-h (A) or a 6-h (B) transmigration duration induced by 100 nM fMLF. Both 16HBE-WT and 16HBE-ΔF508 cells cultured in 5.5 mM glucose and 17.5 mM glucose formed monolayers with resistances (>600 Ω•cm2) measured with EVOM2 before PMN transmigration. Monolayers with resistances below 600 Ω•cm2 were not used in the study. Each symbol represents one experimental measurement.

To view live neutrophils actively transmigrating across the 16HBE cell monolayer, we employed CellTracker live cell staining to label neutrophils with green fluorescence before transmigration[271]. After 2-hour transmigration, neutrophils and epithelial cells were fixed. The monolayer was then stained for Zonula Occludens-1 (ZO-1), shown in red, and the nuclei were stained with DAPI, shown in blue. Representative images collected with confocal microscopy are shown in **Figure 5.8**. ZO-1 staining clearly marked the cell boundaries formed in the monolayer (**Figure 5.8B**) and green color neutrophils are seen migrating across the tight junction (**Figure 5.8C**). Orthogonal views of the images in the YZ direction (**Fig. 5.8E**) and the XZ direction (**Figure 5.8G**) showed neutrophils transmigrating through the tight junction formed by the monolayer as highlighted by the orange arrows. No neutrophils were seen transmigrating across epithelial cell bodies in the study.

Taken together, the data suggest: (a) The tight junctions formed by 16HBE-WT monolayers were healthy and exhibited more elasticity to accommodate neutrophil transmigration than empty Transwells when they were cultured under either glucose condition. (b) 16HBE-WT cells adapted to the hyperglycemia challenge, and their resistance changes well matched the number of transmigrated neutrophils in a 6-h duration. (c) The tight junctions formed by 16HBE-ΔF508 cells cultured under normal glucose competently facilitated neutrophil transmigration, although their remaining resistance ratios remained low. (d) The tight junctions of 16HBE-ΔF508 cells cultured in hyperglycemia failed to facilitate neutrophil transmigration with no difference detected compared to neutrophils transmigrating across empty Transwells with coating only. The findings were also supported by our recent findings that 16HBE-WT cells, not 16HBE-ΔF508s, exhibited adaptation upon hyperglycemia challenge to maintain barrier integrity (**Chapter 2**).

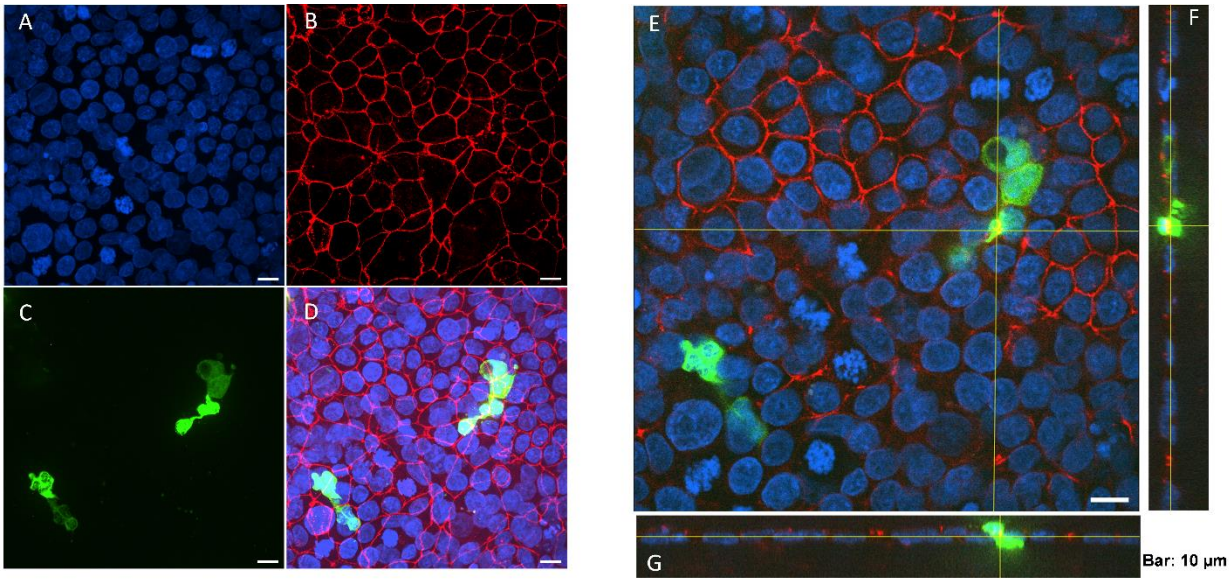

Figure 5.8. Representative confocal microscopy images of neutrophils transmigrating across a 16HBE-WT monolayer induced by 100 nM fMLF.

(A) DAPI staining shown in blue, labeling the location of nuclei. (B) ZO-1 staining shown in red, labeling the location of tight junctions. (C) CellTracker staining shown in green, labeling the location of PMNs. (D) Overlay of the previous three fluorescence channels (note that images A, B, C, and D are maximum projections in the Z direction). (E) Enlarged a Z-plane with all channels overlayed. (F) YZ orthogonal view of overlay image showing a neutrophil transmigrating through the monolayer as highlighted by the yellow lines. (G) XZ orthogonal view of overlay image showing neutrophils transmigrating through the monolayer as highlighted by the yellow lines. Scale bar: 10 µm.

5.3.4. The neutrophils transmigrated across epithelial monolayer exhibited altered morphology

Previous studies reported that neutrophils exhibit a unique behavior (identification of the "GRIM" fate) and turn pathogenic early on upon exposure to the CF airway milieu[47]. In addition, the PMNs transmigrated across HUVEC endothelial monolayers in response to TNF exhibited a significant decrease in the percentage of apoptosis compared to naïve PMNs treated with TNF without transmigration[272]. We collected and observed the morphology changes of the transmigrated PMNs across airway epithelial cells (**Figure 5.9**). Unlike the naïve PMNs shown in **Figure 5.9A,D** and the PMNs transmigrated across empty Transwell with coating only (**Figure 5.9B, E**), the PMNs transmigrated across epithelial monolayers displayed enlarged cell size with large empty looking vesicles and rough plasma membranes. Moreover, the size of the nucleus in the transmigrated PMNs also increased while maintaining normal polymorpho-nucleus character which is different from the apoptotic PMNs with unique condensed single nucleus. Surprisingly, we found net-looking structures presented in some transmigrated PMNs while the cells appeared to retain intact morphology. The unique morphologies were clearly different from the well-known neutrophil extracellular traps (NETs) arising from suicidal NEtosis and vital NEtosis process[273].

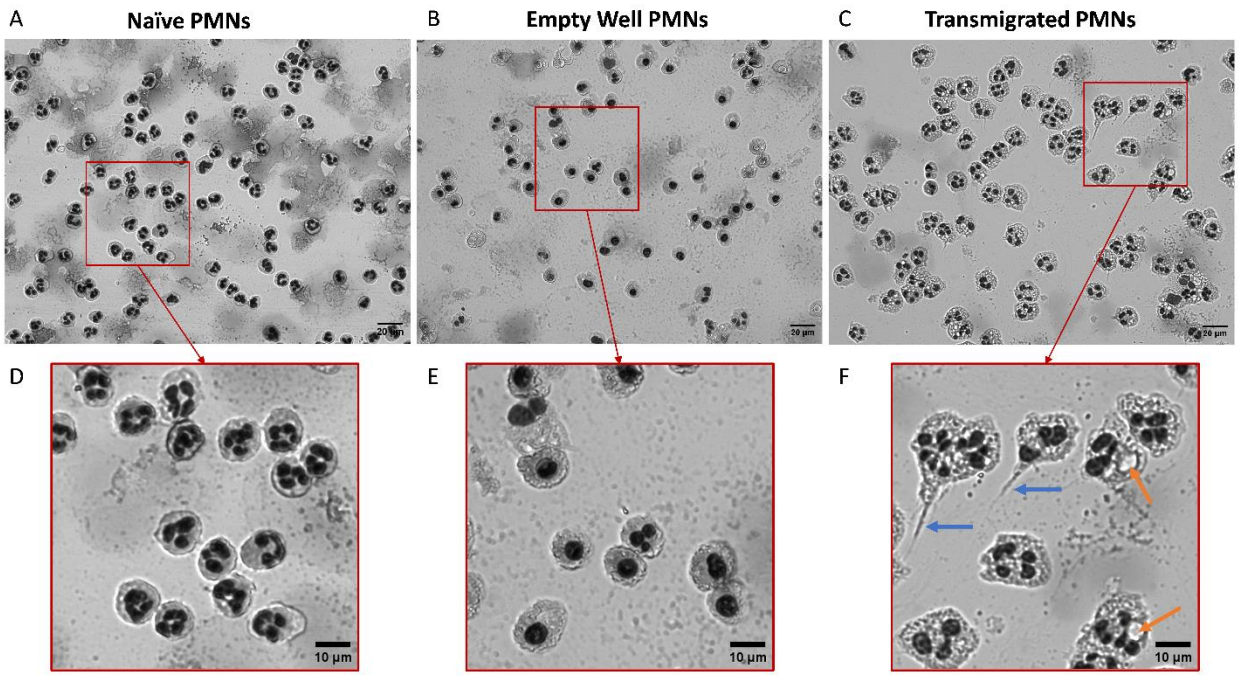

Figure 5.9. PMNs transmigrated across epithelial monolayers in response to fMLF exhibited changes to morphology unlike that of naïve PMNs and PMNs transmigrated across empty Transwells.

PMNs were cytospun to slides and stained with Diff Quik. (A) Naïve PMNs. (B) Transmigrated PMNs collected after 6-hours across empty Transwells with coating only, (C) 16HBE-ΔF508 monolayers conditioned to 5.5 mM glucose. Zoomed in images for each corresponding sample are shown in (D-F). Orange arrow: empty looking vesicles. Blue arrows: possible net release. Top scale bars: 20 µm. Bottom scale bars: 10 µm.

5.3.5. Healthy human neutrophil transmigration across primary human bronchial epithelial monolayers

The data thus far suggest that tight junctions formed by 16HBE cells facilitated neutrophil transmigration across the monolayers. We asked whether this behavior is maintained or recapitulated in primary airway monolayers, including healthy primary bronchial epithelial cell expressing normal CFTR (NhBE) and CF primary bronchial epithelial expressing CFTR-ΔF508 (CFhBE). Primary cells in a basal state from heathy donors as well as CF patients were propagated using rho kinase inhibitors and irradiated fibroblasts ("conditional reprograming conditions", CRC) to generate cells that can subsequently be differentiated into a mature heterogeneous pseudostratified mucociliary monolayer[263]. Both NhBEs and CFhBEs were seeded onto the undersurface of Transwell inserts with 3 μm pore size. After differentiation in ALI culture under conditions E-ALI media containing 5.5 mM glucose for 2 weeks, Transwells were either continually cultured in E-ALI media containing 5.5 mM glucose or switched to E-ALI media containing 17.5 mM glucose for another 2 weeks before conducting neutrophil transmigration.

Results for healthy PMN transmigration across NhBE monolayers induced by 100 nM fMLF are shown in **Figure 5.10**. In a 6-h duration transmigration, the total number of neutrophils transmigrated across NhBE monolayers conditioned in E-ALI/17.5 mM glucose was significantly higher when compared to that of the E-ALI/5.5 mM glucose group (**Figure 5.10A**). The resistances of Transwells measured in pre- as well as post-transmigration of NhBE monolayers cultured in 5.5 mM glucose are shown in **Figure 5.10B** and the resistance for the 17.5 mM glucose group are shown in **Figure 5.10C**. Like 16HBE-WT cultured in 5.5 mM glucose, the resistances for NhBE monolayers significantly decreased after 6-h neutrophil transmigration compared to pre-transmigration.

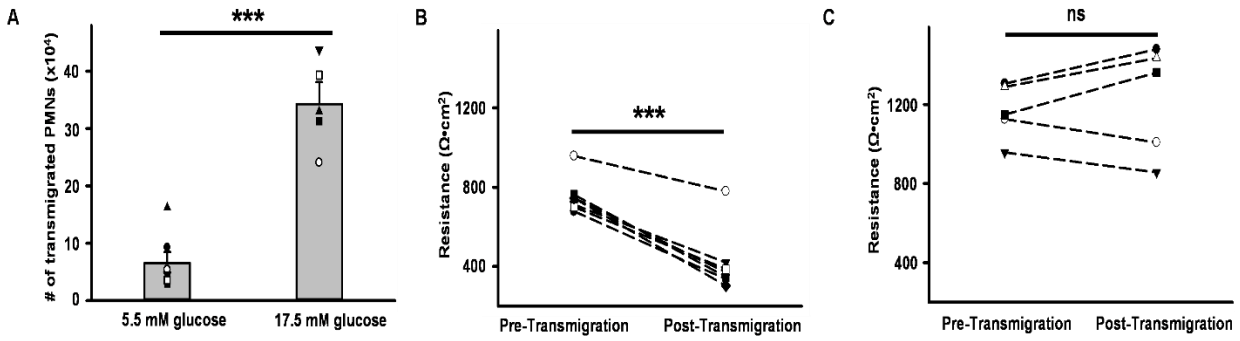

Figure 5.10. PMN transmigration across NhBE monolayers in response to 100 nM fMLF.

Cells were seeded and cultured at air-liquid interface (ALI) with E-ALI media (E-ALI/5.5 mM glucose) on the undersurface of Transwells for differentiation for 2 weeks. Half of the Transwells were continually maintained in E-ALI/5.5 mM glucose and the other half were switched to E-ALI/17.5 mM glucose for 2 weeks. (A) The number of transmigrated PMNs across E-ALI/17.5 mM glucose was significantly higher than that of E-ALI/5.5 mM glucose. The post-transmigration resistances were significantly lower compared to the pre-transmigration in the E-ALI/5.5 mM glucose (B), but not in the E-ALI/17.5 mM glucose group (n=6 for 5.5 mM glucose, n=5 for 17.5 mM glucose; (*** P>0.001, ns=no significant difference).

We next used CellTracker to label neutrophils and observed them transmigrating across NhBE monolayers. Representative images collected with confocal microscopy are shown in **Figure 5.11**. ZO-1 staining clearly marked the tight junction formed in the monolayer and green color neutrophils were migrating across the tight junctions. Orthogonal views of the images in YZ and XZ orientations showed neutrophils transmigrating through the tight junction formed by the monolayer as highlighted by the orange arrows. Like 16HBE-WT monolayers, no neutrophils were seen transmigrating across epithelial cell bodies in the study.

Previous findings from the Koval and McCarty groups suggested that tight junctions formed by CFhBE cells are significant weaker compared to NhBE cells[126], we further studied healthy neutrophil transmigration across CFhBE monolayers induced by 100 nM fMLF (**Figure 5.12**). Unlike NhBE monolayers, the total number of neutrophils transmigrated across CFhBE monolayers was not significantly different when cultured under E-ALI/5.5 mM vs E-ALI/17.5 mM glucose media at 6-h (**Figure 5.12A**). Like NhBE, the resistances of CFhBE monolayers were significantly decreased from pre-transmigration compared to post-transmigration when cultured in 5.5 mM glucose (**Figure 5.12B**). In contrast to NhBE, the resistances of CFhBE monolayers were significantly decreased from pre-transmigration compared to post-transmigration when cultured in 17.5 mM glucose (**Figure 5.12C**). In addition, the data for CFhBE monolayers were closer to that of 16HBE-ΔF508 monolayers and were far different from those of NhBE and 16HBE-WT monolayers.

We further used CellTracker to label neutrophils and observed the neutrophils transmigrating across a CFhBE monolayer. Representative images collected with confocal microscopy are shown in **Figure 5.13**. The green neutrophils were seen transmigrating across tight junctions in CFhBE monolayers.

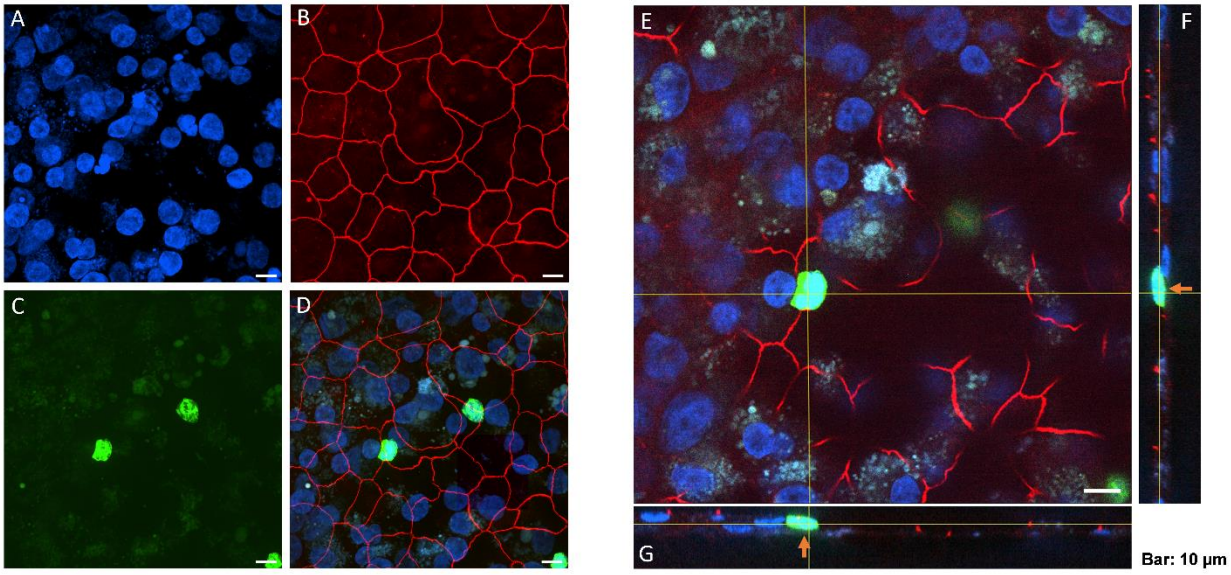

Figure 5.11. Representative confocal microscopy images of PMNs transmigrating across a monolayer of NhBE cells.

Transmigration was induced with 100 nM fMLF. Maximum fluorescence intensity Z-projections of (A) DAPI, (B) ZO1, and (C) CellTracker staining of PMNs. (D) Overlay of the previous three fluorescence channels. (E) Enlarged Z-plane with all channels overlayed. (F) YZ orthogonal view of overlay image, a neutrophil transmigrating through the monolayer as highlighted by the orange arrows (G) XZ orthogonal view of overlay image showing neutrophils transmigrating through the monolayer as highlighted by the yellow lines and orange arrows. Scale bar: 10 µm.

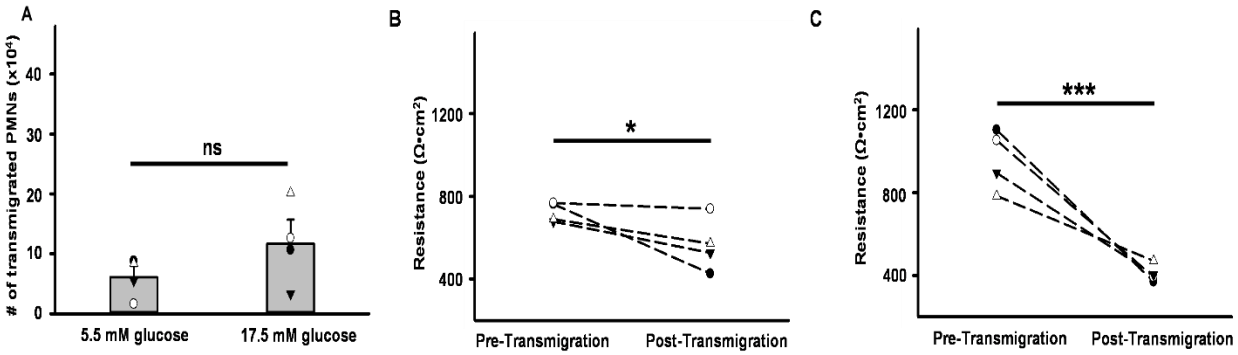

Figure 5.12. CFhBE cells seeded and cultured at air-liquid interface (ALI) with E-ALI media (5.5 mM glucose) on the undersurface of Transwells.

After differentiation, half of the Transwells were continually maintained in E-ALI/5.5 mM glucose and the other half were switched to E-ALI/17.5 mM glucose for 2 weeks. PMN transmigration across NhBE monolayers was induced by 100 nM fMLF. (A) The number of transmigrated PMNs across E-ALI/17.5 mM glucose was low and no significant different from that of E-ALI/5.5 mM glucose. The post-transmigration resistances were significantly lower compared to the pre-transmigration in both the E-ALI/5.5 mM glucose group (B) and the E-ALI/17.5 mM glucose group (C) (n=4 for each group; * $P < 0.05$, *** $P < 0.001$, ns=no significant difference).

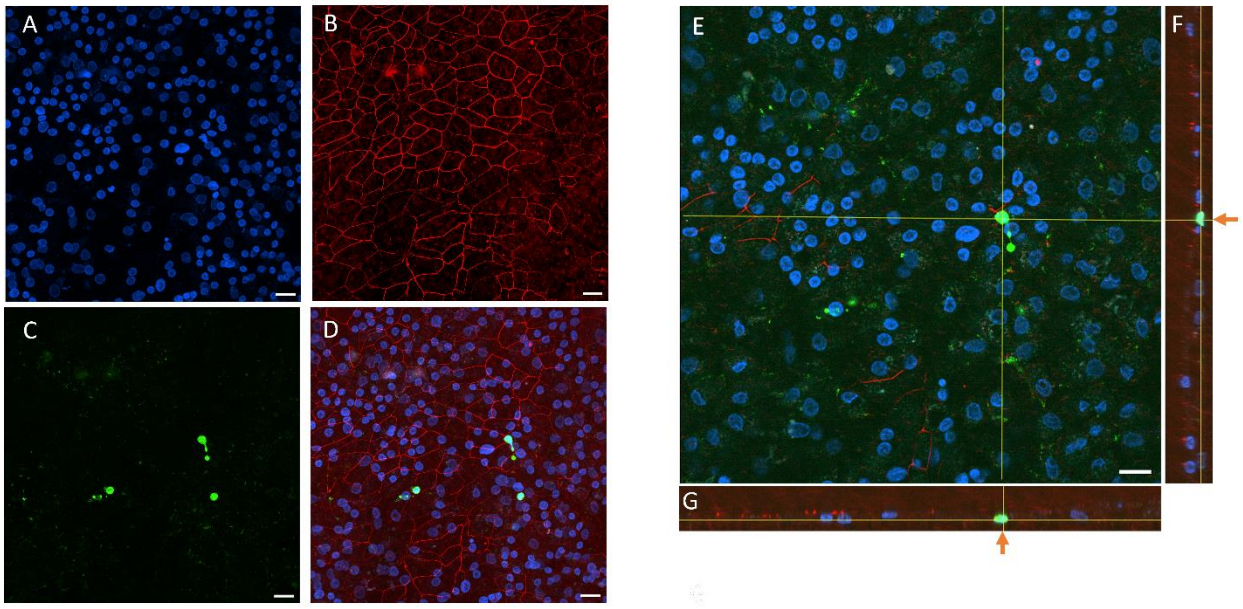

Figure 5.13. Representative confocal microscopy images of PMNs transmigrating across a monolayer of CFhBE cells.

Transmigration was induced with 100 nM fMLF. Maximum fluorescence intensity Z-projections of (A) DAPI, (B) ZO-1, and (C) CellTracker staining of PMNs. (D) Overlay of the previous three fluorescence channels. (E) Enlarged Z-plane with all channels overlayed. (F) YZ orthogonal view of overlay image, a neutrophil transmigrating through the monolayer as highlighted by the orange arrows (G) XZ orthogonal view of overlay image showing neutrophils transmigrating through the monolayer as highlighted by the yellow lines and orange arrows. Scale bar: 10 µm.

5.4. Discussion

A pathological hallmark of the CF chronic inflammatory response is the massive neutrophil influx into the airways which is associated with epithelial injury. In addition, CF PMNs do not function efficiently to clear bacterial infections. The vicious cycle correlates to ongoing disease progression in CF patients' lungs, especially for CFRD patients[90,98,216]. Here, we established a model to study neutrophil transmigration across bronchial epithelial cell monolayers (expressing WT and ΔF508-CFTR) that were conditioned to NG or HG culture conditions. Our data suggest that healthy PMNs transmigrated across tight junctions formed by epithelial monolayers in a manner that is modulated by glucose conditioning. PMN transmigration across ΔF508 cell monolayers exhibited noteworthy differences from across WT cell monolayers. In addition, the transmigrated PMNs displayed unique morphology compared to naïve PMNs and PMNs transmigrated across empty wells with collagen coating only.

It is well known that pulmonary complications in type I and type II diabetes patients arise late in the disease process compared to other organs, such as the kidneys and the eyes[85]. This suggest that the lungs of diabetes patients without CF can well tolerate systemic hyperglycemia. In contrast, hyperglycemia in CF patients (CFRD) leads to faster lung function decline, possibly due to intolerance to the challenge of systemic hyperglycemia[91]. Our data presented here well matched the clinical findings in that both 16HBE-WT and NhBE cells better resisted the HG challenge and efficiently facilitate transmigration PMN. Furthermore, both 16HBE-ΔF508 and CFhBE cells failed to tolerate the HG challenge, which led to insufficiency in PMN transmigration. The data are supported by our previous findings that normal bronchial epithelial cells well adapted to HG conditioning but not CF epithelial cells (Chapter 2). However, we point out that the results for immortalized vs primary cells were not identical in the study. The differences could be due to

multiple reasons, including: (a) cell autonomous characteristics, such as the origins of 16HBE cells and primary cells are different. In addition, primary cells contain multiple different cell types after differentiation compared to 16HBE cells that exhibit less variability[263]. (2) The media for NhBE and CFhBE cells contain many ingredients that do not exist in the media for 16HBE cells[131,263]. (3) 16HBE cells were cultured on Transwells for 8 to 9 days while primary cells were cultured for 4 weeks to 4.5 weeks. (4) HG conditioning duration was about 14 days for primary cells while only 6 to 7 days for 16HBE cells. Therefore, it is reasonable and not surprising to detect some differences in results between different experimental model systems. This observation highlights the importance of using different systems for verifying findings.

The data presented here suggest that epithelial barrier plays an active role in facilitating neutrophil migration across the monolayer and hyperglycemic conditioning of bronchial epithelial cells modulates neutrophil transmigration. In addition, we have reported that CF epithelial cells exhibit weak barrier functions compared to normal epithelia, and that hyperglycemia also led to further dysregulation of tight junctions[126,235]. We further showed that several tight junction proteins are dynamically trafficked in and out of the peripheral plasma membrane at zones contributing to tight junction function, in a manner modulated by hyperglycemia; for example, claudin 4 (Chapter 2). Similarly, we showed here that in normal epithelia, hyperglycemia enhanced the productive epithelial cell-PMN interactions to facilitate PMN transmigration while maintaining tight junction integrity exhibited by a mild drop resistance at the beginning of transmigration and high resistance maintained to the end of the transmigration. While CF epithelia exhibited sub-optimal contribution to facilitating neutrophil transmigration with a less effective epithelial cell-PMN interaction and inability to maintain tight junction integrity, exhibited by a large decrease in resistance at the beginning of transmigration and low resistance maintained to the end of the transmigration. There

are more than thirty different proteins involved in tight junction formation in airway epithelial monolayers. Little is known thus far regarding the possible interactions between tight junction proteins and PMN proteins in regulating the migration process in physiological as well as pathophysiological conditions[127,242]. The proteins contributing to the epithelial tight junctions that serve as the key determinants involving in PMN transmigration may serve as therapeutic targets to regulate the relentless recruitment of PMNs in the CF lung and thereby dampen lung damage.

The primary function for neutrophils to travel from vascular to luminal spaces in different epithelial-lined organs, such as intestine and lungs, is to efficiently bind, engulf, and kill microorganisms by phagocytosis, degranulation, generation of reactive oxygen species, and formation of neutrophil extracellular traps called NETosis[274]. There are three types of NETs identified depending on the morphologic changes in neutrophils: Suicidal NETs, Vital NETs, and Mitochondrial NETs[273,275,276]. Unlike neutrophils from healthy control, neutrophils from the blood of CF patients exhibit a prematurely primed basal state[277]. In addition, neutrophils from CF airways driven by the chemoattractants from the host and varied resources, including bacteria, from blood to the lung exhibited the aberrant immune programming and do not fulfill optimally their role in the lung[46,277,278]. Furthermore, the possible effects of systemic hyperglycemia on neutrophils in blood and consequently the neutrophils in airway of CFRD patients remain unknown.

5.5. Conclusion and Future Directions

We studied PMN transmigration across WT and CF bronchial epithelia conditioned to NG or HG media, with the goal of studying the mechanisms involved in modulating PMN transepithelial migration. Future studies will also use PMNs from CF carriers and pwCF, with and without CFRD, to test whether PMN genotype influences the mechanisms driving transmigration. The effects of hyperglycemia on inducing the neutrophil GRIM phenotype will also be studied.

Chapter 6 – Understanding CFTR function and CFRD pathophysiology through additional projects

6.1. CFTR immunoprecipitation and immunoblotting

6.1.1. Background

There are many immortalized airway epithelial cell lines available used to study airway physiology. We were considering using NCI-H441 cells because they can be grown at air-liquid interface (ALI)[279], which is a requirement to use our programmable automated cell culture system discussed in Chapter 3. H441 cells were derived from the pericardial fluid of a patient with lung adenocarcinoma in 1982[280]. However, based on Ussing Chamber data (**Figure 6.1**), there were some concerns about whether these cells express functional CFTR which agreed with previous reports[281]. Thus, I conducted CFTR immunoprecipitation and immunoblotting to check.

6.1.2. Methods

Cells were plated on Corning 3470 Transwells at a density of 80,000 cells per well at liquid-liquid interface. Cells were put at ALI the next day. Media was changed on Mondays, Wednesdays, and Fridays. Cells were grown with either RPMI with 10% FBS and 1X Pen/Strep or with DMEM-F12 with 1X Pen/Strep and a 1:50 dilution of UltroserG for 14-21 days after being put at ALI. Short-circuit current experiments were performed using an Ussing chamber as previously described in Chapter 2. Normal chloride buffer was used on the basolateral side, while low chloride buffer was used on the apical side. Chambers were bubbled with 95:5% O_2:CO_2 and maintained at 37°C during experiments. Cells in the Ussing chambers were stabilized for 30 min prior to treatment to inhibit or activate channel pathways. Cells were treated with 20 μM amiloride added to the apical side to inhibit ENaC-mediated sodium currents, 10 μM forskolin added to the apical and basolateral sides to activate CFTR currents, and 10 μM INH172 subsequently added to the apical side to inhibit CFTR.

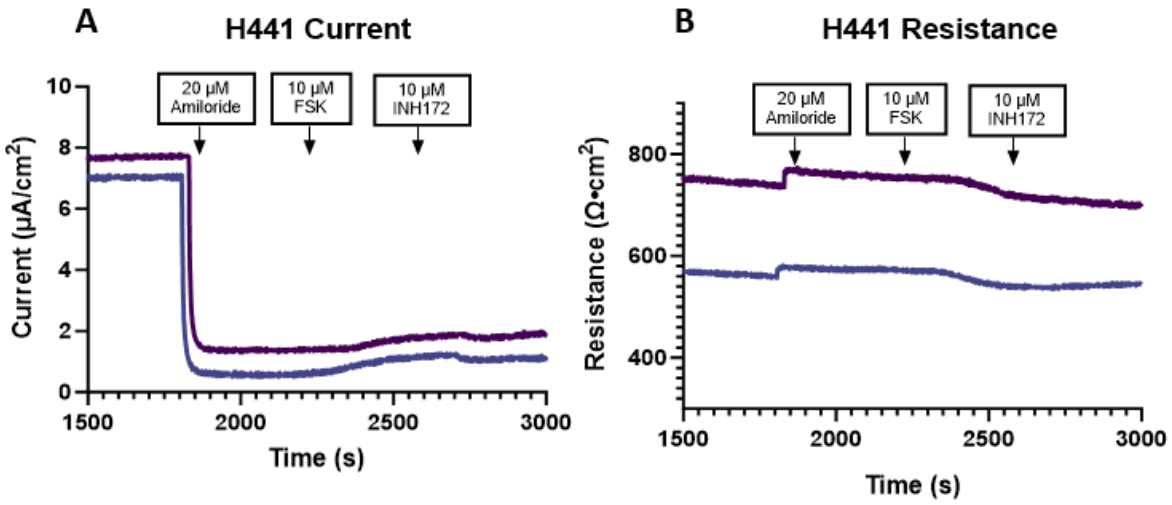

Figure 6.1. Ussing chamber recordings of H441 cells show little to no functional CFTR expression.

(A) Representative current traces of H441 cells. (B) Representative resistance measurements of H441 cells. Small molecules added are labeled at the time points added. Only 2 representative Transwells shown (N=12 Transwells).

After Ussing chamber recordings were completed, cells were washed once with 1XPBS. Cells were scraped and frozen for CFTR immunoprecipitation and immunoblotting. Binding beads (Pierce™ Protein A/G Magnetic Beads, ThermoFisher) were washed with 1X PBS and incubated with 2 μg of anti-CFTR 24-1 (VWR) at 4°C for 1 hour. Cells were thawed on ice and resuspended in 300 μL of lysis buffer containing RIPA (w/3mM EDTA), 1:100 protease inhibitor (1:100 PI specific for CFTR + 1:100 benzophenone). Cells were incubated in the lysis buffer for 30 minutes, followed by a 5-minute centrifugation at 5000g to pellet the nuclei. The supernatant was then transferred to the bead tubes. The cell lysate with antibody/beads mix was incubated at 4°C overnight with rotation. Beads were span down at 1000g for 1 minute and the supernatant was removed. Beads were washed three times with 1X PBS, and then 30 μL 2X Sample Buffer with DTT in PBS was added to the beads. Beads were incubated in sample buffer at 37°C for 30 minutes. This should release bound CFTR to the supernatant. Beads were then span down and the supernatant was transferred to a new tube. Gels (BioRad precast gels, 10-well, 50 uL, 4-15%) were loaded with 25 μL of sample per well. The gel was run for 45 minutes at 150V. Western blotting was then performed using a nitrocellulose membrane (BioRad, 1620213) transfer protocol of 120 mA for 2 hours on ice. Total protein was stained with Ponceau stain (ThermoFisher). The membrane was blocked with Intercept Licor Block for 1 hour at room temperature, and then incubated with CFTR 596 (1:1500, UNC) antibody overnight at 4°C in PBST (PBS+0.01% Tween 20). The membrane was washed three times with PBST for 15 minutes each time, and then incubated with goat anti-mouse 680 (GM 680) Licor secondary antibody at a 1:10,000 dilution in in Licor Block + 0.01% Tween 20. The membrane was washed three times with PBST for 15 minutes each time and imaged. As a positive control, CFTR present in the lysate from 16HBE WT cells was also immunoprecipitated and loaded in parallel.

6.1.3. Results and discussion

Results show little to no CFTR expression in H441 cells cultured with either RPMI or DMEM-F12 with UltroserG, compared to results obtained from the lysate of 16HBE WT cells (**Figure 6.2**). This suggests that NC1-H441 cells do not express functional CFTR regardless of culture conditions. Caution needs to be employed when using these cells for CF related research. Interestingly, these cells do form good tight junctions as evident from resistance measurements seen on Ussing chamber recordings. These cells might still be useful when studying interventions that might impact barrier integrity. Further, functional epithelial sodium channel (ENaC) was detected by Ussing chamber in these cells (**Figure 6.1**), as measured by current changes after the addition of 20μM Amiloride. These cells might still be useful when studying interventions that might impact ENaC function.

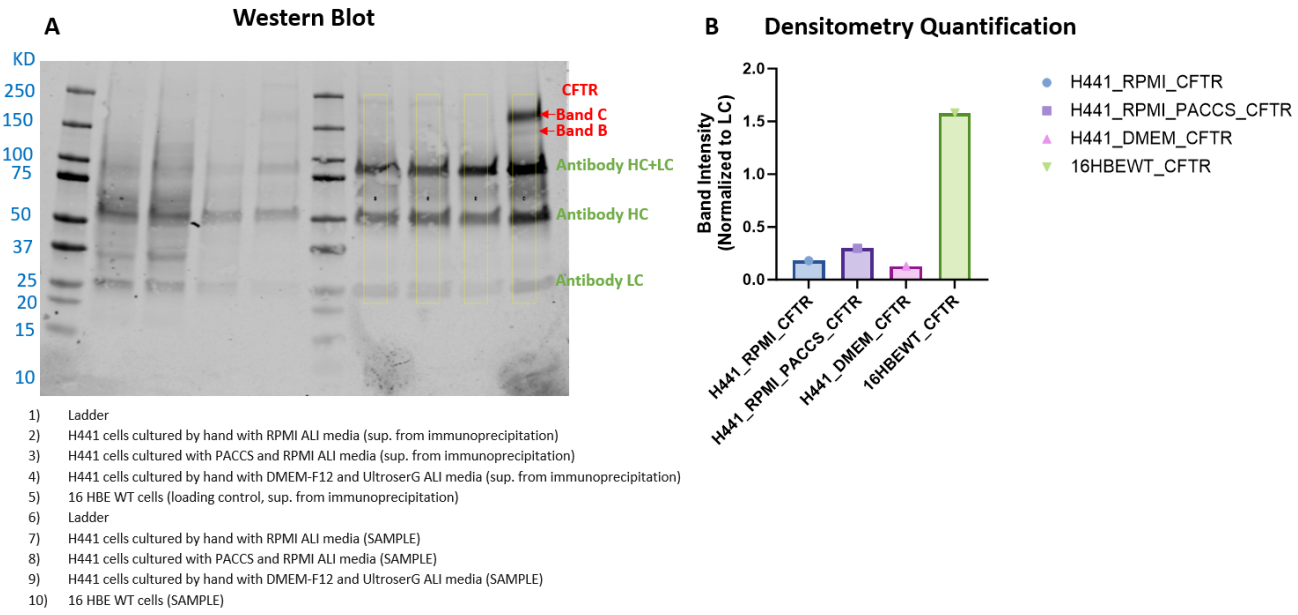

Figure 6.2. Western blot of H441 lysates show little to no CFTR protein in H441 cells regardless of culture conditions.

(A) Western blot image highlighting the absence of band C (~160kDa) and band B (~130kDa) CFTR in H441 cells. Band B is the core-glycosylated form of CFTR present in the endoplasmic reticulum, while band C is the mature and fully processed CFTR protein which has passed through the Golgi. Lanes 2-5 were loaded with the immunoprecipitation supernatant as a control. We expected to see little to no CFTR in these lanes. Lanes 7-10 were loaded with samples resulting from the immunoprecipitation protocol. Concentrated CFTR was expected to be seen on these lanes. The last lane is the positive control, which shows CFTR immunoprecipitated from 16HBEWT samples. (B) Densitometry quantification of lanes 7-10, normalized to band intensity for antibody light chain (LC) present at ~25kDa, showing little to no CFTR detected in lanes 7-9.

6.2. CFTR mutagenesis

Preface

The background information section has been modified from the rotation report of another Molecular and System's Pharmacology student, Lester Manly. I performed CFTR mutagenesis for his project.

6.2.1. Background

CFTR is a member of the ATP-binding cassette superfamily, in which anion permeation is facilitated by the coupling of ATP hydrolysis at the nucleotide binding domains (NBDs) and the channel gating function of the transmembrane domains (TMDs)[282,283]. One of the unique structural features of CFTR lies within transmembrane helix 8 (TM8) within TMD2. TM8 is the only discontinuous transmembrane element with a helix-loop-helix structure instead of a continuous helix structure. The loop break of TM8, sometimes referred to as the "TM8 kink", is located within the plasma membrane[284]. It is hypothesized that TM8 is implicated with the hinging movement of channel opening and closing, and that its loop may interact with ligands based on computational modeling[285–288]. However, the functional role of the TM8 kink is still unknown. To evaluate the functional role of the TM8 kink, there is a salt-bridge interaction between TM7 and TM8, E873-R933 respectively, which could play a role in modulating CFTR pore behavior. We hypothesize that destabilization of the E873-R933 salt-bridge alters CFTR pore behavior. I created human CFTR (hCFTR) mutants with either E873A or R933A substitutions to cause disruption of the salt-bridge interaction. A double mutation variant, E873R and R933E, was also included to test if charge swapping could influence pore behavior (**Table 6.1**). These constructs can be used to make hCFTR cRNA for electrophysiology studies, such as two electrode voltage clamp (TEVC) of *Xenopus laevis* oocytes injected to express the mutant hCFTR cRNAs.

Table 6.1. Plasmid ID names and corresponding mutations introduced in the human CFTR sequence.

Plasmid ID	Mutation
PCF 601	E873A
PCF 602	R933A
PCF 603	E873R
PCF 604	E873R/R933E

6.2.2. Protocol

Plasmid PCF98 from the McCarty Lab expresses wild-type human CFTR using a pGEM-HE vector. This plasmid was used to generate PCF440, which was modified with eGFP attached at extracellular loop 4 at position 901. I used the Q5® Site-Directed Mutagenesis Kit (Qiagen) to introduce the desired mutations using PCF440 as a starting plasmid. The PCR reactions consisted of 25µL of Q5 master mix, 2.5 µL of forward primer (10 µM stock), 2.5 µL of reverse primer (10µM stock), 15 µL of nucleotide free water, and 5 µL of template plasmid DNA (PCF440, 5ng/µL). Primer sequences are shown on **Table 6.2**. The PCR run protocol is shown on **Table 6.3**. The resulting DNA was then transformed into bacteria for cloning utilizing XL10-Gold Ultracompetent Cells (Agilent), which were then plated onto Luria Broth (LB) media plates with ampicillin (75 µg/ml) for selective pressuring. Bacterial plasmid DNA constructs were then isolated using ZymoPURE Plasmid Miniprep Kit (Zymo). All the constructs were verified by Sanger Sequencing across the entire open reading frame (GeneWiz). Quality control of isolated DNA plasmids were performed on DNA gels to check DNA integrity. Plasmid purity and concentrations were then quantified via NanoDrop® ND-1000 spectrophotometer (ThermoFisher).

6.2.3. Results and discussion

After PCR was completed, DNA gels were loaded to check for single band amplification (**Figure 6.3**). After DPNI digestion, the DNA was transformed using competent bacterial cells and plated on LB plates using ampicillin as a selection agent. DNA was isolated and sequenced, confirming the desired single point mutations. DNA was prepped in large quantities and is ready to be used for future electrophysiology experiments. Initial experiments were conducted by Lester Manly during a rotation in the McCarty Lab in the fall of 2022.

Table 6.2. Primer sequences used to create the CFTR mutants.

The primers utilized for the mutations were:	
hCFTR/eGFP E873A (forward)	5’ GCTTAGTAATTTTTCTGGCAGCGGTGGCTGC 3’
hCFTR/eGFP E873A (reverse)	5’ GCAGCCACCGCTGCCAGAAAAATTACTAAG C 3’
hCFTR/eGFP R933A (forward)	5’ GGGATTCTTCGCAGGTCTACCACTGGTGC 3’
hCFTR/eGFP R933A (reverse)	5’ GCACCAGTGGTAGACCTGCGAAGAATCCC 3’
hCFTR/eGFP E873R (forward)	5’ GCTTAGTAATTTTTCTGGCACGGGTGGCTGC 3’
hCFTR/eGFP E873R (reverse)	5’ GCAGCCACCCGTGCCAGAAAAATTACTAAG C 3’
hCFTR/eGFP R933E (forward)	5’ GGGATTCTTCGAAGGTCTACCACTGGTGC 3’
hCFTR/eGFP R933E (reverse)	5’ GCACCAGTGGTAGACCTTCGAAGAATCCC 3’

Table 6.3. PCR protocol used to introduce the single point mutations.

Step 1:	95°C for 2 minutes
Step 2:	95°C for 30 seconds
Step 3:	58°C for 20 seconds
Step 4:	72°C for 6 minutes
Step 5:	Repeat steps 2-4 x25
Step 6:	4°C infinite hold

Lanes
1. Ladder
2. PCF 601 (hCFTR E873A) – PCR4
3. PCF 602 (hCFTR R933A) – PCR4
4. PCF 603 (hCFTR E873R) – PCR4
5. PCF 440 (Control) ~5 ng (same as PCR loaded)
6. PCF 601 (hCFTR E873A) – PCR4 - DPN1 Digested
7. PCF 602 (hCFTR R933A) – PCR4 - DPN1 Digested
8. PCF 603 (hCFTR E873R) – PCR4 - DPN1 Digested
9. PCF 440 (Control) ~5 ng
10. Ladder

Figure 6.3. DNA gel highlighting the amplification of a single product after PCR-based mutagenesis.

Lanes 2-4 show amplified product before *DpnI* digestion. Lane 5 serves as a control. Lanes 6-8 show amplified product after *DpnI* digestion. Lane 9 serves as a control. Ladder is shown on lanes 1 and 10. Molecular weight is labeled on the left in base pair (bp) units. Note that PCF 603 was used as the base plasmid to generate the double mutant PCF 604.

6.3. Airway epithelial and bacterial co-culture experiments

6.3.1. Background

Lung function decline in patients with CFRD is six-fold higher compared to CF patients with normal glycemic control[84,90]. Rapid lung function declined experienced by CFRD patients could be explained by dysfunction of glucose barrier components, which would cause elevated levels of glucose to leak to the airways[40,125]. Opportunistic pathogens present in the airways, such as PAO1 and SA, could then take advantage of this increase in nutrient availability to proliferate and/or change their gene expression causing damage to the airways[8,89].

We hypothesize that CF cells cultured under hyperglycemic conditions would allow for more glucose to leak from the basolateral to the apical side of the Transwell. Bacterial cells would then have access to the glucose that leaked to the apical surface and could use it as an energy source for growth. Greater glucose leak to the apical side of Transwells could then be detected as higher levels of bacterial growth through serial dilutions, plating, and CFU counting.

6.3.2. Methods

The model pathogen used was a strain of SA that does not produce alpha-toxin, and thus should not be harmful to mammalian cells during culture. Briefly, 16HBE cells were cultured on Transwells (Corning 3460) at a seeding density of 250,000 cells per well at liquid-liquid interface. Two days after seeding, the Transwells were conditioned with either normal or high glucose media (5.5 mM or 17.5 mM glucose, respectively) for 5 days. The day before bacterial challenge, Transwells were washed once with 1XPBS. The apical media was replaced with CF sputum-like media (SCFM1) with low glucose (0.5 mM glucose), and the basolateral media was replaced with either normal or high glucose antibiotic free media. Bacteria was grown overnight in LB. The next day, bacteria was diluted to 0.5OD in SCFM1 with low glucose and incubated on a shaker for 1

hour. The OD was measured, and a 0.05 OD dilution was made. The apical and basolateral media on the Transwell was removed, and the basolateral media was replaced with fresh antibiotic-free normal or high glucose media. On the apical side, Transwells were challenged with bacterial suspended in SCFM1 with low glucose (7 µL of the 0.05 OD dilution plus 183 µL of SCFM1 low glucose added per well). The plates were placed in a cell culture incubator at 37°C for 24 hours. The apical fluid was then transferred to a microcentrifuge. SCFM1 (low glucose) containing 0.1% Triton X was then added to the apical surface. Cells were gently scraped and transfer to their corresponding microcentrifuge tubes. Tubes were then vortexed vigorously for 1 minute to lyse open mammalian cells. Serial dilutions were performed for bacterial platting and counting.

6.3.3. Results and discussion

We have successfully simulated bacterial infections *in vitro* using WT and ΔF508 16HBE cells as model mammalian cell lines. Results from preliminary experiments shown that, consistent with our expectations, 16HBE cells expressing ΔF508 CFTR had elevated levels of bacterial growth on their apical surface when cultured with basolateral high glucose media. This suggests that the barrier integrity of CF cells is compromised, allowing for greater flux of glucose to the apical surface and allowing for greater bacterial growth.

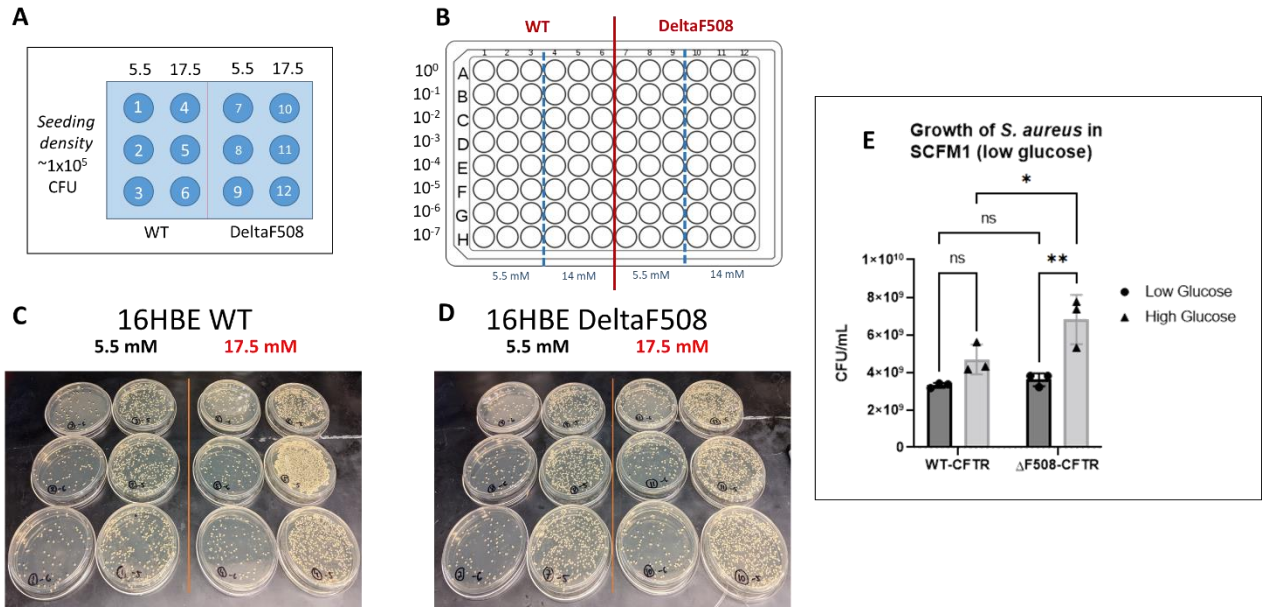

Figure 6.4. Co-culture of 16HBE cells with SA shows increased bacterial growth in the CF hyperglycemic group.

(A) Representative plate layout used to run experiments. (B) Sample collection and serial dilution diagram used to measure bacterial growth. (C) Bacterial dilution plates used to measure growth when exposed to16HBE WT cells conditioned with normal glucose (5.5 mM) or high glucose (17.5 mM). Bacterial growth was measured 24 hours from the start of the experiment. (E) Bacterial growth quantification. Statistics: Two-way ANOVA for multiple comparisons, Tukey corrected (* $p<0.05$, ** $p<0.01$) (N=3).

6.4. Development of the Neutrafluor assay to study live neutrophil transmigration *in vitro*

Preface

This work was done in collaboration with Jonathan Dudkin, an undergraduate student from Mercer University. My primary contributions were assay optimization and image collection. I also assisted with the 3D design of the novel Transwell holder. Results are preliminary and the assay is still being optimized.

6.4.1. Introduction

Cystic fibrosis is an autosomal recessive disease caused by mutations in the cystic fibrosis transmembrane conductance regulator (CFTR) gene[1]. The CFTR protein is a transmembrane protein that allows for the movement of chloride ions outside of cells. This process is essential to maintain water homeostasis throughout the body[5]. CF is a multi-organ disease; however, its leading cause of mortality is respiratory failure. The lungs are particularly susceptible to CFTR dysfunction. The airways are covered by a thin mucus layer, which traps pathogens and other harmful substances for clearance out of the lungs. CFTR dysfunction causes the mucus layer converting the airways to become dehydrated, causing aggregation and mucus plugging[6]. Impaired mucus clearance creates an ideal environment for recurrent bacterial infections to take place[8]. Periods of bacterial overgrowth are called pulmonary exacerbations, and they cause lung tissue damage contributing to the lung function decline seen in CF airway disease[9].

CF airway disease is further worsened by Cystic Fibrosis Related Diabetes (CFRD), the most common CF co-morbidity which affects around half of CF patients by adulthood[79]. Patients with CFRD experience a faster rate of lung function decline compared to non-diabetic CF patients[84]. Research shows that insulin signaling and epithelial barrier integrity is compromised in

CF epithelial cells, leading to increased paracellular flux of solutes. Insulin signaling and barrier integrity is further compromised in the context of CFRD[126].

CF airway disease is also characterized by aberrant neutrophilic infiltration, promoting further inflammation and lung tissue damage in CF[46,47]. It is unclear whether neutrophilic infiltration is worsened by CFRD. Decreasing neutrophil infiltration is one of the main challenges that remains to be addressed in the field. Little is known about how neutrophils transmigrate across epithelial cells and how they impact barrier function.

A multitude of methods have been developed to explore epithelial junctions and their integrity. To measure intensity, assays such as dextran and calcein flow assays, or TER measurements can be employed[103]. While these assays do provide meaningful results, they can only do so regarding the epithelial layer as a whole, quantifying junction integrity on a global scale. On the other hand, assays such as sandwich assays and biotinylation assays allow for inspection of junction integrity on a local level, but only for fixed time points. Recently, a newly published paper described a method by which live local junction integrity could be monitored in an epithelial layer, called the ZnUMBA assay[289].

In order to observe neutrophil and epithelial cell behavior at a local and dynamic level, the recently developed ZnUMBA assay[289] was integrated into a neutrophil transmigration. By utilizing zinc on the apical side of the monolayer, and a fluorescent zinc reporter on the basal side, one can measure the intensity of the fluorescent reporter at the cell layer. Doing so describes the flux/contact of the zinc and reporter, which inversely correlates with junction integrity. Using this assay during a transmigration would allow for quantification and collection of not only the number of neutrophils that transmigrate through an epithelial barrier over a period of time, but also for analysis of localization and impact on junction integrity of transmigrations that occur.

6.4.2. Methods

Cell Culture

16 HBE 14o- Human Bronchial epithelial cells expressing either WT or ΔF508 CFTR were cultured in MEM (Gibco 11095-072), 10%FBS (R&D, S11150H), and 1% Penicillin/Streptomycin (Pen/Strep, Gibco 15070-063) at 37°C. Cells were then grown on inverted Transwells (Corning, 3402) as described in Chapter 5 of this dissertation.

Neutrophil Purification

Healthy human blood neutrophils were purified using Polymorphprep (PMP) according to the company's manual and recommendations from the Tirouvanziam lab (Dobosh B et al, Cell press 2021). In brief, blood was drawn into EDTA tubes, blood was added on top of the PMP, and samples were centrifuged at 400g for 42 minutes at room temperature. The neutrophil band was collected and centrifuged at 800g for 5-10 minutes, and the pellet was resuspended for 30 seconds with ice-cold sterile water to lyse red blood cells. Osmolality was quickly restored using an equal amount of cold 1.8% NaCl, and samples were centrifuged at 800g for 5-10 minutes. Neutrophils were resuspended with cold RPMI-1640, cell numbers were countered, and neutrophils were maintained on ice until needed. Neutrophils were added on the apical side of Transwells at a density of 100,000 per well for Transmigration. Imaging took place 2 hours after the transmigration was started.

Neutrafluor Imaging Chamber

An imaging chamber was designed to hold Transwells in place while performing confocal microscopy. Design iterations were made using Fusion 360 (AutoDESK). Design iterations were printed at Emory's "Tech Lab". STL files were printed using a Prusa MK4 printer with polylactic acid (PLA) filament.

Neutrafluor Assay

An apical (2mM $ZnCl_2$, 100nM fMLF) solution and a basolateral solution (20uM Fluozin-3 (Thermofisher F24194), 2uM Ca-EDTA) were prepared. Extracted neutrophils were stained with CellTracker Blue (Thermofisher CMAC 2210), and the epithelial layer was stained with CellMask Deep Red (Thermofisher C10046). Inverted Transwell cultures were incubated at 37°C with neutrophils added basally for 1 hour. Transwells were moved so RPMI + Zinc would replace the apical solution, and 200 µl of Fluozin-3/Ca-EDTA solution added basally. Cells were incubated for another 30 minutes, and then Transwells were placed in the Neutrafluor imaging chamber, which was then viewed using a Nikon CSU-W1 SoRa Spinning Disk confocal microscope.

6.4.3. Results

A novel Transwell holder was designed to visualize transmigrating neutrophils in real time

There are no commercially available microscopy holders that could be used for our applications. Thus, we designed and 3D-printed a novel Transwell holder. Our design is shown on **Figure 6.5**. The design has two main components: a slide and a cylindrical chamber. The slide resembles the dimensions of a regular microscope slide, but it incorporates a square-shaped insert section in the middle to accommodate a thin coverslip. The cylindrical chamber was designed to hold the Transwell in place at a slight elevation to avoid friction between the epithelial cells cultured at the base of the Transwell and the coverslip. The distance is small enough to allow for an appropriate working distance for confocal imaging. The cylindrical chamber is manually attached to a coverslip using clear nail polish to make the chamber watertight.

The Neutrafluor assay allows to observe live neutrophils transmigrate through airway epithelial cell monolayers *in vitro*, and could be used to assess focal disruptions of tight junctions integrity on the epithelial barrier

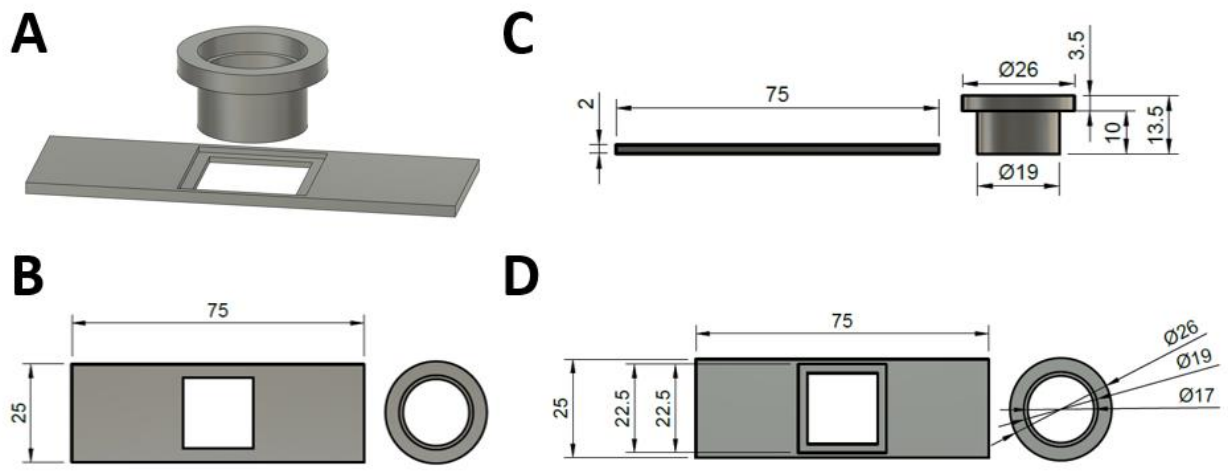

Figure 6.5. Design of our novel Transwell holder for confocal microscopy.

A) Graphical 3D representation of the holder showing its two main components: A slide and the cylindrical holder. The slide has an insert section that fits a square thin coverslip. The cylindrical chamber is attached to the coverslip to create a watertight chamber. It can hold the Transwell in place without touching the coverslip for imaging. B) Top view of the holder components highlighting the outside dimensions of the slide. C) Side view of the slide and cylindrical chambers showing their dimensions. D) Another top view of design providing more detailed measurements of the inner dimensions of the slide and the cylindrical chamber. Note: Measurements shown in millimeters.

To study the dynamics of transmigration of individual neutrophils, we adapted an optical method developed by the Miller lab that uses a zinc-sensitive fluorophore, Fluozin, to study barrier repair[289]. Zinc is used in the media bathing the apical side of the monolayer while Fluozin is added to the basolateral side. Our adaptation enables this method to be used to detect barrier breaches induced by transmigration of individual neutrophils, which appear as regions of more intense green fluorescence signal. To track the location of neutrophils, PMNs were stained with CellTracker blue. To track the location of epithelial cell boundaries, plasma membranes were stained using CellMask magenta. Example images of neutrophils transmigrating across epithelial cell monolayers are shown on **Figure 6.6**.

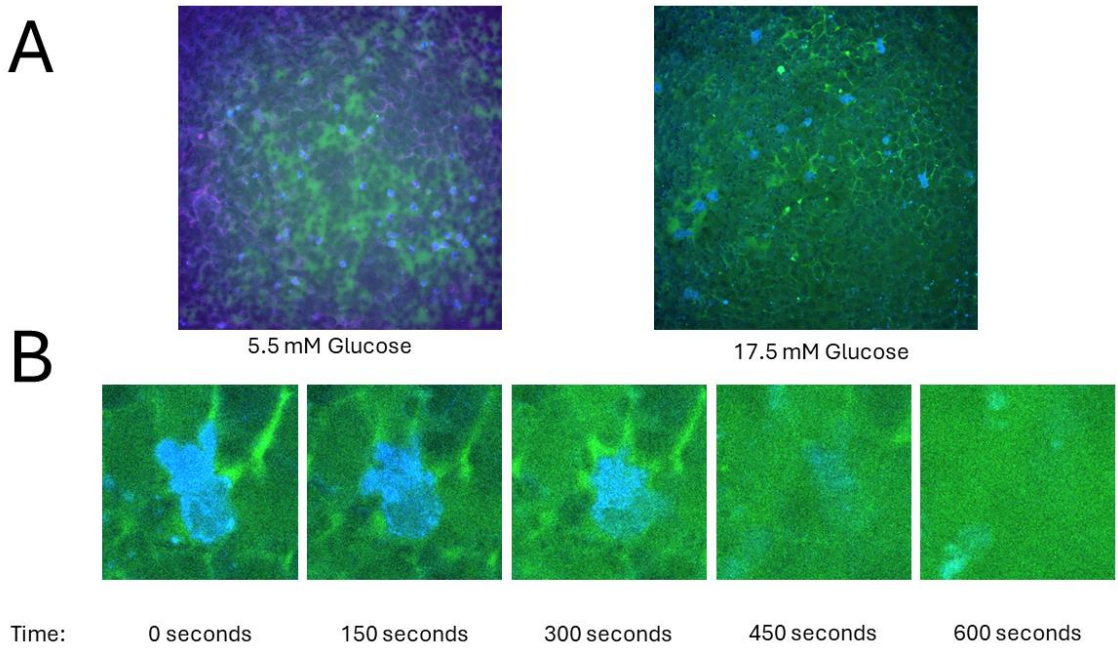

Figure 6.6. Example neutrophil transmigration images through 5.5 mM and 17.5 mM glucose conditioned 16HBE WT monolayers.

A) Comparison of the first frame taken from epithelial cells cultured with either 5.5 mM or 17.5 mM glucose during our Neutrafluor assay. Neutrophils are shown in blue, Zinc/Fluozin interactions are shown in green, and cell membranes are shown in magenta. The magenta channel is only displayed in the 5.5 mM glucose sample to provide an example of cell membrane staining. B) Time lapse of 10 minutes tracking the transmigration of a single neutrophil using the Neutrafluor assay (N=1).

6.4.4. Conclusions and Future Directions

Neutrophilic infiltration and over-activation are hallmarks of CF airway disease[46,47]. However, little is known about the mechanisms that drive neutrophil transmigration across airway epithelial cell monolayers. Further, it is unknown whether patients with CFRD experience higher rates of neutrophil transmigration, although this could explain their worsened pulmonary outcomes. To address these gaps in knowledge, we have developed a novel assay called Neutrafluor to gain a better understanding about the mechanisms driving neutrophil transmigration across airway epithelial cells. So far, we have conducted proof of concept experiments that have shown that the assay can be successfully conducted to watch neutrophils transmigrate across airway epithelial cell monolayers in real time. We look forward to employing this assay to investigate several aspects related to neutrophil-epithelial transmigration.

In the future, we plan to employ our method to identify whether neutrophil transmigration kinetics differ between WT and CF cells, or between cells conditioned with normal or hyperglycemia. Our method could also be used to investigate whether neutrophils tend to use the same junctions for transmigration, where an actively transmigrating neutrophil alters the epithelial barrier to enable successive neutrophils to cross more easily. The method we have developed will also allow us to determine whether neutrophils preferentially transmigrate at tricellular or bicellular junctions. In the future, we will also be able to determine which cell types at present at the junctions preferred for transmigration.

Overall, our Neutrafluor assay is a powerful and novel tool to better understand many unknown aspects about neutrophil-epithelial transmigration and expand our knowledge about CF airway disease.

6.5. Comparing ATPase activity of ATP-binding cassette subfamily C member 4, lamprey CFTR, and human CFTR using Antimony-phosphomolybdate assay

Preface

This work[290] has been published in the journal "*Frontiers in Pharmacology*" in February 2024. I contributed with data analysis and manuscript review.

Citation

Cui, G.; Strickland, K. M.; **Vazquez Cegla, A. J**.; McCarty, N. A. Comparing ATPase Activity of ATP-Binding Cassette Subfamily C Member 4, Lamprey CFTR, and Human CFTR Using an Antimony-Phosphomolybdate Assay. *Front Pharmacol* **2024**, *15*, 1363456. https://doi.org/10.3389/fphar.2024.1363456.

6.5.1. Abstract

ATP-binding cassette (ABC) transporters use the hydrolysis of ATP to power the active transport of molecules, but paradoxically the cystic fibrosis transmembrane regulator (CFTR, ABCC7) forms an ion channel. We previously showed that ATP-binding cassette subfamily C member 4 (ABCC4) is the closest mammalian paralog to CFTR, compared to other ABC transporters. In addition, Lamprey CFTR (Lp-CFTR) is the oldest known CFTR ortholog and has unique structural and functional features compared to human CFTR (hCFTR). The availability of these evolutionarily distant orthologs gives us the opportunity to study the changes in ATPase activity that may be related to their disparate functions.

We utilized the baculovirus expression system with *Sf*9 insect cells and made use of the highly sensitive antimony-phosphomolybdate assay for testing the ATPase activity of human ABCC4 (hABCC4), Lp-CFTR, and hCFTR under similar experimental conditions. This assay measures the production of inorganic phosphate (P_i) in the nanomolar range.

Crude plasma membranes were purified, and protein concentration, determined semi-quantitatively, of hABCC4, Lp-CFTR, and hCFTR ranged from 0.01 to 0.36 μg/μL. No significant difference in expression level was found although hABCC4 trended toward the highest level. hABCC4 was activated by ATP with the equilibrium constant (K_d) 0.55 ± 0.28 mM (n = 8). Estimated maximum ATPase rate (V_{max}) for hABCC4 was about 0.2 nmol/μg/min when the protein was activated with 1 mM ATP at 37°C (n = 7). Estimated maximum ATPase rate for PKA-phosphorylated Lp-CFTR reached about half of hCFTR levels in the same conditions. V_{max} for both Lp-CFTR and hCFTR were significantly increased in high PKA conditions compared to low PKA conditions. Maximum intrinsic ATPase rate of hABCC4 in the absence of substrate was twice that of hCFTR when activated in 1 mM ATP.

The findings here suggest that while both ABCC4 and hCFTR bear one consensus and one degenerate ATPase site, the hCFTR exhibited a reduced intrinsic ATPase activity. In addition, ATPase activity in the CFTR lineage increased from Lp-CFTR to hCFTR. Finally, the studies pave the way to purify hABCC4, Lp-CFTR, and hCFTR from Sf9 cells for their structural investigation, including by cryo-EM, and for studies of evolution in the ABC transporter superfamily.

6.6. Discussion and Conclusions

The additional projects discussed in this section highlight additional approaches I have taken to understand CFTR function and CFRD pathophysiology. I conducted immunoblots and Ussing chamber to measure CFTR expression and function in airway epithelial cell membranes. Further, I conducted mutagenesis to better understand CFTR gating. To better understand CFRD pathophysiology, I conducted co-culture experiments with airway epithelial cells conditioned with normal or high glucose and challenged these monolayers with SA to measure overall bacterial growth. Further, I conducted neutrophil transmigration assays with live imaging to study differences in neutrophil transmigration kinetics between WT and CF cells conditioned with normal or high glucose. Taken together, these additional projects add depth to the breath of the work I conducted. Future studies will continue to use similar approaches to keep studying these mechanisms in depth.

Chapter 7 – Conclusions and Future Directions

We determined that hyperglycemia impairs barrier integrity in CF cells through dysregulation of essential tight junction proteins, and we developed a novel approach to study dysregulation of essential tight junction proteins. Our diabetic S*cnn1b*-Tg mouse model showed elevated glucose concentrations in the airway surface liquid, providing further evidence that the tight junction integrity of the airways is compromised under systemic hyperglycemia in CFRD-like conditions. This mouse model also showed elevated neutrophil counts in bronchoalveolar lavage fluid, even before bacterial challenge, suggesting that immune defects play a role in CFRD disease pathophysiology. We also developed novel approaches to mimic CFRD disease *in vitro*. The first was the creation and optimization of a programmable automated cell culture system (PACCS) to mimic blood glucose fluctuations experienced by CFRD patients throughout the day after meals. The second is a novel approach to study neutrophil transmigration across airway epithelial cells, which identified key differences in transmigration kinetics and neutrophil fate between WT and CF cells.

Immortalized cells were primarily used to study the effects of chronic hyperglycemic conditioning on airway epithelial barrier integrity. 16HBE cells expressing either WT or ΔF508 CFTR were tested. Dye flux experiments showed that paracellular flux of calcein (0.62 kDa) and dextran (10 KDa) was increased in CF cells in response to hyperglycemia and insulin conditioning (400 nM). This is concerning since exogenous insulin administration is the only current approved treatment for CFRD. However, our results suggest that insulin might further impair barrier integrity, via a variety of mechanisms. Further, electrophysiology results showed that insulin treatment did not interfere with CFTR rescue by ETI under normal or high glucose conditions. However, transepithelial resistance in CF cells treated with ETI was lower than controls even after

inactivation of ENaC and CFTR. This suggests that ETI treatment of CF cells induced changes in barrier integrity independent of CFTR and ENaC function.

Ours is the first group, to our knowledge, to observe that essential tight junction proteins, such as claudin-4 (CLDN4), are downregulated in CF cells compared to WT cells at the gene expression level even at normal glucose. We employed a novel confocal microscopy technique to assess CLDN4 protein localization and observed higher protein abundance at the periphery of CF cells in response to hyperglycemia. It is important to note that higher protein expression does not necessarily correlate with improved function or stronger barrier integrity. We think the opposite might be true, where too much CLDN4 protein trafficking to the junctions might interfere with the proper function of other essential tight junction proteins and compromise barrier integrity. Treatment with highly effective modulator therapy, ETI, brought tight-junction CLDN4 localization in CF cells cultured under hyperglycemia closer to WT levels. However, it did not completely reverse CLDN4 improper trafficking which suggests that ETI treatment might not be sufficient to counteract the negative effects of CFRD on barrier integrity. Future studies will focus on implementing the novel microscopy quantification technique I developed to measure TJ localization of other essential tight junction proteins. This technique could also be used to test the effects of future promising small molecules on TJ localization of essential barrier proteins.

Further research into changes in the transcriptome of CF vs WT cells under hyperglycemia by bulk RNA sequencing helped identify protein tyrosine phosphatase receptor type G (PTPRG) as a potential driver of CFRD pathophysiology. Expression of this gene was found to be elevated in CF cells under normal conditions and hyperglycemia compared to WT cells. Interestingly, PTPRG has been shown to inhibit Akt signaling, which is necessary for proper insulin signaling[142]. Aberrant insulin signaling has been shown by our group to compromise airway glucose uptake and

barrier integrity in CF cells[126]. Future studies could focus on testing the effects of knocking out PTPRG in CF cells. Barrier integrity studies could be conducted to test for transepithelial resistance and paracellular flux. Further, changes in the Akt signaling pathway could be investigated by immunoblot.

To further study the consequences of chronic hyperglycemia, our lab developed a novel *in vivo* mouse model to study the impact of CFRD on airway physiology. This model relies on the use of a transgenic mouse strain that overexpresses the epithelial sodium channel (ENaC) β subunit in the airway (S*cnn1b*-Tg), which causes them to exhibit a CF-like obstructive lung phenotype[111,173,174]. We demonstrated, for the first time to our knowledge, that chronic hyperglycemia in *Scnn1b*-Tg mice aggravates lung damage with increasing airway inflammation, neutrophilic infiltration, and lung tissue damage and remodeling. Lung histology data showed enhanced parenchymal destruction, alveolar wall thickening, and neutrophilic infiltration in S*cnn1b*-Tg diabetic mice compared to WT diabetic mice on the same genetic background, consistent with development of a spontaneous lung infection. Further, administration of intranasal PAO1 led to severe lung leukocytic infiltration over 24 hours. Overall, we showed that this novel mouse model can be successfully used to study CFRD-like negative effects in the airways using an *in vivo* setting. Future studies could use this model to test promising therapeutic agents to combat CFRD pathophysiology.

Besides developing a novel *in vivo* CFRD model, we also developed novel *in vitro* models to model CFRD pathophysiology. I created and optimized a programmable automated cell culture system (PACCS) which addresses an unmet need in the field. The way we traditionally culture airway epithelial cells *in vitro* is not physiologically relevant. Cells receive media with very high glucose concentration, which is progressively depleted until the next media change multiple days

later. Because of how quickly cells consume glucose and because cells on Transwells are cultured in chambers with small volumes, cells might even experience periods of hypoglycemia. Furthermore, increased glucose supply every other day is not consistent with the increases in blood glucose after each meal that CFRD patients experience, typically three times per day.

We did not know how the traditional cell culture protocol might negatively influence the results of our studies. Therefore, I decided to address this challenge by creating PACCS, which is capable of changing basolateral media multiple times a day to simulate blood glucose fluctuations experienced by CFRD patients after meals. Creating and optimizing the system required designing a custom 3D printed plate, which required several rounds of prototyping. Results showed that the system can be successfully used to culture airway epithelial cells while mimicking meal-like glucose fluctuations. TEER measurements were even higher when PACCS was used. I think this might be due to cells never leaving the incubator, which decreases external variables that might impact cell health such as changes in temperature and CO_2 levels. Future studies could use PACCS to introduce other agents present in the CF airways, such as cytokines and oxidants, using fluctuation patterns to better mimic human airway physiology.

We also developed another novel *in vitro* model to study neutrophil transmigration across airway epithelial monolayers. Increased neutrophil recruitment and over-activation are important drivers of CF lung disease[46,48]. However, little is known about how neutrophils interact with epithelial cells to allow for their passage to the airway surface. Further, neutrophils release harmful substances when they transmigrate, such as neutrophil elastase (NE) and myeloperoxidase, contributing to the development of bronchiectasis in the CF lung[291,292]. To study neutrophil transmigration across airway epithelial cells *in vitro*, we established a novel culture method. This novel method consists of seeding 16HBE cells, expressing either WT or ΔF508 CFTR, onto the

undersurface of collagen-coated Transwell filters, allowing them to settle and attach, after which the Transwells were inverted back to the traditional configuration. Monolayers were conditioned with either normal or high glucose media; we expected transepithelial migration of neutrophils to be further enhanced under chronic hyperglycemia. Primary human PMNs were induced to transmigrate across epithelia using chemoattractants such as fMLF and LTB4. Similarly, we also established this technique using primary human bronchial epithelial cells, NhBE and CFhBE, to study neutrophil transmigration. As expected, results showed a time-dependent decrease in transepithelial resistance with increased transmigration of neutrophils across WT and CF monolayers. However, the number of transmigrated neutrophils was higher in WT monolayers conditioned with hyperglycemic media compared to the normoglycemic control. No difference in transmigration rate was seen in CF cells in response to hyperglycemia. Results also showed that transmigration across epithelial layers was higher than across empty collagen-coated Transwells. The morphology and activation state of neutrophils was also changed after migrating though epithelial cell monolayers, while cells that migrated across empty collagen-coated Transwells behaved like naïve neutrophils. These observations suggest that productive interactions between epithelial cells and PMNs take place to facilitate PMN transmigration and influence neutrophil fate. To our knowledge, ours is the first group that was able to capture and image neutrophils actively transmigrating across epithelial monolayers. Future studies will focus on gaining a better understanding of neutrophil transmigration patterns across epithelial cell monolayers. Example questions that will be addressed include whether neutrophils prefer to transmigrate though bicellular or tricellular junctions, and whether multiple neutrophils transmigrate through the same junction, as well as the identification of proteins that contribute to productive interactions between epithelial cells and transmigrating neutrophils.

Taken together, these conclusions serve as a starting point to explain the underlying mechanisms driving the rapid lung function decline seen in patients with CFRD, with the goal of informing the development of future therapeutics to improve the quality of life and life expectancy of patients with CFRD.

Chapter 8 – Protocols

8.1. Cell culture of 16HBE cells

8.1.1. Media composition

Cells were cultured with complete media containing MEM (ThermoFisher, 11095098), 10% FBS (R&D, S11150H), and 1% Pen/Strep (Gibco, 15070-063). Media was filtered and stored at 4°C. Media was used within 3 months.

Freezing media consisted of 40% complete media mentioned above, 50% additional FBS(R&D, S11150H), and 10% DMSO (Sigma, 472301) made fresh on the day of freezing. Freezing media was filtered before use.

8.1.2. Pulling from the freezer

1. Open and spray down the hood.
2. Start warming up the media (5 mL in a T-25).
    a. The T25 can be warmed in the incubator.
3. Take the vial you need from the liquid nitrogen tank.
4. Hold the vial in the 37 *C water bath, not submerging the cap under the liquid level, until the pellet is thawed.
5. Spray down the vial before putting into the hood.
6. Pull the cells out of the vial with a 1 mL tip and transfer directly to the T25 with warm media.
7. Label the 25 with the cell type, passage number, and date.
8. Change the media on the T25 flask the <u>next day.</u>

8.1.3. Changing Media

- T25 Flask:

1. Remove old media
2. Add 5 mL new media

- Corning 3470 filters (24-well plate):
    1. Remove old media
    2. Add 500 µL media to basolateral side
    3. Add 200 µL to the apical side
- Corning 3460 filters (12-well plate):
    - Remove old media
    - Add 500 µL media to basolateral side
    - Add 200 µL to the apical side

8.1.4. Splitting Cells from a T25 (when 80-90% confluent)

1. Warm 5 mL media in a new T25 in the incubator.
2. Remove old media.
3. Add 5 mL PBS (no Ca2+/Mg2+).
4. Let sit 1-5 min.
5. Remove PBS.
6. Add 1.5 mL 0.25 % trypsin.
7. Let incubate at 37 °C until cells start to sluff off ~10 minutes.
    a. May need to hit side of flask.
8. Add 4.5 mL media, removing cells from plate.
9. Move cells to 15 mL conical tube.
    a. You will probably need to count the cells as well, which you can do during the next step.

b. To count cells, remove 20 uL from this conical tube and add to a microcentrifuge tube.
c. Add 20 uL Trypan Blue to the conical tube and mix gently.
d. Add 10 uL of the cells/trypan blue mixture to the hemocytometer.
e. Count the cells in the four quadrants of the hemocytometer.
f. Take the average number of cells per quadrant (total count/4), multiple by 2 (because you diluted the cells 1:1 in Trypan Blue), then multiple by 10,000. This gives you the number of cells per mL. Based on how many mLs you have, you can calculate the total number of cells you have.

10. Centrifuge at 500 xg for 10 min.
    a. The goal is to remove the trypsin from the cells.
11. Remove supernatant media without disturbing the pellet.
12. Resuspend the pellet in an appropriate amount of media. I usually resuspend to a density of 1,000,0000 cells/mL. When platting on Transwells:
    a. For 3470s, we plate 150K cells/well. I add 150 µL of my cell suspension and 50 µL of complete media per well.
    b. For 3460s, we plate 250K cells/well. I add 250 µL of my cell suspension and 250 µL of complete media per well.
13. Make sure to split some of the cells into a new T25
    a. For 16HBEs, a 1:20-30 dilution is recommended for cells to be confluent again in 7 days.

8.1.5. Splitting Cells from a T75 (when 80-90% confluent)

1. Warm 10 mL media in a new T75 in the incubator.

2. Remove old media.
3. Add 10 mL PBS (no Ca2+/Mg2+).
4. Let sit 1-5 min.
5. Remove PBS.
6. Add 3 mL 0.25 % trypsin.
7. Let incubate at 37 °C until cells start to sluff off ~10 minutes.
8. Add 6 mL media, removing cells from plate
9. Transfer to a 15 mL conical tube.
10. The next steps are the same as mentioned on the previous section, steps 10-13.

8.1.6. Freezing cells

1. Split cells like mentioned in the previous sections
2. Count the number of cells to know how much freezing media to use
3. After the final centrifugation step, remove the supernatant.
4. Resuspend the pellet using freezing media to a concentration of 1,000,000 cells/mL
5. Transfer 1mL of the cell suspension to cryopreservation tubes previously labeled with cell type, passage number, your initials and the date
6. Place on a freezing container, such as Mr. Frosty™ (ThermoFisher, 5100-0001) and place inside a -80°C freezer overnight.
7. The next day, transfer frozen vials to liquid nitrogen for long-term storage.

8.2. Ussing chamber protocol

8.2.1. Warm up

1. Turn on water bath (42°C).
    a. BS measured, and this makes the chamber ~37°C.
    b. Make sure water is between the two lines, otherwise the bath will not heat up.
2. Place recording solutions in 37°C water bath.
    a. Takes ~1 hr to warm up.
3. Place Chambers in 37 *C incubator.
    a. Takes ~1 hr to warm up.

8.2.2. Blanking

4. Put chambers in blue holder.
5. Insert slider with a blank filter into the chambers, tighten down thumb screw to compress chambers.
6. Insert electrodes into chamber (**Figure 8.1A**).
    a. White, current-passing electrodes go in the outside positions.
    b. Black, voltage sensing electrodes go in the inside positions.
    c. Make sure that the electrode leads with the black band are on the same side of the chamber.
7. Fill chamber with solution
    a. 3 mLs on each side is sufficient for this step.
    b. Make sure that there are no bubbles at the end of the electrode tips or inside chambers.
8. Turn on amplifier (Ussing Chamber) and computer.

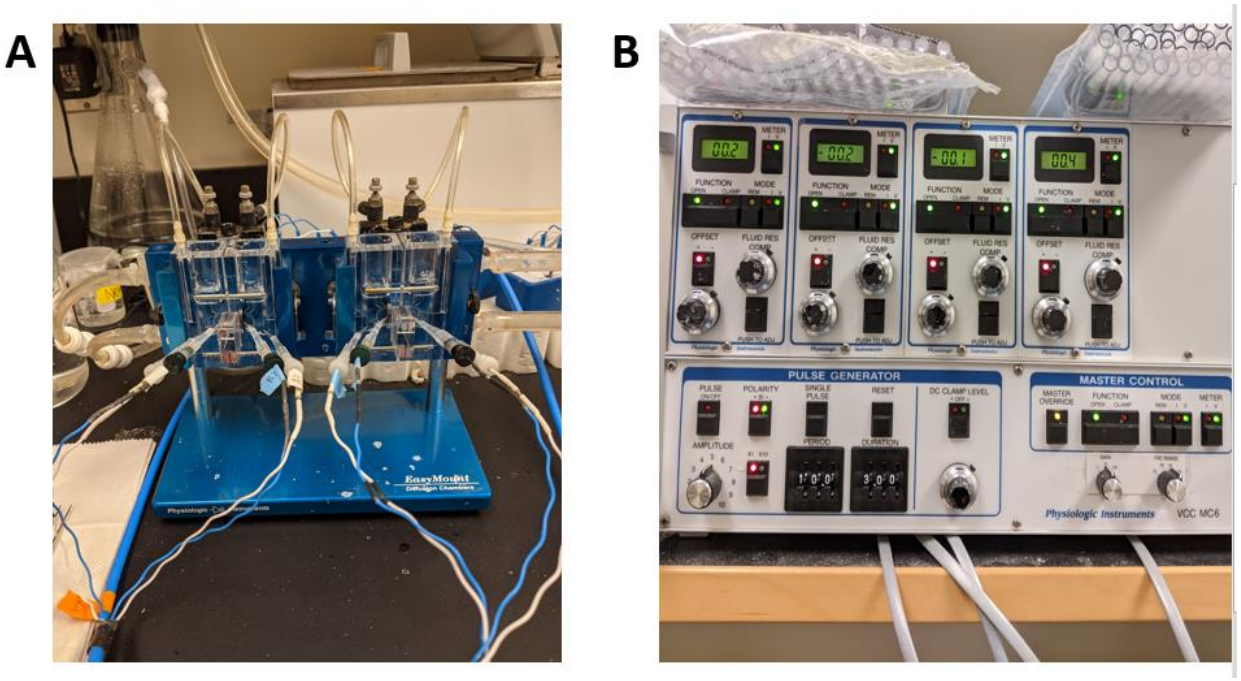

Figure 8.1. Ussing chamber set-up example.

(A) Picture highlighting the chamber set-up with electrodes placed in the correct orientation, sample loaded and solution added to both apical and basolateral side. (B) Picture showing the main sections of the amplifier box. This box is used to zero the chambers when a blank Transwell is loaded. The box also controls communication to the computer.

9. Correct electrode offset potential
    a. Switch FUNCTION key to OPEN and METER to V.

    The panel meter will display the difference potential between the pairs of voltage-sensing electrodes.

    b. Press the OFFSET button to the polarity opposite that displayed on the meter and use the dial to adjust the offset so that the meter reads 0.0. NOTE: this value will drift if chamber are filled with different solutions (i.e. if chloride is not symmetrical) due to diffusion. Set at the beginning and do not readjust (**Figure 8.1B**).

8.2.3. Loading Samples

1. Mount the tissues into the chamber.
    a. Remove solutions for each side of the chamber.
    b. Loosen thumb screw and spread chamber apart.
    c. Remove slider, replace blank filter with one containing cells.
    d. Place tissue back into chambers and make sure slider is pressed all the way back to avoid leaks.
        i. If the slider is pressed all the way back and the chamber is still leaking, check the black O-ring that sits between the slider and each side of the chamber.
    e. Tighten down thumb screws.
    f. Fill the chamber with 4 mLs of solution.
        i. Fill basolateral side first because it is detrimental for the BL side of epithelial cells to be exposed to air for extended periods of time.

g. Insert air tubes and begin the flow of gas to bubble solutions.
    i. In most cases this is 95% O2/5% CO2.
    ii. All solutions containing bicarbonate should be bubbled with a CO2 containing gas.

2. Turn on MASTER OVERRIDE, Press the FUNCTION button to CLAMP and the METER button to V – at this point the voltage should read 0.
    a. As of the writing of this protocol, our amplifier shows 2.9 V in clamp mode
    b. This is offset to 0.0 using the DC current knob.
3. Press the REM button to enable computer control of the amp
    a. As of the writing of this protocol, our amplifier shows a 1 V offset upon hitting the REM button. Again, adjust V to 0 using the DC current knob.

8.2.4. Setting up the software

1. In the A&A, software create new experiment file, select chambers from which to collect data, and set surface area to appropriate value depending on filters being used.
    a. File>new experiment.
2. Reference tissues
    a. Acquire>Reference.
    b. Boxes should remain white, yellow indicates a small offset, red indicates a significant offset.
3. Click the appropriate “traffic light” button to determine acquisition rate.
    a. We usually use the green light, faster setting.
4. Click the “running man” button to begin data acquisition.
5. When the experiment is done, click the stop hand and save the experiment.

6. Export the data into the excel format.
7. To speed analysis, use the “Boss Excel_for ussing.xls” spreadsheet created by Kirsten Cottrill. It can be found in the Ephys>Ussing chamber folder.

8.2.5. Other notes

1. Electrodes are usually the issue with these experiments. If something is adding oddly or values can’t be compensated, check for bubbles and try swapping electrodes. As the gold contacts get worn out, issues can arise more frequently
2. If the electrodes become white, they should be submerged in bleach. DO NOT SUBMERGE THE PLASTIC OR GOLD CONTACTS. DO NOT COVER AND BLEACH OVERNIGHT AS IT CAUSES CORROSION OF THE GOLD CONTACT.
3. VX-770 is relatively difficult to remove from the chambers. The physiologic instrument folks provided the clean-up protocol that we have adopted, which seems to work well. After an experiment with VX-770, add chamber to very hot water containing “CONTRAD 70” detergent and let soak for at least 2 hours.
4. To wash chambers, I usually soaked overnight in detergent solution, rinsed in the morning with tap water, and performed a final rinse with DI H20 before allowing to (mostly) dry on a paper towel.
5. Make sure to turn off gas at the main valve. Closing the regulator while keeping the main valve open will cause a slow leak.

8.3. Dye flux protocol to measure paracellular permeation

8.3.1. Cell Culture

- Day 0 → Plate 250K cells per well using Corning 3460 Transwells.
- Day 2 → Start glucose conditioning using media with 5.5 mM vs 17.5 mM glucose.
- Day 7 → Start treatment with small molecules, Elexacaftor and Tezacaftor (ET) only +/- insulin (400 nM).
    a. Elexacaftor (5 μM) + Tezacaftor (18 μM).
        i. Make 50 mLs with normal glucose media.
            1. Add 50 μL of Elexacafrot stock (5 mM).
            2. and 50 μL of Tezacaftor stock (18 mM).
        ii. Make 50 mL with high glucose media.
            1. Add 50 μL of Elexacafrot stock (5 mM).
            2. and 50 μL of Tezacaftor stock (18 mM).
    b. Control → Media + DMSO.
        i. 50 mL of media (normal and high glucose) + 50 μL DMSO.
- Day 8 → Add treatment with Elexacaftor (5 μM) + Tezacaftor (18 μM) + Ivacaftor (1μM) +/- insulin (400 nM).
    a. Add 25 μL of Ivacaftor stock (1 mM) to 25 mL leftover media from day 7.
    b. Control.
        i. 25 mL plus of leftover control media (normal and high glucose) from day 7 + 25 μL DMSO.

8.3.2. Plate maps

Plate 1

16HBE WT 5.5 mM	16HBE WT 5.5 mM + ETI	16HBE WT 17.5 mM	16HBE WT 17.5 mM + ETI
16HBE WT 5.5 mM	16HBE WT 5.5 mM + ETI + Insulin	16HBE WT 17.5 mM	16HBE WT 17.5 mM + ETI + Insulin
16HBE WT 5.5 mM + ETI	16HBE WT 5.5 mM + ETI + Insulin	16HBE WT 17.5 mM + ETI	16HBE WT 17.5 mM + ETI + Insulin

Plate 2

16HBE WT 5.5 mM	16HBE WT 5.5 mM + ETI	16HBE WT 17.5 mM	16HBE WT 17.5 mM + ETI
16HBE WT 5.5 mM	16HBE WT 5.5 mM + ETI + Insulin	16HBE WT 17.5 mM	16HBE WT 17.5 mM + ETI + Insulin
16HBE WT 5.5 mM + ETI	16HBE WT 5.5 mM + ETI + Insulin	16HBE WT 17.5 mM + ETI	16HBE WT 17.5 mM + ETI + Insulin

Plate 3

16HBE CF 5.5 mM	16HBE CF 5.5 mM + ETI	16HBE CF 17.5 mM	16HBE CF 17.5 mM + ETI
16HBE CF 5.5 mM	16HBE CF 5.5 mM + ETI + Insulin	16HBE CF 17.5 mM	16HBE CF 17.5 mM + ETI + Insulin
16HBE CF 5.5 mM + ETI	16HBE CF 5.5 mM + ETI + Insulin	16HBE CF 17.5 mM + ETI	16HBE CF 17.5 mM + ETI + Insulin

Plate 4

16HBE CF 5.5 mM	16HBE CF 5.5 mM + ETI	16HBE CF 17.5 mM	16HBE CF 17.5 mM + ETI
16HBE CF 5.5 mM	16HBE CF 5.5 mM + ETI + Insulin	16HBE CF 17.5 mM	16HBE CF 17.5 mM + ETI + Insulin
16HBE CF 5.5 mM + ETI	16HBE CF 5.5 mM + ETI + Insulin	16HBE CF 17.5 mM + ETI	16HBE CF 17.5 mM + ETI + Insulin

8.3.3. Dye Flux Test

1. Remove plate with sample Transwells from the incubator and wash both apical and basolateral sides with warm KRH buffer once.
2. Add fresh KRH solution (bilateral) and incubate for 90 minutes in the incubator to remove all growth factors and media supplements.

During the 90-minute wash

3. Prepare a new Costar 3513 tray (12 well plate without Transwells), add 1 mL of warm KRH solution in the tray → Put in the incubator at 37°C.
4. Prepare dyes in KRH solution.
    1) Need 8 mL of dye solution per 12 Transwell.
        i. 0.5 mL for each well (apical) → 0.5x12= 6 mL.
        ii. Need 2 mL for standard curve.
    b. Stock concentration for calcein (1mg/ml) and for dextran (5 mg/ml).
    2) Add 320 ul of calcein and 160 ul of dextran to 8 ml of KRH solution to get final concentration of 4 ug/ml of calcein and 0.1 mg/ml of Dextran.

Compound	Stock Concentration	Volume needed to make 8 ml master mix	Final Concentration
Calcein (0.62kDa)	0.1 mg/ml	320 µl	4 µg/ml
Dextran (10kDa)	5 mg/ml	160 µl	0.1 mg/ml

5. Standard curve of dye: in 96 well for empty control and measurement (corning 3610).
    a. Make the following dilutions:

Dilution	1	0.9	0.75	0.5	0.25	0.2	0.15	0.1	0.05	0.04	0.01	0
Add	500 uL dye + 0 uL of KRH	450 uL dye + 50 uL of KRH	375 uL dye + 125 uL of KRH	250 uL dye + 250 uL of KRH	125 uL dye + 375 uL of KRH	100 uL dye + 400 uL of KRH	75 uL dye + 425 uL of KRH	50 uL dye + 450 uL of KRH	25 uL dye + 475 uL of KRH	20 uL dye + 480 uL of KRH	5 uL dye + 495 uL of KRH	0 uL dye + 500 uL of KRH

When running 4 12-well plates

1) Add 2560 µL of calcein and 1280 µL of dextran to final 64 ml of KRH solution to get final concentration of 4 µg/ml of calcein and 0.1 mg/ml of Dextran.

When the 90-minute wash if about to finish (~75 minutes)

6. Measure TER resistance using chopsticks (this should take around 10 minutes).
7. Aspirate off KRH from the old plate and transfer Transwells to the new plate with fresh and warm KRH.
8. Add 500 µl of dye solution per Transwell to the apical side.
    a. Be careful not to drip any die on the basolateral side.
9. Remove 100 µL of media from the basolateral side and transfer to a 96-well plate.
    a. Keep this plate covered in foil (light sensitive).
    b. Leave the last 3 rows of the plate empty for the standard curve
10. Collect 100 µL samples from the basolateral side and transfer to the 96 well plate
    a. At time 0 hours
    b. At 1 hour
    c. At 2 hours
    d. At 2.5 hours
    e. At 3 hours
11. Aspirate off apical and basolateral media, wash once with KRH (1ml bottom, 500 ul top), and replace with fresh KRH (1ml bottom, 500 ul top)
    a. This counts as the washing step for the next experiment
12. Measure TER resistance using chopsticks
13. Read the plate of collected samples using a plate reader

8.3.4. Testing with insulin

1. Make KRH with insulin and add insulin to your remaining dye.

   a. To make 8 ml of 400nM insulin KRH media, add 32 µl of insulin (100uM stock) to 8 ml of KRH.
      i. For 4 plates, add 128 µL of insulin (100 µM) to 32 mL of KRH.
      ii. If you need to make more 100 µM insulin.
      iii. Add 29 µL insulin (688 µM stock) + 171 µL KRH buffer.
2. Prepare a new Costar 3513 tray (12 well plate without Transwells), add 1 ml KRH with insulin solution in the tray and warm it in 37°C incubator.
3. Aspirate off KRH from the old plate and transfer Transwells to the new plate with pre-warmed KRH + insulin.
4. Add 500 µl of dye solution + insulin per Transwell to the apical side
   a. Be careful not to drip any die on the basolateral side
5. Remove 100 µl of media from the basolateral side and transfer to a 96-well plate.
   a. Keep this plate covered in foil (light sensitive).
   b. Leave the last 3 rows of the plate empty for the standard curve.
6. Collect 100 µl samples from the basolateral side and transfer to the 96 well plate
   a. At time 0 hours
   b. At 1 hour
   c. At 2 hours
   d. At 2.5 hours
   e. At 3 hours
7. Measure TER resistance using chopsticks.
8. Read the plate using a plate reader.

8.4. Running qRT-PCR to test for changes in gene expression

8.4.1. Background

This protocol was used to isolate RNA from 16HBE cells cultured with different glucose concentrations and test the differences in gene expression of a subset of genes of interest.

8.4.2. RNA isolation

RNA was isolated using an RNA isolation kit (Zymo Research, R1054)[293]. Steps followed are mentioned below. Note that this protocol is also used to isolate RNA for RNA sequencing.

1. Wash Transwells (Corning, 3460) once with 1XPBS.
2. Add 250 µL of 1XPBS on the apical surface.
3. Scrape cells using a 1mL pipette tip and transfer to RNAse-free microcentrifuge tubes.
    a. Combining cells from 2 wells per tube.
4. Wash each well with 250 µL of 1X PBS to collect any remaining cells and transfer to the corresponding microcentrifuge tube.
    a. Each microcentrifuge tube should hold 1mL of cells in 1XPBS.
5. Spin down at 500xg for 5 minutes to pellet the cells.
6. Remove the supernatant and resuspend in 300 µL of lysis buffer.
7. Load the lysed sample into the Spin-Away™ Filter1 (yellow) in a collection tube.
8. Spin down at 16,000xg for 30 seconds.
    a. Note: All future centrifugation steps are performed at this speed for this duration unless otherwise noted.
9. Save the flow-through and add 300 µL of 100% ethanol. Mix well.

10. Transfer the sample into a Zymo-Spin™ IIICG Column1 (green) in a collection tube. Centrifuge and discard the flow-through.
11. Perform DNase treatment directly onto the membrane of the spin column.
    a. Wash the column with 400 µL of RNA Wash Buffer.
    b. Add 75 µL of DNAse Digestion Buffer and 5 µL DNase I previously mixed.
    c. Incubate at room temperature for 15 minutes.
12. Add 400 µl RNA Prep Buffer to the column and centrifuge. Discard the flow-through.
13. Add 700 µl RNA Wash Buffer to the column and centrifuge. Discard the flow-through.
14. Add 400 µl RNA Wash Buffer and centrifuge the column for 1 minute to ensure complete removal of the wash buffer.
15. Transfer the column into a nuclease-free tube and add 30 µl DNase/RNase-Free Water directly to the column matrix and centrifuge.
16. Measure RNA concentration using a nano-drop machine.

8.4.3. Reverse Transcription

Follow instructions from QuantiTect Reverse Transcription Kit (Qiagen, 205311) to remove gDNA and turn the RNA into cDNA[294]. Plan to use 100 ng of RNA per PCR reaction.

8.4.4. Real Time PCR

1. Dilute the cDNA to in RNAse-free water (1:10 dilution).
2. Add SYBR Green PCR master mix (Applied Biosystems, 4368706) to the diluted cDNA (1:1 dilution).
3. Add 20 uL cDNA/SYBR Green mix to each well.

4. Seal the plate with the optical seal.
5. Centrifuge the plate briefly in the plate centrifuge in the Fitzpatrick lab.
6. Log into the StepOne Plus computer in the Fitzpatrick lab.
    a. User: Admin
    b. Password: BoomBoomPow
7. Set up the protocol
    a. 95 °C, 10 min.
    b. 95 °C, 15 sec.
    c. 60 °C, 1 min.
    d. Repeat steps 2-3, 40 x.
    e. Melt Curve analysis.
        i. 95 °C, 15 sec.
        ii. 60 °C, 1 min.
        iii. 0.3 °C steps up to 95 °C, 15 sec each.

8.5. Immunostaining Protocol

8.5.1. Background

This protocol was used to fix and stain 16HBE cells and primary cells. I tested claudin expression and localization using this protocol. Neutrophil transmigration was also tested using this protocol.

8.5.2. Protocol

Notes: All steps were conducted at room temperature unless otherwise noted. A final volume of 500 µL was added to the basolateral side, and 200 µL was added to the apical side for all solutions unless otherwise noted.

1. Wash Transwells (Corning, 3470) 3X with 1XPBS.
2. Fix cells with 2% paraformaldehyde (PFA) diluted with 1X PBS for 10 min.
3. Wash cells 3X with 1XPBS.
4. Fix/Permeabilize with 1:1 Methanol/acetone - for EXACTLY 2 minutes.
5. Wash cells 3X with 1XPBS.
6. Wash/Block 2X with PBS/BSA (5 min/wash)
    a. PBS/BSA is 2% BSA in 1X PBS and it is made by diluting 1 gram of BSA (Sigma, A9418) into 50 mL of 1XPBS.
        i. I like to make my blocking buffer fresh each time.
        ii. Note: You can also use 2% goat-serum as a blocking agent, but it's more expensive and gets easily contaminated. This is the preferred blocking agent by the Koval Lab, although I have not noticed any differences from BSA. To make it, put 1 mL goat serum in a

microcentrifuge tube and spin for 5 min at max speed (~17,000xg). Then add 0.4 mL of the supernatant per 20 mL of 1X PBS.

7. Make primary antibody dilution in cold PBS/BSA. Keep on ice.
    a. These are the antibodies I used the most throughout this dissertation. Their species and recommended dilations are also noted.
        i. ZO-1 (Thermo-Fischer, 33-9100) (mouse) (1:200)
        ii. CLDN-4 (Thermo-Fisher, 36-4800) (rabbit) (1:100)
8. Add primary antibody solution to your samples.
    a. For Corning 3470 Transwells, add 300 uL on bottom and 70 uL on top.
9. Incubate at 4°C overnight with gentle agitation.
10. The next day, wash 3X with PBS/BSA (5 min/wash)
11. Make secondary antibody solution in cold PBS/BSA. Keep on ice and covered from light.
    a. Alexa Fluor 488 anti-rabbit (Invitrogen, A-11008) (1:1000)
    b. Alexa Fluor 594 anti-mouse (Invitrogen, A-11005) (1:1000)
12. Add secondary antibody solution to your samples.
    a. For 3470 Transwells, add 300 uL on bottom and 70 uL on top.
13. Incubate on a shaker 1 h at room temperature.
14. Wash 3X with PBS/BSA (5 min/wash).
15. Wash 3X with PBS.
16. Carefully cut out the membrane from the Transwell using a razor blade and transfer to a microscope slide with cells pointing up.

17. Cover the membrane with VECTASHIELD Antifade Mounting Medium with DAPI (Vector Laboratories, H-1200-10). Place a coverslip on top and seal the sides with clear nail polish. Let dry in a dark place overnight.
18. Samples were imaged using a Nikon CSU-W1 SoRa Spinning Disk confocal microscope from Emory's Integrated Cellular Imaging (ICI) core located in the HSRBI basement.

8.6. Analyzing tight junction protein localization with confocal microscopy

1. Open FIJI (**F**iji **I**s **J**ust **I**mageJ).
2. Open the raw file image that you are interested in analyzing.
    a. Select "separate channels" when opening the image.
    b. The file should load in as 16-bit hyperstacks.
3. You can close the DAPI stack, since it will not be needed to analyze tight junction localization.
4. Assign the appropriate Lookup Table (LUT) color to each stack by clicking the "LUT" key on the toolbar.
    a. I usually assign the color "green" to my claudin channel the color "red" to my ZO-1 channel.
    b. If the image is not visible, you can go to Image > Adjust > Brightness/Contrast > Auto
5. Take the maximum projection of each stack on the z-plane to generate single images instead of stacks
    a. Click the by clicking the "Stk" key on the toolbar, and then select "Z Project…"

6. Using the ZO1 max-z projected image, use the “Multi-point Tool” to label all the visible cells.
7. Press “t” to add the selected points to the region-of-interest (ROI) manager
    a. Make sure the “show all” box is checked
8. Use a random number generator to select 8 integers between 1 and the number of cells counted.
9. Still working with the ZO1 max-z projected image, use the “segmented line tool” (right click on the line tool, select “segmented line”),to trace the circumference of each cell.
    a. Click ALT when making the first point!! Only need to do it once for the first cell outline.
    b. Right click to end the trace. Don’t put your final dot too close to the first dot, or it will end the trace at the previous spot.
    c. Press “t” after drawing each cell outline to save it to your ROI manager.
    d. You can rename the object created on the ROI manager with the cell number
10. When you are done drawing all the cell outlines, select all the cell outlines on the ROI manager and click “Measure”.
    a. This will generate a result window with the ZO1 fluorescence intensity coming from each cell outline drawn.
11. Save the result window as an excel file
    a. Make sure to identify this file as ZO1 results.
12. Close the results window.

13. You can now open your other max-z projection image for the claudin channel and repeat the measuring process.
14. Select all the cell outlines on the ROI manager again and click “Measure”.
15. When done, save the result window as an excel file.
    a. Make sure to identify this file as CLDN results.
16. Close the result window.
17. Save and overlay of the cell numbers and outlines for each max-z projected image.
    a. In the ROI manager, make sure the “show all” box is selected and “labels” is unselected.
    b. Press the “Flatten” button.
    c. Save the resulting image as TIFF file.
18. Before closing the file, MAKE SURE TO SAVE ROI WINDOW TOO!! (right click and save as) and name it “ROI_Image X”. You can always open the image with this ROI file in the future if you need to make measurements again or export new images.

8.7. Running meal-like patters using PACCS

8.7.1. Initial set-up

The morning you need to start PACCS:

4. Autoclave the media bottle and water reservoir

    5.3.3. I usually cover the water reservoir with aluminum foil and add autoclave tape

    5.3.4. Leave the media bottle unscrew and cover the top openings with aluminum foil and autoclave tape

    5.3.5. Run under “gravity” cycle on the autoclave

5. Sterilize the PACCS lines

    5.3.3. Add ~100 mls of 70% Ethanol in a bottle

    5.3.4. Screw the input adapters

    5.3.5. Run 70% ethanol on the lines

        i. In the PACCS controller, go to “Manual Mode” and open channels 1 and 2

        ii. You can use a beaker to collect the 70% ethanol coming out of the lines

        iii. Suction the ethanol you collected by submerging the vacuum lines in your beaker and opening channel 8

    5.3.6. Let ethanol sit on the lines for 15 minutes

    5.3.7. Cover the ends of the line with aluminum foil

    5.3.8. Drain the lines to remove the 70 % ethanol

i. I do this by reversing the direction of fluid flow from the peristaltic pump

1. Switch the +/- cables and run channels 1 and 2

ii. The reminder ethanol should evaporate by itself

6. Sterilize the incubator

5.3.3. I spray the inside the incubator with abundant 70% ethanol and wipe it with paper towels

5.3.4. Let it air dry for ~5 minutes

7. Turn on the incubator

5.3.3. Add the autoclaved water reservoir with sterile water on the bottom

5.3.4. Close the door and let the temperature and CO2 equilibrate for at least 1 hour

8. Sterilize the PACCS Plate

5.3.3. I usually spray down the plate, tray and lid with abundant 70% ethanol and put it in the cell culture hood to dry

5.3.4. I also leave the plate under UV light for 30 minutes to sterilize

5.3.5. I like to cover the inputs and outputs with aluminum foil

i. I also spray down the foil before putting it in the hood

5.3.6. Before adding Transwells to the plate, I like to wash the inside with 3mls of 1X PBS per side

8.7.2. Starting PACCS

1. In the cell culture hood, add the required amount of media to your media bottle and transfer the bottle to the incubator.

a. Around 8 mL is needed per media change.

Channel 1 (low glucose) changes media 6X a day = 48 mL/day

Channel 2 (low glucose) changes media 3X a day = 24 mL/day

Channel 3 (high glucose) changes media 3X a day = 24 mL/day

Low glucose needed/day = 48+24 = 72 mL

High glucose needed/day = 24 mL

2. Connect the input adapters to the bottle.
3. In the PACCS controller, go to "Manual Mode" and open channels 1 and 2 so media goes into the lines.
4. You can run off some of the media to clear out any remaining 70% ethanol that could have been left behind from the line cleaning process.
5. Make sure to collect the media in a beaker and cover the openings with sterile aluminum foil right away.
6. In the cell culture hood, transfer Transwells to the PACCS plate.
7. Quickly take the plate to the incubator. Connect the inputs and outputs.
8. Run program 7 to add media to the plate (**Table 8.1**).

Table 8.1. PACCS meal-like pattern settings. This is currently stored in the ValveBank controller as program 7.

Channel 1 (First input Low Glucose Control Plate)	Channel 2 (Second input Low Glucose Meal Plate)	Channel 3 (Third input High Glucose Meal Plate)	Channel 8 (Vacuum)
00:00:00.00 Loop Start (07)	00:00:00.00 Loop Start (07)	00:00:00.00 Loop Start (07)	00:00:00.00 Loop Start (07)
00:00:00.00 Open Valve	00:00:00.00 Open Valve		00:00:00.00 Open Valve
00:00:28.00 Close Valve	00:00:28.00 Close Valve		00:00:12.00 Close Valve
04:00:00.00 Open Valve		04:00:00.00 Open Valve	03:59:40.00 Open Valve
04:00:28.00 Close Valve		04:00:28.00 Close Valve	04:00:12.00 Close Valve
08:00:00.00 Open Valve	08:00:00.00 Open Valve		07:59:40.00 Open Valve
08:00:28.00 Close Valve	08:00:28.00 Close Valve		08:00:12.00 Close Valve
12:00:00.00 Open Valve		12:00:00.00 Open Valve	11:59:40.00 Open Valve
12:00:28.00 Close Valve		12:00:28.00 Close Valve	12:00:12.00 Close Valve
16:00:00.00 Open Valve	16:00:00.00 Open Valve		15:59:40.00 Open Valve
16:00:28.00 Close Valve	16:00:28.00 Close Valve		16:00:12.00 Close Valve
20:00:00.00 Open Valve		20:00:00.00 Open Valve	19:59:40.00 Open Valve
20:00:28.00 Close Valve		20:00:28.00 Close Valve	20:00:12.00 Close Valve
24:00:00.00 Loop End	24:00:00.00 Loop End	24:00:00.00 Loop End	23:59:40.00 Open Valve
68:00:00.00 End of List	68:00:00.00 End of List	68:00:00.00 End of List	24:00:00.00 Close Valve
			24:00:00.00 Loop End
			68:00:00.00 End of List

Note: This program changes the media 3 times a day. The flow rate is ~285 ul/second. Opening the inputs for 28 seconds dispenses ~8 mls of media, which gets divided into 4 mls of media per plate side. The vacuum runs for 20 seconds by itself and later overlaps with the inputs for 12 seconds to wash away any waste media left in the plate.

8.7.3. While PACCS is running

1. Once a day, check that PACCS correctly changes the media on your plates.
2. Remember to manually change the media on your controls.
    a. Manual media changes used as a comparison (once a day).
3. Store the plate with control Transwells in the same incubator.
4. You can also store your media aliquot for your controls in the incubator.

4. I usually let this program run for 5 days and take Ussing chamber readings on the fifth day.

References

(1) Elborn, J. S. Cystic Fibrosis. *Lancet Lond. Engl.* **2016**, *388* (10059), 2519–2531. https://doi.org/10.1016/S0140-6736(16)00576-6.

(2) Guo, J.; Garratt, A.; Hill, A. Worldwide Rates of Diagnosis and Effective Treatment for Cystic Fibrosis. *J. Cyst. Fibros. Off. J. Eur. Cyst. Fibros. Soc.* **2022**, *21* (3), 456–462. https://doi.org/10.1016/j.jcf.2022.01.009.

(3) *Addressing Health Inequities in the Cystic Fibrosis Community | Cystic Fibrosis Foundation*. https://www.cff.org/about-us/addressing-health-inequities-cystic-fibrosis-community (accessed 2024-06-05).

(4) Bergeron, C.; Cantin, A. M. Cystic Fibrosis: Pathophysiology of Lung Disease. *Semin. Respir. Crit. Care Med.* **2019**, *40* (06), 715–726. https://doi.org/10.1055/s-0039-1694021.

(5) Saint-Criq, V.; Gray, M. A. Role of CFTR in Epithelial Physiology. *Cell. Mol. Life Sci. CMLS* **2017**, *74* (1), 93–115. https://doi.org/10.1007/s00018-016-2391-y.

(6) Bustamante-Marin, X. M.; Ostrowski, L. E. Cilia and Mucociliary Clearance. *Cold Spring Harb. Perspect. Biol.* **2017**, *9* (4), a028241. https://doi.org/10.1101/cshperspect.a028241.

(7) Quinton, P. M. Chloride Impermeability in Cystic Fibrosis. *Nature* **1983**, *301* (5899), 421–422. https://doi.org/10.1038/301421a0.

(8) Ciofu, O.; Hansen, C. R.; Høiby, N. Respiratory Bacterial Infections in Cystic Fibrosis. *Curr. Opin. Pulm. Med.* **2013**, *19* (3), 251–258. https://doi.org/10.1097/MCP.0b013e32835f1afc.

(9) Breuer, O.; Caudri, D.; Stick, S.; Turkovic, L. Predicting Disease Progression in Cystic Fibrosis. *Expert Rev. Respir. Med.* **2018**, *12* (11), 905–917. https://doi.org/10.1080/17476348.2018.1519400.

(10) ANDERSEN, D. H. CYSTIC FIBROSIS OF THE PANCREAS AND ITS RELATION TO CELIAC DISEASE: A CLINICAL AND PATHOLOGIC STUDY. *Am. J. Dis. Child.* **1938**, *56* (2), 344–399. https://doi.org/10.1001/archpedi.1938.01980140114013.

(11) Andersen, D. H.; Hodges, R. G. Celiac Syndrome; Genetics of Cystic Fibrosis of the Pancreas, with a Consideration of Etiology. *Am. J. Dis. Child. 1911* **1946**, *72*, 62–80. https://doi.org/10.1001/archpedi.1946.02020300069004.

(12) Riordan, J. R.; Rommens, J. M.; Kerem, B.; Alon, N.; Rozmahel, R.; Grzelczak, Z.; Zielenski, J.; Lok, S.; Plavsic, N.; Chou, J. L. Identification of the Cystic Fibrosis Gene: Cloning and Characterization of Complementary DNA. *Science* **1989**, *245* (4922), 1066–1073. https://doi.org/10.1126/science.2475911.

(13) Tsui, L.-C.; Dorfman, R. The Cystic Fibrosis Gene: A Molecular Genetic Perspective. *Cold Spring Harb. Perspect. Med.* **2013**, *3* (2), a009472. https://doi.org/10.1101/cshperspect.a009472.

(14) *CFTR*. Johns Hopkins Cystic Fibrosis Center. https://hopkinscf.org/knowledge/cftr/ (accessed 2024-06-04).

(15) Cassano, W. F. Cystic Fibrosis and the Plague. *Med. Hypotheses* **1985**, *18* (1), 51–52. https://doi.org/10.1016/0306-9877(85)90119-7.

(16) Jorde, L. B.; Lathrop, G. M. A Test of the Heterozygote-Advantage Hypothesis in Cystic Fibrosis Carriers. *Am. J. Hum. Genet.* **1988**, *42* (6), 808–815.

(17) Berger, H. A.; Anderson, M. P.; Gregory, R. J.; Thompson, S.; Howard, P. W.; Maurer, R. A.; Mulligan, R.; Smith, A. E.; Welsh, M. J. Identification and Regulation of the Cystic Fibrosis Transmembrane Conductance Regulator-Generated Chloride Channel. *J. Clin. Invest.* **1991**, *88* (4), 1422–1431. https://doi.org/10.1172/JCI115450.

(18) Locher, K. P. Mechanistic Diversity in ATP-Binding Cassette (ABC) Transporters. *Nat. Struct. Mol. Biol.* **2016**, *23* (6), 487–493. https://doi.org/10.1038/nsmb.3216.
(19) Cheng, S. H.; Gregory, R. J.; Marshall, J.; Paul, S.; Souza, D. W.; White, G. A.; O'Riordan, C. R.; Smith, A. E. Defective Intracellular Transport and Processing of CFTR Is the Molecular Basis of Most Cystic Fibrosis. *Cell* **1990**, *63* (4), 827–834. https://doi.org/10.1016/0092-8674(90)90148-8.
(20) Farinha, C. M.; Penque, D.; Roxo-Rosa, M.; Lukacs, G.; Dormer, R.; McPherson, M.; Pereira, M.; Bot, A. G. M.; Jorna, H.; Willemsen, R.; DeJonge, H.; Heda, G. D.; Marino, C. R.; Fanen, P.; Hinzpeter, A.; Lipecka, J.; Fritsch, J.; Gentzsch, M.; Edelman, A.; Amaral, M. D. Biochemical Methods to Assess CFTR Expression and Membrane Localization. *J. Cyst. Fibros.* **2004**, *3*, 73–77. https://doi.org/10.1016/j.jcf.2004.05.017.
(21) Csanády, L.; Vergani, P.; Gadsby, D. C. STRUCTURE, GATING, AND REGULATION OF THE CFTR ANION CHANNEL. *Physiol. Rev.* **2019**, *99* (1), 707–738. https://doi.org/10.1152/physrev.00007.2018.
(22) Polgreen, P. M.; Comellas, A. P. Clinical Phenotypes of Cystic Fibrosis Carriers. *Annu. Rev. Med.* **2022**, *73*, 563–574. https://doi.org/10.1146/annurev-med-042120-020148.
(23) Miller, A. C.; Comellas, A. P.; Hornick, D. B.; Stoltz, D. A.; Cavanaugh, J. E.; Gerke, A. K.; Welsh, M. J.; Zabner, J.; Polgreen, P. M. Cystic Fibrosis Carriers Are at Increased Risk for a Wide Range of Cystic Fibrosis-Related Conditions. *Proc. Natl. Acad. Sci. U. S. A.* **2020**, *117* (3), 1621–1627. https://doi.org/10.1073/pnas.1914912117.
(24) Fanen, P.; Wohlhuter-Haddad, A.; Hinzpeter, A. Genetics of Cystic Fibrosis: CFTR Mutation Classifications toward Genotype-Based CF Therapies. *Int. J. Biochem. Cell Biol.* **2014**, *52*, 94–102. https://doi.org/10.1016/j.biocel.2014.02.023.
(25) *Types of CFTR Mutations | Cystic Fibrosis Foundation*. https://www.cff.org/research-clinical-trials/types-cftr-mutations (accessed 2024-06-05).
(26) Orenti, A.; Pranke, I.; Faucon, C.; Varilh, J.; Hatton, A.; Golec, A.; Dehillotte, C.; Durieu, I.; Reix, P.; Burgel, P.-R.; Grenet, D.; Tasset, C.; Gachelin, E.; Perisson, C.; Lepissier, A.; Dreano, E.; Tondelier, D.; Chevalier, B.; Weiss, L.; Kiefer, S.; Laurans, M.; Chiron, R.; Lemonnier, L.; Marguet, C.; Jung, A.; Edelman, A.; Kerem, B.-S.; Girodon, E.; Taulan-Cadars, M.; Hinzpeter, A.; Kerem, E.; Naehrlich, L.; Sermet-Gaudelus, I.; ECFSPR Steering group. Nonsense Mutations Accelerate Lung Disease and Decrease Survival of Cystic Fibrosis Children. *J. Cyst. Fibros. Off. J. Eur. Cyst. Fibros. Soc.* **2023**, *22* (6), 1070–1079. https://doi.org/10.1016/j.jcf.2023.06.005.
(27) Bobadilla, J. L.; Macek, M.; Fine, J. P.; Farrell, P. M. Cystic Fibrosis: A Worldwide Analysis of CFTR Mutations--Correlation with Incidence Data and Application to Screening. *Hum. Mutat.* **2002**, *19* (6), 575–606. https://doi.org/10.1002/humu.10041.
(28) Wang, W.; Fu, L.; Liu, Z.; Wen, H.; Rab, A.; Hong, J. S.; Kirk, K. L.; Rowe, S. M. G551D Mutation Impairs PKA-Dependent Activation of CFTR Channel That Can Be Restored by Novel GOF Mutations. *Am. J. Physiol. Lung Cell. Mol. Physiol.* **2020**, *319* (5), L770–L785. https://doi.org/10.1152/ajplung.00262.2019.
(29) Yu, Y.-C.; Sohma, Y.; Hwang, T.-C. On the Mechanism of Gating Defects Caused by the R117H Mutation in Cystic Fibrosis Transmembrane Conductance Regulator. *J. Physiol.* **2016**, *594* (12), 3227–3244. https://doi.org/10.1113/JP271723.
(30) Dickinson, K. M.; Collaco, J. M. Cystic Fibrosis. *Pediatr. Rev.* **2021**, *42* (2), 55–67. https://doi.org/10.1542/pir.2019-0212.

(31) Dana, J.; Debray, D.; Beaufrère, A.; Hillaire, S.; Fabre, M.; Reinhold, C.; Baumert, T. F.; Berteloot, L.; Vilgrain, V. Cystic Fibrosis-Related Liver Disease: Clinical Presentations, Diagnostic and Monitoring Approaches in the Era of CFTR Modulator Therapies. *J. Hepatol.* **2022**, *76* (2), 420–434. https://doi.org/10.1016/j.jhep.2021.09.042.
(32) Malik, S. S.; Padmanabhan, D.; Hull-Meichle, R. L. Pancreas and Islet Morphology in Cystic Fibrosis: Clues to the Etiology of Cystic Fibrosis-Related Diabetes. *Front. Endocrinol.* **2023**, *14*, 1269139. https://doi.org/10.3389/fendo.2023.1269139.
(33) De Lisle, R. C.; Borowitz, D. The Cystic Fibrosis Intestine. *Cold Spring Harb. Perspect. Med.* **2013**, *3* (9), a009753. https://doi.org/10.1101/cshperspect.a009753.
(34) Barben, J.; Massie, J. Newborn Screening for CF - The Good, the Bad and the Ugly. *J. Cyst. Fibros. Off. J. Eur. Cyst. Fibros. Soc.* **2023**, *22* (1), 5–6. https://doi.org/10.1016/j.jcf.2023.01.011.
(35) Lissens, W.; Mercier, B.; Tournaye, H.; Bonduelle, M.; Ferec, C.; Seneca, S.; Devroey, P.; Silber, S.; Van Steirteghem, A.; Liebaers, I. Cystic Fibrosis and Infertility Caused by Congenital Bilateral Absence of the Vas Deferens and Related Clinical Entities. *Hum. Reprod.* **1996**, *11* (suppl 4), 55–80. https://doi.org/10.1093/humrep/11.suppl_4.55.
(36) *Congenital Bilateral Absence of the Vas Deferens - PubMed*. https://pubmed.ncbi.nlm.nih.gov/35222530/ (accessed 2024-06-05).
(37) Hjelm, M.; Hente, E.; Miller, J.; Moore, S.; Peugh, J.; Swetland, D. V.; Tadesse, D. G.; Hossain, M. M.; Siracusa, C.; Filigno, S. S. Longitudinal Mental Health Trends in Cystic Fibrosis. *J. Cyst. Fibros. Off. J. Eur. Cyst. Fibros. Soc.* **2023**, *22* (6), 1093–1099. https://doi.org/10.1016/j.jcf.2023.06.009.
(38) Blanchard, A. C.; Waters, V. J. Opportunistic Pathogens in Cystic Fibrosis: Epidemiology and Pathogenesis of Lung Infection. *J. Pediatr. Infect. Dis. Soc.* **2022**, *11* (Supplement_2), S3–S12. https://doi.org/10.1093/jpids/piac052.
(39) LiPuma, J. J. The Changing Microbial Epidemiology in Cystic Fibrosis. *Clin. Microbiol. Rev.* **2010**, *23* (2), 299–323. https://doi.org/10.1128/CMR.00068-09.
(40) Brennan, A. L.; Gyi, K. M.; Wood, D. M.; Johnson, J.; Holliman, R.; Baines, D. L.; Philips, B. J.; Geddes, D. M.; Hodson, M. E.; Baker, E. H. Airway Glucose Concentrations and Effect on Growth of Respiratory Pathogens in Cystic Fibrosis. *J. Cyst. Fibros.* **2007**, *6* (2), 101–109. https://doi.org/10.1016/j.jcf.2006.03.009.
(41) Bonyadi, P.; Saleh, N. T.; Dehghani, M.; Yamini, M.; Amini, K. Prevalence of Antibiotic Resistance of Pseudomonas Aeruginosa in Cystic Fibrosis Infection: A Systematic Review and Meta-Analysis. *Microb. Pathog.* **2022**, *165*, 105461. https://doi.org/10.1016/j.micpath.2022.105461.
(42) Cystic Fibrosis Foundation. Cystic Fibrosis Foundation Patient Registry. Annual Data Report. **2022**.
(43) De Rose, V.; Burgel, P.-R.; Gaggar, A.; Greene, C. Airway Inflammatory/Immune Responses in COPD and Cystic Fibrosis. *Mediators Inflamm.* **2018**, *2018*, 7280747. https://doi.org/10.1155/2018/7280747.
(44) Bruscia, E. M.; Bonfield, T. L. Cystic Fibrosis Lung Immunity: The Role of the Macrophage. *J. Innate Immun.* **2016**, *8* (6), 550–563. https://doi.org/10.1159/000446825.
(45) Lara-Reyna, S.; Scambler, T.; Holbrook, J.; Wong, C.; Jarosz-Griffiths, H. H.; Martinon, F.; Savic, S.; Peckham, D.; McDermott, M. F. Metabolic Reprograming of Cystic Fibrosis Macrophages via the IRE1α Arm of the Unfolded Protein Response Results in Exacerbated Inflammation. *Front. Immunol.* **2019**, *10*, 1789. https://doi.org/10.3389/fimmu.2019.01789.

(46) Tirouvanziam, R.; Gernez, Y.; Conrad, C. K.; Moss, R. B.; Schrijver, I.; Dunn, C. E.; Davies, Z. A.; Herzenberg, L. A.; Herzenberg, L. A. Profound Functional and Signaling Changes in Viable Inflammatory Neutrophils Homing to Cystic Fibrosis Airways. *Proc. Natl. Acad. Sci. U. S. A.* **2008**, *105* (11), 4335–4339. https://doi.org/10.1073/pnas.0712386105.

(47) Giacalone, V. D.; Giraldo, D. M.; Silva, G. L.; Hosten, J.; Peng, L.; Guglani, L.; Tirouvanziam, R. Pulmonary Exacerbations in Early Cystic Fibrosis Lung Disease Are Marked by Strong Modulation of CD3 and PD-1 on Luminal T Cells. *Front. Immunol.* **2023**, *14*, 1194253. https://doi.org/10.3389/fimmu.2023.1194253.

(48) *The role of neutrophils in cystic fibrosis*. https://oce-ovid-com.proxy.library.emory.edu/article/00062752-201401000-00005/PDF (accessed 2024-06-06).

(49) Giacalone, V. D.; Dobosh, B. S.; Gaggar, A.; Tirouvanziam, R.; Margaroli, C. Immunomodulation in Cystic Fibrosis: Why and How? *Int. J. Mol. Sci.* **2020**, *21* (9), 3331. https://doi.org/10.3390/ijms21093331.

(50) O'Rawe, A. Energy Metabolism in Cystic Fibrosis. *Proc. Nutr. Soc.* **1992**, *51* (2), 237–244. https://doi.org/10.1079/PNS19920034.

(51) *Getting Your Nutrients | Cystic Fibrosis Foundation*. https://www.cff.org/managing-cf/getting-your-nutrients (accessed 2024-06-06).

(52) Worgall, T. S. Lipid Metabolism in Cystic Fibrosis. *Curr. Opin. Clin. Nutr. Metab. Care* **2009**, *12* (2), 105–109. https://doi.org/10.1097/MCO.0b013e32832595b7.

(53) Gao, L.; Kim, K. J.; Yankaskas, J. R.; Forman, H. J. Abnormal Glutathione Transport in Cystic Fibrosis Airway Epithelia. *Am. J. Physiol.-Lung Cell. Mol. Physiol.* **1999**, *277* (1), L113–L118. https://doi.org/10.1152/ajplung.1999.277.1.L113.

(54) *Systemic deficiency of glutathione in cystic fibrosis | Journal of Applied Physiology*. https://journals-physiology-org.proxy.library.emory.edu/doi/abs/10.1152/jappl.1993.75.6.2419 (accessed 2024-06-19).

(55) Innis, S. M.; Davidson, A. G. F. Cystic Fibrosis and Nutrition: Linking Phospholipids and Essential Fatty Acids with Thiol Metabolism. *Annu. Rev. Nutr.* **2008**, *28* (Volume 28, 2008), 55–72. https://doi.org/10.1146/annurev.nutr.27.061406.093625.

(56) Bernhard, W.; Lange, R.; Graepler-Mainka, U.; Engel, C.; Machann, J.; Hund, V.; Shunova, A.; Hector, A.; Riethmüller, J. Choline Supplementation in Cystic Fibrosis—The Metabolic and Clinical Impact. *Nutrients* **2019**, *11* (3), 656. https://doi.org/10.3390/nu11030656.

(57) Davies, G.; Rowbotham, N. J.; Smith, S.; Elliot, Z. C.; Gathercole, K.; Rayner, O.; Leighton, P. A.; Herbert, S.; Duff, A. J.; Chandran, S.; Daniels, T.; Nash, E. F.; Smyth, A. R. Characterising Burden of Treatment in Cystic Fibrosis to Identify Priority Areas for Clinical Trials. *J. Cyst. Fibros.* **2020**, *19* (3), 499–502. https://doi.org/10.1016/j.jcf.2019.10.025.

(58) Narayanan, S.; Mainz, J. G.; Gala, S.; Tabori, H.; Grossoehme, D. Adherence to Therapies in Cystic Fibrosis: A Targeted Literature Review. *Expert Rev. Respir. Med.* **2017**, *11* (2), 129–145. https://doi.org/10.1080/17476348.2017.1280399.

(59) Stefani, S.; Campana, S.; Cariani, L.; Carnovale, V.; Colombo, C.; Lleo, M. M.; Iula, V. D.; Minicucci, L.; Morelli, P.; Pizzamiglio, G.; Taccetti, G. Relevance of Multidrug-Resistant Pseudomonas Aeruginosa Infections in Cystic Fibrosis. *Int. J. Med. Microbiol.* **2017**, *307* (6), 353–362. https://doi.org/10.1016/j.ijmm.2017.07.004.

(60) López-Causapé, C.; Rojo-Molinero, E.; Macià, M. D.; Oliver, A. The Problems of Antibiotic Resistance in Cystic Fibrosis and Solutions. *Expert Rev. Respir. Med.* **2015**, *9* (1), 73–88. https://doi.org/10.1586/17476348.2015.995640.

(61) Savant, A.; Lyman, B.; Bojanowski, C.; Upadia, J. Cystic Fibrosis. In *GeneReviews®*; Adam, M. P., Feldman, J., Mirzaa, G. M., Pagon, R. A., Wallace, S. E., Bean, L. J., Gripp, K. W., Amemiya, A., Eds.; University of Washington, Seattle: Seattle (WA), 1993.
(62) Trimble, A.; Zeman, K.; Wu, J.; Ceppe, A.; Bennett, W.; Donaldson, S. Effect of Airway Clearance Therapies on Mucociliary Clearance in Adults with Cystic Fibrosis: A Randomized Controlled Trial. *PloS One* **2022**, *17* (5), e0268622. https://doi.org/10.1371/journal.pone.0268622.
(63) Southern, K. W.; Clancy, J. P.; Ranganathan, S. Aerosolized Agents for Airway Clearance in Cystic Fibrosis. *Pediatr. Pulmonol.* **2019**, *54* (6), 858–864. https://doi.org/10.1002/ppul.24306.
(64) Terlizzi, V.; Castellani, C.; Taccetti, G.; Ferrari, B. Dornase Alfa in Cystic Fibrosis: Indications, Comparative Studies and Effects on Lung Clearance Index. *Ital. J. Pediatr.* **2022**, *48* (1), 141. https://doi.org/10.1186/s13052-022-01331-5.
(65) Goor, F. V.; Hadida, S.; Grootenhuis, P. D. J.; Burton, B.; Cao, D.; Neuberger, T.; Turnbull, A.; Singh, A.; Joubran, J.; Hazlewood, A.; Zhou, J.; McCartney, J.; Arumugam, V.; Decker, C.; Yang, J.; Young, C.; Olson, E. R.; Wine, J. J.; Frizzell, R. A.; Ashlock, M.; Negulescu, P. Rescue of CF Airway Epithelial Cell Function in Vitro by a CFTR Potentiator, VX-770. 6.
(66) Eckford, P. D. W.; Li, C.; Ramjeesingh, M.; Bear, C. E. Cystic Fibrosis Transmembrane Conductance Regulator (CFTR) Potentiator VX-770 (Ivacaftor) Opens the Defective Channel Gate of Mutant CFTR in a Phosphorylation-Dependent but ATP-Independent Manner. *J. Biol. Chem.* **2012**, *287* (44), 36639–36649. https://doi.org/10.1074/jbc.M112.393637.
(67) Van Goor, F.; Hadida, S.; Grootenhuis, P. D. J.; Burton, B.; Stack, J. H.; Straley, K. S.; Decker, C. J.; Miller, M.; McCartney, J.; Olson, E. R.; Wine, J. J.; Frizzell, R. A.; Ashlock, M.; Negulescu, P. A. Correction of the F508del-CFTR Protein Processing Defect in Vitro by the Investigational Drug VX-809. *Proc. Natl. Acad. Sci. U. S. A.* **2011**, *108* (46), 18843–18848. https://doi.org/10.1073/pnas.1105787108.
(68) Cholon, D. M.; Quinney, N. L.; Fulcher, M. L.; Esther, C. R.; Das, J.; Dokholyan, N. V.; Randell, S. H.; Boucher, R. C.; Gentzsch, M. Potentiator Ivacaftor Abrogates Pharmacological Correction of ΔF508 CFTR in Cystic Fibrosis. *Sci. Transl. Med.* **2014**, *6* (246), 246ra96. https://doi.org/10.1126/scitranslmed.3008680.
(69) Taylor-Cousar, J. L.; Munck, A.; McKone, E. F.; van der Ent, C. K.; Moeller, A.; Simard, C.; Wang, L. T.; Ingenito, E. P.; McKee, C.; Lu, Y.; Lekstrom-Himes, J.; Elborn, J. S. Tezacaftor-Ivacaftor in Patients with Cystic Fibrosis Homozygous for Phe508del. *N. Engl. J. Med.* **2017**, *377* (21), 2013–2023. https://doi.org/10.1056/NEJMoa1709846.
(70) Heijerman, H. G. M.; McKone, E. F.; Downey, D. G.; Van Braeckel, E.; Rowe, S. M.; Tullis, E.; Mall, M. A.; Welter, J. J.; Ramsey, B. W.; McKee, C. M.; Marigowda, G.; Moskowitz, S. M.; Waltz, D.; Sosnay, P. R.; Simard, C.; Ahluwalia, N.; Xuan, F.; Zhang, Y.; Taylor-Cousar, J. L.; McCoy, K. S.; VX17-445-103 Trial Group. Efficacy and Safety of the Elexacaftor plus Tezacaftor plus Ivacaftor Combination Regimen in People with Cystic Fibrosis Homozygous for the F508del Mutation: A Double-Blind, Randomised, Phase 3 Trial. *Lancet Lond. Engl.* **2019**, *394* (10212), 1940–1948. https://doi.org/10.1016/S0140-6736(19)32597-8.
(71) Elexacaftor/Tezacaftor/Ivacaftor (Trikafta) for Cystic Fibrosis. *Med. Lett. Drugs Ther.* **2020**, *62* (1589), 5–7.
(72) Keating, D.; Marigowda, G.; Burr, L.; Daines, C.; Mall, M. A.; McKone, E. F.; Ramsey, B. W.; Rowe, S. M.; Sass, L. A.; Tullis, E.; McKee, C. M.; Moskowitz, S. M.; Robertson, S.;

Savage, J.; Simard, C.; Van Goor, F.; Waltz, D.; Xuan, F.; Young, T.; Taylor-Cousar, J. L.; VX16-445-001 Study Group. VX-445-Tezacaftor-Ivacaftor in Patients with Cystic Fibrosis and One or Two Phe508del Alleles. *N. Engl. J. Med.* **2018**, *379* (17), 1612–1620. https://doi.org/10.1056/NEJMoa1807120.

(73) *Path to a Cure: Many Routes, One Mission | Cystic Fibrosis Foundation*. https://www.cff.org/research-clinical-trials/path-cure-many-routes-one-mission (accessed 2024-09-04).

(74) Da Silva Sanchez, A.; Paunovska, K.; Cristian, A.; Dahlman, J. E. Treating Cystic Fibrosis with mRNA and CRISPR. *Hum. Gene Ther.* **2020**, *31* (17–18), 940–955. https://doi.org/10.1089/hum.2020.137.

(75) Sui, H.; Xu, X.; Su, Y.; Gong, Z.; Yao, M.; Liu, X.; Zhang, T.; Jiang, Z.; Bai, T.; Wang, J.; Zhang, J.; Xu, C.; Luo, M. Gene Therapy for Cystic Fibrosis: Challenges and Prospects. *Front. Pharmacol.* **2022**, *13*, 1015926. https://doi.org/10.3389/fphar.2022.1015926.

(76) Ongun, M.; Lokras, A. G.; Baghel, S.; Shi, Z.; Schmidt, S. T.; Franzyk, H.; Rades, T.; Sebastiani, F.; Thakur, A.; Foged, C. Lipid Nanoparticles for Local Delivery of mRNA to the Respiratory Tract: Effect of PEG-Lipid Content and Administration Route. *Eur. J. Pharm. Biopharm. Off. J. Arbeitsgemeinschaft Pharm. Verfahrenstechnik EV* **2024**, *198*, 114266. https://doi.org/10.1016/j.ejpb.2024.114266.

(77) Swahn, H.; Harris, A. Cell-Selective Regulation of CFTR Gene Expression: Relevance to Gene Editing Therapeutics. *Genes* **2019**, *10* (3), 235. https://doi.org/10.3390/genes10030235.

(78) Wang, G. Genome Editing for Cystic Fibrosis. *Cells* **2023**, *12* (12), 1555. https://doi.org/10.3390/cells12121555.

(79) Merjaneh, L.; Hasan, S.; Kasim, N.; Ode, K. L. The Role of Modulators in Cystic Fibrosis Related Diabetes. *J Clin Transl Endocrinol* **2022**, *27*, 100286. https://doi.org/10.1016/j.jcte.2021.100286.

(80) Bellin, M. D.; Laguna, T.; Leschyshyn, J.; Regelmann, W.; Dunitz, J.; Billings, J.; Moran, A. Insulin Secretion Improves in Cystic Fibrosis Following Ivacaftor Correction of CFTR: A Small Pilot Study. *Pediatr Diabetes* **2013**, *14* (6), 417–421. https://doi.org/10.1111/pedi.12026.

(81) Kelly, A.; De Leon, D. D.; Sheikh, S.; Camburn, D.; Kubrak, C.; Peleckis, A. J.; Stefanovski, D.; Hadjiliadis, D.; Rickels, M. R.; Rubenstein, R. C. Islet Hormone and Incretin Secretion in Cystic Fibrosis after Four Months of Ivacaftor Therapy. *Am J Respir Crit Care Med* **2019**, *199* (3), 342–351. https://doi.org/10.1164/rccm.201806-1018OC.

(82) Piona, C.; Mozzillo, E.; Tosco, A.; Volpi, S.; Rosanio, F. M.; Cimbalo, C.; Franzese, A.; Raia, V.; Zusi, C.; Emiliani, F.; Boselli, M. L.; Trombetta, M.; Bonadonna, R. C.; Cipolli, M.; Maffeis, C. Impact of CFTR Modulators on Beta-Cell Function in Children and Young Adults with Cystic Fibrosis. *J Clin Med* **2022**, *11* (14). https://doi.org/10.3390/jcm11144149.

(83) Crow, H.; Bengtson, C.; Shi, X.; Graves, L.; Anabtawi, A. CGM Patterns in Adults with Cystic Fibrosis-Related Diabetes before and after Elexacaftor-Tezacaftor-Ivacaftor Therapy. *J. Clin. Transl. Endocrinol.* **2022**, *30*, 100307. https://doi.org/10.1016/j.jcte.2022.100307.

(84) Baker, E. H.; Janaway, C. H.; Philips, B. J.; Brennan, A. L.; Baines, D. L.; Wood, D. M.; Jones, P. W. Hyperglycaemia Is Associated with Poor Outcomes in Patients Admitted to Hospital with Acute Exacerbations of Chronic Obstructive Pulmonary Disease. *Thorax* **2006**, *61* (4), 284–289. https://doi.org/10.1136/thx.2005.051029.

(85) Hsia, C. C. W.; Raskin, P. Lung Function Changes Related to Diabetes Mellitus. *Diabetes Technol. Ther.* **2007**, *9 Suppl 1*, S73-82. https://doi.org/10.1089/dia.2007.0227.

(86) Goldman, M. D. Lung Dysfunction in Diabetes. *Diabetes Care* **2003**, *26* (6), 1915–1918. https://doi.org/10.2337/diacare.26.6.1915.
(87) Pitocco, D.; Fuso, L.; Conte, E. G.; Zaccardi, F.; Condoluci, C.; Scavone, G.; Incalzi, R. A.; Ghirlanda, G. The Diabetic Lung--a New Target Organ? *Rev. Diabet. Stud. RDS* **2012**, *9* (1), 23–35. https://doi.org/10.1900/RDS.2012.9.23.
(88) Baker, E. H.; Clark, N.; Brennan, A. L.; Fisher, D. A.; Gyi, K. M.; Hodson, M. E.; Philips, B. J.; Baines, D. L.; Wood, D. M. Hyperglycemia and Cystic Fibrosis Alter Respiratory Fluid Glucose Concentrations Estimated by Breath Condensate Analysis. *J. Appl. Physiol. Bethesda Md 1985* **2007**, *102* (5), 1969–1975. https://doi.org/10.1152/japplphysiol.01425.2006.
(89) Hunt, W. R.; Zughaier, S. M.; Guentert, D. E.; Shenep, M. A.; Koval, M.; McCarty, N. A.; Hansen, J. M. Hyperglycemia Impedes Lung Bacterial Clearance in a Murine Model of Cystic Fibrosis-Related Diabetes. *Am. J. Physiol.-Lung Cell. Mol. Physiol.* **2014**, *306* (1), L43–L49. https://doi.org/10.1152/ajplung.00224.2013.
(90) Kelsey, R.; Manderson Koivula, F. N.; McClenaghan, N. H.; Kelly, C. Cystic Fibrosis-Related Diabetes: Pathophysiology and Therapeutic Challenges. *Clin. Med. Insights Endocrinol. Diabetes* **2019**, *12*, 1179551419851770. https://doi.org/10.1177/1179551419851770.
(91) Stecenko, A. A.; Moran, A. Update on Cystic Fibrosis-Related Diabetes. *Curr. Opin. Pulm. Med.* **2010**, *16* (6), 611–615. https://doi.org/10.1097/MCP.0b013e32833e8700.
(92) Norris, A. W.; Ode, K. L.; Merjaneh, L.; Sanda, S.; Yi, Y.; Sun, X.; Engelhardt, J. F.; Hull, R. L. Survival in a Bad Neighborhood: Pancreatic Islets in Cystic Fibrosis. *J. Endocrinol.* **2019**. https://doi.org/10.1530/JOE-18-0468.
(93) Koivula, F. N. M.; McClenaghan, N. H.; Harper, A. G. S.; Kelly, C. Islet-Intrinsic Effects of CFTR Mutation. *Diabetologia* **2016**, *59* (7), 1350–1355. https://doi.org/10.1007/s00125-016-3936-1.
(94) Khare, S.; Desimone, M.; Kasim, N.; Chan, C. L. Cystic Fibrosis-Related Diabetes: Prevalence, Screening, and Diagnosis. *J. Clin. Transl. Endocrinol.* **2022**, *27*, 100290. https://doi.org/10.1016/j.jcte.2021.100290.
(95) Bonhoure, A.; Potter, K. J.; Colomba, J.; Boudreau, V.; Bergeron, C.; Desjardins, K.; Carricart, M.; Tremblay, F.; Lavoie, A.; Rabasa-Lhoret, R. Peak Glucose during an Oral Glucose Tolerance Test Is Associated with Future Diabetes Risk in Adults with Cystic Fibrosis. *Diabetologia* **2021**, *64* (6), 1332–1341. https://doi.org/10.1007/s00125-021-05423-5.
(96) Godbout, A.; Hammana, I.; Potvin, S.; Mainville, D.; Rakel, A.; Berthiaume, Y.; Chiasson, J.-L.; Coderre, L.; Rabasa-Lhoret, R. No Relationship between Mean Plasma Glucose and Glycated Haemoglobin in Patients with Cystic Fibrosis-Related Diabetes. *Diabetes Metab.* **2008**, *34* (6), 568–573. https://doi.org/10.1016/j.diabet.2008.05.010.
(97) Umpierrez, G. E.; Klonoff, D. C. Diabetes Technology Update: Use of Insulin Pumps and Continuous Glucose Monitoring in the Hospital. *Diabetes Care* **2018**, *41* (8), 1579–1589. https://doi.org/10.2337/dci18-0002.
(98) Putman, M. S.; Norris, A. W.; Hull, R. L.; Rickels, M. R.; Sussel, L.; Blackman, S. M.; Chan, C. L.; Ode, K. L.; Daley, T.; Stecenko, A. A.; Moran, A.; Helmick, M. J.; Cray, S.; Alvarez, J. A.; Stallings, V. A.; Tuggle, K. L.; Clancy, J. P.; Eggerman, T. L.; Engelhardt, J. F.; Kelly, A. Cystic Fibrosis–Related Diabetes Workshop: Research Priorities Spanning Disease

Pathophysiology, Diagnosis, and Outcomes. *Diabetes Care* **2023**, *46* (6), 1112–1123. https://doi.org/10.2337/dc23-0380.

(99) Prentice, B. J.; Potter, K. J.; Coriati, A.; Boudreau, V.; Rusnell, L.; Kherani, T.; Senior, P. A.; Hameed, S.; Rabasa-Lhoret, R. Cystic Fibrosis-Related Diabetes: Clinical Approach and Knowledge Gaps. *Paediatr. Respir. Rev.* **2023**, *46*, 3–11. https://doi.org/10.1016/j.prrv.2022.10.001.

(100) *Cell Model Resources | Cystic Fibrosis Foundation*. https://www.cff.org/researchers/cell-model-resources (accessed 2024-06-12).

(101) Gottschalk, L. B.; Vecchio-Pagan, B.; Sharma, N.; Han, S. T.; Franca, A.; Wohler, E. S.; Batista, D. A. S.; Goff, L. A.; Cutting, G. R. Creation and Characterization of an Airway Epithelial Cell Line for Stable Expression of CFTR Variants. *J. Cyst. Fibros.* **2016**, *15* (3), 285–294. https://doi.org/10.1016/j.jcf.2015.11.010.

(102) Cozens, A. L.; Yezzi, M. J.; Kunzelmann, K.; Ohrui, T.; Chin, L.; Eng, K.; Finkbeiner, W. E.; Widdicombe, J. H.; Gruenert, D. C. CFTR Expression and Chloride Secretion in Polarized Immortal Human Bronchial Epithelial Cells. *Am. J. Respir. Cell Mol. Biol.* **1994**, *10* (1), 38–47. https://doi.org/10.1165/ajrcmb.10.1.7507342.

(103) Callaghan, P. J.; Ferrick, B.; Rybakovsky, E.; Thomas, S.; Mullin, J. M. Epithelial Barrier Function Properties of the 16HBE14o- Human Bronchial Epithelial Cell Culture Model. *Biosci. Rep.* **2020**, *40* (10), BSR20201532. https://doi.org/10.1042/BSR20201532.

(104) Whitsett, J. A. Airway Epithelial Differentiation and Mucociliary Clearance. *Ann. Am. Thorac. Soc.* **2018**, *15* (Supplement_3), S143–S148. https://doi.org/10.1513/AnnalsATS.201802-128AW.

(105) Hewitt, R. J.; Lloyd, C. M. Regulation of Immune Responses by the Airway Epithelial Cell Landscape. *Nat. Rev. Immunol.* **2021**, *21* (6), 347–362. https://doi.org/10.1038/s41577-020-00477-9.

(106) Montoro, D. T.; Haber, A. L.; Biton, M.; Vinarsky, V.; Lin, B.; Birket, S. E.; Yuan, F.; Chen, S.; Leung, H. M.; Villoria, J.; Rogel, N.; Burgin, G.; Tsankov, A. M.; Waghray, A.; Slyper, M.; Waldman, J.; Nguyen, L.; Dionne, D.; Rozenblatt-Rosen, O.; Tata, P. R.; Mou, H.; Shivaraju, M.; Bihler, H.; Mense, M.; Tearney, G. J.; Rowe, S. M.; Engelhardt, J. F.; Regev, A.; Rajagopal, J. A Revised Airway Epithelial Hierarchy Includes CFTR-Expressing Ionocytes. *Nature* **2018**, *560* (7718), 319–324. https://doi.org/10.1038/s41586-018-0393-7.

(107) Miller, A. J.; Yu, Q.; Czerwinski, M.; Tsai, Y.-H.; Conway, R. F.; Wu, A.; Holloway, E. M.; Walker, T.; Glass, I. A.; Treutlein, B.; Camp, J. G.; Spence, J. R. In Vitro and In Vivo Development of the Human Airway at Single-Cell Resolution. *Dev. Cell* **2020**, *53* (1), 117-128.e6. https://doi.org/10.1016/j.devcel.2020.01.033.

(108) *A medium composition containing normal resting glucose that supports differentiation of primary human airway cells | Scientific Reports*. https://www.nature.com/articles/s41598-022-05446-x (accessed 2024-04-02).

(109) Semaniakou, A.; Croll, R. P.; Chappe, V. Animal Models in the Pathophysiology of Cystic Fibrosis. *Front. Pharmacol.* **2018**, *9*, 1475. https://doi.org/10.3389/fphar.2018.01475.

(110) McCarron, A.; Parsons, D.; Donnelley, M. Animal and Cell Culture Models for Cystic Fibrosis: Which Model Is Right for Your Application? *Am. J. Pathol.* **2021**, *191* (2), 228–242. https://doi.org/10.1016/j.ajpath.2020.10.017.

(111) Zhou, L.; Dey, C. R.; Wert, S. E.; DuVall, M. D.; Frizzell, R. A.; Whitsett, J. A. Correction of Lethal Intestinal Defect in a Mouse Model of Cystic Fibrosis by Human CFTR. *Science* **1994**, *266* (5191), 1705–1708.

(112) French, P. J.; van Doorninck, J. H.; Peters, R. H.; Verbeek, E.; Ameen, N. A.; Marino, C. R.; de Jonge, H. R.; Bijman, J.; Scholte, B. J. A Delta F508 Mutation in Mouse Cystic Fibrosis Transmembrane Conductance Regulator Results in a Temperature-Sensitive Processing Defect in Vivo. *J. Clin. Invest.* **1996**, *98* (6), 1304–1312.

(113) Livraghi, A.; Grubb, B. R.; Hudson, E. J.; Wilkinson, K. J.; Sheehan, J. K.; Mall, M. A.; O'Neal, W. K.; Boucher, R. C.; Randell, S. H. Airway and Lung Pathology Due to Mucosal Surface Dehydration in {beta}-Epithelial Na+ Channel-Overexpressing Mice: Role of TNF-{alpha} and IL-4R{alpha} Signaling, Influence of Neonatal Development, and Limited Efficacy of Glucocorticoid Treatment. *J. Immunol. Baltim. Md 1950* **2009**, *182* (7), 4357–4367. https://doi.org/10.4049/jimmunol.0802557.

(114) Rogers, C. S.; Abraham, W. M.; Brogden, K. A.; Engelhardt, J. F.; Fisher, J. T.; McCray, P. B.; McLennan, G.; Meyerholz, D. K.; Namati, E.; Ostedgaard, L. S.; Prather, R. S.; Sabater, J. R.; Stoltz, D. A.; Zabner, J.; Welsh, M. J. The Porcine Lung as a Potential Model for Cystic Fibrosis. *Am. J. Physiol. Lung Cell. Mol. Physiol.* **2008**, *295* (2), L240-263. https://doi.org/10.1152/ajplung.90203.2008.

(115) Rogers, C. S.; Hao, Y.; Rokhlina, T.; Samuel, M.; Stoltz, D. A.; Li, Y.; Petroff, E.; Vermeer, D. W.; Kabel, A. C.; Yan, Z.; Spate, L.; Wax, D.; Murphy, C. N.; Rieke, A.; Whitworth, K.; Linville, M. L.; Korte, S. W.; Engelhardt, J. F.; Welsh, M. J.; Prather, R. S. Production of CFTR-Null and CFTR-DeltaF508 Heterozygous Pigs by Adeno-Associated Virus-Mediated Gene Targeting and Somatic Cell Nuclear Transfer. *J. Clin. Invest.* **2008**, *118* (4), 1571–1577. https://doi.org/10.1172/JCI34773.

(116) Stoltz, D. A.; Meyerholz, D. K.; Pezzulo, A. A.; Ramachandran, S.; Rogan, M. P.; Davis, G. J.; Hanfland, R. A.; Wohlford-Lenane, C.; Dohrn, C. L.; Bartlett, J. A.; Nelson, G. A.; Chang, E. H.; Taft, P. J.; Ludwig, P. S.; Estin, M.; Hornick, E. E.; Launspach, J. L.; Samuel, M.; Rokhlina, T.; Karp, P. H.; Ostedgaard, L. S.; Uc, A.; Starner, T. D.; Horswill, A. R.; Brogden, K. A.; Prather, R. S.; Richter, S. S.; Shilyansky, J.; McCray, P. B.; Zabner, J.; Welsh, M. J. Cystic Fibrosis Pigs Develop Lung Disease and Exhibit Defective Bacterial Eradication at Birth. *Sci. Transl. Med.* **2010**, *2* (29), 29ra31. https://doi.org/10.1126/scitranslmed.3000928.

(117) Sun, X.; Olivier, A. K.; Liang, B.; Yi, Y.; Sui, H.; Evans, T. I. A.; Zhang, Y.; Zhou, W.; Tyler, S. R.; Fisher, J. T.; Keiser, N. W.; Liu, X.; Yan, Z.; Song, Y.; Goeken, J. A.; Kinyon, J. M.; Fligg, D.; Wang, X.; Xie, W.; Lynch, T. J.; Kaminsky, P. M.; Stewart, Z. A.; Pope, R. M.; Frana, T.; Meyerholz, D. K.; Parekh, K.; Engelhardt, J. F. Lung Phenotype of Juvenile and Adult Cystic Fibrosis Transmembrane Conductance Regulator-Knockout Ferrets. *Am. J. Respir. Cell Mol. Biol.* **2014**, *50* (3), 502–512. https://doi.org/10.1165/rcmb.2013-0261OC.

(118) Sun, X.; Sui, H.; Fisher, J. T.; Yan, Z.; Liu, X.; Cho, H.-J.; Joo, N. S.; Zhang, Y.; Zhou, W.; Yi, Y.; Kinyon, J. M.; Lei-Butters, D. C.; Griffin, M. A.; Naumann, P.; Luo, M.; Ascher, J.; Wang, K.; Frana, T.; Wine, J. J.; Meyerholz, D. K.; Engelhardt, J. F. Disease Phenotype of a Ferret CFTR-Knockout Model of Cystic Fibrosis. *J. Clin. Invest.* **2010**, *120* (9), 3149–3160. https://doi.org/10.1172/JCI43052.

(119) Rosen, B. H.; Evans, T. I. A.; Moll, S. R.; Gray, J. S.; Liang, B.; Sun, X.; Zhang, Y.; Jensen-Cody, C. W.; Swatek, A. M.; Zhou, W.; He, N.; Rotti, P. G.; Tyler, S. R.; Keiser, N. W.; Anderson, P. J.; Brooks, L.; Li, Y.; Pope, R. M.; Rajput, M.; Hoffman, E. A.; Wang, K.; Harris, J. K.; Parekh, K. R.; Gibson-Corley, K. N.; Engelhardt, J. F. Infection Is Not Required for Mucoinflammatory Lung Disease in CFTR-Knockout Ferrets. *Am. J. Respir. Crit. Care Med.* **2018**, *197* (10), 1308–1318. https://doi.org/10.1164/rccm.201708-1616OC.

(120) Yan, Z.; Vorhies, K.; Feng, Z.; Park, S. Y.; Choi, S. H.; Zhang, Y.; Winter, M.; Sun, X.; Engelhardt, J. F. Recombinant Adeno-Associated Virus-Mediated Editing of the G551D Cystic Fibrosis Transmembrane Conductance Regulator Mutation in Ferret Airway Basal Cells. *Hum. Gene Ther.* **2022**, *33* (19–20), 1023–1036. https://doi.org/10.1089/hum.2022.036.

(121) Yuan, F.; Gasser, G. N.; Lemire, E.; Montoro, D. T.; Jagadeesh, K.; Zhang, Y.; Duan, Y.; Ievlev, V.; Wells, K. L.; Rotti, P. G.; Shahin, W.; Winter, M.; Rosen, B. H.; Evans, I.; Cai, Q.; Yu, M.; Walsh, S. A.; Acevedo, M. R.; Pandya, D. N.; Akurathi, V.; Dick, D. W.; Wadas, T. J.; Joo, N. S.; Wine, J. J.; Birket, S.; Fernandez, C. M.; Leung, H. M.; Tearney, G. J.; Verkman, A. S.; Haggie, P. M.; Scott, K.; Bartels, D.; Meyerholz, D. K.; Rowe, S. M.; Liu, X.; Yan, Z.; Haber, A. L.; Sun, X.; Engelhardt, J. F. Transgenic Ferret Models Define Pulmonary Ionocyte Diversity and Function. *Nature* **2023**, *621* (7980), 857–867. https://doi.org/10.1038/s41586-023-06549-9.

(122) Lopes-Pacheco, M. CFTR Modulators: The Changing Face of Cystic Fibrosis in the Era of Precision Medicine. *Front. Pharmacol.* **2019**, *10*, 1662. https://doi.org/10.3389/fphar.2019.01662.

(123) Felipe Montiel, A.; Álvarez Fernández, A.; Traversi, L.; Polverino, E. The Ageing of Cystic Fibrosis Patients with New Modulators: Current Gaps and Challenges. *Expert Rev. Respir. Med.* **2023**, *17* (12), 1091–1094. https://doi.org/10.1080/17476348.2024.2311109.

(124) Baker, E. H.; Clark, N.; Brennan, A. L.; Fisher, D. A.; Gyi, K. M.; Hodson, M. E.; Philips, B. J.; Baines, D. L.; Wood, D. M. Hyperglycemia and Cystic Fibrosis Alter Respiratory Fluid Glucose Concentrations Estimated by Breath Condensate Analysis. *J. Appl. Physiol.* **2007**, *102* (5), 1969–1975. https://doi.org/10.1152/japplphysiol.01425.2006.

(125) Molina, S. A.; Stauffer, B.; Moriarty, H. K.; Kim, A. H.; McCarty, N. A.; Koval, M. Junctional Abnormalities in Human Airway Epithelial Cells Expressing F508del CFTR. 13.

(126) Molina, S. A.; Moriarty, H. K.; Infield, D. T.; Imhoff, B. R.; Vance, R. J.; Kim, A. H.; Hansen, J. M.; Hunt, W. R.; Koval, M.; McCarty, N. A. Insulin Signaling via the PI3-Kinase/Akt Pathway Regulates Airway Glucose Uptake and Barrier Function in a CFTR-Dependent Manner. *Am. J. Physiol.-Lung Cell. Mol. Physiol.* **2017**, *312* (5), L688–L702. https://doi.org/10.1152/ajplung.00364.2016.

(127) Lynn, K. S.; Peterson, R. J.; Koval, M. Ruffles and Spikes: Control of Tight Junction Morphology and Permeability by Claudins. *Biochim. Biophys. Acta BBA - Biomembr.* **2020**, *1862* (9), 183339. https://doi.org/10.1016/j.bbamem.2020.183339.

(128) Koval, M. Claudin Heterogeneity and Control of Lung Tight Junctions. *Annu. Rev. Physiol.* **2013**, *75*, 551–567. https://doi.org/10.1146/annurev-physiol-030212-183809.

(129) Schlingmann, B.; Molina, S. A.; Koval, M. Claudins: Gatekeepers of Lung Epithelial Function. *Semin. Cell Dev. Biol.* **2015**, *42*, 47–57. https://doi.org/10.1016/j.semcdb.2015.04.009.

(130) Soini, Y. Claudins in Lung Diseases. *Respir. Res.* **2011**, *12* (1), 70. https://doi.org/10.1186/1465-9921-12-70.

(131) Valley, H. C.; Bukis, K. M.; Bell, A.; Cheng, Y.; Wong, E.; Jordan, N. J.; Allaire, N. E.; Sivachenko, A.; Liang, F.; Bihler, H.; Thomas, P. J.; Mahiou, J.; Mense, M. Isogenic Cell Models of Cystic Fibrosis-Causing Variants in Natively Expressing Pulmonary Epithelial Cells. *J. Cyst. Fibros. Off. J. Eur. Cyst. Fibros. Soc.* **2019**, *18* (4), 476–483. https://doi.org/10.1016/j.jcf.2018.12.001.

(132) Subramanian, A.; Tamayo, P.; Mootha, V. K.; Mukherjee, S.; Ebert, B. L.; Gillette, M. A.; Paulovich, A.; Pomeroy, S. L.; Golub, T. R.; Lander, E. S.; Mesirov, J. P. Gene Set Enrichment Analysis: A Knowledge-Based Approach for Interpreting Genome-Wide Expression Profiles. *Proc. Natl. Acad. Sci.* **2005**, *102* (43), 15545–15550. https://doi.org/10.1073/pnas.0506580102.

(133) Wray, C.; Mao, Y.; Pan, J.; Chandrasena, A.; Piasta, F.; Frank, J. A. Claudin-4 Augments Alveolar Epithelial Barrier Function and Is Induced in Acute Lung Injury. *Am. J. Physiol.-Lung Cell. Mol. Physiol.* **2009**, *297* (2), L219–L227. https://doi.org/10.1152/ajplung.00043.2009.

(134) Rokkam, D.; LaFemina, M. J.; Lee, J. W.; Matthay, M. A.; Frank, J. A. Claudin-4 Levels Are Associated with Intact Alveolar Fluid Clearance in Human Lungs. *Am. J. Pathol.* **2011**, *179* (3), 1081–1087. https://doi.org/10.1016/j.ajpath.2011.05.017.

(135) Mitchell, L. A.; Overgaard, C. E.; Ward, C.; Margulies, S. S.; Koval, M. Differential Effects of Claudin-3 and Claudin-4 on Alveolar Epithelial Barrier Function. *Am. J. Physiol.-Lung Cell. Mol. Physiol.* **2011**, *301* (1), L40–L49. https://doi.org/10.1152/ajplung.00299.2010.

(136) Sharma, S.; Tripathi, P.; Sharma, J.; Dixit, A. Flavonoids Modulate Tight Junction Barrier Functions in Hyperglycemic Human Intestinal Caco-2 Cells. *Nutrition* **2020**, *78*, 110792. https://doi.org/10.1016/j.nut.2020.110792.

(137) Villarroel, M.; García-Ramírez, M.; Corraliza, L.; Hernández, C.; Simó, R. Effects of High Glucose Concentration on the Barrier Function and the Expression of Tight Junction Proteins in Human Retinal Pigment Epithelial Cells. *Exp. Eye Res.* **2009**, *89* (6), 913–920. https://doi.org/10.1016/j.exer.2009.07.017.

(138) Mongelli-Sabino, B. M.; Canuto, L. P.; Collares-Buzato, C. B. Acute and Chronic Exposure to High Levels of Glucose Modulates Tight Junction-Associated Epithelial Barrier Function in a Renal Tubular Cell Line. *Life Sci.* **2017**, *188*, 149–157. https://doi.org/10.1016/j.lfs.2017.09.004.

(139) Kage, H.; Flodby, P.; Gao, D.; Kim, Y. H.; Marconett, C. N.; DeMaio, L.; Kim, K.-J.; Crandall, E. D.; Borok, Z. Claudin 4 Knockout Mice: Normal Physiological Phenotype with Increased Susceptibility to Lung Injury. *Am. J. Physiol.-Lung Cell. Mol. Physiol.* **2014**, *307* (7), L524–L536. https://doi.org/10.1152/ajplung.00077.2014.

(140) Boni, C.; Laudanna, C.; Sorio, C. A Comprehensive Review of Receptor-Type Tyrosine-Protein Phosphatase Gamma (PTPRG) Role in Health and Non-Neoplastic Disease. *Biomolecules* **2022**, *12* (1), 84. https://doi.org/10.3390/biom12010084.

(141) Brenachot, X.; Ramadori, G.; Ioris, R. M.; Veyrat-Durebex, C.; Altirriba, J.; Aras, E.; Ljubicic, S.; Kohno, D.; Fabbiano, S.; Clement, S.; Goossens, N.; Trajkovski, M.; Harroch, S.; Negro, F.; Coppari, R. Hepatic Protein Tyrosine Phosphatase Receptor Gamma Links Obesity-Induced Inflammation to Insulin Resistance. *Nat. Commun.* **2017**, *8* (1), 1820. https://doi.org/10.1038/s41467-017-02074-2.

(142) Cheung, A. K. L.; Ip, J. C. Y.; Chu, A. C. H.; Cheng, Y.; Leong, M. M. L.; Ko, J. M. Y.; Shuen, W. H.; Lung, H. L.; Lung, M. L. PTPRG Suppresses Tumor Growth and Invasion via Inhibition of Akt Signaling in Nasopharyngeal Carcinoma. *Oncotarget* **2015**, *6* (15), 13434–13447. https://doi.org/10.18632/oncotarget.3876.

(143) Sieber, P.; Schäfer, A.; Lieberherr, R.; Caimi, S. L.; Lüthi, U.; Ryge, J.; Bergmann, J. H.; Le Goff, F.; Stritt, M.; Blattmann, P.; Renault, B.; Rammelt, P.; Sempere, B.; Freti, D.; Studer, R.; White, E. S.; Birker-Robaczewska, M.; Boucher, M.; Nayler, O. NF-κB Drives Epithelial-

Mesenchymal Mechanisms of Lung Fibrosis in a Translational Lung Cell Model. *JCI Insight* **2023**, *8* (3), e154719. https://doi.org/10.1172/jci.insight.154719.

(144) Garnett, J. P.; Gray, M. A.; Tarran, R.; Brodlie, M.; Ward, C.; Baker, E. H.; Baines, D. L. Elevated Paracellular Glucose Flux across Cystic Fibrosis Airway Epithelial Monolayers Is an Important Factor for Pseudomonas Aeruginosa Growth. *PLoS One* **2013**, *8* (10), e76283. https://doi.org/10.1371/journal.pone.0076283.

(145) Coyne, C. B.; Vanhook, M. K.; Gambling, T. M.; Carson, J. L.; Boucher, R. C.; Johnson, L. G. Regulation of Airway Tight Junctions by Proinflammatory Cytokines. *Mol Biol Cell* **2002**, *13* (9), 3218–3234. https://doi.org/10.1091/mbc.e02-03-0134.

(146) Tirouvanziam, R.; Gernez, Y.; Conrad, C. K.; Moss, R. B.; Schrijver, I.; Dunn, C. E.; Davies, Z. A.; Herzenberg, L. A.; Herzenberg, L. A. Profound Functional and Signaling Changes in Viable Inflammatory Neutrophils Homing to Cystic Fibrosis Airways. *Proc Natl Acad Sci U A* **2008**, *105* (11), 4335–4339. https://doi.org/10.1073/pnas.0712386105.

(147) Zhang, Y.; Black, K. E.; Phung, T.-K. N.; Thundivalappil, S. R.; Lin, T.; Wang, W.; Xu, J.; Zhang, C.; Hariri, L. P.; Lapey, A.; Li, H.; Lerou, P. H.; Ai, X.; Que, J.; Park, J.-A.; Hurley, B. P.; Mou, H. Human Airway Basal Cells Undergo Reversible Squamous Differentiation and Reshape Innate Immunity. *Am. J. Respir. Cell Mol. Biol. 68* (6), 664–678. https://doi.org/10.1165/rcmb.2022-0299OC.

(148) Granados, A.; Chan, C. L.; Ode, K. L.; Moheet, A.; Moran, A.; Holl, R. Cystic Fibrosis Related Diabetes: Pathophysiology, Screening and Diagnosis. *J. Cyst. Fibros.* **2019**, *18*, S3–S9. https://doi.org/10.1016/j.jcf.2019.08.016.

(149) Elborn, J. S. Cystic Fibrosis. *Lancet Lond. Engl.* **2016**, *388* (10059), 2519–2531. https://doi.org/10.1016/S0140-6736(16)00576-6.

(150) Cystic Fibrosis Foundation. 2022 Patient Registry Annual Report. https://www.cff.org/medical-professionals/patient-registry.

(151) Bierlaagh, M. C.; Muilwijk, D.; Beekman, J. M.; van der Ent, C. K. A New Era for People with Cystic Fibrosis. *Eur. J. Pediatr.* **2021**, *180* (9), 2731–2739. https://doi.org/10.1007/s00431-021-04168-y.

(152) Boucher, R. C. An Overview of the Pathogenesis of Cystic Fibrosis Lung Disease. *Adv. Drug Deliv. Rev.* **2002**, *54* (11), 1359–1371. https://doi.org/10.1016/S0169-409X(02)00144-8.

(153) *11965 - DMEM, high glucose - US*. https://www.thermofisher.com/us/en/home/technical-resources/media-formulation.8.html (accessed 2021-11-23).

(154) CDC. *Diabetes Testing*. Centers for Disease Control and Prevention. https://www.cdc.gov/diabetes/basics/getting-tested.html (accessed 2021-11-15).

(155) Torimoto, K.; Okuno, K.; Kuroda, R.; Shanas, N.; Cicalese, S. M.; Eguchi, K.; Elliott, K. J.; Kawai, T.; Corbett, C. B.; Peluzzo, A. M.; St. Paul, A. K.; Autieri, M. V.; Scalia, R.; Rizzo, V.; Hashimoto, T.; Eguchi, S. Glucose Consumption of Vascular Cell Types in Culture: Toward Optimization of Experimental Conditions. *Am. J. Physiol. - Cell Physiol.* **2022**, *322* (1), C73–C85. https://doi.org/10.1152/ajpcell.00257.2021.

(156) Winkler, S.; Menke, J.; Meyer, K. V.; Kortmann, C.; Bahnemann, J. Automation of Cell Culture Assays Using a 3D-Printed Servomotor-Controlled Microfluidic Valve System. *Lab. Chip* **2022**, *22* (23), 4656–4665. https://doi.org/10.1039/D2LC00629D.

(157) Byun, C. K.; Abi-Samra, K.; Cho, Y.-K.; Takayama, S. Pumps for Microfluidic Cell Culture. *ELECTROPHORESIS* **2014**, *35* (2–3), 245–257. https://doi.org/10.1002/elps.201300205.

(158) Dkhar, D. S.; Kumari, R.; Malode, S. J.; Shetti, N. P.; Chandra, P. Integrated Lab-on-a-Chip Devices: Fabrication Methodologies, Transduction System for Sensing Purposes. *J. Pharm. Biomed. Anal.* **2023**, *223*, 115120. https://doi.org/10.1016/j.jpba.2022.115120.

(159) Cui, G.; Moustafa, D. A.; Zhao, S.; Vazquez Cegla, A.; Lyles, J. T.; Goldberg, J. B.; Chandler, J. D.; McCarty, N. A. Chronic Hyperglycemia Aggravates Lung Function in a Scnn1b-Tg Murine Model. *Am. J. Physiol. Lung Cell. Mol. Physiol.* **2024**. https://doi.org/10.1152/ajplung.00279.2023.

(160) Cottrill, K. A.; Peterson, R. J.; Lewallen, C. F.; Koval, M.; Bridges, R. J.; McCarty, N. A. Sphingomyelinase Decreases Transepithelial Anion Secretion in Airway Epithelial Cells in Part by Inhibiting CFTR-Mediated Apical Conductance. *Physiol. Rep.* **2021**, *9* (15), e14928. https://doi.org/10.14814/phy2.14928.

(161) Ohta, A.; Kawai, S.; Pretemer, Y.; Nishio, M.; Nagata, S.; Fuse, H.; Yamagishi, Y.; Toguchida, J. Automated Cell Culture System for the Production of Cell Aggregates with Growth Plate-like Structure from Induced Pluripotent Stem Cells. *SLAS Technol.* **2023**, *28* (6), 433–441. https://doi.org/10.1016/j.slast.2023.08.002.

(162) Seiler, S. T.; Mantalas, G. L.; Selberg, J.; Cordero, S.; Torres-Montoya, S.; Baudin, P. V.; Ly, V. T.; Amend, F.; Tran, L.; Hoffman, R. N.; Rolandi, M.; Green, R. E.; Haussler, D.; Salama, S. R.; Teodorescu, M. Modular Automated Microfluidic Cell Culture Platform Reduces Glycolytic Stress in Cerebral Cortex Organoids. *Sci. Rep.* **2022**, *12* (1), 20173. https://doi.org/10.1038/s41598-022-20096-9.

(163) Bluhmki, T.; Bitzer, S.; Gindele, J. A.; Schruf, E.; Kiechle, T.; Webster, M.; Schymeinsky, J.; Ries, R.; Gantner, F.; Bischoff, D.; Garnett, J.; Heilker, R. Development of a Miniaturized 96-Transwell Air–Liquid Interface Human Small Airway Epithelial Model. *Sci. Rep.* **2020**, *10* (1), 13022. https://doi.org/10.1038/s41598-020-69948-2.

(164) Stalvey, M. S.; Brusko, T. M.; Mueller, C.; Wasserfall, C. H.; Schatz, D. A.; Atkinson, M. A.; Flotte, T. R. CFTR Mutations Impart Elevated Immune Reactivity in a Murine Model of Cystic Fibrosis Related Diabetes. *Cytokine* **2008**, *44* (1), 154–159. https://doi.org/10.1016/j.cyto.2008.07.468.

(165) Yung, B.; Noormohamed, F. H.; Kemp, M.; Hooper, J.; Lant, A. F.; Hodson, M. E. Cystic Fibrosis-Related Diabetes: The Role of Peripheral Insulin Resistance and Beta-Cell Dysfunction. *Diabet Med* **2002**, *19* (3), 221–226. https://doi.org/10.1046/j.1464-5491.2002.00666.x.

(166) Johannesson, B.; Hirtz, S.; Schatterny, J.; Schultz, C.; Mall, M. A. CFTR Regulates Early Pathogenesis of Chronic Obstructive Lung Disease in βENaC-Overexpressing Mice. *PLoS One* **2012**, *7* (8), e44059. https://doi.org/10.1371/journal.pone.0044059.

(167) Leclercq, A.; Gauthier, B.; Rosner, V.; Weiss, L.; Moreau, F.; Constantinescu, A. A.; Kessler, R.; Kessler, L. Early Assessment of Glucose Abnormalities during Continuous Glucose Monitoring Associated with Lung Function Impairment in Cystic Fibrosis Patients. *J Cyst Fibros* **2014**, *13* (4), 478–484. https://doi.org/10.1016/j.jcf.2013.11.005.

(168) Pezzulo, A. A.; Gutiérrez, J.; Duschner, K. S.; McConnell, K. S.; Taft, P. J.; Ernst, S. E.; Yahr, T. L.; Rahmouni, K.; Klesney-Tait, J.; Stoltz, D. A.; Zabner, J. Glucose Depletion in the Airway Surface Liquid Is Essential for Sterility of the Airways. *PLoS One* **2011**, *6* (1), e16166. https://doi.org/10.1371/journal.pone.0016166.

(169) Garnett, J. P.; Gray, M. A.; Tarran, R.; Brodlie, M.; Ward, C.; Baker, E. H.; Baines, D. L. Elevated Paracellular Glucose Flux across Cystic Fibrosis Airway Epithelial Monolayers Is

an Important Factor for Pseudomonas Aeruginosa Growth. *PLOS ONE* **2013**, *8* (10), e76283. https://doi.org/10.1371/journal.pone.0076283.

(170) Baker, E. H.; Baines, D. L. Airway Glucose Homeostasis: A New Target in the Prevention and Treatment of Pulmonary Infection. *Chest* **2018**, *153* (2), 507–514. https://doi.org/10.1016/j.chest.2017.05.031.

(171) Welsh, M. J.; Rogers, C. S.; Stoltz, D. A.; Meyerholz, D. K.; Prather, R. S. Development of a Porcine Model of Cystic Fibrosis. *Trans Am Clin Clim. Assoc* **2009**, *120*, 149–162.

(172) Chen, J. H.; Stoltz, D. A.; Karp, P. H.; Ernst, S. E.; Pezzulo, A. A.; Moninger, T. O.; Rector, M. V.; Reznikov, L. R.; Launspach, J. L.; Chaloner, K.; Zabner, J.; Welsh, M. J. Loss of Anion Transport without Increased Sodium Absorption Characterizes Newborn Porcine Cystic Fibrosis Airway Epithelia. *Cell* **2010**, *143* (6), 911–923. https://doi.org/10.1016/j.cell.2010.11.029.

(173) Mall, M.; Grubb, B. R.; Harkema, J. R.; O'Neal, W. K.; Boucher, R. C. Increased Airway Epithelial Na+ Absorption Produces Cystic Fibrosis-like Lung Disease in Mice. *Nat Med* **2004**, *10* (5), 487–493. https://doi.org/10.1038/nm1028.

(174) Zhou, Z.; Duerr, J.; Johannesson, B.; Schubert, S. C.; Treis, D.; Harm, M.; Graeber, S. Y.; Dalpke, A.; Schultz, C.; Mall, M. A. The ENaC-Overexpressing Mouse as a Model of Cystic Fibrosis Lung Disease. *J Cyst Fibros* **2011**, *10 Suppl 2*, S172-82. https://doi.org/10.1016/s1569-1993(11)60021-0.

(175) Gehrig, S.; Duerr, J.; Weitnauer, M.; Wagner, C. J.; Graeber, S. Y.; Schatterny, J.; Hirtz, S.; Belaaouaj, A.; Dalpke, A. H.; Schultz, C.; Mall, M. A. Lack of Neutrophil Elastase Reduces Inflammation, Mucus Hypersecretion, and Emphysema, but Not Mucus Obstruction, in Mice with Cystic Fibrosis-like Lung Disease. *Am J Respir Crit Care Med* **2014**, *189* (9), 1082–1092. https://doi.org/10.1164/rccm.201311-1932OC.

(176) Mall, M. A.; Harkema, J. R.; Trojanek, J. B.; Treis, D.; Livraghi, A.; Schubert, S.; Zhou, Z.; Kreda, S. M.; Tilley, S. L.; Hudson, E. J.; O'Neal, W. K.; Boucher, R. C. Development of Chronic Bronchitis and Emphysema in Beta-Epithelial Na+ Channel-Overexpressing Mice. *Am J Respir Crit Care Med* **2008**, *177* (7), 730–742. https://doi.org/10.1164/rccm.200708-1233OC.

(177) Livraghi-Butrico, A.; Kelly, E. J.; Klem, E. R.; Dang, H.; Wolfgang, M. C.; Boucher, R. C.; Randell, S. H.; O'Neal, W. K. Mucus Clearance, MyD88-Dependent and MyD88-Independent Immunity Modulate Lung Susceptibility to Spontaneous Bacterial Infection and Inflammation. *Mucosal Immunol* **2012**, *5* (4), 397–408. https://doi.org/10.1038/mi.2012.17.

(178) Tucker, S. L.; Sarr, D.; Rada, B. Neutrophil Extracellular Traps Are Present in the Airways of ENaC-Overexpressing Mice with Cystic Fibrosis-like Lung Disease. *BMC Immunol* **2021**, *22* (1), 7. https://doi.org/10.1186/s12865-021-00397-w.

(179) Moustafa, D. A.; Wu, A. W.; Zamora, D.; Daly, S. M.; Sturge, C. R.; Pybus, C.; Geller, B. L.; Goldberg, J. B.; Greenberg, D. E. Peptide-Conjugated Phosphorodiamidate Morpholino Oligomers Retain Activity against Multidrug-Resistant Pseudomonas Aeruginosa In Vitro and In Vivo. *mBio* **2021**, *12* (1). https://doi.org/10.1128/mBio.02411-20.

(180) Cui, G.; Cottrill, K. A.; Strickland, K. M.; Mashburn, S. A.; Koval, M.; McCarty, N. A. Alteration of Membrane Cholesterol Content Plays a Key Role in Regulation of Cystic Fibrosis Transmembrane Conductance Regulator Channel Activity. *Front Physiol* **2021**, *12*, 652513. https://doi.org/10.3389/fphys.2021.652513.

(181) Cui, G.; Stauffer, B. B.; Imhoff, B. R.; Rab, A.; Hong, J. S.; Sorscher, E. J.; McCarty, N. A. VX-770-Mediated Potentiation of Numerous Human CFTR Disease Mutants Is Influenced

by Phosphorylation Level. *Sci. Rep.* **2019**, *9* (1), 13460. https://doi.org/10.1038/s41598-019-49921-4.

(182) Cui, G.; Cottrill, K. A.; McCarty, N. A. Electrophysiological Approaches for the Study of Ion Channel Function. *Methods Mol Biol* **2021**, *2302*, 49–67. https://doi.org/10.1007/978-1-0716-1394-8_4.

(183) Sun, F.; Xiao, G.; Qu, Z. Murine Bronchoalveolar Lavage. *Bio Protoc* **2017**, *7* (10). https://doi.org/10.21769/BioProtoc.2287.

(184) Dobin, A.; Davis, C. A.; Schlesinger, F.; Drenkow, J.; Zaleski, C.; Jha, S.; Batut, P.; Chaisson, M.; Gingeras, T. R. STAR: Ultrafast Universal RNA-Seq Aligner. *Bioinformatics* **2013**, *29* (1), 15–21. https://doi.org/10.1093/bioinformatics/bts635.

(185) Liao, Y.; Smyth, G. K.; Shi, W. featureCounts: An Efficient General Purpose Program for Assigning Sequence Reads to Genomic Features. *Bioinformatics* **2014**, *30* (7), 923–930. https://doi.org/10.1093/bioinformatics/btt656.

(186) Guo, Y.; Zhao, S.; Sheng, Q.; Ye, F.; Li, J.; Lehmann, B.; Pietenpol, J.; Samuels, D. C.; Shyr, Y. Multi-Perspective Quality Control of Illumina Exome Sequencing Data Using QC3. *Genomics* **2014**, *103* (5–6), 323–328. https://doi.org/10.1016/j.ygeno.2014.03.006.

(187) Love, M. I.; Huber, W.; Anders, S. Moderated Estimation of Fold Change and Dispersion for RNA-Seq Data with DESeq2. *Genome Biol* **2014**, *15* (12), 550. https://doi.org/10.1186/s13059-014-0550-8.

(188) Zhao, S.; Guo, Y.; Sheng, Q.; Shyr, Y. Advanced Heat Map and Clustering Analysis Using Heatmap3. *Biomed Res Int* **2014**, *2014*, 986048. https://doi.org/10.1155/2014/986048.

(189) Wang, J.; Vasaikar, S.; Shi, Z.; Greer, M.; Zhang, B. WebGestalt 2017: A More Comprehensive, Powerful, Flexible and Interactive Gene Set Enrichment Analysis Toolkit. *Nucleic Acids Res* **2017**, *45* (W1), W130-w137. https://doi.org/10.1093/nar/gkx356.

(190) Turner, K. H.; Wessel, A. K.; Palmer, G. C.; Murray, J. L.; Whiteley, M. Essential Genome of Pseudomonas Aeruginosa in Cystic Fibrosis Sputum. *Proc Natl Acad Sci U A* **2015**, *112* (13), 4110–4115. https://doi.org/10.1073/pnas.1419677112.

(191) Hirche, T. O.; Benabid, R.; Deslee, G.; Gangloff, S.; Achilefu, S.; Guenounou, M.; Lebargy, F.; Hancock, R. E.; Belaaouaj, A. Neutrophil Elastase Mediates Innate Host Protection against Pseudomonas Aeruginosa. *J Immunol* **2008**, *181* (7), 4945–4954. https://doi.org/10.4049/jimmunol.181.7.4945.

(192) Livraghi-Butrico, A.; Grubb, B. R.; Kelly, E. J.; Wilkinson, K. J.; Yang, H.; Geiser, M.; Randell, S. H.; Boucher, R. C.; O'Neal, W. K. Genetically Determined Heterogeneity of Lung Disease in a Mouse Model of Airway Mucus Obstruction. *Physiol Genomics* **2012**, *44* (8), 470–484. https://doi.org/10.1152/physiolgenomics.00185.2011.

(193) Livraghi-Butrico, A.; Wilkinson, K. J.; Volmer, A. S.; Gilmore, R. C.; Rogers, T. D.; Caldwell, R. A.; Burns, K. A.; Esther, C. R.; Mall, M. A.; Boucher, R. C.; O'Neal, W. K.; Grubb, B. R. Lung Disease Phenotypes Caused by Overexpression of Combinations of α-, β-, and γ-Subunits of the Epithelial Sodium Channel in Mouse Airways. *Am J Physiol Lung Cell Mol Physiol* **2018**, *314* (2), L318-l331. https://doi.org/10.1152/ajplung.00382.2017.

(194) Grubb, B. R. Bioelectric Measurement of CFTR Function in Mice. *Methods Mol Med* **2002**, *70*, 525–535. https://doi.org/10.1385/1-59259-187-6:525.

(195) Cui, G.; McCarty, N. A. Murine and Human CFTR Exhibit Different Sensitivities to CFTR Potentiators. *Am J Physiol Lung Cell Mol Physiol* **2015**, *309* (7), L687-99. https://doi.org/10.1152/ajplung.00181.2015.

(196) Rock, J. R.; O'Neal, W. K.; Gabriel, S. E.; Randell, S. H.; Harfe, B. D.; Boucher, R. C.; Grubb, B. R. Transmembrane Protein 16A (TMEM16A) Is a Ca2+-Regulated Cl- Secretory Channel in Mouse Airways. *J Biol Chem* **2009**, *284* (22), 14875–14880. https://doi.org/10.1074/jbc.C109.000869.

(197) Seys, L. J.; Verhamme, F. M.; Dupont, L. L.; Desauter, E.; Duerr, J.; Seyhan Agircan, A.; Conickx, G.; Joos, G. F.; Brusselle, G. G.; Mall, M. A.; Bracke, K. R. Airway Surface Dehydration Aggravates Cigarette Smoke-Induced Hallmarks of COPD in Mice. *PLoS One* **2015**, *10* (6), e0129897. https://doi.org/10.1371/journal.pone.0129897.

(198) Ito, M.; Kondo, Y.; Nakatani, A.; Hayashi, K.; Naruse, A. Characterization of Low Dose Streptozotocin-Induced Progressive Diabetes in Mice. *Env. Toxicol Pharmacol* **2001**, *9* (3), 71–78. https://doi.org/10.1016/s1382-6689(00)00064-8.

(199) Livraghi-Butrico, A.; Kelly, E. J.; Wilkinson, K. J.; Rogers, T. D.; Gilmore, R. C.; Harkema, J. R.; Randell, S. H.; Boucher, R. C.; O'Neal, W. K.; Grubb, B. R. Loss of Cftr Function Exacerbates the Phenotype of Na(+) Hyperabsorption in Murine Airways. *Am J Physiol Lung Cell Mol Physiol* **2013**, *304* (7), L469-80. https://doi.org/10.1152/ajplung.00150.2012.

(200) Lee, S.; Islam, M. N.; Boostanpour, K.; Aran, D.; Jin, G.; Christenson, S.; Matthay, M. A.; Eckalbar, W. L.; DePianto, D. J.; Arron, J. R.; Magee, L.; Bhattacharya, S.; Matsumoto, R.; Kubota, M.; Farber, D. L.; Bhattacharya, J.; Wolters, P. J.; Bhattacharya, M. Molecular Programs of Fibrotic Change in Aging Human Lung. *Nat Commun* **2021**, *12* (1), 6309. https://doi.org/10.1038/s41467-021-26603-2.

(201) Mathy, N. W.; Chen, X. M. Long Non-Coding RNAs (lncRNAs) and Their Transcriptional Control of Inflammatory Responses. *J Biol Chem* **2017**, *292* (30), 12375–12382. https://doi.org/10.1074/jbc.R116.760884.

(202) Bassuk, J. A.; Cochrane, K.; Mitchell, M. E. Induction of Urothelial Cell Proliferation by Fibroblast Growth Factor-7 in RAG1-Deficient Mice. *Adv Exp Med Biol* **2003**, *539* (Pt B), 623–633. https://doi.org/10.1007/978-1-4419-8889-8_40.

(203) Sutherland, T. E.; Logan, N.; Rückerl, D.; Humbles, A. A.; Allan, S. M.; Papayannopoulos, V.; Stockinger, B.; Maizels, R. M.; Allen, J. E. Chitinase-like Proteins Promote IL-17-Mediated Neutrophilia in a Tradeoff between Nematode Killing and Host Damage. *Nat Immunol* **2014**, *15* (12), 1116–1125. https://doi.org/10.1038/ni.3023.

(204) Tseng, H. Y.; Thorausch, N.; Ziegler, T.; Meves, A.; Fässler, R.; Böttcher, R. T. Sorting Nexin 31 Binds Multiple β Integrin Cytoplasmic Domains and Regulates B1 Integrin Surface Levels and Stability. *J Mol Biol* **2014**, *426* (18), 3180–3194. https://doi.org/10.1016/j.jmb.2014.07.003.

(205) Higham, A.; Quinn, A. M.; Cançado, J. E. D.; Singh, D. The Pathology of Small Airways Disease in COPD: Historical Aspects and Future Directions. *Respir Res* **2019**, *20* (1), 49. https://doi.org/10.1186/s12931-019-1017-y.

(206) Fritzsching, B.; Zhou-Suckow, Z.; Trojanek, J. B.; Schubert, S. C.; Schatterny, J.; Hirtz, S.; Agrawal, R.; Muley, T.; Kahn, N.; Sticht, C.; Gunkel, N.; Welte, T.; Randell, S. H.; Länger, F.; Schnabel, P.; Herth, F. J.; Mall, M. A. Hypoxic Epithelial Necrosis Triggers Neutrophilic Inflammation via IL-1 Receptor Signaling in Cystic Fibrosis Lung Disease. *Am J Respir Crit Care Med* **2015**, *191* (8), 902–913. https://doi.org/10.1164/rccm.201409-1610OC.

(207) Daddaoua, A.; Krell, T.; Ramos, J. L. Regulation of Glucose Metabolism in Pseudomonas: The Phosphorylative Branch and Entner-Doudoroff Enzymes Are Regulated by a Repressor

Containing a Sugar Isomerase Domain. *J Biol Chem* **2009**, *284* (32), 21360–21368. https://doi.org/10.1074/jbc.M109.014555.

(208) Meganathan, V.; Moyana, R.; Natarajan, K.; Kujur, W.; Kusampudi, S.; Mulik, S.; Boggaram, V. Bacterial Extracellular Vesicles Isolated from Organic Dust Induce Neutrophilic Inflammation in the Lung. *Am J Physiol Lung Cell Mol Physiol* **2020**, *319* (6), L893-l907. https://doi.org/10.1152/ajplung.00107.2020.

(209) Tomotsune, K.; Raya Tonetti, F.; Mizuno, H.; Elean, M.; Fukuyama, K.; Zhou, B.; Ikeda-Ohtsubo, W.; Nishiyama, K.; Yamamura, A.; Karasawa, H.; Ohnuma, S.; Horii, A.; Saito, T.; Kitazawa, H.; Villena, J. The Mucus Binding Factor Is Not Necessary for Lacticaseibacillus Rhamnosus CRL1505 to Exert Its Immunomodulatory Activities in Local and Distal Mucosal Sites. *Int J Mol Sci* **2022**, *23* (22). https://doi.org/10.3390/ijms232214357.

(210) Rossi, A.; Bragonzi, A.; Medede, M.; De Fino, I.; Lippi, G.; Prosdocimi, M.; Tamanini, A.; Cabrini, G.; Dechecchi, M. C. β-Sitosterol Ameliorates Inflammation and Pseudomonas Aeruginosa Lung Infection in a Mouse Model. *J Cyst Fibros* **2023**, *22* (1), 156–160. https://doi.org/10.1016/j.jcf.2022.08.005.

(211) Saini, Y.; Dang, H.; Livraghi-Butrico, A.; Kelly, E. J.; Jones, L. C.; O'Neal, W. K.; Boucher, R. C. Gene Expression in Whole Lung and Pulmonary Macrophages Reflects the Dynamic Pathology Associated with Airway Surface Dehydration. *BMC Genomics* **2014**, *15* (1), 726. https://doi.org/10.1186/1471-2164-15-726.

(212) Bayes, H. K.; Ritchie, N.; Irvine, S.; Evans, T. J. A Murine Model of Early Pseudomonas Aeruginosa Lung Disease with Transition to Chronic Infection. *Sci Rep* **2016**, *6*, 35838. https://doi.org/10.1038/srep35838.

(213) Brao, K. J.; Wille, B. P.; Lieberman, J.; Ernst, R. K.; Shirtliff, M. E.; Harro, J. M. Scnn1b-Transgenic BALB/c Mice as a Model of Pseudomonas Aeruginosa Infections of the Cystic Fibrosis Lung. *Infect Immun* **2020**, *88* (9). https://doi.org/10.1128/iai.00237-20.

(214) Song, Y.; Thiagarajah, J.; Verkman, A. S. Sodium and Chloride Concentrations, pH, and Depth of Airway Surface Liquid in Distal Airways. *J Gen Physiol* **2003**, *122* (5), 511–519. https://doi.org/10.1085/jgp.200308866.

(215) Riordan, J. R.; Rommens, J. M.; Kerem, B.; Alon, N.; Rozmahel, R.; Grzelczak, Z.; Zielenski, J.; Lok, S.; Plavsic, N.; Chou, J. L. Identification of the Cystic Fibrosis Gene: Cloning and Characterization of Complementary DNA. *Science* **1989**, *245* (4922), 1066–1073. https://doi.org/10.1126/science.2475911.

(216) Tirouvanziam, R.; Khazaal, I.; Péault, B. Primary Inflammation in Human Cystic Fibrosis Small Airways. *Am J Physiol Lung Cell Mol Physiol* **2002**, *283* (2), L445-51. https://doi.org/10.1152/ajplung.00419.2001.

(217) Pallin, M.; Kumar, S.; Daley, C.; Dawadi, S.; Leong, P.; Carr, E.; Soldatos, G. Continuous Glucose Monitoring Indices Predict Poor FEV(1) Recovery Following Cystic Fibrosis Pulmonary Exacerbations. *J Cyst Fibros* **2021**, *20* (5), 785–791. https://doi.org/10.1016/j.jcf.2021.03.004.

(218) Van Sambeek, L.; Cowley, E. S.; Newman, D. K.; Kato, R. Sputum Glucose and Glycemic Control in Cystic Fibrosis-Related Diabetes: A Cross-Sectional Study. *PLoS One* **2015**, *10* (3), e0119938. https://doi.org/10.1371/journal.pone.0119938.

(219) Jensen, P.; Nielsen, B. U.; Kolpen, M.; Pressler, T.; Faurholt-Jepsen, D.; Mathiesen, I. H. M. Increased Sputum Lactate during Oral Glucose Tolerance Test in Cystic Fibrosis. *Apmis* **2022**, *130* (8), 535–539. https://doi.org/10.1111/apm.13233.

(220) Prentice, B. J.; Ooi, C. Y.; Strachan, R. E.; Hameed, S.; Ebrahimkhani, S.; Waters, S. A.; Verge, C. F.; Widger, J. Early Glucose Abnormalities Are Associated with Pulmonary Inflammation in Young Children with Cystic Fibrosis. *J Cyst Fibros* **2019**, *18* (6), 869–873. https://doi.org/10.1016/j.jcf.2019.03.010.

(221) Nielsen, B. U.; Kolpen, M.; Jensen, P.; Katzenstein, T.; Pressler, T.; Ritz, C.; Mathiesen, I. H. M.; Faurholt-Jepsen, D. Neutrophil Count in Sputum Is Associated with Increased Sputum Glucose and Sputum L-Lactate in Cystic Fibrosis. *PLoS One* **2020**, *15* (9), e0238524. https://doi.org/10.1371/journal.pone.0238524.

(222) Konstan, M. W.; Hilliard, K. A.; Norvell, T. M.; Berger, M. Bronchoalveolar Lavage Findings in Cystic Fibrosis Patients with Stable, Clinically Mild Lung Disease Suggest Ongoing Infection and Inflammation. *Am J Respir Crit Care Med* **1994**, *150* (2), 448–454. https://doi.org/10.1164/ajrccm.150.2.8049828.

(223) Noah, T. L.; Ivins, S. S.; Abode, K. A.; Stewart, P. W.; Michelson, P. H.; Harris, W. T.; Henry, M. M.; Leigh, M. W. Inhaled versus Systemic Antibiotics and Airway Inflammation in Children with Cystic Fibrosis and Pseudomonas. *Pediatr Pulmonol* **2010**, *45* (3), 281–290. https://doi.org/10.1002/ppul.21176.

(224) Stites, S. W.; Plautz, M. W.; Bailey, K.; O'Brien-Ladner, A. R.; Wesselius, L. J. Increased Concentrations of Iron and Isoferritins in the Lower Respiratory Tract of Patients with Stable Cystic Fibrosis. *Am J Respir Crit Care Med* **1999**, *160* (3), 796–801. https://doi.org/10.1164/ajrccm.160.3.9811018.

(225) Dakin, C. J.; Numa, A. H.; Wang, H.; Morton, J. R.; Vertzyas, C. C.; Henry, R. L. Inflammation, Infection, and Pulmonary Function in Infants and Young Children with Cystic Fibrosis. *Am J Respir Crit Care Med* **2002**, *165* (7), 904–910. https://doi.org/10.1164/ajrccm.165.7.2010139.

(226) Essilfie, A. T.; Houston, N.; Maniam, P.; Hartel, G.; Okano, S.; Reid, D. W. Anti-Protease Levels in Cystic Fibrosis Are Associated with Lung Function, Recovery from Pulmonary Exacerbations and May Be Gender-Related. *Respirology* **2023**, *28* (6), 533–542. https://doi.org/10.1111/resp.14450.

(227) Osika, E.; Cavaillon, J. M.; Chadelat, K.; Boule, M.; Fitting, C.; Tournier, G.; Clement, A. Distinct Sputum Cytokine Profiles in Cystic Fibrosis and Other Chronic Inflammatory Airway Disease. *Eur Respir J* **1999**, *14* (2), 339–346. https://doi.org/10.1034/j.1399-3003.1999.14b17.x.

(228) Ratjen, F.; Waters, V.; Klingel, M.; McDonald, N.; Dell, S.; Leahy, T. R.; Yau, Y.; Grasemann, H. Changes in Airway Inflammation during Pulmonary Exacerbations in Patients with Cystic Fibrosis and Primary Ciliary Dyskinesia. *Eur Respir J* **2016**, *47* (3), 829–836. https://doi.org/10.1183/13993003.01390-2015.

(229) Ratjen, F.; Rietschel, E.; Griese, M.; Ballmann, M.; Kleinau, I.; Döring, G.; Reinhardt, D.; Paul, K. Fractional Analysis of Bronchoalveolar Lavage Fluid Cytology in Cystic Fibrosis Patients with Normal Lung Function. Bronchoalveolar Lavage for the Evaluation of Anti-Inflammatory Treatment (BEAT) Study Group. *Eur Respir J* **2000**, *15* (1), 141–145. https://doi.org/10.1183/09031936.00.15114100.

(230) Paul, K.; Rietschel, E.; Ballmann, M.; Griese, M.; Worlitzsch, D.; Shute, J.; Chen, C.; Schink, T.; Döring, G.; van Koningsbruggen, S.; Wahn, U.; Ratjen, F. Effect of Treatment with Dornase Alpha on Airway Inflammation in Patients with Cystic Fibrosis. *Am J Respir Crit Care Med* **2004**, *169* (6), 719–725. https://doi.org/10.1164/rccm.200307-959OC.

(231) Reinhardt, N.; Chen, C. I.; Loppow, D.; Schink, T.; Kleinau, I.; Jörres, R. A.; Wahn, U.; Magnussen, H.; Paul, K. P. Cellular Profiles of Induced Sputum in Children with Stable Cystic Fibrosis: Comparison with BAL. *Eur Respir J* **2003**, *22* (3), 497–502. https://doi.org/10.1183/09031936.03.00043603.

(232) Smountas, A. A.; Lands, L. C.; Mohammed, S. R.; Grey, V. Induced Sputum in Cystic Fibrosis: Within-Week Reproducibility of Inflammatory Markers. *Clin Biochem* **2004**, *37* (11), 1031–1036. https://doi.org/10.1016/j.clinbiochem.2004.07.008.

(233) Dittrich, A. S.; Kühbandner, I.; Gehrig, S.; Rickert-Zacharias, V.; Twigg, M.; Wege, S.; Taggart, C. C.; Herth, F.; Schultz, C.; Mall, M. A. Elastase Activity on Sputum Neutrophils Correlates with Severity of Lung Disease in Cystic Fibrosis. *Eur Respir J* **2018**, *51* (3). https://doi.org/10.1183/13993003.01910-2017.

(234) Meyer, K. C.; Sharma, A. Regional Variability of Lung Inflammation in Cystic Fibrosis. *Am J Respir Crit Care Med* **1997**, *156* (5), 1536–1540. https://doi.org/10.1164/ajrccm.156.5.9701098.

(235) Molina, S. A.; Stauffer, B.; Moriarty, H. K.; Kim, A. H.; McCarty, N. A.; Koval, M. Junctional Abnormalities in Human Airway Epithelial Cells Expressing F508del CFTR. **2015**, *309* (5), L475-87. https://doi.org/10.1152/ajplung.00060.2015.

(236) Reutershan, J.; Basit, A.; Galkina, E. V.; Ley, K. Sequential Recruitment of Neutrophils into Lung and Bronchoalveolar Lavage Fluid in LPS-Induced Acute Lung Injury. *Am J Physiol Lung Cell Mol Physiol* **2005**, *289* (5), L807-15. https://doi.org/10.1152/ajplung.00477.2004.

(237) Burns, A. R.; Smith, C. W.; Walker, D. C. Unique Structural Features That Influence Neutrophil Emigration into the Lung. *Physiol Rev* **2003**, *83* (2), 309–336. https://doi.org/10.1152/physrev.00023.2002.

(238) Bou Ghanem, E. N.; Clark, S.; Du, X.; Wu, D.; Camilli, A.; Leong, J. M.; Meydani, S. N. The α-Tocopherol Form of Vitamin E Reverses Age-Associated Susceptibility to Streptococcus Pneumoniae Lung Infection by Modulating Pulmonary Neutrophil Recruitment. *J Immunol* **2015**, *194* (3), 1090–1099. https://doi.org/10.4049/jimmunol.1402401.

(239) Mayadas, T. N.; Cullere, X.; Lowell, C. A. The Multifaceted Functions of Neutrophils. *Annu Rev Pathol* **2014**, *9*, 181–218. https://doi.org/10.1146/annurev-pathol-020712-164023.

(240) Zemans, R. L.; Colgan, S. P.; Downey, G. P. Transepithelial Migration of Neutrophils: Mechanisms and Implications for Acute Lung Injury. *Am J Respir Cell Mol Biol* **2009**, *40* (5), 519–535. https://doi.org/10.1165/rcmb.2008-0348TR.

(241) Lin, W. C.; Fessler, M. B. Regulatory Mechanisms of Neutrophil Migration from the Circulation to the Airspace. *Cell Mol Life Sci* **2021**, *78* (9), 4095–4124. https://doi.org/10.1007/s00018-021-03768-z.

(242) Brazil, J. C.; Parkos, C. A. Pathobiology of Neutrophil-Epithelial Interactions. *Immunol Rev* **2016**, *273* (1), 94–111. https://doi.org/10.1111/imr.12446.

(243) Burns, A. R.; Walker, D. C.; Brown, E. S.; Thurmon, L. T.; Bowden, R. A.; Keese, C. R.; Simon, S. I.; Entman, M. L.; Smith, C. W. Neutrophil Transendothelial Migration Is Independent of Tight Junctions and Occurs Preferentially at Tricellular Corners. *J Immunol* **1997**, *159* (6), 2893–2903.

(244) Burns, A. R.; Bowden, R. A.; MacDonell, S. D.; Walker, D. C.; Odebunmi, T. O.; Donnachie, E. M.; Simon, S. I.; Entman, M. L.; Smith, C. W. Analysis of Tight Junctions

during Neutrophil Transendothelial Migration. *J Cell Sci* **2000**, *113 (Pt 1)*, 45–57. https://doi.org/10.1242/jcs.113.1.45.

(245) Ayres-Sander, C. E.; Lauridsen, H.; Maier, C. L.; Sava, P.; Pober, J. S.; Gonzalez, A. L. Transendothelial Migration Enables Subsequent Transmigration of Neutrophils through Underlying Pericytes. *PLoS One* **2013**, *8* (3), e60025. https://doi.org/10.1371/journal.pone.0060025.

(246) Lauridsen, H. M.; Pober, J. S.; Gonzalez, A. L. A Composite Model of the Human Postcapillary Venule for Investigation of Microvascular Leukocyte Recruitment. *Faseb J* **2014**, *28* (3), 1166–1180. https://doi.org/10.1096/fj.13-240986.

(247) Sumagin, R.; Parkos, C. A. Epithelial Adhesion Molecules and the Regulation of Intestinal Homeostasis during Neutrophil Transepithelial Migration. *Tissue Barriers* **2015**, *3* (1–2), e969100. https://doi.org/10.4161/21688362.2014.969100.

(248) Sumagin, R.; Robin, A. Z.; Nusrat, A.; Parkos, C. A. Transmigrated Neutrophils in the Intestinal Lumen Engage ICAM-1 to Regulate the Epithelial Barrier and Neutrophil Recruitment. *Mucosal Immunol* **2014**, *7* (4), 905–915. https://doi.org/10.1038/mi.2013.106.

(249) Parkos, C. A.; Delp, C.; Arnaout, M. A.; Madara, J. L. Neutrophil Migration across a Cultured Intestinal Epithelium. Dependence on a CD11b/CD18-Mediated Event and Enhanced Efficiency in Physiological Direction. *J Clin Invest* **1991**, *88* (5), 1605–1612. https://doi.org/10.1172/jci115473.

(250) Zemans, R. L.; McClendon, J.; Aschner, Y.; Briones, N.; Young, S. K.; Lau, L. F.; Kahn, M.; Downey, G. P. Role of β-Catenin-Regulated CCN Matricellular Proteins in Epithelial Repair after Inflammatory Lung Injury. *Am J Physiol Lung Cell Mol Physiol* **2013**, *304* (6), L415-27. https://doi.org/10.1152/ajplung.00180.2012.

(251) Kidney, J. C.; Proud, D. Neutrophil Transmigration across Human Airway Epithelial Monolayers: Mechanisms and Dependence on Electrical Resistance. *Am J Respir Cell Mol Biol* **2000**, *23* (3), 389–395. https://doi.org/10.1165/ajrcmb.23.3.4068.

(252) Butin-Israeli, V.; Houser, M. C.; Feng, M.; Thorp, E. B.; Nusrat, A.; Parkos, C. A.; Sumagin, R. Deposition of Microparticles by Neutrophils onto Inflamed Epithelium: A New Mechanism to Disrupt Epithelial Intercellular Adhesions and Promote Transepithelial Migration. *Faseb J* **2016**, *30* (12), 4007–4020. https://doi.org/10.1096/fj.201600734R.

(253) Liu, L.; Mul, F. P.; Lutter, R.; Roos, D.; Knol, E. F. Transmigration of Human Neutrophils across Airway Epithelial Cell Monolayers Is Preferentially in the Physiologic Basolateral-to-Apical Direction. *Am J Respir Cell Mol Biol* **1996**, *15* (6), 771–780. https://doi.org/10.1165/ajrcmb.15.6.8969272.

(254) Louis, N. A.; Hamilton, K. E.; Kong, T.; Colgan, S. P. HIF-Dependent Induction of Apical CD55 Coordinates Epithelial Clearance of Neutrophils. *Faseb J* **2005**, *19* (8), 950–959. https://doi.org/10.1096/fj.04-3251com.

(255) Herbert, J. A.; Deng, Y.; Hardelid, P.; Robinson, E.; Ren, L.; Moulding, D.; Smyth, R. L.; Smith, C. M. β(2)-Integrin LFA1 Mediates Airway Damage Following Neutrophil Transepithelial Migration during Respiratory Syncytial Virus Infection. *Eur Respir J* **2020**, *56* (2). https://doi.org/10.1183/13993003.02216-2019.

(256) Balsam, L. B.; Liang, T. W.; Parkos, C. A. Functional Mapping of CD11b/CD18 Epitopes Important in Neutrophil-Epithelial Interactions: A Central Role of the I Domain. *J Immunol* **1998**, *160* (10), 5058–5065.

(257) Serikov, V. B.; Choi, H.; Chmiel, K. J.; Wu, R.; Widdicombe, J. H. Activation of Extracellular Regulated Kinases Is Required for the Increase in Airway Epithelial

Permeability during Leukocyte Transmigration. *Am J Respir Cell Mol Biol* **2004**, *30* (3), 261–270. https://doi.org/10.1165/rcmb.2003-0053OC.

(258) Hurley, B. P.; Sin, A.; McCormick, B. A. Adhesion Molecules Involved in Hepoxilin A3-Mediated Neutrophil Transepithelial Migration. *Clin Exp Immunol* **2008**, *151* (2), 297–305. https://doi.org/10.1111/j.1365-2249.2007.03551.x.

(259) Lee, W. Y.; Chin, A. C.; Voss, S.; Parkos, C. A. In Vitro Neutrophil Transepithelial Migration. *Methods Mol Biol* **2006**, *341*, 205–215. https://doi.org/10.1385/1-59745-113-4:205.

(260) Liu, L.; Mul, F. P.; Kuijpers, T. W.; Lutter, R.; Roos, D.; Knol, E. F. Neutrophil Transmigration across Monolayers of Endothelial Cells and Airway Epithelial Cells Is Regulated by Different Mechanisms. *Ann N Acad Sci* **1996**, *796*, 21–29. https://doi.org/10.1111/j.1749-6632.1996.tb32563.x.

(261) Kusek, M. E.; Pazos, M. A.; Pirzai, W.; Hurley, B. P. In Vitro Coculture Assay to Assess Pathogen Induced Neutrophil Trans-Epithelial Migration. *J Vis Exp* **2014**, No. 83, e50823. https://doi.org/10.3791/50823.

(262) Liu, Y.; Nusrat, A.; Schnell, F. J.; Reaves, T. A.; Walsh, S.; Pochet, M.; Parkos, C. A. Human Junction Adhesion Molecule Regulates Tight Junction Resealing in Epithelia. *J Cell Sci* **2000**, *113 (Pt 13)*, 2363–2374. https://doi.org/10.1242/jcs.113.13.2363.

(263) Morgan, R.; Manfredi, C.; Easley, K. F.; Watkins, L. D.; Hunt, W. R.; Goudy, S. L.; Sorscher, E. J.; Koval, M.; Molina, S. A. A Medium Composition Containing Normal Resting Glucose That Supports Differentiation of Primary Human Airway Cells. *Sci Rep* **2022**, *12* (1), 1540. https://doi.org/10.1038/s41598-022-05446-x.

(264) Yonker, L. M.; Mou, H.; Chu, K. K.; Pazos, M. A.; Leung, H.; Cui, D.; Ryu, J.; Hibbler, R. M.; Eaton, A. D.; Ford, T. N.; Falck, J. R.; Kinane, T. B.; Tearney, G. J.; Rajagopal, J.; Hurley, B. P. Development of a Primary Human Co-Culture Model of Inflamed Airway Mucosa. *Sci Rep* **2017**, *7* (1), 8182. https://doi.org/10.1038/s41598-017-08567-w.

(265) Weber, D. A.; Sumagin, R.; McCall, I. C.; Leoni, G.; Neumann, P. A.; Andargachew, R.; Brazil, J. C.; Medina-Contreras, O.; Denning, T. L.; Nusrat, A.; Parkos, C. A. Neutrophil-Derived JAML Inhibits Repair of Intestinal Epithelial Injury during Acute Inflammation. *Mucosal Immunol* **2014**, *7* (5), 1221–1232. https://doi.org/10.1038/mi.2014.12.

(266) Fleck, R. A.; Romero-Steiner, S.; Nahm, M. H. Use of HL-60 Cell Line to Measure Opsonic Capacity of Pneumococcal Antibodies. *Clin Diagn Lab Immunol* **2005**, *12* (1), 19–27. https://doi.org/10.1128/cdli.12.1.19-27.2005.

(267) Jennings, S.; Ng, H. P.; Wang, G. Establishment of a ΔF508-CF Promyelocytic Cell Line for Cystic Fibrosis Research and Drug Screening. *J Cyst Fibros* **2019**, *18* (1), 44–53. https://doi.org/10.1016/j.jcf.2018.06.007.

(268) Dobosh, B.; Giacalone, V. D.; Margaroli, C.; Tirouvanziam, R. Mass Production of Human Airway-like Neutrophils via Transmigration in an Organotypic Model of Human Airways. *STAR Protoc* **2021**, *2* (4), 100892. https://doi.org/10.1016/j.xpro.2021.100892.

(269) Carrigan, S. O.; Weppler, A. L.; Issekutz, A. C.; Stadnyk, A. W. Neutrophil Differentiated HL-60 Cells Model Mac-1 (CD11b/CD18)-Independent Neutrophil Transepithelial Migration. *Immunology* **2005**, *115* (1), 108–117. https://doi.org/10.1111/j.1365-2567.2005.02131.x.

(270) Babatunde, K. A.; Wang, X.; Hopke, A.; Lannes, N.; Mantel, P. Y.; Irimia, D. Chemotaxis and Swarming in Differentiated HL-60 Neutrophil-like Cells. *Sci Rep* **2021**, *11* (1), 778. https://doi.org/10.1038/s41598-020-78854-6.

(271) Plebani, R.; Potla, R.; Soong, M.; Bai, H.; Izadifar, Z.; Jiang, A.; Travis, R. N.; Belgur, C.; Dinis, A.; Cartwright, M. J.; Prantil-Baun, R.; Jolly, P.; Gilpin, S. E.; Romano, M.; Ingber, D. E. Modeling Pulmonary Cystic Fibrosis in a Human Lung Airway-on-a-Chip. *J Cyst Fibros* **2022**, *21* (4), 606–615. https://doi.org/10.1016/j.jcf.2021.10.004.

(272) McGettrick, H. M.; Lord, J. M.; Wang, K. Q.; Rainger, G. E.; Buckley, C. D.; Nash, G. B. Chemokine- and Adhesion-Dependent Survival of Neutrophils after Transmigration through Cytokine-Stimulated Endothelium. *J Leukoc Biol* **2006**, *79* (4), 779–788. https://doi.org/10.1189/jlb.0605350.

(273) Tan, C.; Aziz, M.; Wang, P. The Vitals of NETs. *J Leukoc Biol* **2021**, *110* (4), 797–808. https://doi.org/10.1002/jlb.3ru0620-375r.

(274) Lawrence, S. M.; Corriden, R.; Nizet, V. How Neutrophils Meet Their End. *Trends Immunol* **2020**, *41* (6), 531–544. https://doi.org/10.1016/j.it.2020.03.008.

(275) Yousefi, S.; Mihalache, C.; Kozlowski, E.; Schmid, I.; Simon, H. U. Viable Neutrophils Release Mitochondrial DNA to Form Neutrophil Extracellular Traps. *Cell Death Differ* **2009**, *16* (11), 1438–1444. https://doi.org/10.1038/cdd.2009.96.

(276) Cristinziano, L.; Modestino, L.; Loffredo, S.; Varricchi, G.; Braile, M.; Ferrara, A. L.; de Paulis, A.; Antonelli, A.; Marone, G.; Galdiero, M. R. Anaplastic Thyroid Cancer Cells Induce the Release of Mitochondrial Extracellular DNA Traps by Viable Neutrophils. *J Immunol* **2020**, *204* (5), 1362–1372. https://doi.org/10.4049/jimmunol.1900543.

(277) Hu, Y.; Bojanowski, C. M.; Britto, C. J.; Wellems, D.; Song, K.; Scull, C.; Jennings, S.; Li, J.; Kolls, J. K.; Wang, G. Aberrant Immune Programming in Neutrophils in Cystic Fibrosis. *J Leukoc Biol* **2024**, *115* (3), 420–434. https://doi.org/10.1093/jleuko/qiad139.

(278) Patel, S.; Nugent, K. Neutrophil Bactericidal Activity and Host Defenses in Cystic Fibrosis: A Narrative Review. *J Thorac Dis* **2023**, *15* (10), 5773–5783. https://doi.org/10.21037/jtd-23-846.

(279) Salomon, J. J.; Muchitsch, V. E.; Gausterer, J. C.; Schwagerus, E.; Huwer, H.; Daum, N.; Lehr, C.-M.; Ehrhardt, C. The Cell Line NCl-H441 Is a Useful in Vitro Model for Transport Studies of Human Distal Lung Epithelial Barrier. *Mol. Pharm.* **2014**, *11* (3), 995–1006. https://doi.org/10.1021/mp4006535.

(280) Brower, M.; Carney, D. N.; Oie, H. K.; Gazdar, A. F.; Minna, J. D. Growth of Cell Lines and Clinical Specimens of Human Non-Small Cell Lung Cancer in a Serum-Free Defined Medium. *Cancer Res.* **1986**, *46* (2), 798–806.

(281) Hunter, M.; Treharne, K.; Winter, A.; Cassidy, D.; Land, S.; Mehta, A. Expression of Wild-Type CFTR Suppresses NF-κB-Driven Inflammatory Signalling. *PloS One* **2010**, *5*, e11598. https://doi.org/10.1371/journal.pone.0011598.

(282) Alzamora, R.; King, J. D.; Hallows, K. R. CFTR Regulation by Phosphorylation. In *Cystic Fibrosis: Diagnosis and Protocols, Volume I: Approaches to Study and Correct CFTR Defects*; Amaral, M. D., Kunzelmann, K., Eds.; Humana Press: Totowa, NJ, 2011; pp 471–488. https://doi.org/10.1007/978-1-61779-117-8_29.

(283) Ketchum, C. J.; Rajendrakumar, G. V.; Maloney, P. C. Characterization of the Adenosinetriphosphatase and Transport Activities of Purified Cystic Fibrosis Transmembrane Conductance Regulator. *Biochemistry* **2004**, *43* (4), 1045–1053. https://doi.org/10.1021/bi035382a.

(284) Liu, F.; Zhang, Z.; Levit, A.; Levring, J.; Touhara, K. K.; Shoichet, B. K.; Chen, J. Structural Identification of a Hotspot on CFTR for Potentiation. *Science* **2019**, *364* (6446), 1184–1188. https://doi.org/10.1126/science.aaw7611.

(285) Corradi, V.; Gu, R.-X.; Vergani, P.; Tieleman, D. P. Structure of Transmembrane Helix 8 and Possible Membrane Defects in CFTR. *Biophys. J.* **2018**, *114* (8), 1751–1754. https://doi.org/10.1016/j.bpj.2018.03.003.

(286) Farkas, B.; Tordai, H.; Padányi, R.; Tordai, A.; Gera, J.; Paragi, G.; Hegedűs, T. Discovering the Chloride Pathway in the CFTR Channel. *Cell. Mol. Life Sci.* **2020**, *77* (4), 765–778. https://doi.org/10.1007/s00018-019-03211-4.

(287) Laselva, O.; Qureshi, Z.; Zeng, Z.-W.; Petrotchenko, E. V.; Ramjeesingh, M.; Hamilton, C. M.; Huan, L.-J.; Borchers, C. H.; Pomès, R.; Young, R.; Bear, C. E. Identification of Binding Sites for Ivacaftor on the Cystic Fibrosis Transmembrane Conductance Regulator. *iScience* **2021**, *24* (6). https://doi.org/10.1016/j.isci.2021.102542.

(288) Zhang, Z.; Liu, F.; Chen, J. Molecular Structure of the ATP-Bound, Phosphorylated Human CFTR. *Proc. Natl. Acad. Sci.* **2018**, *115* (50), 12757–12762. https://doi.org/10.1073/pnas.1815287115.

(289) Higashi, T.; Stephenson, R. E.; Schwayer, C.; Huljev, K.; Higashi, A. Y.; Heisenberg, C.-P.; Chiba, H.; Miller, A. L. ZnUMBA – a Live Imaging Method to Detect Local Barrier Breaches. *J. Cell Sci.* **2023**, *136* (15), jcs260668. https://doi.org/10.1242/jcs.260668.

(290) Cui, G.; Strickland, K. M.; Vazquez Cegla, A. J.; McCarty, N. A. Comparing ATPase Activity of ATP-Binding Cassette Subfamily C Member 4, Lamprey CFTR, and Human CFTR Using an Antimony-Phosphomolybdate Assay. *Front. Pharmacol.* **2024**, *15*, 1363456. https://doi.org/10.3389/fphar.2024.1363456.

(291) Voynow, J. A.; Shinbashi, M. Neutrophil Elastase and Chronic Lung Disease. *Biomolecules* **2021**, *11* (8), 1065. https://doi.org/10.3390/biom11081065.

(292) Lin, W.; Chen, H.; Chen, X.; Guo, C. The Roles of Neutrophil-Derived Myeloperoxidase (MPO) in Diseases: The New Progress. *Antioxid. Basel Switz.* **2024**, *13* (1), 132. https://doi.org/10.3390/antiox13010132.

(293) *Quick-RNA Miniprep Kit*. ZYMO RESEARCH. https://www.zymoresearch.com/products/quick-rna-miniprep-kit (accessed 2024-06-27).

(294) *QuantiTect Reverse Transcription Kit*. https://www.qiagen.com/us/products/discovery-and-translational-research/pcr-qpcr-dpcr/real-time-pcr-enzymes-and-kits/reverse-transcription-cdna-synthesis-qpcr/quantitect-reverse-transcription-kit (accessed 2024-06-27).